ISSN 1512-1127

საქართველოს გეოფიზიკური საზოგადოების ჟურნალი

სერია ბ. ატმოსფეროს, ოკეანისა და კოსმოსური პლაზმის ფიზიკა

JOURNAL
OF THE GEORGIAN GEOPHYSICAL SOCIETY

Issue B. Physics of Atmosphere, Ocean and Space Plasma

ტომი 16ბ 2013
vol. 16B 2013

საქართველოს გეოფიზიკური საზოგადოების ჟურნალი

სერია ბ. ატმოსფეროს, ოკეანისა და კოსმოსური პლაზმის ფიზიკა

მისამართი:
საქართველო, 0193, თბილისი, ალექსიძის ქ. 1,
საქართველოს მეცნიერებათა აკადემიის მ. ნოდიას სახ. გეოფიზიკის ინსტიტუტი
ტელ.: 33-28-67; 94-35-91; Fax; (99532 332867); e-mail: ***avtokor@ig.acnet.ge***

ჟურნალის შინაარსი:
ჟურნალი მოიცავს ატმოსფეროს, ოკეანისა და კოსმოსური პლაზმის ფიზიკის ყველა მიმართულებას. გამოქვეყნებული იქნება: კვლევითი წერილები, მიმოხილვები, მოკლე ინფორმაციები, დისკუსიები, წიგნების მიმოხილვები, განცხადებები.

გამოქვეყნების განრიგი და ხელმოწერა:
სერია (ბ) გამოიცემა წელიწადში ერთხელ.
ხელმოწერის ფასია (უცხოელი ხელმომწერისათვის) 50 დოლარი, საქართველოში – 10 ლარი, ხელმოწერის მოთხოვნა უნდა გაიგზავნოს რედაქციის მისამართით.

ЖУРНАЛ ГРУЗИНСКОГО ГЕОФИЗИЧЕСКОГО ОБЩЕСТВА

серия Б. Физика Атмосферы, Океана и Космической Плазмы

Адрес:
Грузия, 0193, Тбилиси, ул. Алексидзе, 1.
Институт геофизики им. М. Нодия АН Грузии
Тел: 33-28-67; 94-35-91; Fax: (99532) 332867; e-mail: *avtokor@ig.acnet.ge*

Содержание журнала:
Журнал охватывает все направления физики атмосферы, океана и космической плазмы. В журнале будут опубликованы научные статьи, обозрения, краткие информации, дискуссии, обозрения книг, объявления

Порядок издания и условия подписи:
Том серии (Б) издается по одному номеру в год.
Подписная цена 50 долларов США, включая стоимость пересылки.
Заявка о подписи высылается в адрес редакции.

JOURNAL OF THE GEORGIAN GEOPHYSICAL SOCIETY

Issue B. Physics of Atmosphere, Ocean and Space Plasma

Address:
M. Nodia Institute of Geophysics, Georgian Academy of Sciences, 1 Alexidze Str., 0193 Tbilisi, Georgia
Tel.: 33-28-67; 94-35-91; Fax: (99532) 332867; e-mail: ***avtokor@ig.acnet.ge***

Scope of the Journal:
The Journal is devoted to all branches of the Physics of Atmosphere, Ocean and Space Plasma. Types of contributions are: research papers, reviews, short communications, discussions, books reviews, announcements**.**

Publication schedule and subscription information:
One volume issue (B) per year is scheduled to be published.
The subscription price is 50 $, including postage.

Journal of the Georgian Geophysical Society,
Issue B. Physics of Atmosphere, Ocean and Space Plasma, v.16b, 2013, pp 3-12.

Dynamical processes developed in the easternmost part of the Black Sea in warm period for 2010-2013

Avtandil A. Kordzadze, Demuri I. Demetrashvili, Aleksandre A. Surmava

Iv. Javakhishvili Tbilisi State University, M. Nodia Institute of Geophysics,
1, Aleksidze Str., 0160, Tbilisi, Georgia, e-mail:aasurmava@yahoo.com

Abstract

In the paper the prognostic hydrophysical fields in warm period for 2010-2013, calculated on the basis of the regional forecasting system of the Black Sea state for the easternmost part of the Black Sea, are analyzed. The analysis of these results shows that the regional circulating processes in the warm and cold periods are in the certain degree different. In the warm period the main element of the regional circulation is frequently the Batumi anticyclonic eddy which predetermines a specific hydrological mode in this part of the Black Sea, but except this eddy here strongly non-stationary processes of generation, evolution, and dissipation of cyclonic and anticyclonic vortexes of different sizes permanently develop.

1. Introduction

In [1-5] the regional forecasting system of the dynamical state for the Black Sea easternmost part was described, which is developed at M. Nodia Institute of Geophysics of Iv. Javakhishvili Tbilisi State University. The regional forecasting system provides 3 days' forecast of sea current, temperature and salinity with 1 km spacing for this water area (the regional area of forecasting is separated from the open part by the western liquid boundary coinciding approximately with the meridian 39.08° E). As a result of functioning of the forecasting system the database with significant volume of prognostic hydrophysical fields is created, which by high spatial - temporary detailing reflects development of dynamic processes in the Georgian sector of the Black Sea and its adjacent water area for 2010-2013. In [6-8] the some features of regional circulating processes are investigated on the basis of the analysis of this database. The analysis of calculated prognostic fields for 2010-2013 allows to reveal the basic features of variability of dynamic processes in the easternmost water area of the Black Sea. General regularity is that during the entire year in the considered sea water area the non-stationary processes develop, where there is a continuous generation, evolution and disappearance of cyclonic and anticyclonic eddies of different sizes, but the circulating structure in the sea upper layer is different in warm (April - October) and cold (November - March) seasons of the year.

The main goal of the paper is to investigate in more detail dynamical processes developed in the easternmost part of the Black Sea during the warm period for 2010-2013 on the basis of the analysis of forecasted hydrophysical fields. Thus, this paper may be consider as continuation of the researches started in [6-8].

2. Results and Discussion

The regional model of Black Sea dynamics, which is the core of the regional forecasting system [1-5], uses a grid having 215 x 347 points on horizons with 1 km spacing. On the vertical the non-uniform grid with 30 calculated levels on depths: 2, 4, 6, 8, 12, 16, 26, 36, 56, 86, 136, 206, 306,…, 2006 m are considered. The time step is equal to 0.5 h.

The analysis of results of calculated forecasted fields for 2010-2013 shows, that in the early spring begins to be formed the specific structure of the surface regional circulation, which

considerably differs from circulation of the cold period. The main component of the regional circulation in the warm season is frequently the Batumi anticyclonic eddy which usually arises in March or April and in the most cases persists during the all warm season. It disappears in process of approach of a cold season in October, but sometimes in the second half of November. The Batumi eddy is one of the quasi-stable anticyclonic eddies generated on the coastal side of the Rim current and is characterized by more stability and intensity among the coastal eddies in the Black Sea [9, 10]. There are also other cyclonic and anticyclonic eddies of different sizes generated and evaluated in the easternmost part of the Black Sea.

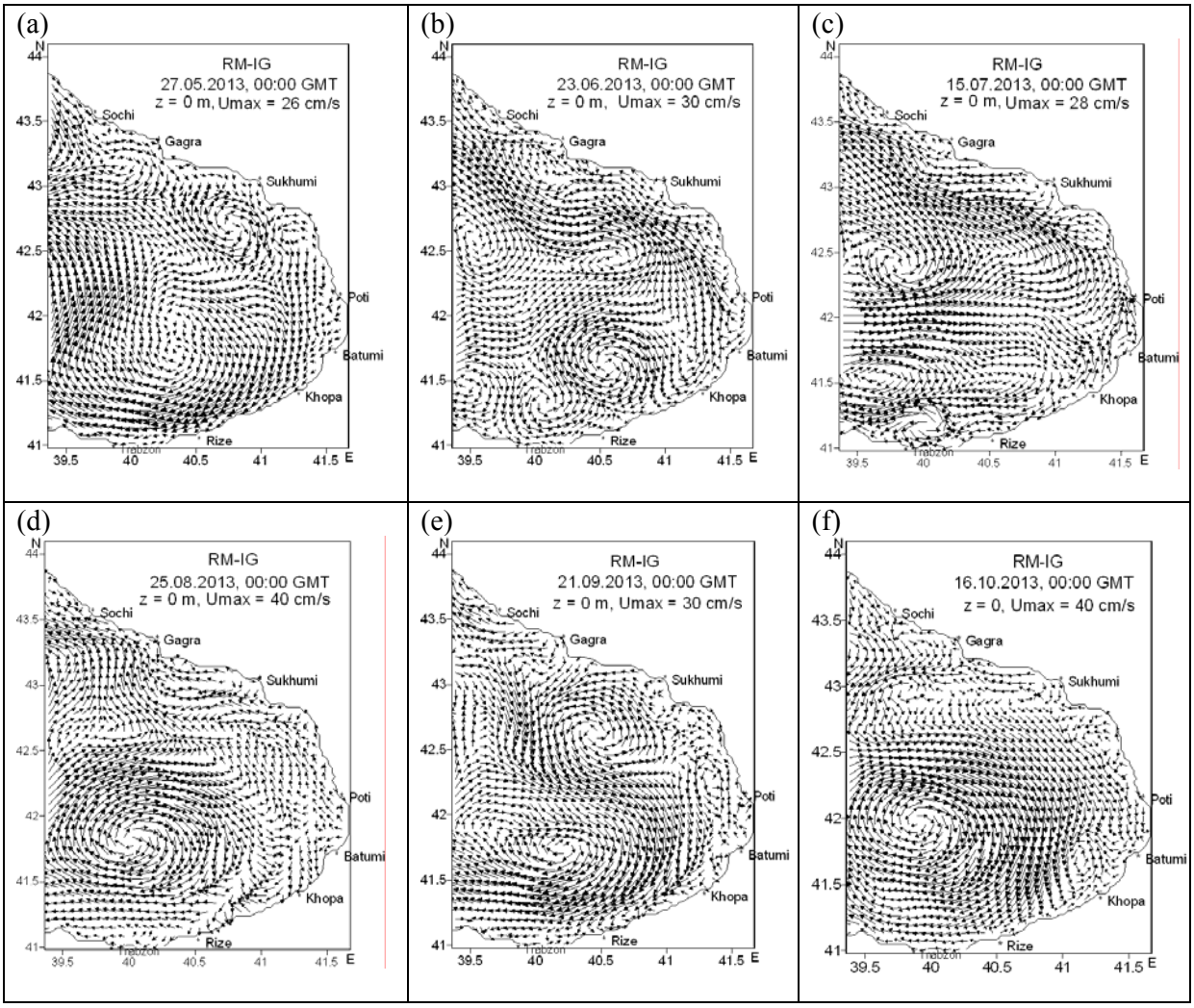

Fig.1. The evolution of the surface regional circulation in the easternmost part of the Black Sea in
2013: (a) – May 27, (b) – June 23, (c) – July 15, (d) – August 25, (e) – September 21,
(f) – October 16.

Figs. 1-4 evidently illustrate the evolution of the regional surface circulation in the warm season for 2010-2013 in the easternmost part of the Black Sea. In 2013 the Batumi eddy began to be formed practically in March in the south part of the considered easternmost water area and in April was a little bit increased in the sizes up to a diameter 60-80 km. It should be noted that the generation of the anticyclonic eddy in this area was also observed in the winter season, but it has not received the further development and has disappeared. Fig.1 illustrates further evolution of the regional circulation in May, and summer and autumn months. Except for the Batumi eddy, in May

in water area near the city of Sukhumi there is observed formation of the small anticyclonic eddy (Fig.1a). Formation of such eddy near Sukhumi is also noted in [9]. Besides, there are also very small nearshore unstable eddies near Gagra and in the south water area from Sukhumi. We have to note that along the

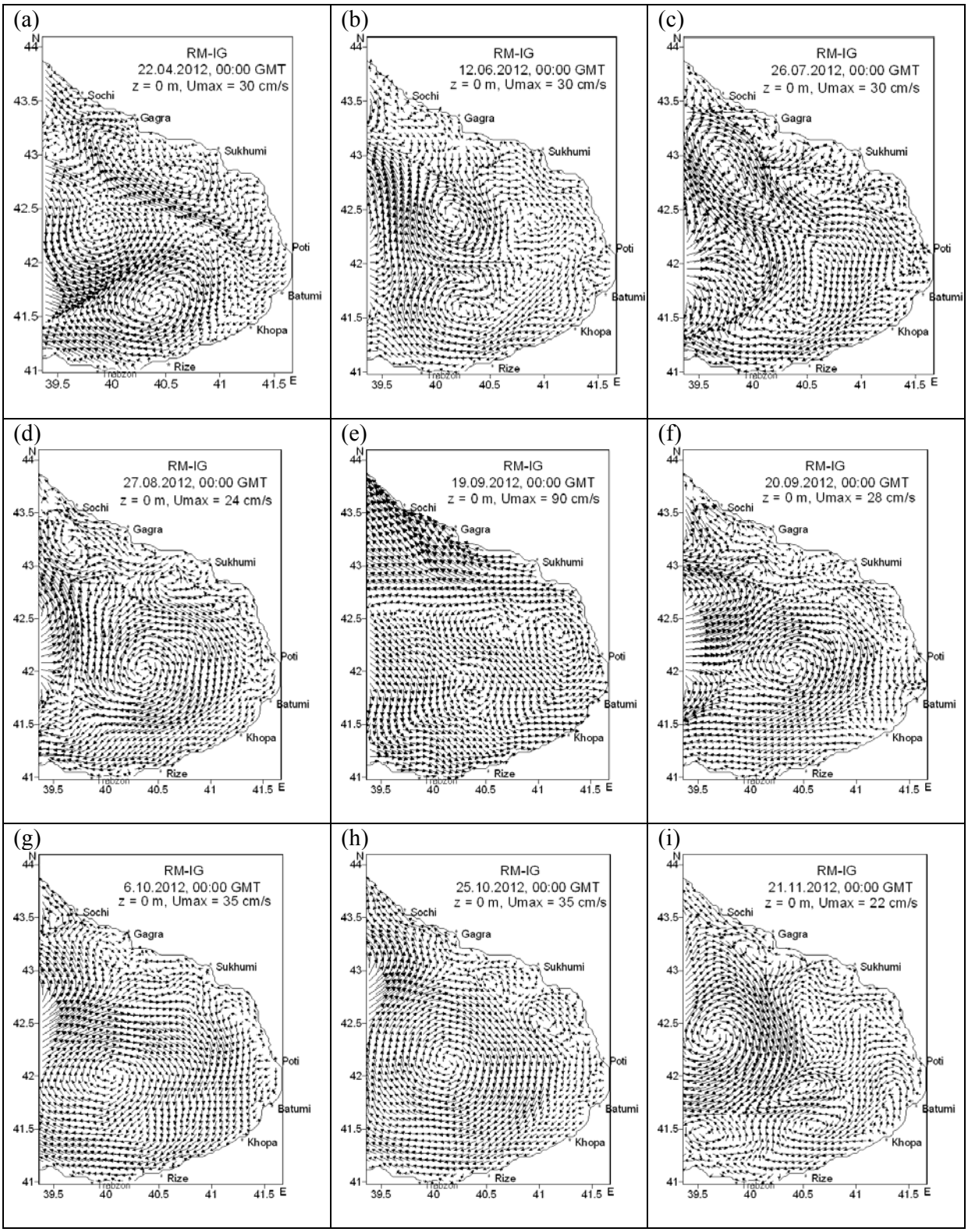

Fig.2. The evolution of the surface regional circulation in the easternmost part of the Black Sea in

2012: (a) - April 22, (b) – June 12, (c) – July 26, (d) – August 27, (e) – September 19, (f)- September
20, (g)- October 6, (h) – October 25, (i) – November 21.

Caucasus shoreline the formation of the narrow zone is very often observed, where generation of small unstable eddied are taking place. About such phenomenon was noted in [3, 6-8]. The Batumi eddy in June 2013 was less intensive then in May 2013, but in June the formation of other cyclonic and anticyclonic eddies was observed (Fig. 1b). These eddies were with diameter about 25-40 km and were exposed to fast changes.

The structure of 2013 summer circulation appreciably differed from circulation structure of the previous years by that the Batumi anticyclonic eddy in July circulation was practically absent (Fig. 1c). Since August the Batumi eddy arose again (Fig.1d) and became more intensive in September and October (Fig. 1e and 1f). In circulating pictures the formation of small coastal vortical formations along the Caucasian coast is well visible as well**.** For example, there are well visible the cyclonic eddies near the city of Poti (Fig.1e), between Sukhumi and Poti (Fig.1f), near Khopa (Fig.1f). These small coastal eddies have time of few days' existence and quickly disintegrate. It should be noted that the formation of analogical small eddies with a diameter of 2-8 km were observed in the Gelendzhik region in the autumns seasons of 2007-2008 using methods of hydrophysical investigations [11]. The Black Sea circulation in the easternmost water area in the warm season for 2013 differed with that the disintegration of the Batumi eddy in this year began in the late autumn. The weakening of intensity of the Batumi eddy and transformation of circulation to a new mode characteristic for the cold period was not observed up to the end of November.

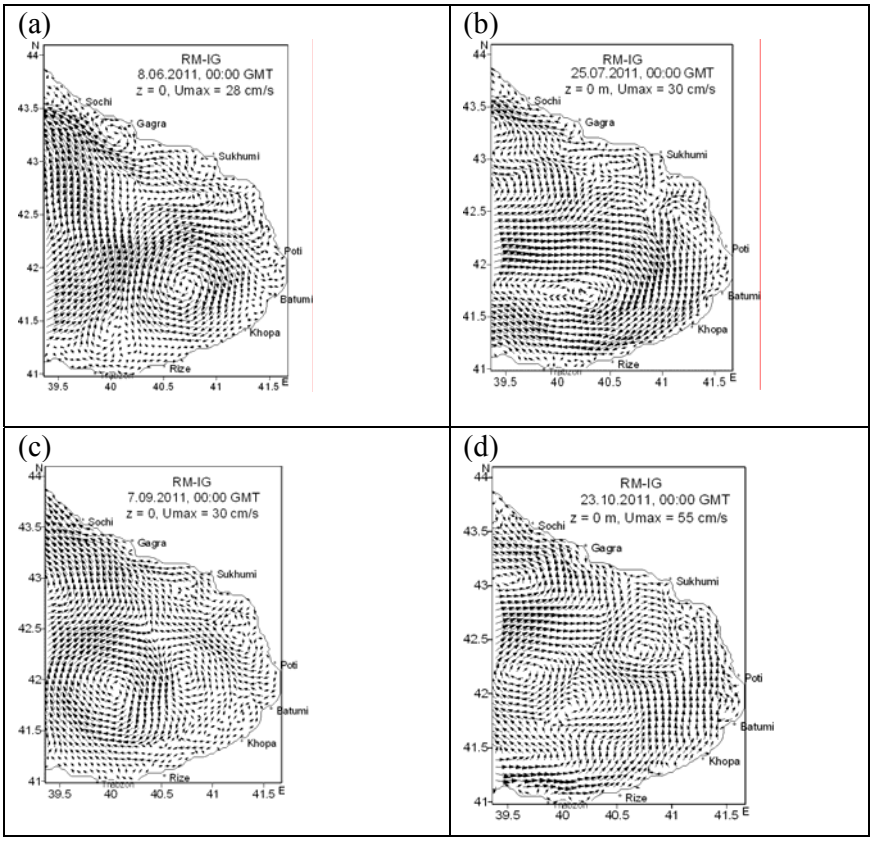

Fig.3. The evolution of the surface regional circulation in the easternmost part of the Black Sea in 2011: (a) - June 8, (b) - July 25, (c) – September 7, (d) – October 23.

In 2012 the common features of the regional circulation during the warm season (Fig. 2) were similar to 2013 warm season regional circulation (Fig.1), but differed by some specific

features. The generation of the Batumi eddy was observed by the end of March in the southwestern part of the considered area. In April this anticyclonic eddy grew in the sizes and was present throughout the month. From Fig.2a is well visible very interesting circulating structure formed on 00:00 GMT, 22 April 2012: there is formed specific vortex structure, which has a form of the dipole consisting from cyclonic and anticyclonic eddies. These eddies plays a role of obstacle, between of which the current is passing through narrow strip. Therefore, here a zone of the current intensification with speed about 30 cm/s is observed. Analogical phenomenon is observed in the second narrow zone between one of the components of the dipole – cyclonic eddy and relatively small anticyclonic eddy formed near Sukhumi, were the high speeds of the current are observed too. In the middle of May, the anticyclonic eddy amplified and by the end of the month weakened. At the beginning of summer 2012, the Batumi anticyclonic eddy was stretched along the meridian and as a result, in mid-June two anticyclonic eddies were formed (Fig.2b). At the beginning of July, the Batumi eddy was observed in the northwestern part of the considered easternmost water area and by the end of July this vortex extended

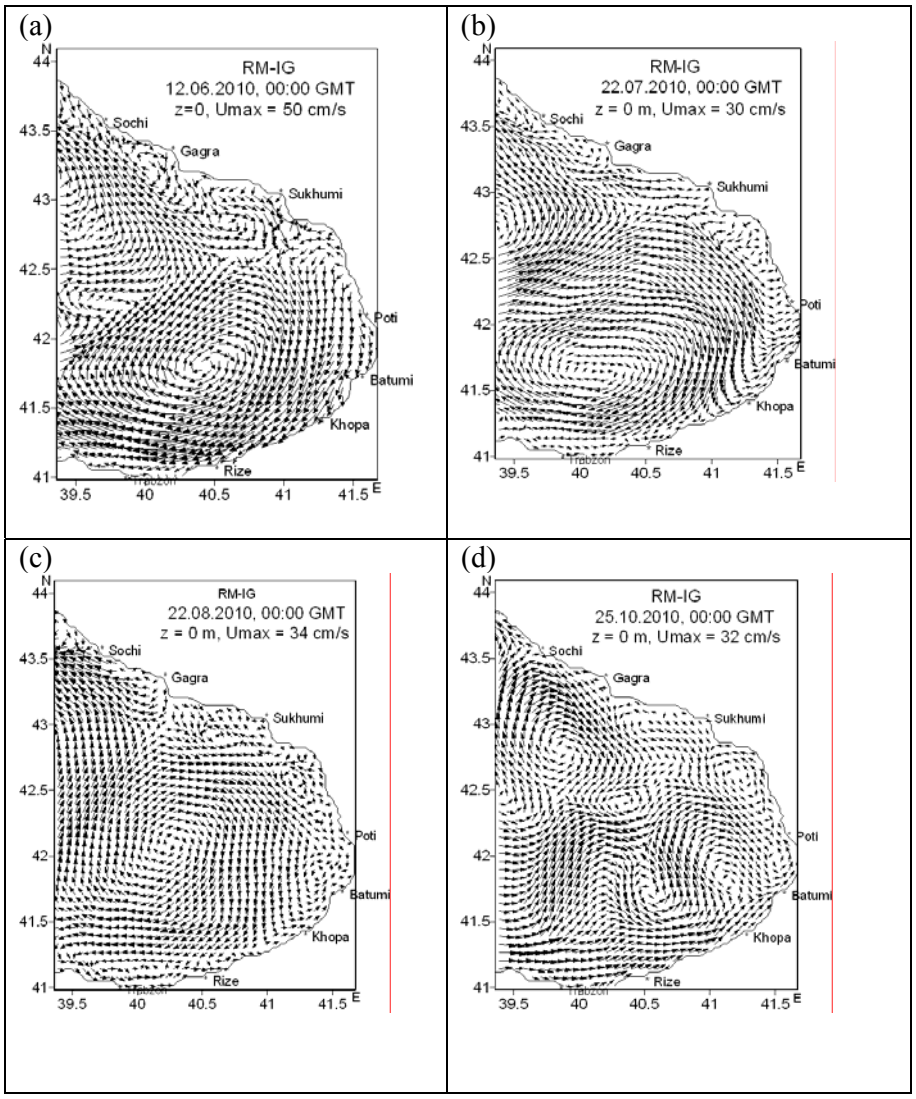

Fig.4. The evolution of the surface regional circulation in the easternmost part of the Black Sea in 2010: (a) - June 12, (b) - July 22, (c) - August 22, (d) - October 25.

in a southern direction (Fig.2c). In August the Batumi eddy was observed in the central area with diameter about 100 km (Fig.2d). The arrangement and intensity of the Batumi eddy was practically kept during September except for some cases.

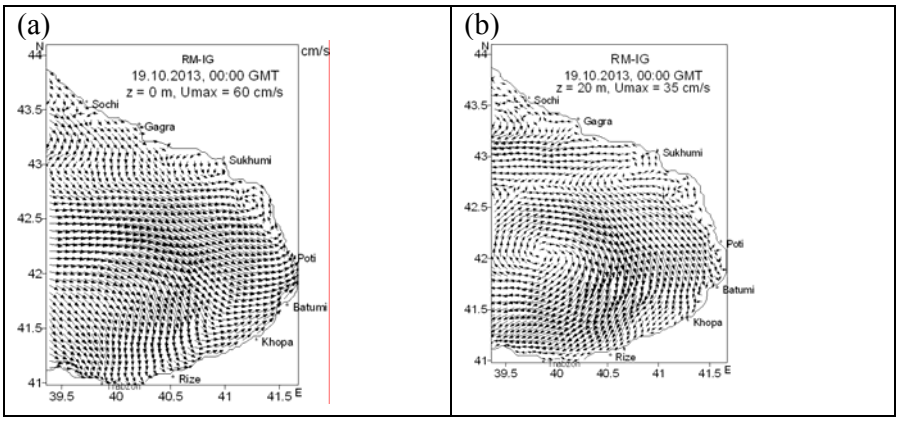

Fig.5. The surface circulation in the easternmost part of the Black Sea on 19 October 2013 on horizons (a) z = 0 m and (b) z = 20 m.

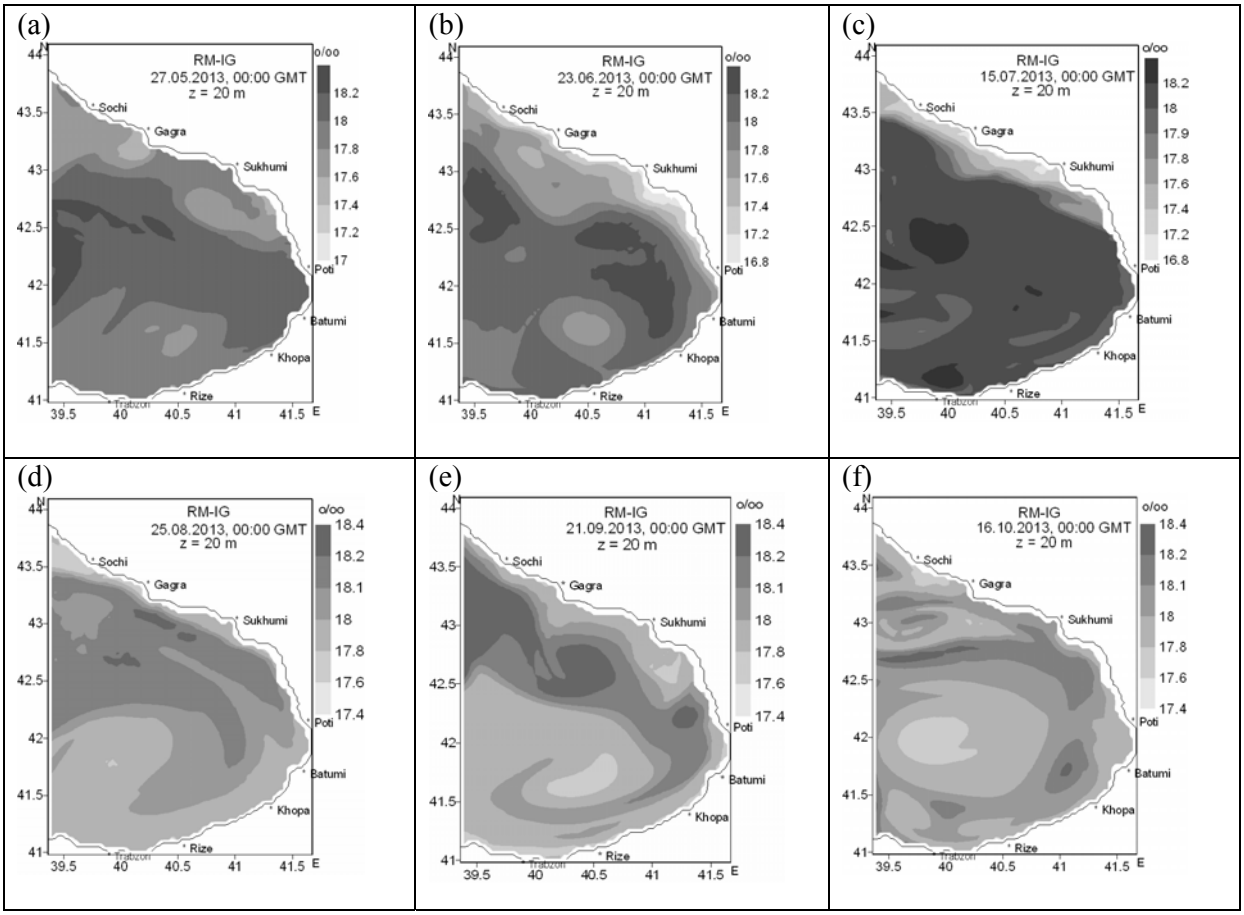

Fig. 6. The evolution of the salinity field on z = 20 m in the easternmost part of the Black Sea in 2013: (a) - May 27, (b) - June 23, (c) -July 15, (d) - August 25, (e) - September 21, (f) - October 16.

In Figs. 2e and 2f are shown circulation patterns in two next days - on 19 and 20 September 2012, when the surface circulating structures were significantly different in these days. On 19

September the Batumi eddy practically did not exist, but the next day it was well advanced. It is possible to explain these phenomenon by sharp change of meteorological conditions above the Black Sea during this short time interval. Strong winds developed on 19 September 2012 (Fig.2e) provided disappearance of the Batumi eddy and strengthening of the sea current speed up to 60 cm/s. After the atmospheric wind became less intensive the eddy was restored for the short period of time (Fig.2f). In October the Batumi eddy became more intensive and has covered almost all easternmost areas (Fig.2g and 2h) except for a narrow zone of small vortex formations along the Caucasus sealine. This zone plays a role of the interfering factor for the right peripheral current of the Batumi eddy to reach the Georgian coast. The Batumi eddy existed in November 2012 too, but in the sizes it decreased and its centre moved to north – west (Fig. 2i). From Fig.2i is well visible that except for this eddy, in the considered part of the sea basin other cyclonic and anticyclonic eddies of the rather smaller sizes are also formed. By the end of November 2012 the gradual disintegration of this eddy was observed and circulation was transformed to circulation of the cold period.

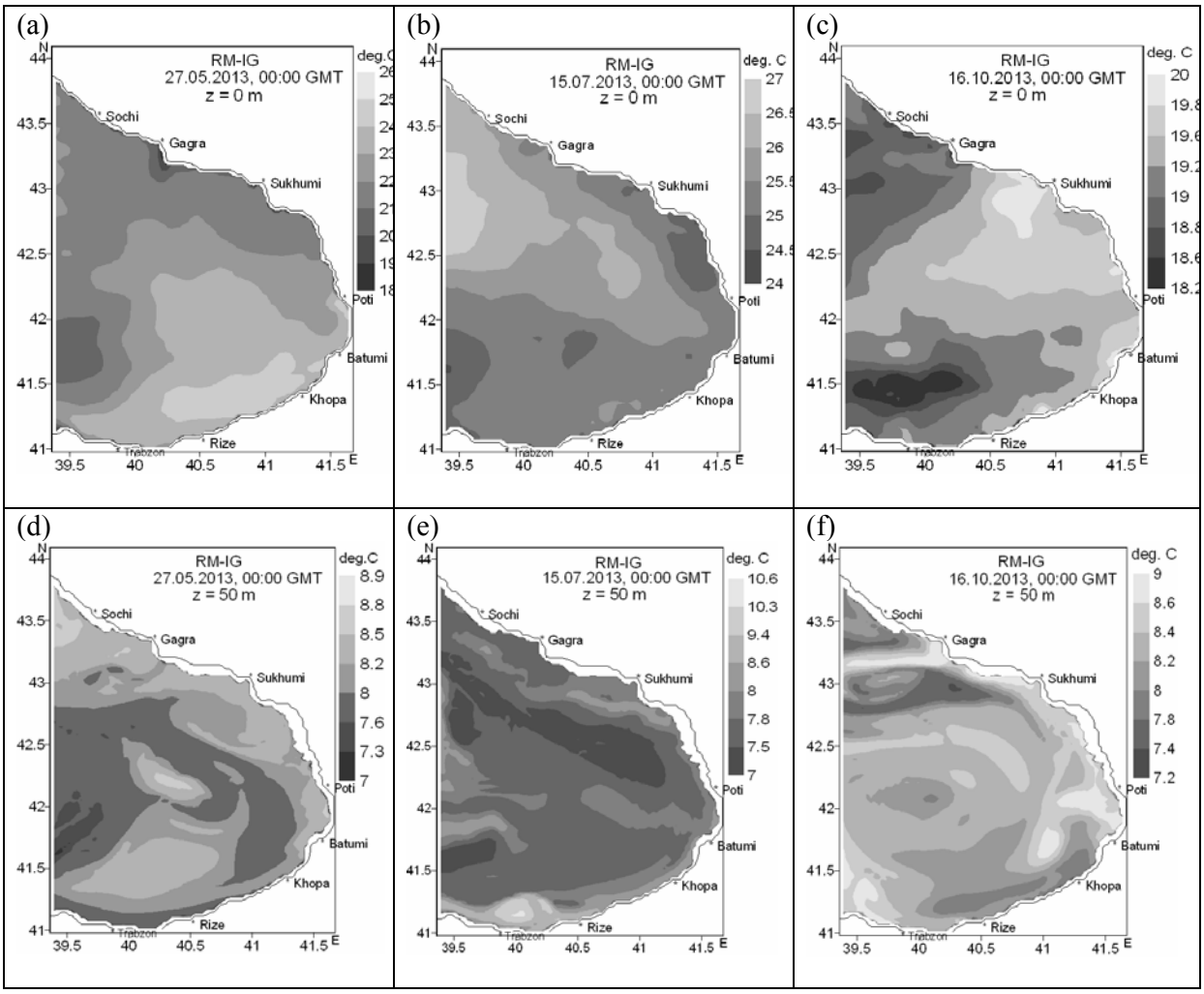

Fig. 7. The evolution of the temperature field in the easternmost part of the Black Sea in 2013: (a) - z = 0, May 27; (b) - z = 0, July 15; (c) - z = 0, October 16; (d) - z = 50 m, May 27; (e) - z = 50 m, July 15; (f) - z = 50 m,October 16.

Fig.3 Illustrates the evolution of the regional circulation in the easternmost part of the Black Sea during June-October 2011. The summer circulation structure in 2011 was characterized relatively by more expressed anticyclonic eddy. This eddy began disintegration at the beginning of

October and as a result in this month the regional circulation was already transformed into the current with small vortexes and the circulating mode already had structure characteristic for a cold season (Fig.3e).

Unlike summer circulation for 2011-2013 summer circulation in 2010 was characterized by sharply distinguished features [7]. The main feature was that the Batumi eddy was the steadiest and most intensive vortical formation during all summer period (Fig.4). It achieved maximal intensity in August and covered the significant part of the considered regional area. In the October the disintegration of the Batumi eddy was observed. The warm season of 2010 was especial not only from the point of view of the regional circulating characteristics of the easternmost part of the Black Sea, but also abnormal meteorological conditions. The summer 2010 was very hot last decades not only in Georgia, also on the territory of Europe. In [7] the opinion was stated that the anomalous temperature regime obviously influenced the mode of evaporation and precipitation, and, eventually, the thermohaline conditions were favorable for the formation of an intense anticyclonic vortex. The opinion on a paramount role of atmospheric thermohaline forcing on formation and evolutions of the Batumi anticyclonic eddy becomes more argued by numerical researches carried out in [12], which have shown significant sensitivity of the Batumi eddy generation to variable thermohaline conditions.

Strong winds over the Black Sea can disappear the Batumi eddy only in the sea uppermost layer, but in lower layers it is kept practically without change. This fact illustrates Fig.5, where circulation patters corresponding to 00:00 GMT, 19 October 2013 are shown on the sea surface and on the horizon z = 20 m. During 19 October the strong winds operated over the Eastern Black Sea. From Fig.5 is well visible that strong winds provided the disappearance of the Batumi eddy on z = 0 m and amplification of the surface current speed up to 60 cm/s, but on z = 20 m the Batumi eddy was kept practically without change. The maximal current speeds have decreased within upper 20 m layer from 60 cm/s up to 35 cm/s. Our previous investigations showed that when the Batumi eddy is very intensive formation it covers deep layers approximately up to 300 м, below which there is a disintegration of this eddy into smaller vortical formations [6-7].

With the purpose of illustrating annual evolution of the salinity field in Fig. 6 the evolution of the salinity field from May to October 2013 on z = 20 m is shown. The time moments, when the calculated salinity fields are shown in this Figure, are the same as in Fig.1. Comparison of Figs.1 and 6 shows good correlation between salinity and flow fields. There is obvious that generally, to the central area of cyclonic eddies corresponds waters with high salinity and to the central areas of anticyclonic eddies – the waters with low salinity. This fact is well known [13] and it is easy to explain by features of circulation processes. In particular, the upward flows in the center of the cyclonic eddy promote more salty waters being carried from deep layers in the upper layers and the downward flows in the central part of the anticyclones eddy transfer less salty waters from the upper layers downwards.

The temperature field is exposed to significant quantitative and qualitative changes during the warm season. This fact is illustrated by Fig.7, when the temperature fields are shown on z = 0 and z = 50 m. the character of change of the surface temperature is basically determined by heat exchange between the sea and atmosphere. on the horizon z = 50 m formation of the cold intermediate layer is evidently observed, which is well expressed in summer season end covers significant part of the considered area.

3. Conclusion

Researches carried out on the basis of the analyses of the database of hydrophysical fields created as a result of functioning of the Black Sea regional forecasting system led to increase our present level of knowledge about variability of the Black Sea circulation in its easternmost water area. Our investigations based on the database 2010-2013 showed that the regional circulation structure for the warm period from March to October is characterized by features distinctive from the cold period. The main element of the regional circulation for this period is frequently, the

Batumi anticyclonic eddy, the intensity and extent of which varieties during this period. The weakening and disappearance of this eddy occurred in September or October in 2010 and 2011, but in 2012 and 2013 it continued existing even in November. Apparently among the external factors the atmospheric thermohaline forcing has a prime role in formation and evolution of the Batumi eddy, but the strong winds developed over the Black Sea easternmost area, which render smoothing action on sea circulation, can reduce intensity of the Batumi eddy or temporarily disappear it. The Batumi eddy is observed up to depths approximately 300-400 kms, and in more deep layers the gradual transformation of the circulation structure and formation of more small eddies takes place. Most intensive and steady the Batumi eddy was in summer 2010, when was abnormal hot for last decades. In that case when the Batumi eddy is intensive and occupies a significant part of the easternmost water area, it forms the certain mode of salinity: salinity of waters considerably decreases in the central part of the vortex and the peripheral current of the Batumi eddy promotes penetration of more salty waters from the open part of the Black Sea in the easternmost part.

Our investigations show also that the anticyclonic formations similar to the Batumi eddy can also occur in winter season in the easternmost part of the Black Sea, but they are less steady and can not exist for the long period as in warm period.

Except for the Batumi eddy, there is continuously generation, deformation and disappearance of the cyclonic and anticyclonic vortex formations of difference sizes in the easternmost water area. Among such eddies are the small nearshore eddies which are frequently formed in the narrow zone along the Georgian shoreline.

Acknowledgement: The significant part of the results presented in the paper is received within the framework of Shota Rustaveli National Science Foundation (project number: AR/373/9-120/12).

References

[1] Kordzadze A. A., Demetrashvili D. I. Forecast of the Black Sea state in the Georgian coastal zone. Proceed. of the Intern. Conference **"**Environment and Global Warning**"** devoted 100-years of acad. T. Davitaia , Tbilisi, 15-17 September 2011.

[2] Kordzadze A. A., Demetrashvili D. I. Regional operational forecasting system of the state of the eastern part of the Black Sea. Ecological Safety of Coastal and Shelf Zones and Comprehensive Use of Shelf Recourses. Collected scientific papers. Iss.25, Vol.2 / NAS of Ukraine, MHI, IGS, OD IBSS. Sevastopol, 2011, pp.136-146 (in Russian).

[3] Kordzadze A. A, Demetrashvili D. I. Operational forecast of hydrophysical fields in the Georgian Black Sea coastal zone within the ECOOP. *Ocean Science*, 2011, 7, *pp.* 793- 803, www.ocean-sci.net/7/793/2011/ , doi: 10.5194/os-7-793-2011.

[4] Kordzadze A. A., Demetrashvili D. I. Coastal forecasting system for the easternmost part of the Black Sea. *Turkish Journal of Fisheries and Aquatic Sciences*. 2012, 12, pp.471-477, doi: 10.4194/1303-2712- v12_2_38. www.trjfas.org.

[5] Kordzadze A., Demetrashvili D. Some results of forecast of hydrodynamic processes in the Easternmost part of the Black Sea. J. Georgian Geophys. Soc., 2010, v.14b, pp. 37-52.

[6] Kordzadze A. A., Demetrashvili D. I., Kukhalashvili V. G. Circulation processes in the easternmost part of the Black Sea in 2011-2012. Results of simulation and forecast. J.Georgian Geoph. Soc., 2011-2012, v.15b, pp.3-13.

[7] Kordzadze A. A., Demetrashvili D. I. Short-range forecast of Hydrophysical fields in the eastern part of the Black Sea. Izvestiya AN, Fizika Atmosfery i Okeana, 2013, Vol. 49, No 6, pp.733-745 (in Russian).

[8] Kordzadze A. A., Demetrashvili D. I., Surmava A. A., Kukhalashvili V. G. Some features of a dynamic mode of the easternmost part of the Black Sea by results of modeling and forecast of hydrophysical fields for 2010-2013. Proceed. of M. Nodia Institute of Geophysics. Tbilisi, 2013, Vol. LXIV, (in Russian).

[9] Korotaev G., Oguz T., Nikiforov A., Koblinsky,C. Seasonal, interannual, and mesoscale

variability of the Black Sea upper layer circulation derived from altimeter data. J. Geophys. Res., 2003, v.108, No. C4, 3122, pp. 19-15.
[10] Staneva J. V., Dietrich D. E., Stanev E. V., Bowman M. J. Rim current and coastal eddy mechanisms in an eddy-resolving Black Sea general circulation model. J. Marine Systems. 2001, 31, pp. 137-157.
[11] Zatsepin A. G., Baranov V. I., Kondrashov A. A., Korzh A. O., Kremenetskiy V. V., Ostrovskii A. G., Soloviev D. M. Submesoscale eddies at the Caucasus Black Sea shelf and the Mechanisms of their generation. Okeanologiya, 2011, vol.51, N 4, pp.592-605.
[12] Demetrashvili D. I. Modeling of hydrophysical fields in the Black Sea. *J. Georgian Geophys. Soc.,* 2003, v.8b, pp.19-27.
[13] Kordzadze A. A. Mathematical modeling of the dynamics of sea currents (theory, algorithms, numerical experiments). Moscow, OVM AN SSSR, 1989, 218 p (in Russian).

Динамические процессы, развивающиеся в восточной части Черного моря в теплый период 2010-2013 гг.

Автандил А. Кордзадзе, Демури И. Деметрашвили, Александр А. Сурмава

Резюме

В статье анализируются прогностические гидрофизические поля, рассчитанные на основе региональной ситемы прогноза состояния Черного моря для крайне восточной части морского бассейна и соответствующие теплому периоду 2010-2013 гг. Анализ этих результатов показывает, что региональные циркуляционные процессы в теплый и холодный периоды года в значительной степени различны. В теплый период главным элементом региональной циркуляции часто является Батумский антициклонический вихрь, который предопределяет специфический гидрологический режим в этой части Черного моря, но кроме этого вихря здесь постоянно развиваются сильно нестационарные процессы генерации, эволюции и диссипации циклонических и антициклонических вихрей различных масштабов.

შავი ზღვის აღმოსავლეთ ნაწილში განვითარებული დინამიკური პროცესები 2010-2013 წწ. თბილ სეზონში

ავთანდილ კორძაძე, დემური დემეტრაშვილი, ალექსანდრე სურმავა

სტატიაში გაანალიზებულია 2010-2013 წწ. თბილი პერიოდის შესაბამისი პროგნოზული ჰიდროფიზიკური ველები, რომლებიც გამოთვლილია შავი ზღვის მდგომარეობის პროგნოზის რეგიონული სისტემის საფუძველზე ზღვის უკიდურესი აღმოსავლეთ ნაწილისათვის. ამ შედეგების ანალიზი გვიჩვენებს, რომ რეგიონული ცირკულაციური პროცესები წლის ცივ და თბილ პერიოდებში მნიშვნელოვნად განსხვავდებიან. წლის თბილ პერიოდში ხშირ შემთხვევაში რეგიონული ცირკულაციის ძირითადი ელემენტია ბათუმის ანტიციკლონური გრიგალი, რომელიც განსაზღვრავს სპეციფიკურ ჰიდროლოგიურ რეჟიმს შავი ზღვის ამ ნაწილში, მაგრამ გარდა ამ გრიგალისა აქ მუდმივად ვითარდება სხვადასხვა მასშტაბის ციკლონური და ანტიციკლონური გრიგალების გენერაციის, ევოლუციისა და დისიპაციის ძლიერი არასტაციონარული პროცესები.

Journal of the Georgian Geophysical Society,
Issue B, Physics of Atmosphere, Ocean and Space Plasma, v.16, 2013, pp. 13-23

Numerical investigation of the air possible pollution in case of large hypothetical accidents in some industrial territories of the Caucasus

Avtandil A. Kordzadze, Aleksandre A. Surmava, Vepkhia G. Kukhalashvili

Iv. Javakhishvili Tbilisi State University, M. Nodia Institute of Geophysics,
1, Aleksidze Str., 0160, Tbilisi, Georgia, e-mail:aasurmava@yahoo.com

Abstract

The distribution of anthropogenic passive and radioactive pollutions emitted in the atmosphere in the industrial centers of the Caucasus are investigated by means of a regional model of development of atmospheric processes in the Caucasian Region and the equation of substance displacements. The distribution of pollution is simulated in cases for the four basis synoptic situations, when the south, east, west and south-east background large scale winds blow.

It is shown, that the relief of the Caucasus significantly influences the trajectory of the pollution displacements. The north-west oriented Main Caucasian Range resists air motion to the north, constrains the pollution substance in the boundary layer to flow around the Main Caucasian Range from the west or east sides. The Likhi Range resists the distribution of the pollution emitted in atmosphere in the vicinity of t. Poti and causes its displacement to the south. It is obtained that 48 hours are mainly necessary for the pollution cloud to overflow the South Caucasus and distribute over the territory of the North Caucasus.

The radioactive pollute can fall out mainly in the central, southeast and northwest parts of the South Caucasus. The zone of the radioactive deposition is extended along the background wind and deformed by the influence of the relief. The maximal length of the zone of a significant deposition of radioactive substance equals approximately 750 km in case of the background south-east wind and 350 km in other cases. The maximum width of this zone approximately equals 150 km.

1. Introduction

The South Caucasus is the region that has a high hazard-index of the environmental pollution. There, on a small territory of the Earth the some industrial centers, gas and oil-producing regions are located. The oil and gas are transfer by railway and pipelines between the main Caucasus and Minor Caucasus Ranges. The railways also used to transfer many other hazardous substances from Europe to the Middle Asia via Georgian seaports Batumi and Poti, and Azerbaijan seaport Baku.

The Armenian Nuclear Power Plant (ANPP) is one of such hazardous objects, also. It lies in Metsamor 20 km from the capital of Armenia Yerevan on a one of the Earth's most earthquake-prone terrain. The accidents of the Chernobyl, Fukushima and other power plants show that the nuclear reactors carry the great potential hazards for population and environment especially when plants are located in the seismic hazardous regions [1, 3]. ANPP, as a very dangerous object, was closed after earthquake in Armenia in 1988 but was reopened in 1995. ANPP has one of just a few remaining Soviet nuclear power reactors that were built without the primary containment structures. Consequently, the hazard of the radioactive pollution of the environment in the Caucasus becomes highly probable event. The neighbouring countries, Turkey and Azerbaijan, protest the operation renewal of ANPP, and Azerbaijan has called on the UN Security Council to suspend the operation of

the nuclear power plant in Metsamor [4-6].

The pollution substances emitted in the atmosphere of the Caucasus can be distributed over the large territory of the region and cause the significant negative influence of health of population and ecological state of an environment. Therefore, an investigation of the distribution of pollution emitted in the atmosphere of Caucasus in result of an accident has significant practical importance. Some questions of this problem were considered in [7].

In the present article we continue an approach made in [7]. Using the regional model of evolution of the atmospheric processes in Caucasus region [8] and equation of distribution of substance in the atmosphere we will simulate and investigate the dispersion of the passive and non-passive pollution substances in the atmosphere of the Caucasus Region.

2. Formulation of the Problem

The equation of the substance transport in the atmosphere is

$$\frac{\partial C}{\partial t}+u\frac{\partial C}{\partial x}+v\frac{\partial C}{\partial y}+(\tilde{w}\quad\frac{W_{sed}}{h})\frac{\partial C}{\partial \zeta}=\mu\Delta C+\frac{\partial}{\partial \zeta}\nu\frac{\partial C}{\partial \zeta}\quad+\alpha C\ ,\qquad(1)$$

where t is time; x, y , and z are the axes of the Cartesian coordinate directed to the east, north and vertically upwards, respectively; $\zeta=(z-\delta)/h$ is the dimensionless vertical coordinate; δ is height of the relief; $H(t, x\ y)$ is the height of the tropopause; $h=H-\delta$; u, v and $\tilde{w}$ are the wind velocity components along the axes x, y, and ζ , respectively; C is the concentration of substance; the index $\alpha=\ln 2/T_{rad}$ is the decay constant; T_{dec} is a decay period; W_{sed} is an aerosol deposition velocity. μ and ν are the horizontal and vertical turbulent diffusion coefficients, respectively. u, v, $\tilde{w}$, μ and ν are known functions of temporary and spatial coordinates; W_{sed} determined by Stockes formula, T_{dec} is known parameter.

The initial and boundary conditions for (1) are following:

$C=C_0$ if $0\le t\le T$ and x, y and $\in\Omega$;

$\partial C/\partial x=0$ if $x=0,\ X$; $\partial C/\partial y=0$ if $y=0, Y$; (2)

$\nu\partial C/\partial =A|v_0|C$ *if* $\zeta=0$; $\partial C/\partial\varsigma=0$ if $\zeta=1$.

Where Ω is the rectangular area where the emission of the pollutant substance takes place; $v_0=(u^2(t,x,y,0)+v^2(t,x,y,0))^{1/2}$ is the wind velocity on the upper boundary of the surface layer $\zeta=0$, *X* and *Y* are the lateral boundaries of the area of solution along the axes x and y, respectively. The coefficient $\mu=5\times10^3$ m^2/s; A= 0.001.

Equation (1) is numerically integrated using the implicit monotonic scheme [6]. The finite-difference-grid with horizontal and vertical steps equal to 10 km and 1/17, respectively, is used. The time step is 1 min. For the every time step the wind velocity components were calculated by the Regional Model of the atmospheric processes [8].

The equation (4) shows that any functions that equal to $C(t,x,y,\zeta)\times$ const obey also the equation (4). Therefore we will consider $C(t,x,y,\zeta)$ as unit value and then in order to obtain the real magnitude of concentration we must multiply the calculated field of C on a const .

The equations (1) is solved in the coordinate systems **(t, x, y,** ζ**)** and *(t, x, y, z)*, respectively.The initial and boundary conditions, the values of background fields, and methods of parameterization of the separate meteorological processes are selected in accordance with specific objectives of modeling.

3. Analyses of results

Since we limit ourselves by the Caucasus Region, the calculations were performed for the winds that are most characteristic for this territory. For this purpose we consider the cases of the passive substance emission in the vicinity of t. Poti, Batumi and Baku, and emission of the radioactive nuclide ^{131}I in the vicinity of t. Metsamor (Fig.1). The calculations are performed for a period up of 48 h. The pollutant substances during first 6 h are emit in the atmosphere into rectangular prism area Ω (10 km×10 km×0.8km), in the vicinity the sources. The initial concentration $q_0 = 100$ arbitrary unit (a.u.). Such situation can take place in cases of accident on the oil tankers or the oil storages and in other processes of transfer of the air pollutants.

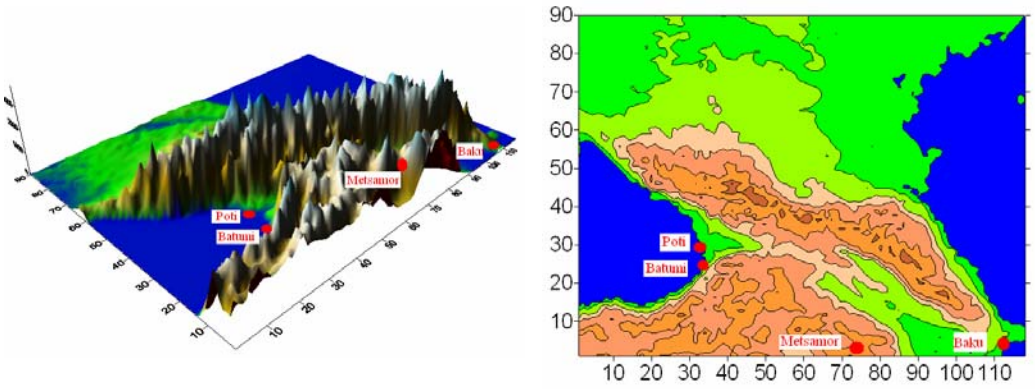

Fig. 1. The Caucasus Region relief and topography (heights in km) and the location of the ANPP (the red circle).

The temporary change of the spatial distributions of the pollutant substance emitted in the atmosphere in the vicinity of seaport t. Poti is shown in Fig. 2. This figure shows that the main part of the pollution cloud in the surface level $z \leq \delta$ is moved to the north-west direction and at t = 24 h is distributed over the north-east part of the Black Sea and west part of the Main Caucasus. The small part of the pollution substances is carried out to the east over the Colchis Lowland and passing over the Rikoti Pass is spread on the East Georgia over Kartli Plain. The maximal value of the concentration for 24 h interval of time in the boundary layer is decreased from its initial value 100 a.u. to 70 a.u. (z = 1 km).

For t = 48 h and 144 h the concentration of the pollution over the Georgian territory is significantly decreased (about 10^4 times when t = 144h). On the surface level the maximal value of the concentration is in interval 0.16-0.18 a.u. and it is obtained in the north of the modeling area over the north- east part of the Caspian Sea. In other areas the concentration is less 0.01 a.u. The concentration decreases with a height and on the level z = 3 km, the concentration 0.01 a. u. is obtained only in a small area over the north-east part of the Main Caucasus Range.

When the background northern wind blows (Fig. 3.) the spatial distribution of the pollution substance is significantly different than it is obtained in case of the western wind. The orography of the Main Caucasus and Likhi Ranges resists the pollution cloud movement to the north and east, and constrains the pollution distribution from north to south. During all 48 h the pollution clouds are located over the west part of Georgia, northern Turkey and Armenia.

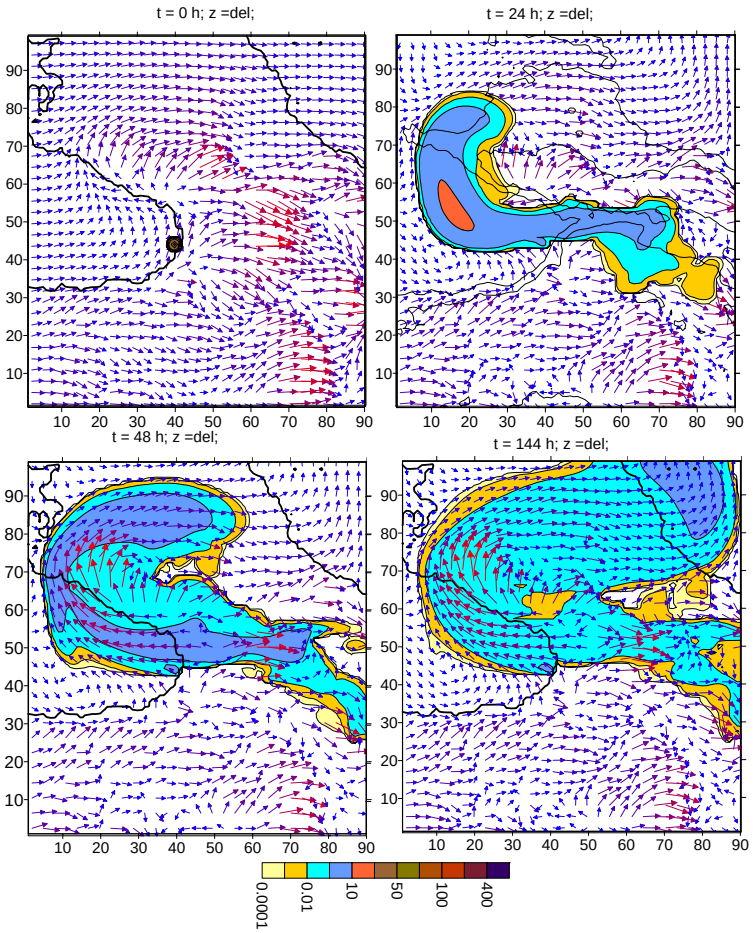

Fig. 2. The spatial distribution of the concentration C(a.u.) of the passive pollution substance emitted in the vicinity of t. Poti in t = 0, 6, 24 and 48 h on the levels $z = \delta(x, y)$ and 2 km in case of the background western wind.

If the emission takes place in the vicinity of t. Batumi the pollution cloud during first five-six hours moves to the north along the east shore of the Black Sea and after the process of the pollution the diffusion continues as it was described in case of emission in the vicinity of t. Poti. In Fig. 4 and 5 the spatial distributions of passive pollution substance emitted in the vicinity of t. Baku in cases of the eastern and south-eastern winds are shown. By these figures we can conclude that the pollution emitted in atmosphere in the vicinity of t. Baku distributes in the South Caucasus atmosphere when the eastern wind blows. The pollution cloud during first 6 h is located in the vicinity of the Absheron Peninsula into area heaving 300 km length and 150 km width. Then the pollution cloud moves along the northern incline of the Minor Caucasus Range over the Mugami and Shirvani Lowlands, and occupies almost all territory of the Armenia and Azerbaijan. When t = 48 h, the pollution is distributed over of the South Caucasus from the Caspian Sea to the Black Sea.

The pollution cloud when the south-east background wind takes place, the displacement is over the territory of the North Caucasus (Fig. 5). At t = 24 h the pollution cloud is distributed over the Dagestan and Chechen Autonomy Republics, and reaches the south-west part of the Stavropol Krai. Then the pollution moves to the north-west and at t = 48 it is distributed over the territory of the Stavropol Krai. The zone of a maximal concentration is in the centre of the pollution cloud and its magnitude varies in interval 0.1a.u.– 10 a.u.

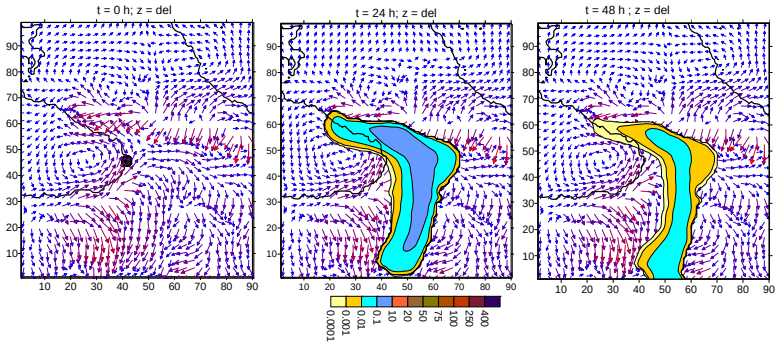

Fig. 3. The spatial distribution of the concentration C(a.u.) of the passive pollution substance emitted in the vicinity of t. Poti in t = 0, 24 and 48 h on the atmosphere surface level $z = \delta(x, y)$ in case of the background northern wind.

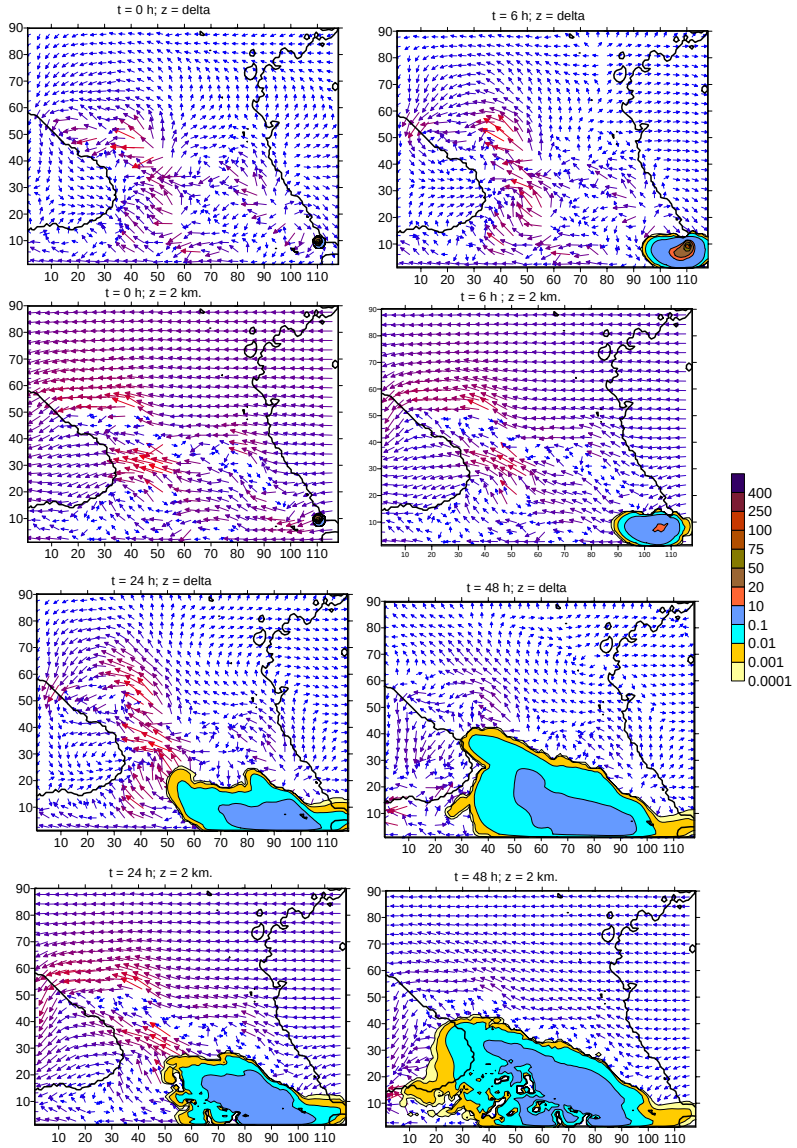

Fig. 4. The spatial distribution of the concentration C(a.u.) of the passive pollution substance emitted in the vicinity of t. Baki t = 0, 6, 24 and 48 h on the atmosphere surface level $z = \delta(x, y)$ and z = 0 in case of the background eastern wind.

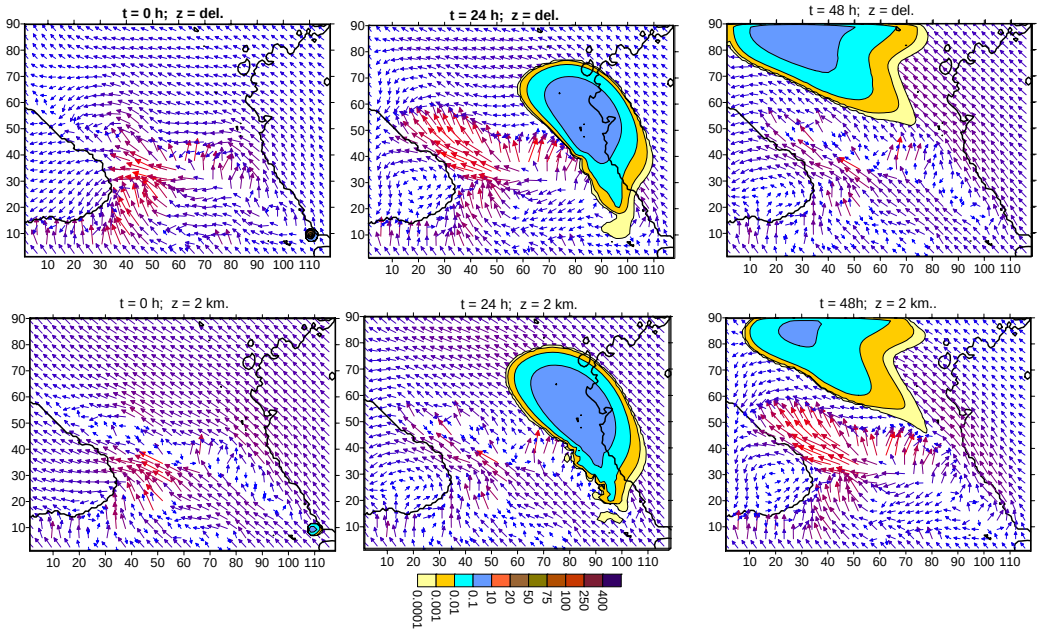

Fig. 5. The spatial distribution of the concentration C(a.u.) of the passive pollution substance emitted in the vicinity of t. Baku in t = 0, 24 and 48 h on the atmosphere surface level z $=\delta(x,y)$ and 2 km in case of the background north wind.

The possible pollutions of the Caucasus Region in case of hypothetical emission I^{131} from the Armenian Power Plant were also simulated. Were considered emissions of the iodine particles with a radius equal 10 μm. A corresponding fall-out velocity of the particles calculated by Stokes formula is equal to W_{sed} = 1cm/s [9], the decay period T_{rad} =8.02 day.

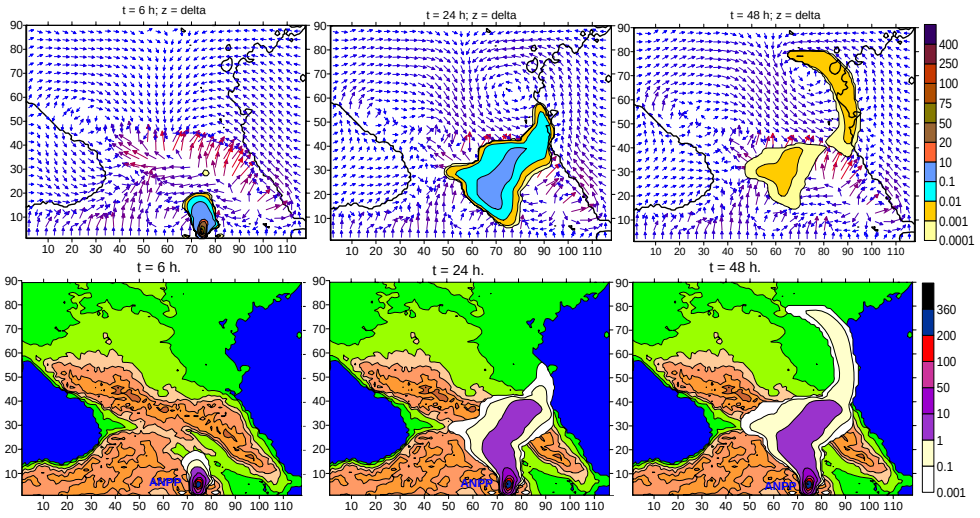

Fig. 6. The spatial distribution of the concentration in the atmosphere surface layer (upper row) and surface density of the sediment on the earth (lower row) of the radioactive pollution I^{131} (a.u./m^2) at t = 0, 24 and 48 in case of the background southern wind.

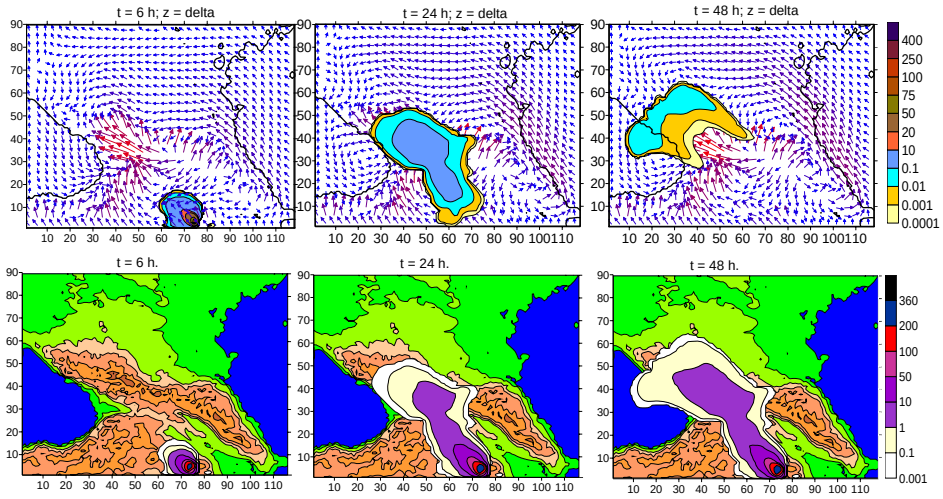

Fig. 7. The spatial distribution of the concentration in the atmosphere surface layer (upper row) and surface density of the sediment on the earth (lower row) of the radioactive pollution I^{131} (a.u./m^2) at t = 0, 24 and 48 in case of the background south-east wind.

Figs. 6 and 7 show the distribution of the concentration of I^{131} and the wind fields obtained in case of the background south wind on the surface level $z = = \delta(x, y)$ and surface density of the sediment radioactive pollution at the moment of the time t = 6, 24 and 48 h, respectively. In Fig. 6 we can note that during 6 h the radioactive emission forms the radioactive cloud over ANPP that by wind and atmosphere turbulence is stretched to the north along the direction of the background wind. The radioactive cloud is located into ellipsoid columns area with maximum horizontal sizes 100 km and 170 km along x and y coordinates, respectively. By calculation it is also obtained that the vertical width of the radioactive cloud approximately equals 9 km. The magnitude of the concentration is equal to 100 a. u. into the emission plume in the 4 km layer and exponentially decreases on the periphery of this area.

After six hours the radioactive cloud increases step-by-step in size because of the movement along the wind and atmospheric turbulence. Simultaneously the concentration of the pollutant substance decreases in result of the processes of dispersion, deposition, and radioactive-decay. The radioactive cloud in the surface layer at t = 24 h is obtained over the central part of the South Caucasus mainly up of the territory of the north part of the Armenia and the east part of Georgia. Over this surface layer the size of the polluted atmosphere volume gradually increases up to 6 km. The zone of the higher concentration is displaced from the South Caucasus to the North Caucasus (from the East Georgia to the Stavropol Kray). The magnitude of maximal concentration during the 24 hours is decreased down to 0.48 a. u.

During two days (Fig. 6) the radioactive cloud mainly moves over territory of the North Caucasus and localizes over the Stavropol Kray. In the South Caucasus the radioactive cloud is obtained over a small territory of the central part of Georgia. The concentration there is small and is varying between 0.001a.u. - 0.006 a.u. The maximal value of concentration in the plume of pollution caused by the processes of dispersion, deposition, and radioactive-decay is decreased about 2000 times from 100 a. u. to 0.05a.u. The spatial distribution of the radioactive deposition on the earth surface is shown in Fig. 6, also. As it is shown here, the main part of the radioactive dust falls on the territory of Armenia and Georgia into the stripe of 100 km in width and about 400 km in length. The radioactive ingredient up to 12 h falls out only on the territory of the South Caucasus. After this time the process of fallout begins also on the territory of the North Caucasus. After 20 h

from the beginning of emission the radioactive fallout happens mainly on the territory of the North Caucasus and at t = 48 h the surface density of ^{131}I on the territory of the north slope of the Main Caucasus Range reaches 10 a.u. on 1 m^2. The radioactive deposition on the territory of the South Caucasus ends after 30 h.

The results of the numerical modeling of the radioactive diffusion when the background south-east wind blows, are show in Fig.7. The calculation shows that the radioactive pollution moves to the north firstly on the territory of Armenia and then over the central and north-west parts of the Caucasus Region. At t = 24 h the main part of atmosphere over Georgia is polluted by radioactive ingredient. Further, the radioactive cloud falls over the Main Caucasus Range, splits in two parts and at t = 48 h we obtain two zones of the radioactive pollution. One of these zones is located over the Black Sea and another over the north slope of the Main Caucasus Range. The radioactive deposition obtained at t =0, 24 h and 48 h are also shown in Fig. 7. We see that in 48 h the radioactive fallout mainly happens on the territory of the north part of Armenia, the south, central, and north-west parts of Georgia. The small amounts of the radioactivity are also deposited on the territories of Turkey and Russian. The maximal magnitude of he surface density at t = 48 h is equal to 360 a.u./m^2 and is obtained in the vicinity of the source of emission.

4. Discussion

In the article the possible pollution of the atmosphere of the South Caucasus is numerically simulated. It considers the four main cases when the pollution is distributed from four, most hazardous in sense of accident, industrial territories. As the regional air circulation significantly depends of the large scale background wind we have limited our simulation by cases of regional transport of pollution into the South Caucasus. We consider the cases when the background wind in the surface layer of the atmosphere is $\vec{v} \leq 5$ m/s.

The numerical modeling shows that the regional orography significantly deforms the trajectory of the pollution cloud. In case of the background western wind the pollution emitted in the atmosphere in the vicinity of t. Poti can by distributed in the surface layer of atmosphere both to east and to north-west. The pollution emitted in the atmosphere in the vicinity of t. Baku can cause a pollution of the South Caucasus atmosphere only in one case – when it blows the background eastern wind. When the background south- east wind blows the pollution distributes in the North Caucasus and it does not cause a pollution of the South Caucasus Atmosphere.

The simulation shows the radioactive emission from ANPP pollutes the atmosphere of the South Caucasus in two cases when the east and south-east winds take place. The radioactive pollution falls out mainly on the central, southeast, and northwest parts of the South Caucasus. The zone of radioactive deposition is extended along the background wind and deformed by influence of the relief. In case of the background southeast wind the maximal length of the zone of significant deposition of radioactive substance approximately equals 750 km, and 350 km in other cases. The maximal width of this zone equals approximately 150 km. The concentration of deposited radioactive element in the zone of radioactive fall-out decreases from 360 a.u./m^2 down to 1 a.u./m^2.

For the reason of the absence of the observation data it isn't possible to estimate a quantitative reality of the obtained results. But, having compared the trajectory and shape of the radioactive cloud (Fig. 8.) obtained in this article and in other works [10, 11], it may be concluded that the obtained results properly describe the main features of the radioactive dispersion process in the Caucasus. Therefore, the model and results obtained here can be considered as first approximation for the further investigation and practical use. In addition, in our opinion, the spatial grid step 10 km is rather large for adequate description of studied process over complex terrain of Caucasus. We intended simulating the diffusion processes of radioactive pollution with the horizontal step approximately equal to 1-5 km in the atmosphere of the Caucasus.

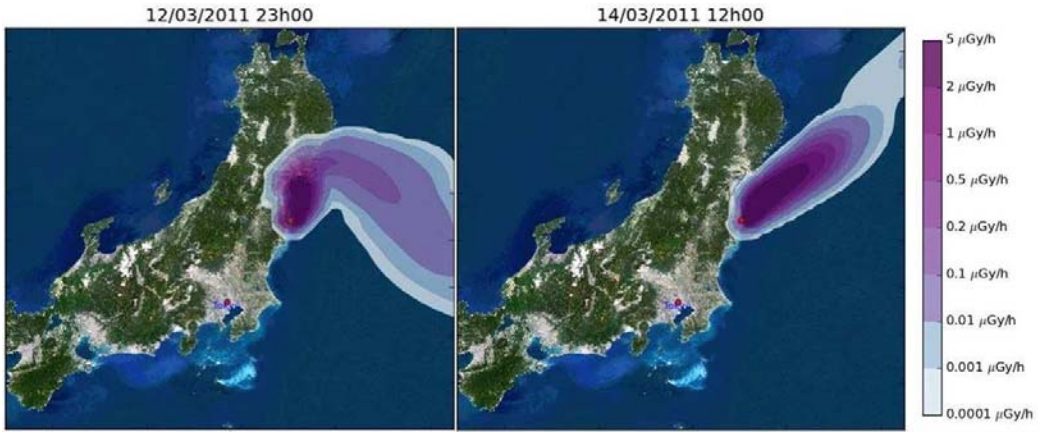

Fig. 8. Atmospheric dispersion of radionuclides from the Fukushima-Daichii Nuclear Power Plant [10].

Acknowledgement: This work has been supported by Shota Rustaveli National Science Foundation: (Grant AR/373/9-120/12).

.

References

[1] UNSCEAR, 1988 REPORT. Annex D. Exposures from the Chernobyl accident. http://www.unscear.org/docs/reports/1988annexd.pdf

[2] Fukushima Accident 2011. http://www.world-nuclear.org/info/fukushima_accident_inf129.html.

[3] Sources and Effects of Ionizing Radiation. United Nations Scientific Committee on the Effects of Atomic Radiation. UNSCEAR - 2008. Peported to General Assembly with Scientific Annexes/ 179 p. http://www.unscear.org/docs/reports/2008/11-80076_Report_2008_Annex_D.pdf

[4] Turkey's Energy Minister: "Metsamor Nuclear Power Plant in Armenia must be closed" http://en.apa.az/news.

[5] Turkey warns Armenia about 40-year old nuclear plant http://www.trdefence.com/2011/04/18 /turkey-warns-armenia-about-40-yo-nuclear plant/.

[6] Azerbaijan Urges UN to Halt Armenian Nuclear Plant http://en.rian.ru/world/20120423/172992199.html.

[7] A. A. Surmava, B. A. Mishveladze, T. P. Davitashvili. Numerical modeling of the pollution transfer in the Caucasus atmosphere emitted from hypothetical source in case of background western wind. J. Georgian Geophys. Soc., 2009, v. 13 B,pp. 15-21.

[8] A. Surmava, A. A. Kordzadze, D. I. Demetrashvili, V. G. Kukhalashvili. Numerical investigation of the influence of the Caucasus relief on the distribution of hydrometeorological fields. Izvestia, Atmospheric and Oceanic Physics, 2007, v. 43, No. 6, pp. 722-730.

[9] Berliand M. E. The current problems of the atmospheric diffusion and diffusion of atmosphere.Gidrometeoizdat, Leningrad. 1975, 448 p.

[10] Y. Roustan, C. Birman, M. Bocquet, Camille Birman, P. Tran. Atmospheric dispersion of radionuclides from the Fukushima-Daichii nuclear power plant. Map of ground deposition of caesium-137 for the Fukushima-Daichii accident. http://cerea.enpc.fr/en/fukushima.html.

[11] J. Brandt, J. H. Christensen, and L. M. Frohn. Modelling transport and deposition f cesium and iodine from Chernobyl accident using the DREAM model. Atmos. Chem. Phys. Discuss. 2002, v. 2, pp. 828-874. www. Atmos-che-phys.org/acpd/2/825 /.

კავკასიის ინდუსტრიულ ცენტრებში ჰიპოთეტური მძლავრი ავარიების შემთხვევებში ჰაერის შესაძლო დაბინძურების რიცხვითი გამოკვლევა

ა.ა. კორძაძე, ა. ა. სურმავა, ვ. გ კუხალაშვილი

რეზიუმე

კავკასიაში ატმოსფერული პროცესების განვითარების რეგიონალური რიცხვითი მოდელისა, პასიური და რადიოაქტიური მინარევის გავრცელების განტოლების გამოყენებით შესწავლილია კავკასიის ატმოსფეროს შესაძლო დაბინძურება კავკასიის ინდუსტრიულ ცენტრებში დამაბინძურებელი ნივთიერებების ჰიპოთეტური ავარიული ამოფრქვევების შემთხვევებში. დაბინძურების გავრცელება შესწავლილია ოთხი ძირითადი სინოპტიკური სიტუაციის დროს, როდესაც ქრიან დასავლეთის, ჩრდილოეთის, აღმოსავლთის და სამხრეთის ფონური ქარები.

ნაჩვენებია, რომ კავკასიის რეგიონის რელიეფი ძლიერ მოქმედებს მინარევების გავრცელების ტრაექტორიაზე. ჩრდილო-დასავლეთით ორიენტირებული მთავარი კავკასიონის ქედი ეწინააღმდეგება რა ჰაერის მოძრაობას ჩრდილოეთის მიმართულებით აიძულებს დამაბინძურებელ ნივთიერებას ატმოსფეროს სასაზღვრო ფენაში გარსშემოედინოს ქედს ჩრდილო-დასავლეთისა და აღმოსავლეთის მხრებიდან და შემდგომ გავრცელდეს ჩრდილოეთ კავკასიაში. ლიხის ქედი, ეწინააღმდეგება რა ქ. ფოთში ამოფრქვეულ დამაბინძურებელ ნივთიერებას გავრცელდეს აღმოსავლეთით იწვევს დაბინძურების გავრცელებას სამხრეთით. ნაჩვენებია, რომ 48 საათია საჭირო იმისათვის, რომ დაბინძურების ღრუბელი გადაევლოს სამხრეთ კავკასიასა და გავრცელდეს ჩრდილოეთ კავკასიაში.

რადიოაქტიური ნუკლიდები შეიძლება დაილექოს სამხრეთ კავკასიის ცენტრალურ, სამხრეთ-აღმოსავლეთ და ჩრდილო-დასავ;ეთ ნაწილებში. რადიოაქტიური დანალექის ზონა არის გაჭიმული ფონური დინების გასწვრივ და დეფორმირებულია რელიეფის გავლენით. მნიშვნელოვანი რადიაციული დანლექის ზონის სიგრძე დაახლოებით 750 კმ-ს შეადგენს სამხრეთ-დასავლეთის ფონური ქარის შემთხვევაში და 350 კმ-ს სხვა შემთხვევებში. ამ ზონის მაქსიმალური სიგანე არ აღემატება 150 კმ-ს.

Численное исследование возможного загрязнения воздуха в случаях гипотетических крупных аварий в индустриальных центрах Кавказа

А. А. Кордзадзе, А. А. Сурмава В. Г. Кухалашвили

Резюме

С помощью региональной модели развития атмосферных процессов в Кавказском регионе, уравнений переноса пассивной и радиоактивной примесей исследовано возможное загрязнение атмосферного воздуха Кавказа в случаях гипотетических аварийных выбросов загрязняющих веществ в индустриальных центрах Кавказа.. Распространение загрязнения исследовано для четырёх основных синоптических ситуаций, когда имеются западный, северный, восточный и южный фоновые ветры.

Показано, что рельеф Кавказа в приземном слое атмосферы существенно влияет на траекторию распространения примесей. Ориентированный на северо-запад Большой

кавказский хребет, препятствуя перемещению воздуха на север, заставляет основную часть загрязнения обтекать препятствие с северо-взападной или с северо-восточной, стороны, и далее распространиться над территорией Северного кавказа. Лихский хребет препятствуя распространению загрязнения, выброшенного в атмосферу на восток, заставляет его перемещаться на юг. Получено, что проблизительно 48 часов нужны облаку загрязнения для перетекания через Южный кавказский хребет и распространения над Северным кавказом.

Основная масса радиоактивных веществ могут выпасть над центральной, северо-западной и юго-восточной частями Южного кавказа. Зоны радиоактивного осаждения вытянуты вдоль фоновых ветров и частично деформированы под влиянием рельефа территории. Максимальная длина зоны значительного выпадения радиоактивных веществ приблизительно равна 750 км в случае фонового юго-восточного ветра и - 350 км для других направлений фоновых ветров.

Journal of the Georgian Geophysical Society,
Issue B. Physics of Atmosphere, Ocean, and Space Plasma, v.16, 2013, pp.24-30

New data about the aeroionization characteristics of the territory of National Botanical Garden of Georgia as the factor of the expansion of its sanitation properties for the visitors

[1]A. Amiranashvili, [1]T. Bliadze, [1]V. Chikhladze, [1]Z. Machaidze, [1]G. Melikadze, [2]N.Saakashvili, [2]E.Khatiashvili, [2]I.Tarkhan-Mouravi, [3]Sh. Sikharulidze, [3]T. Nakaidze, [4]M. Tavartkiladze

[1] Iv. Javakhishvili Tbilisi State University, M. Nodia Institute of Geophysics, 1, Aleksidze Str., 0160, Tbilisi, Georgia, [2]Tbilisi Balneological Health Resort - Practical-Scientific Center of Physiotherapy, Rehabilitation and Medical Tourism of Georgia, [3]Institute of Botanic of Ilia University , [4] National Botanical Garden of Georgia

Abstract

Results of the preliminary studies of the content of light ions in air on the territory of the National Botanical Garden of Georgia are represented. Ion concentration was measured at 25 points over area 90 hectare, and also near the main waterfall at 33 points over area 1152 m^2. The maps of the distribution of the content of positive and negative light ions for the territory of waterfall and Botanical Garden as a whole are make. It is obtained that the content of ions in the Botanical Garden, especially in the gorge near the River Tsavkisi and waterfalls, corresponds to hygienic levels "minimally necessary" and "optimum". In the built-on parts of Tbilisi city at this time the content of ions its corresponded to the level "less than minimally necessary". Thus, the conducted investigations revealed the new functions of Tbilisi botanical garden for the visitors: sanitation, reducing and therapeutic. It is recommended in the future in the Botanical Garden make to more detail investigate the content of ions into different seasons of year taking into account weather conditions.

Key words: light ions concentration, tourism, health resorts

1. Introduction

The importance of study of the light ions content in the atmosphere is well known. The content of light ions in the atmosphere plays important role in molding of the physiological state of population. Simultaneously light ions are the indicator of the purity of air [1-4]. Regular observations of the parameters of atmospheric electricity (including air electrical conductivity) in Georgia after the Soviet Union decay were ended. In recent years, the experimental investigations of the content of light ions in air in Georgia were renewed [5-7].

For evaluating the health resort-tourist of the resources of Georgia in the correspondence with the contemporary requirements, the detailed studies of the ionizing state of the air medium of known, little-known and promising recreational-tourist regions are necessary. Special attention should be given to places with the waterfalls, fountains, national parks, preserves, forests, alpine regions, mountain gorges, the coast of rivers and sea, the tectonic breakings (increased concentration of Radon), karstic caves, etc., where the ionization level of air can be suitable for the sessions of ionotherapy [5-8].

Under the conditions of a "good weather" (cloudless or light cloud dry weather with the calm) in urban air the concentration of light ions is approximately 500 cm^{-3} , while in the rural locality -1000 cm^{-3} [1-3, 6,7,9]. Thus, from a biological point of view the condition in the city and a rural locality are completely different. The health of people depends on the concentrations and ratio between a quantity of positive and negative ions per unit of volume of air [4]. Under the "good weather" condition, the minimally necessary level of the sum light ions content for the favorable influence on the health is 1000 cm^{-3} and more (table 1).

Urban smokes cause the decrease of a quantity of negative ions. Ventilation in the compartments causes the decrease of a quantity of positive ions, without decreasing the concentration of negative ions [9].

In Tbilisi for the stationary point of the measurements (territory of cloud chamber laboratory of Mikheil Nodia Institute of Geophysics of Ivane Javakhishvili Tbilisi State University) cases for the favorable influence on the health not more than 30 % (without taking into account weather conditions). The distribution of the light ions content in Tbilisi city has very irregular nature and considerably depends on the level of air pollution, conditions of ventilation, etc. [7]. Therefore great practical value has searches for places in the environments of Tbilisi city with the content in air of light ions with the concentration of useful for the health of people. First of all it is expedient to investigate the existing health resort-tourist resources of Tbilisi city and its environments for the purpose of the development of their new possibilities as the sanitation-reducing functions. Subsequently should be continued the searches for similar places for their integration into the health resort-tourist infrastructure of city.

On the basis of that indicated above we have decided to conduct the preliminary analyses of the content of light ions on the territory of National Botanical Garden of Georgia (or Tbilisi Botanical Garden). Tbilisi botanical garden exists almost 400 years and this is one of the most dear places for the inhabitants of city and the guests of the Georgian Capital [10].

2. Method and date descriptipn

Light ions concentration (cm^{-3}) measurements in Tbilisi were conducted 4 times a day at height 3 floor of the building of the cloud chamber of the Institute of Geophysics (stationary point of measurement, 8 meters above the level of soil, 41.754º N, 44.927º E, the height - 450 m above sea level), into 9, 12, 15 and 18 hour (in the winter season - 17 hours), and in 20 points in different city locations. Stationary monitoring by Gerdien's type instruments was conducted. Mobile studies on the territory of Tbilisi Botanical Garden with the aid of the portable ions counter of the production of firm "AlphaLab, Inc." are conducted.

Work gives the results of two day measurements for Tbilisi (stationary point of measurement) and Tbilisi Botanical Garden. 30.07.2011 the measurements of the light ions concentration at 25 points in territory 90 hectare (1125x802 m) of Botanical Garden were carried out. 2.08.2011 the measurements of the light ions concentration at 33 points in territory 1152 m^2 (72x16 m) near main waterfall were carried out.

The following designations will be used below: n (+) - concentration of positive light ions, n (-) - concentration of negative light ions, n (+)/n (-) - coefficient of unipolarity.

3. Results

The results in Fig. 1-4 are given.

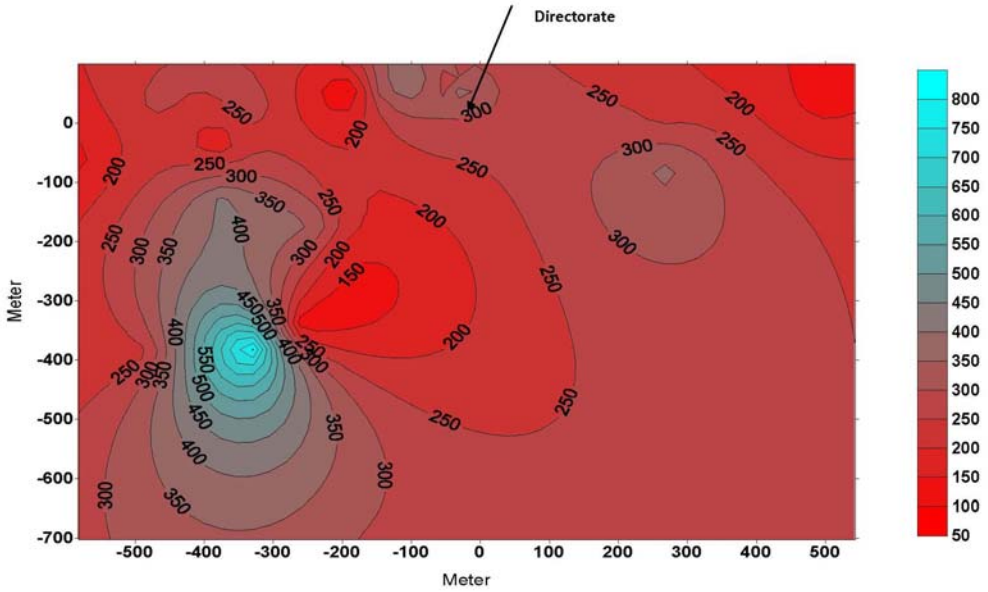

Fig.1 Distribution of positive light ions concentration in air in Tbilisi Botanic Garden

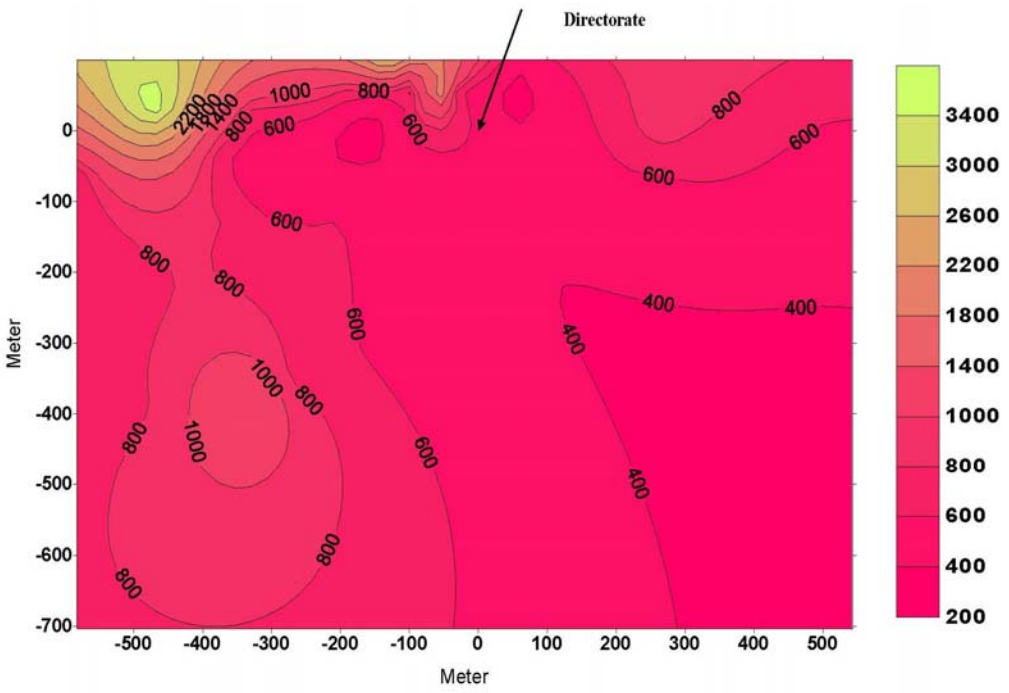

Fig.2 Distribution of negative light ions concentration in air in Tbilisi Botanic Garden 30.07.2011

Distribution of positive and negative light ions concentration in air in Tbilisi Botanical Garden 30.07.2011 in Fig. 1 and 2 are given. As follows from these figures on the territory of Botanical Garden the concentration of positive ions changes from 90 cm^{-3} to 825 cm^{-3} , with average value 281 cm^{-3} and negative - from 420 cm^{-3} to 3700 cm^{-3}, with average value 995 cm^{-3}. It is important to note that for the entire territory of Botanical Garden a quantity of negative ions predominates above the positive (coefficient of unipolarity changes from 0.07 to 0.92 with average value 0.37). This is a known effect the influence of vegetation on the formation of negative ions.

The high concentrations of negative ions near the main waterfall with the height of 24 m (1680-2350 cm^{-3}, coefficient of unipolarity = 0.14), the small waterfall (3700 cm^{-3}, coefficient of unipolarity =0.07) and also under the Tamara bridge (2900 cm^{-3}, coefficient of unipolarity = 0.13) are observed (minimally necessary – optimum, table 1).

Table 1. Content of Light Ions in Air and Their Physiological Action on the Human Organism

Ions concentration cm^{-3}		**Level**	**Physiological action**
n (+)	**n (-)**		
<300	<300	Less than the minimum	Fatigue, weakening attention, retarding of reactions, worsening in the memory, headache, the disturbance of the regime of blood pressure, etc.
400	600	Minimally necessary	Positive action, in particular during exceeding of the concentration of the negative ions above the positive
1500-3000	3000-5000	Optimum	Optimization of blood pressure, positive influence on the course of the diseases of respiratory organs, bronchial asthma, antiseptic action, etc.
≥50000	≥50000	Maximum	Negative reaction of organism

Without taking into account factor by hydro-ionization (21 measuring point) on the territory of Botanical Garden the concentration of positive ions changes from 90 cm^{-3} to 825 cm^{-3}, with average value 278 cm^{-3} and negative - from 420 cm^{-3} to 1350 cm^{-3}, with average value 930 cm^{-3}. Coefficient of unipolarity changes from 0.13 to 0.92 with average value 0.42.

Let us note that in Tbilisi on the stationary point of measurement 30.07.2011 from 12 through 18 hours on the average the ionic air composition was: n (+) = 370 cm^{-3}, n (-) = 460 cm^{-3}, n (+)/n (-) = 0.80 (less than the minimally necessary, table 1).

Distribution of positive and negative light ions concentration in air near the waterfall in Tbilisi Botanic Garden 2.08.2011 in Fig. 3 and 4 are given. As follows from these figures on the territory near of the main waterfall the concentration of positive ions changes from 200 cm^{-3} to 1200 cm^{-3}, with average value 704 cm^{-3} and negative - from 700 cm^{-3} to 4500 cm^{-3}, with average value 1800 cm^{-3}. Value of n (+)/n (-) varied from 0.1 to 0.86 with average value 0.48 (minimally necessary – optimum, table 1).

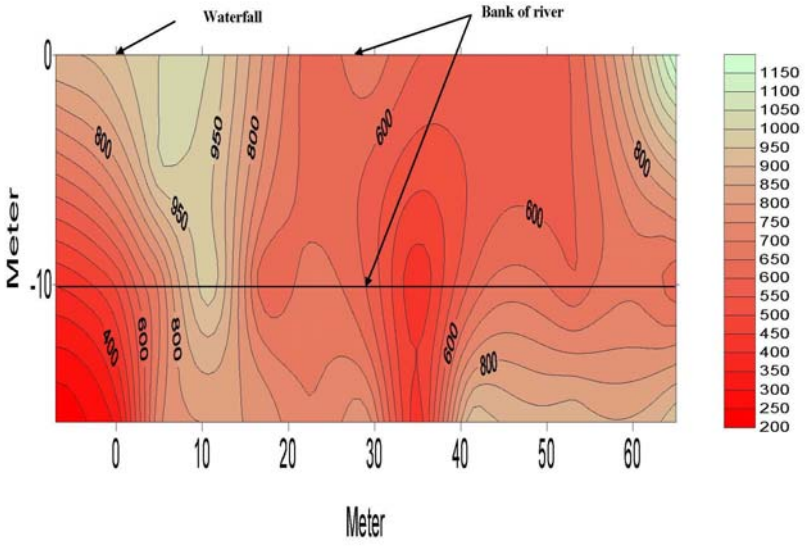

Fig.3 Distribution of positive light ions concentration in air near the waterfall in Tbilisi Botanic Garden 2.08.2011

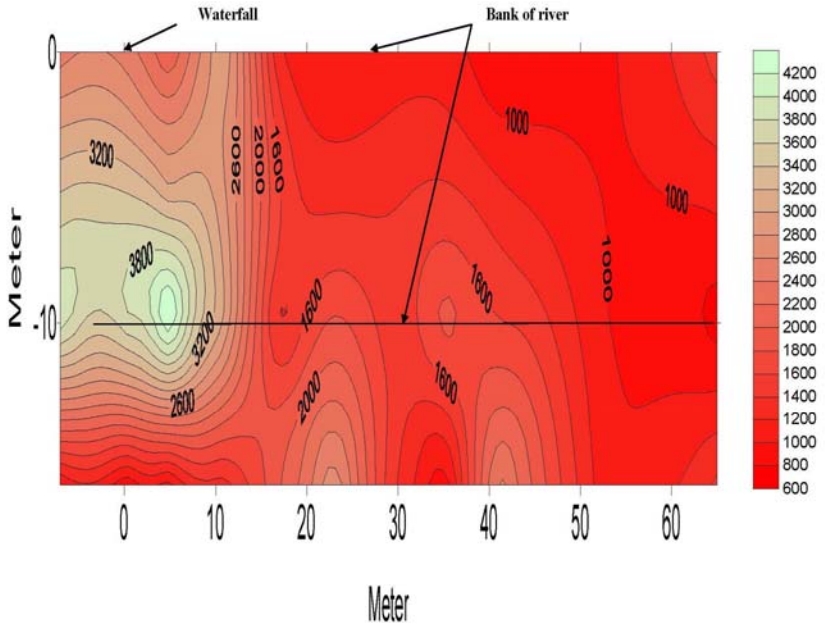

Fig.4 Distribution of negative light ions concentration in air near the waterfall in Tbilisi Botanic Garden 2.08.2011

In Tbilisi on the stationary point of measurement 2.08.2011 from 15 through 18 hours on the average the ionic air composition was: n (+) = 390 cm^{-3}, n (-) = 366 cm^{-3}, n (+)/n (-) = 1.07 (less than the minimally necessary, table 1).

It is interesting to note that the range of the concentrations of light ions on the territory of Botanical Garden is practically commensurate with the values of the content of ions in different health resort- tourist places of Georgia (Fig. 5).

Thus, Tbilisi Botanical Garden besides its previous known functions (science, excursion, leisure, tourism, etc.) can acquire the new: medical and sanitary. The territory of Botanical Garden as a whole completely satisfies the requirements of sanitation-reducing localities. Separate zones of Botanical Garden (near the waterfalls, in the separate places of the gorge of the River Tsavkisi, etc.) can be used also for therapeutic purposes - ionotherapy.

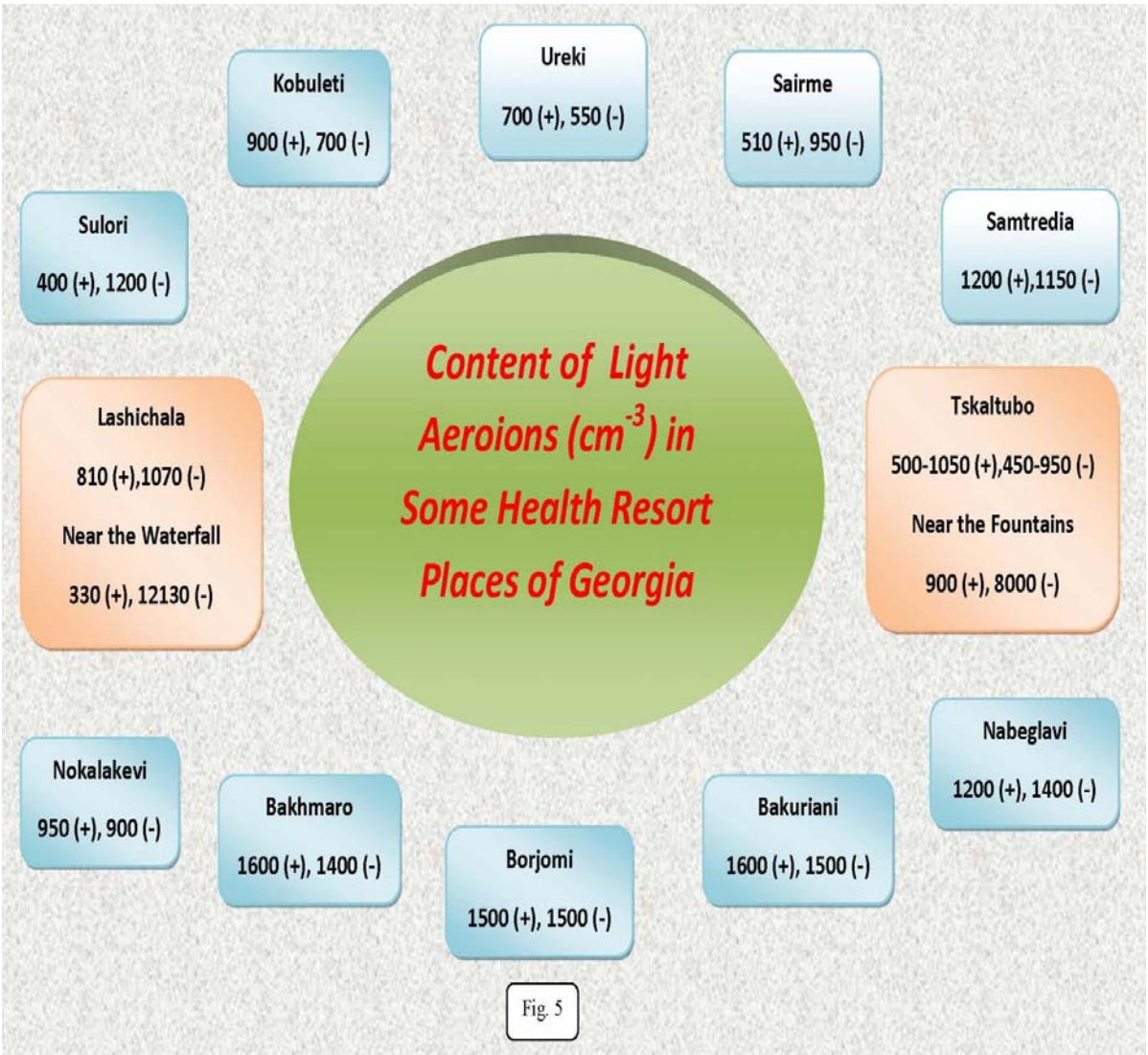

Fig. 5

Therefore, subsequently it is expedient to conduct the detailed analyses of the content of light ions in the entire territory of Tbilisi Botanical Garden into different seasons of year taking into account weather conditions. These studies will make it possible to clearly determine places with the therapeutic properties and to develop the appropriate procedures of sanitation, rehabilitation and treatment of visitors.

However, even without the detailed analyses of ions it is possible to recommend to the inhabitants of Tbilisi city (to especially elderly people and to children) to more frequently visit Botanical Garden. The air here is much cleaner and more useful than in the built-on districts of Tbilisi.

4. Conclusions

Tbilisi Botanical Garden besides its previous known functions (science, excursion, leisure, tourism, etc.) can acquire the new: medical and sanitary. The territory of Botanical Garden as a whole completely satisfies the requirements of sanitation-reducing localities. Separate zones of Botanical Garden (near the waterfalls, in the separate places of the gorge of the river Tsavkisi, etc.) can be used also for therapeutic purposes - ionotherapy.

Therefore, subsequently it is expedient to conduct the detailed analyses of the content of light ions in the entire territory of Tbilisi Botanical Garden into different seasons of year taking into account weather conditions. These studies will make it possible to clearly determine places with the therapeutic properties and to develop the appropriate procedures of sanitation, rehabilitation and treatment of visitors.

However, even without the detailed analyses of ions it is possible to recommend to the inhabitants of Tbilisi city (to especially elderly people and to children) to more frequently visit Botanical Garden. The air here is much cleaner and more useful than in the built-on districts of Tbilisi.

This work is reported at the International Conference "Applied Geophysics and Geoecology", Dedicated to the Prof. L. Chanturishvili 90th Anniversary, September 14-15, 2011, Tbilisi, Georgia.

References

[1] Tammet, H. - Atmospheric Ions, Proc. 12th Int. Conf. on Atmospheric Electricity, Versailles, France, 9-13 June,2003, vol.1, pp. 275-178, 2003.

[2] Sheftel, V.M., Chernishev A.K., Chernisheva S.P. - Air conductivity and atmospheric electric field as an indicator of anthropogenic atmospheric pollution, Proc. 9th Int. Conf. on Atmospheric Electricity, St. 3, pp. 588-590, 1992.

[3] Amiranashvili A., Matiashvili T., Nodia A., Nodia Kh., Kharchilava J., Khunjua A., Khurodze T., Chikhladze V. - Air Electrical Conductivity Changeability as the Factor of Atmosphere Purity, Proc. of Mikheil Nodia Institute of Geophysics, ISSN 1512-1135, vol. 60, Tbilisi, 2008, pp. 186 – 194 (in Russian).

[4] Sanitarily and Hygiene Standards of the Permissible Ionization Levels of Air of Production and Public Compartments, (СНиП 2152-80), (in Russian).

[5] Amiranashvili A., Bliadze T., Chikhladze V. - Assumed Ecological Consequences of Forest Fire in the Natural Preserve of Borjomi – Kharagauli During August 2008, Papers of the Int. Conference International Year of the Planet Earth "Climate, Natural Resources, Disasters in the South Caucasus", Trans. of the Institute of Hydrometeorology, vol. No 115, ISSN 1512-0902, Tbilisi, 18 – 19 November, 2008, pp. 291 – 298, 2008, (in Russian).

[6] Amiranashvili A., Bliadze T., Melikadze G., Tarkhan-Mouravi I., Chikhladze V. - Content of Light Aeroions as Factor of the Air Purity of Some Health Resorts of Georgia, Modern Problems of Using of Health Resort Resources, Collection of Scientific Works of International Conference, Sairme, Georgia, June 10-13, 2010, ISBN 978-9941-0-2529-7, Tbilisi, pp. 145-151, 2010, (in Russian).

[7] Amiranashvili A. Bliadze T., Chankvetadze A., Chikhladze V., Melikadze G., Kirkitadze D., Nikiforov G., Nodia A. - Comparative Characteristics of Light Ions Content in the Urban and Ecologically Clean Locality in Georgia, Proc. 14th Int. Conf. on Atmospheric Electricity, Rio de Janeiro, Brazil, 8-12 August, 2011

[8] Saakashvili N.M., Tabidze M.Sh., Tarkhan-Mouravi I.D., Amiranashvili A.G., Melikadze G.I., Chikhladze V.A - To a Question About the Organization of Ionotherapy at the Health Resorts of Georgia, Modern Problems of Using of Health Resort Resources, Collection of Scientific Works of International Conference, Sairme, Georgia, June 10-13, 2010, ISBN 978-9941-0-2529-7, Tbilisi, pp. 168-174, 2010, (in Russian).

[9] Jura Z., Niziol B., Schiffer Z., Zakrocki Z. – Proba Okreslenia Wplywu Zmian Barycznych na Jonizacje Powietrza, Wplyw Czynnikow Meteorol. Na Organizm Ludzi I Zwierzat, Wroclaw, 1977, pp. 5-16. (8)

[10] Kekelidze J., Loria M., Elbakidze M. – Tbilisi Botanic Garden 365, ISBN 99928-899-4-2, Tbililsi, "Dedaena", 2001, 190 p. (in Georgian)

საქართველოს ეროვნული ბოტანიკური ბაღის ტერიტორიის აეროიონიზაციური მახასიათებლების შესახებ ახალი მონაცემები როგორც მისი გამაჯანსაღებელი თვისებების გაფართოების ფაქტორი მომსვლელებისათვის

ა.ამირარაშვილი, თ. ბლიაძე, ვ. ჩიხლაძე, ზ. მაჩაიძე, გ. მელიქაძე, ნ.სააკაშვილი, ე. ხატიაშვილი, ი. თარხან-მოურავი, შ. სიხარულიძე, თ. ნაკაიძე, მ.თავართქილაზე

რეზიუმე

წარმოდგენილია ჰაერში მსუბუქი იონების შემცველობის წინასწარი გამოკვლევის შედეგები საქართველოს ნაციონალური ბოტანიკური ბაღის ტერიტორიაზე. იონების კონცენტრაცია იყო გაზომილი 25 წერტილში 90 ჰა ფართობზე, აგრეთვე მთავარი ჩანჩქერის სიახლოვეს 33 წერტილში 1152 მ^2 ფართობზე. აგებულია განაწილების რუკები დადებითი და უარყოფითი მსუბუქი იონების კონცენტრაციებისათვის ჩანჩქერის და მთლიანობაში ბოტანიკური ბაღის ტერიტორიისათვის. დადგენილია, რომ იონების შემცველობა ბოტანიკურ ბაღში, განსაკუთრებით ხეობაში მდინარე წავკისის მახლობლად და ჩანჩქერებთან შესაბამისობაშია ჰიგიენურ დონესთან "მინიმალურად აუცილებელი" და "ოპტიმალური". ამავე დროს ქალაქ თბილისის გაშენებულ უბნებში იონების შემცველობა შესაბამისობაშია დონესთან "მინიმალურად აუცილებელზე ნაკლები". ამგვარად, წინასწარ ჩატარებულმა კვლევებმა გამოავლინა ქალაქ თბილისის ბოტანიკური ბაღის ახალი ფუნქციები მომსვლელებისათვის: გამაჯანსაღებელი, სარეაბილიტაციო და სამკურნალო. რეკომენდირებულია მომავალში ჩატარდეს ბოტანიკურ ბაღში იონების შემცველობის უფრო დეტალური გამოკვლევა წლის სხვადასხვა სეზონის დროს ამინდის პირობების გათვალისწინებით.

НОВЫЕ ДАННЫЕ ОБ АЭРОИОНИЗАЦИОННЫХ ХАРАКТЕРИСТИКАХ ТЕРРИТОРИИ НАЦИОНАЛЬНОГО БОТАНИЧЕСКОГО САДА ГРУЗИИ КАК ФАКТОР РАСШИРЕНИЯ ЕГО ОЗДОРОВИТЕЛЬНЫХ СВОЙСТВ ДЛЯ ПОСЕТИТЕЛЕЙ

А. Амиранашвили, Т. Блиадзе, В. Чихладзе, З. Мачаидзе, Г. Меликадзе, Н. Саакашвили, Э. Хатиашвили, И. Тархан-Моурави, Ш. Сихарулидзе, Т. Накаидзе, М. Таварткиладзе

Резюме

Представлены результаты предварительных исследований содержания легких ионов в воздухе на территории национального ботанического сада Грузии. Концентрация ионов была измерена в 25 точках на площади 90 га, а также вблизи главного водопада в 33 точках на площади 1152 м^2. Построены карты распределения содержания положительных и отрицательных легких ионов для территории водопада и ботанического сада в целом. Получено, что содержание ионов в ботаническом саду, особенно в ущелье вблизи реки Цавкиси и водопадов, соответствует гигиеническим уровням "минимально необходимый" и "оптимальный". В застроенных частях города Тбилиси в это же время содержание ионов соответствовала уровню "меньше минимально необходимого". Таким образом, проведенные исследования выявили новые функции Тбилисского ботанического сада для посетителей: оздоровительные, восстановительные и лечебные. В дальнейшем рекомендуется провести в ботаническом саду более детальные исследования содержания ионов в различные сезоны года с учетом погодных условий.

Journal of the Georgian Geophysical Society,
Issue B. Physics of Atmosphere, Ocean, and Space Plasma, v.16b, 2013, pp.31-38

Dynamics of the mortality of the population of Tbilisi City and its connection with the surface ozone concentration

[1]A. Amiranashvili, [2]T.Khurodze, [3]P. Shavishvili, [4]R. Beriashvili, [4]I. Iremashvili

[1] Iv. Javakhishvili Tbilisi State University, M. Nodia Institute of Geophysics, 1, Aleksidze Str., 0160, Tbilisi, Georgia
[2]Niko Muskhelishvili Institute of Applied Mathematics of Georgian Technical University
[3]National Statistics Office of Georgia
[4] The Emergency Care Medical Centre of Tbilisi City Hall

Abstract

Results of detailed statistical analysis of the changeability of mortality on 1000 inhabitants (M) of the population of Tbilisi city in 1984-2010 are represented. The characteristics of the indicated time series is studied (autocorrelation, trend, random components, etc.). In particular, the values of M varies from 8.03 to 12.35, the changeability of mortality is described by the fifth order power polynomial, etc. The influence of the content of surface ozone on the mortality is studied. It is shown, that under the conditions of Tbilisi city the concentration of surface ozone 50 mcg/m^3 and above very negative influences the health of people and it leads to an increase in the mortality.

Key words: *mortality, trend, surface ozone concentration, air pollution*

Introduction

It is known that the mortality of population is closely related to social, economic, ecological and other conditions. In connection with similar that indicated special attention is paid to studies in different countries. In the last 20 years in Georgia several times were observed political, social and economic shakings (war, unstable political situation, the sharp oscillations of economic development, etc.). As a whole, within the indicated period of time an increase in the mortality of population was observed. Although, in recent years in the dynamics of mortality a certain stabilization and even positive tendencies are observed (decrease) [1,2].

As it was noted above by one of the important factors, which cause the mortality of population, appears ecological situation, including – air pollution. In the large cities the pollution of atmosphere is frequently connected with the presence of a smog of different types. One of the types of smog is the so-called photochemical smog [3].

Photochemical smog can't be detected by apparatus. It is the joint phenomena, i.e. result of action of many variables (factors). Ground high concentration of ozone is a characterizing attribute of photochemical smog. Ozone is not formed directly during burning of fuel, and is secondary pollutant.

Besides in photochemical smog there are reactions between oxides of nitrogen and the burned organic compounds. With participation of ozone actively there is a reaction for formation of so-called secondary aerosols of the submicron sizes under the scheme gas → particle (sulfates, nitrates, etc.). In products of these reactions there are many cancerogenic substances. Thus, photochemical smog represents multi component mix of primary and secondary formation of gases and aerosols. The basic components of smog are: ozone, oxides of nitrogen and sulfur, organic compounds of dioxide nature which in aggregate is referred to as photos-oxidants.

Photochemical smog reduces visibility, fatally acts on plants, negatively acts on human health, can cause damage of respiratory ways, vomiting, excitation of a mucous membrane of an eye and the general malaise. In photochemical smog there can be such compounds of nitrogen which increase probability of occurrence of malignant diseases. Intensive and long smog can become the reason of growth of disease and

death rate. As ozone shows strongly oxidizing properties, it negatively acts on human health and destructively acts on many materials.

Thus, with the photochemical smog on the health of people simultaneously act both the high concentrations of the primary and secondary contaminators of the atmosphere (gases and aerosols) and the high concentrations of surface ozone. In this case the high concentrations of ozone are also the indicator of the high atmospheric content of other forming ozone admixtures. With the smog of other types ozone concentration is low, and its action on the health of people is insignificant [4-8].

The first officially registered case of atmospheric pollution which had serious consequences was in the Donor (USA) in 1948. During 36 hours has died twenty people, and hundreds inhabitants felt badly. After four years, in December, 1952, in London has occurred more tragic case. In consequence of air pollution during five days has died 4000 people. Though the next years both in London and in other cities repeatedly were strong smog but such catastrophic case have not repeated.

According to the data of the World Health Organization (WHO), lasting pollution of air by the machines in Austria, Switzerland and France is the reason for premature death more than 21 000 people yearly, in essence, from the diseases of the heart and respiratory tract. This index exceeds a quantity of people, which yearly perish in these 3 countries with the road- transport incidents. In eight the largest cities of world yearly it could it takes away the lives of 3500 people. In 5% of cases the poisons, which are contained in air, are the reason for lethal outcome. In Europe each year the victims of the pollution of the atmosphere become, at least, 100 thousand people. In USA a quantity of victims reaches 70 thousands. So many people they die from cancer of light and prostate [9 - 11].

In Georgia the first observation of ground ozone have begun in 1980 in Tbilisi in Institute of Geophysics of the Academy of Sciences of Georgia. From 1984 to this day these observations have regular nature [4,5,12,13]. To this day are carried out many scientific researches. Thus, according to average monthly data of 1980-1990 it is obtained that in Tbilisi because of the high concentrations of ozone into the cold half-year occurs an increase in the mortality for reasons of heart - vascular diseases to 5%, and into and the warm - to 9% [14].

Work presents the analysis of the dynamics of the common annual mortality of the population of Tbilisi city taking into account contemporary conditions (period from 1984 through 2010) and the evaluations of the influence on it of the concentration of surface ozone. Also the preliminary evaluations of the influence of ozone concentrations on the daily mortality of the population of Tbilisi city in 2009-2010 are given.

Method and data description

In the work the data of National Statistics Office of Georgia about the common mortality (1984-2010) , and data of the Emergency Care Medical Centre of Tbilisi City Hall about the daily mortality (2009-2010) of the population of Tbilisi city are used [1,2]. The common annual mortality of population to 1000 inhabitants is normalized.

The measurements of ozone were conducted by the electro chemical ozone instrument OMG-200. Observational data for 15 hours are presented [12,13]. The unit of the ozone measurement is mcg/m^3.

In the proposed work the analysis of data is carried out with the use of the standard statistical analysis methods of random events and methods of mathematical statistics for the non accidental time-series of observations [15, 16].

The following designations will be used below: M – mortality, SOC - surface ozone concentration, Min – minimal values, Max - maximal values, Range - variational scope, Range/ Mean (%) - relative variational scope, σ - standard deviation, σ_m - standard error (68% - confidence interval of mean values), C_v - coefficient of variation (%), A - coefficient of skewness, K - coefficient of kurtosis, R - coefficient of linear correlation, R_i - index of correlation, R^2 – coefficient of determination, R_s – Spearman's rank correlation coefficient, R_k – Kendall's rank correlation coefficient, R_a - autocorrelation coefficient, K_{DW} – Durbin-Watson statistic, t - Stiudent criterion, α - the level of significance.

Results of detailed statistical analysis of the changeability of mean annual values of SOC in Tbilisi in 1984-2010 in [13] are represented. In particular, the changeability of the indicated time series is described by the fourth power polynomial. An increase in the SOC in the period from 1984 through 1995-1997 was observed, then - decrease. Thus, in average: in 1984 SOC = 37 mcg/m^3, into 1998 – 58 mcg/m^3, into 2010 – 40 mcg/m^3. Data about daily SOC in Tbilisi in 2009-2010 in the work [12] is presented.

Results

The results are given in Tables 1-4 and Fig. 1-4.

Analysis of the mortality dynamics in 1984-2010.

Table 1. The statistical characteristics of mortality on 1000 inhabitants in Tbilisi in 1984-2010

Standard statistics of time series			
Mean	10.30	**σ_m**	0.25
Min	8.03	**C_v (%)**	12.6
Max	12.35	**A**	-0.58
Range	4.32	**K**	-0.64
Median	10.61	**σ_m /Mean (%)**	2.43
σ	1.30	**Range/ Mean (%)**	41.9
The non-randomness characteristic of time series			
Correlation with year		**Trend + background ($Y = a \cdot X^5 + b \cdot X^4 + c \cdot X^3 + d \cdot X^2 + e \cdot X + f$)**	
R with year	0.62	**a**	-0.0000278
(α) R	0.01	**b**	0.00206
R_k	0.305	**c**	-0.05523756
(α) R_k	0.026	**d**	0.62867
R_s	0.48	**e**	-2.528
(α) R_s	0.015	**f**	10.277
R_a, Lag = 1	0.842	**R_i**	0.93
(α) R_a	0.001	**(α) R_i**	0.001
K_{DW}	0.4	**K_{DW}**	1.45
(α) K_{DW}	Not significance	**(α) K_{DW}**	0.05
Standard statistics of trend + background and random components			
Trend + background		**Random components**	
Mean	9.66	**Mean**	0.65
Min	7.02	**Max**	1.60
Max	10.85	**σ**	0.49
Range	3.83	**C_v (%)**	75.2
σ	10.14	**Range/ Mean (%)**	247
C_v (%)	1.21	**Share of real data**	6.3
Range/ Mean (%)	39.6		
Share of real data	93.7		

The standard statistical characteristics values of M in the upper part of table 1 are represented.

As follows from this table the values of M varies from 8.03 to 12.35, variational scope is 4.32, mean value - 10.30, median - 10.6, standard deviation - 1.30, standard error - 0, coefficient of variation 12.6%.

Coefficient of skewness is -0.58, coefficient of kurtosis - -0.64. The absolute values of the calculated coefficients of skewness and kurtosis are less than the trebled theoretical value of their standard deviations. Accordingly in general set of function of distribution of M should be close to normal. The relative variational scope is 41.9 %.

The non-randomness characteristic of the time series of M in the middle part of table 1 are submitted.

Coefficient of linear correlation between M and years is 0.62 , the value of Kendall's rank correlation coefficient is 0.305, the value of Spearmen's rank correlation coefficient is 0.48, the value of autocorrelation coefficient with a Lag = 1 year is 0.842. The values of level of significance α for the above mentioned parameters of stability also are given in this table.

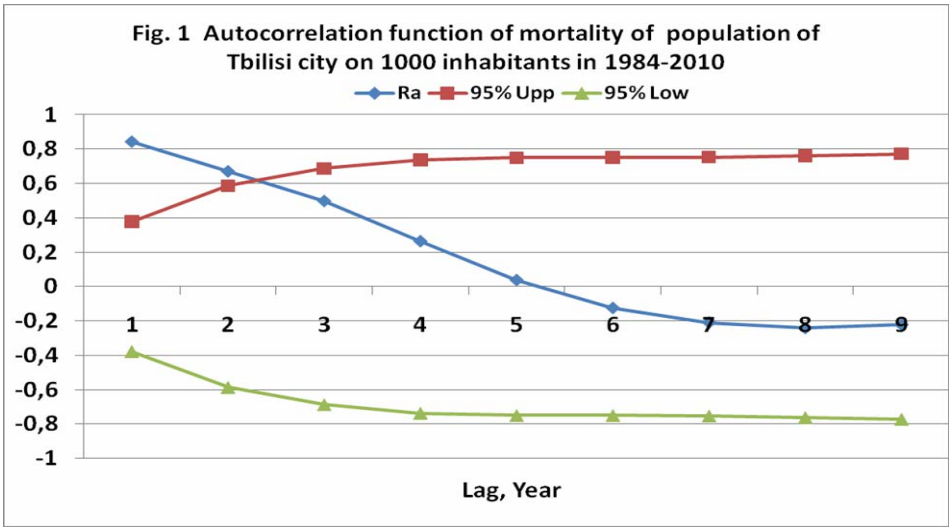

The value of autocorrelation function of M is significance in the limits of two lag (fig. 1). This can be caused by the strong influence of external factors (including of environment) on the changeability of M.

At first glance it can seem that the trend of M takes the linear form. However, in the case of linear trend the analysis of residual component shows their auto-correlation (K_{DW} = 0.4, not significance). Thus, the time series of M is autocorrelate and trend has a nonlinear nature.

As showed analysis, the trend of values M takes the form of the polynomial of fifth degree ($\mathbf{R_i}$ = 0.93, K_{DW} = 1.45, table 1).

The statistical characteristic of trend + background and random components of M in the low part of table 1 and fig. 2 are presented.

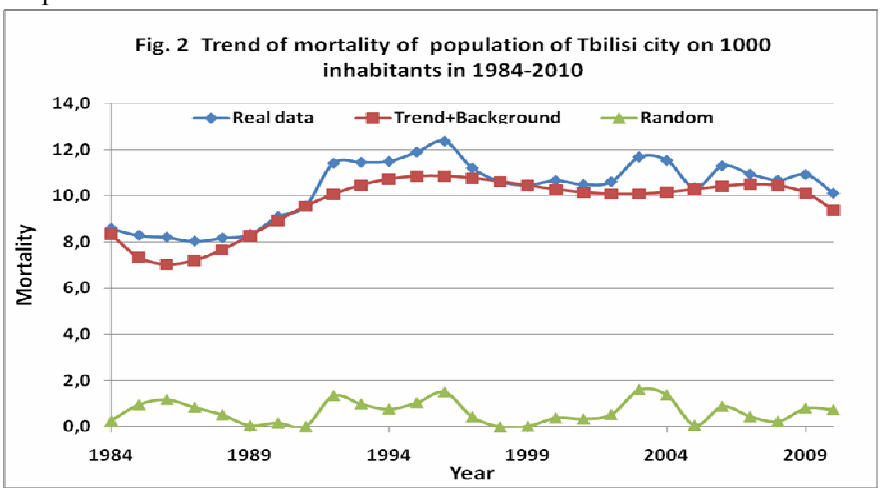

The average value of trend + background component of M is 9.66, the minimal value - 7.02, maximal - 10.85, the relative variational scope - 39.6 %. A share of the mean values of the component of trend+background from the mean value of real data of M constitute 93.7 %.

The average value of random component of M is 0.65, the maximal - 1.60, the relative variational scope - 247 % . A share of the mean value of the random component from the mean value of real data of M

constitute 6.3 %. Thus, the changeability of values M in the investigated period practically caused by its trend component.

Analysis of the connections between mean annual maximum surface ozone concentration and annual mortality in Tbilisi in 1984-2010.

The absence of the clearly expressed tendencies in the changeability of SOC and M (increase or decrease) makes it possible to carry out the correlation and regression analysis of the connection between their real data. The results of this analysis in tables 2-3 and fig. 3 are given.

Table 2. Correlation between mean annual surface ozone concentration in 15 hour and mortality of population of Tbilisi city on 1000 inhabitants in 1984-2010

R	(α) R	R_k	(α) R_k	R_s	(α) R_s
0.39	0.1	0.2	0.14	0.33	0.1

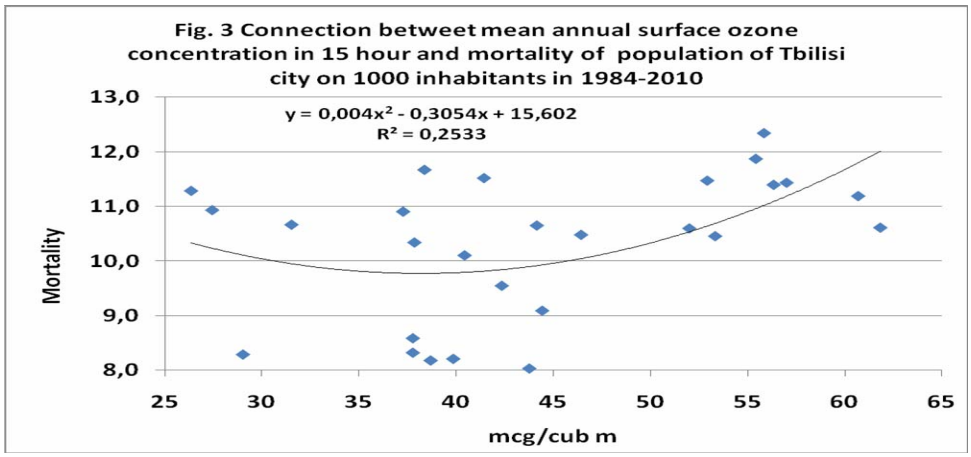

Table 3. Effect of the mean annual surface ozone concentration in 15 hour on the mortality of population of Tbilisi city in 1984-2010

Range of ozone concentration mcg/m^3	Mean ozone concentration mcg/m^3	Mean mortality on 1000 inhabitants	Range of ozone concentration mcg/m^3	Mean ozone concentration mcg/m^3	Mean mortality on 1000 inhabitants
26.3-46.4	38	9.82	52.0-61.6	56.2	11.27
Increase in the mortality on 1000 inhabitants	**Stiudent criterion t**	**(α) t**	**Mean mortality on 1000 inhabitants in 1984-2010**	**Share of the increase in the mortality of mean mortality (%)**	**Mean annual increase in the mortality on population of Tbilisi city**
1.45	3	0.01	10.3	14.1	1680

As follows from table 2 between the values SOC and M the significant correlation is observed. This connection takes the form of the second power polynomial (fig. 3).

In table 3 the estimation of effect of mean annual surface ozone concentration in 15 hour on the mortality of population of Tbilisi city are presented.

As follows from this table in the years, when ozone concentration on the average was equal to 56.2 mcg/m^3 (range from 52 mcg/m^3 to 61.6 mcg/m^3) value of mortality to 1000 inhabitants was equal to 11.27. When ozone concentration on the average was equal to 38 mcg/m^3 (range from 26.3 mcg/m^3 to 46.4 mcg/m^3) mortality to 1000 inhabitants was equal to 9.82.

Thus, the increased of surface ozone concentrations (and its accompanying harmful for the health people the components of smog) on the average increase yearly mortality of the inhabitants of Tbilisi city by 1680 people. This is equal to 14.1 % of entire average annual mortality of the population of Tbilisi city, which is approximately 3 times higher than the same indices for the advanced countries.

Analysis of the connections between daily maximum surface ozone concentration and daily mortality in Tbilisi in 2009-2010.

Results of the evaluation of effect of the surface ozone concentration on the mortality of population of Tbilisi city in 2009-2010 in fig. 4 and table 4 are presented. As follows from fig. 4 connection between surface ozone concentration in 15 hour and daily mortality in Tbilisi has the form of the second power polynomial.

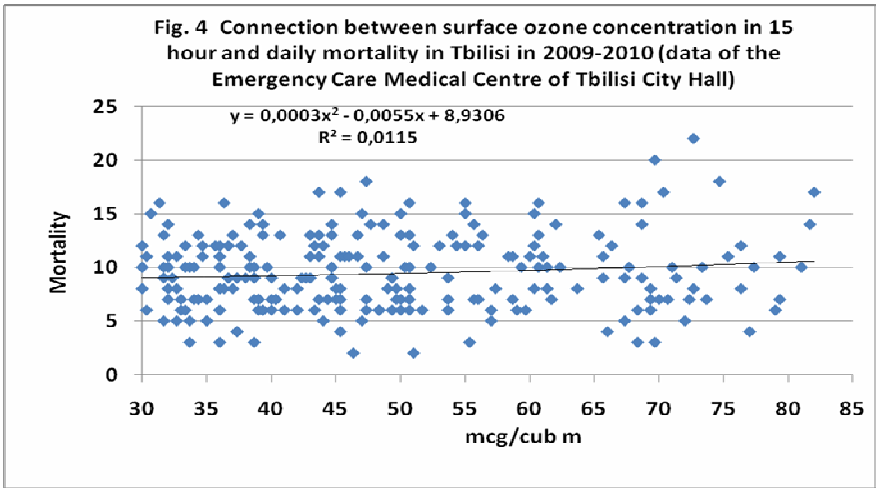

Table 4. Effect of the surface ozone concentration in 15 hour on the daily mortality of population of Tbilisi city in 2009-2010 (data of the Emergency Care Medical Centre of Tbilisi City Hall)

Range of ozone concentration mcg/m^3	**Mean ozone concentration mcg/m^3**	**Mean mortality in day**	**Range of ozone concentration mcg/m^3**	**Mean ozone concentration mcg/m^3**	**Mean mortality in day**
30-49	39.3	9.2 (Count=134)	50-82	62.7	9.85 (Count=97)
Increase in the mortality in day	**Stiudent criterion t**	**(α) t**	**Mean mortality in day**	**Share of the increase in the mortality of mean mortality (%)**	
0.65	1.33	0.15	9.47 (Count=231)	6.9	

Data of the Emergency Care Medical Centre of Tbilisi City Hall confirm an increase in the mortality with the increased concentrations of surface ozone also. In this case the share of the increase in the mortality

of mean mortality equal 6.9 % (table 4). Subsequently in proportion to the accumulation of data these estimations will be refined.

It should be noted that under the conditions of Tbilisi city the daily maximum concentration of surface ozone 50 mcg/m^3 and above very negative influences the health of people. This concentration is considerably less (3-5 times) than accepted in Europe and USA the values of the maximum permissible concentrations of surface ozone [11].

Conclusions

Trend of the mortality in Tbilisi city in 1984-2010 has a nonlinear nature and by the fifth order power polynomial is described.

The increased of surface ozone concentrations (and its accompanying harmful for the health people the components of smog) on the average increase yearly mortality of the inhabitants of Tbilisi city by 1680 people.

Data of the Emergency Care Medical Centre of Tbilisi City Hall confirm an increase in the daily mortality with the increased concentrations of surface ozone also.

Under the conditions of Tbilisi city the concentration of surface ozone 50 mcg/m^3 and above very negative influences the health of people. This concentration is considerably less (3-5 times) than accepted in Europe and USA the values of the maximum permissible concentrations of surface ozone.

This work is reported at the International Conference "Applied Geophysics and Geoecology", Dedicated to the Prof. L. Chanturishvili 90th Anniversary, September 14-15, 2011, Tbilisi, Georgia.

Acknowledgements:

The designated project has been fulfilled by financial support of the Shota Rustaveli National Science Foundation (Grant N GNSF/ST08/5-437). Any idea in this publication is processed by the authors and may not represent the opinion of the Shota Rustaveli National Science Foundation itself.

References

[1] Statistical Yearbook 2009, Ministry of Economic Development of Georgia, Department of Statistics, ISBN 978-99928-72-38-3, Tbilisi, 2009, 322 p.

[2] http://www.geostat.ge

[3] http://www.epa.gov/airnow

[4] Kharchilava J.. Amiranashvili A. - Studies of Atmospheric Ozone Variations in Soviet Georgia. Results of Researches on the International Geophysical Projects. SGC. Moscow. 1988. p.p.1-114 (in Russian).

[5] Amiranashvili A.G., Amiranashvili V.A., Gzirishvili T.G., Kharchilava J.F., Tavartkiladze K.A. – Modern Climate Change in Georgia. Radiatively Active Small Atmospheric Admixtures, Institute of Geophysics, Monograph, Trans. of M.Nodia Institute of Geophysics of Georgian Acad. of Sci. , ISSN 1512-1135, vol. LIX, 2005, 128 p.

[6] Muraleedharan T.S., Subba Ramu M.S., Vohra K.G. – Experimental studies of the formation of Aitken Nuclei in the atmosphere, Proc. 11th Int. Conf. on atmospheric aerosols, Condensation and Ice Nuclei, Budapest,Hungary, 3-8 September,vol.1, 1984, 52-57 .

[7] NARSTO (North American Research Strategy for Tropospheric Ozone) Synthesis Team, 2000. An Assessment of Tropospheric Ozone Pollution: A North American Perspective (www.cgenv.com/Narsto).

[8] Hygienic norms HN 2.1.6.1338-03 (from 25.06.03) the "Maximum permissible concentrations (PDC) of contaminants in atmospheric air of the populated places ".

[9] http://www.ecology.md/section.php?section=news&id=51

[10] http://www.pogoda.ru.net/health.htm

[11] Amiranashvili A., Chikhladze V., Bliadze T. - Contemporary State of a Question About the Action of Photochemical Smog and Surface Ozone on Human Health, Transactions of Mikheil Nodia Institute of Geophysics, vol. LXII, ISSN 1512-1135, Tbilisi, 2010, pp. 177-188, (in Russian).
[12] Amiranashvili A., Bliadze T., Kirkitadze D., Nikiforov G., Nodia A., Kharchilava J., Chankvetadze A., Chikhladze V., Chochishvili K., Chkhaidze G. - Some Preliminary Results of the Complex Monitoring of Surface Ozone Concentration (SOC), Intensity of Summary Solar Radiation and Sub-Micron Aerosols Content in Air in Tbilisi in 2009-2010, Transactions of Mikheil Nodia Institute of Geophysics, vol. LXII, ISSN 1512-1135, Tbilisi, 2010, pp. 189-196, (in Russian).
[13] Kharchilava J., Chikhladze V., Chochishvili K., Chkhaidze G. - Changeability of Surface Ozone Concentration in Tbilisi in 1984-2010, Proc. Int. Sc. Conference on "Environment and Global Warming", Tbilisi, Georgia, 15-17 September 2011, in press.
[14] Kharchilava J., Amiranashvili A., Amiranashvili V., Chikhladze V., Gabedava V. - Long-term variations of atmospheric ozone in Georgia and their connection with human health, Proc. 1st Int. Conf . on Ecology and Environmental Management in Caucasus, Tbilisi, Georgia, October 6-7, 2001, p. 80-82.
[15] M.G. Kendall, Time-series, Moscow, 1-200, 1981, (in Russian).
[16] Kobisheva N., Narovlianski G. - Climatological processing of the meteorological information, Leningrad, Gidrometeoizdat, 1978, pp. 1-294.

ქ. თბილისის მოსახლეობის სიკვდილიანობის დინამიკა და მისი კავშირი მიწისპირა ოზონის კონცენტრაციასთან

ა.ამირარაშვილი, თ. ხუროძე, პ. შავიშვილი,
რ. ბერიაშვილი, ი. ირემაშვილი

რეზიუმე

მოყვანილია ქალაქ თბილისში 1984-დან 2010 წლებში 1000 მოსახლეზე სიკვდილიანობის (M) ცვალებადობის დეტალური სტატისტიკური ანალიზის შედეგები. შესწავლილია მოცემული დროითი რიგის მახასიათებლები (ავტოკორელაცია, ტრენდი, შემთხვევითი კომპონენტები და ა.შ.). კერძოდ, M-ის მნიშვნელობა იცვლება 8.03-დან 12.35-მდე, სიკვდილიანობის ტრენდი აიღწერება მეხუთე რიგის პოლინომით და ა.შ. შესწავლილია მიწისპირა ოზონის კონცენტრაციის გავლენა სიკვდილიანობაზე. ნაჩვენებია, რომ ქალაქ თბილისის პირობებში მიწისპირა ოზონის კონცენტრაცია 50 მკგ/მ^3 და ზემოთ ძალზე ნეგატიურად მოქმედებს ადამიანების ჯანმრთელობაზე და იწვევს სიკვდილიანობის ზრდას.

ДИНАМИКА СМЕРТНОСТИ НАСЕЛЕНИЯ ГОРОДА ТБИЛИСИ И ЕЕ СВЯЗЬ С КОНЦЕНТРАЦИЕЙ ПРИЗЕМНОГО ОЗОНА

А. Амиранашвили, Т.Хуродзе, П. Шавишвили, Р. Бериашвили,
И. Иремашвили

Резюме

Представлены результаты детального статистического анализа изменчивости смертности населения города Тбилиси на 1000 жителей (M) в 1984-2010 гг. Изучены характеристики указанного временного ряда (автокорреляция, тренд, случайные компоненты, и т.д.). В частности, значение M меняется от 8.03 до 12.35, тренд смертности описывается полиномом пятой степени и т.д. Изучено влияние содержания приземного озона на смертность. Показано, что в условиях города Тбилиси концентрация приземного озона 50 мкг/м^3 и выше очень негативно влияет на здоровье людей и приводит к росту смертности.

Journal of the Georgian Geophysical Society,
Issue B. Physics of Atmosphere, Ocean, and Space Plasma, v.16b, 2013, pp. 39-46

Modeling of the frequency spectrum of magnetogradient waves in the equatorial magnetopause in the case of variable electric conductivity of the solar wind plasma

M. Chkhitunidze , Z. Kereselidze

I.Javakhishvili Tbilisi State University, M.Nodia Institute of Geophysics,1 Aleqsidze str. ,0171,Tbilisi

Abstract

It is known that after a bow shock in front of the day-side of the magnetosphere, i.e. in the magnetosheath, the solar wind flow decelerates. Therefore, the solar wind an anomalous resistance develops, which causes an increase in the magnetic viscosity of the plasma. This effect is especially felt in the focal area of the magnetosheath (the stagnation zone before the magnetosphere) where, according to our discussion, unlike in the peripheral areas of the magnetosheath, the approximation of single-fluid magnetic hydrodynamics (MHD) is not correct. This is especially characteristic of the base of the stagnation zone, which is the central area of the Earth's magnetic boundary layer (the magnetopause). Thus, it will be correct to describe the large scale motion of the solar wind plasma, having finite electric conductivity, with an equation system of double-fluid magnetic hydrodynamics. Generally, working out self-consistent analytical solutions to the magnetic and velocity fields, except in extremely simple cases, is impossible due to mathematical complications. However, there is a solution to this problem in the case of the flow around of the magnetosphere as due to violent deceleration of the solar wind. In the focal area of the magnetosheath it is possible to determine the flow topology in the kinematic approximation. Such a solution enables to solve the equation of the magnetic induction, constituent of the MHD equations system and corresponding to the magnetopause, by analytical approximation methods. Among different kinematic models, which include the solar wind deceleration effect near the critical point of the magnetosphere, Parker's plane (two dimensional) kinematic model for incompressible medium is especially simple [1]. This model and its spatial modification were effectively used in different tasks [2]. Namely, it appeared convenient for obtaining the magnetosphere parameters in quasi-stationary approximation by means of different models of variations in time of the magnetic viscosity of the solar wind [3,4].

Key words*: Solar wind, magnetosphere, magnetosheath, critical point, stagnation zone.*

Magnetogradient waves of Rossby type. Variation of the thermodynamic parameters of the plasma due to the solar wind deceleration in the magnetosheath may cause different kinematic and hydrodynamic phenomena. Namely, near the dayside boundary of the magnetosphere there is a possibility of generation of so-called magneto- gradient (MG) waves of Rossby's atmospheric planetary wave type. The existence of such waves in the Earth's ionosphere was independently supposed in the papers [5,6]. For activation of the physical mechanism for generating the MG waves it is necessary for the plasma to move with low hydrodynamic velocity or stagnate at the background of transverse electric conductivity (so-called Hall effect) towards the inhomogeneous magnetic field. It appeared that besides in the ionosphere the generation of the MG waves is also possible in the stagnation zone before the magnetosphere where the solar wind velocity becomes commensurable to the electromagnetic drift velocity of the electric component of the plasma [7, 8-Aburdjania, et.al, 2007,9]. In these papers the discrete spectral time characteristics of the MG wave frequencies were obtained as the stationary MHD conditions were considered. Then these

conditions were generalized for a quasi-stationary case. Thus we suppose that it is useful to use the results of the paper [3]. In such case, as it will be shown below, it will be possible to determine continuous spectral time characteristics of the MG waves by means of the quasi-stationary parameters of the magnetopause.

Let us enter the rectangular coordinate system with its zero point in the critical (front) point of the magnetosphere. The **x-** axis is directed to the sun, the **y** -axis coincides with the direction of the geomagnetic field boundary force line perpendicular to the equatorial plane, the **z** -axis is directed to the central equatorial section of the magnetosphere alongside the magnetosphere boundary. It is known that in a double-fluid MHD approximation two types (fast and slow) of MG waves may generate. Such waves may also generate in the stagnation zone of the magnetosheath, especially in the central area of the equatorial magnetopause. The phrasal velocities of these waves are determined by the expressions [8,9]:

A fast MG wave:

$$C_\varphi = C_+ = -\left(\frac{|C_H|}{2} + \sqrt{\frac{C_H^2}{4} + |C_H| C'_p} \right), \qquad (1)$$

A slow MG wave:

$$C_\varphi = C_- = -\frac{|C_H|}{2} + \sqrt{\frac{C_H^2}{4} + |C_H| C'_p} \, . \qquad (2)$$

where $C_H = c/(4\pi en)(\partial H_y/\partial x)$ is a magneto-gradient wave (so-called Khantadze wave), $C'_p = -\beta_H / k_x^2 > 0$ is the Rossby's type wave, $\beta_H = e/(Mc)(\partial H_y/\partial x)$ is the parameter of the magnetic field inhomogeneity (so-called magnetic parameter of Rossby), $k_z = 2\pi/\lambda$ is the wave number connected with the scale of the linear inhomogeneity of the task, e -is the elementary charge, n – the electron density, M – the proton mass, c – the light velocity . In a single-fluid approximation, i.e. when there is no Hall electric conductivity effect, there will be only stable MG wave.

According to (1) and (2) expressions, in order to determine the spectral characteristics of the wave in the equatorial magnetopause by means of the dispersive relationship it is necessary to analytically determine the magnetopause thickness and the distribution of the geomagnetic field in it. In addition, in the first approximation we may use the magnetopause thickness as the inhomogeneity linear scale determining the wave number [8]. Let us refer to the papers [3,4], in which by use of the Parker kinematic model, by analytical method of the Schwec successive approximation [10] the quasi-stationary solutions of the equation of the magnetic field induction are obtained. These solutions correspond to different models of time variation of the electric conductivity of the solar wind. In the previous results the impulsive time variation of either the electric resistance of the solar wind plasma, or the parameter depended on it - the magnetic viscosity, were not considered [11]. But obtained experimental data proved the possibility of anomalous increase of the electric resistance of the solar wind that has been used in modern computer experiments [12]. Therefore, it is obvious that qualitative and quantitative corrections of the previous results of modeling of magnetopause carried out earlier are necessary.

Let us not take into account the curvilinearity of the extreme force line of the geomagnetic field on the boundary of dayside magnetosphere. In case of such admission for determining topologic image of nonstationary distribution of the magnetic field in the Zhigulev second category plane boundary layer we may use a single-component equation of magnetic induction H

$$\frac{\partial H_y}{\partial t} + u\frac{\partial H_y}{\partial x} + v\frac{\partial H_y}{\partial z} = \lambda_m \frac{\partial^2 H_y}{\partial^2 x} \, . \qquad (3)$$

This equation involves magnetic viscosity λ_m as a coefficient that is defined by σ specific electric conductivity

$$\lambda_m = \frac{c^2}{4\pi\sigma}, \tag{4}$$

Let us use the following expressions for modeling of the impulsive time variation of σ parameter during perturbation of the solar wind

$$1)\ \lambda_m = \lambda_{0m} e^{-\frac{t}{\tau_0}}; \qquad 2)\ \lambda_m = \lambda_{0m}(1 - e^{-\frac{t}{\tau_0}}), \tag{5}$$

where λ_{0m} is the value characterizing the magnetic viscosity, τ_0 - the time characterizing the impulsive variation of this parameter. It is obvious that these models are physically similar and show the change of the electric conductivity of the plasma from the finite to the ideal and vice versa.

According to the Shwec successive approximation analytical method suppose that the value of the Earth's dipole magnetic field in the lower boundary of the magnetopause is constant and gradually decreases in latitudinal direction of the δ_H thickness of the magnetic boundary layer. Thus, the infinite upper boundary of the integration may be replaced by the finite thickness of the magnetic boundary layer. Then this parameter is defined in analytically clear form. Such a possibility is main advantage of the Schwec successive approximation.

Thus, we have the following boundary conditions for the (3) equation

$$H_y = H_0, \text{ when } x = 0; \quad H_y = 0, \quad \text{when } x = \delta_H. \tag{6}$$

Near the critical point of the magnetosphere the velocity field of the noncompressible plasma is determined by the Parker's plane kinematic model

$$u = -\alpha x, \qquad v = \alpha z, \tag{7}$$

where α is the reverse value of the time characteristic for the overflow of the magnetosphere day side. Further we will use value α=0.01, which corresponds to the velocity of the electromagnetic drift in the stagnation zone V=5 km/ sec in the case of minimal linear scale of this structure: 1000 km. Thus, by means of (7), in case of the (5) model, we will have the equation

$$\frac{\partial H_y}{\partial t} - \alpha x \frac{\partial H_y}{\partial x} = \lambda_m \frac{\partial^2 H_y}{\partial x^2}. \tag{8}$$

In the (6) boundary conditions, for solving the (8) equation by Shwec method, also the corresponding equation of the (5.2) model and for gaining information on the determination scheme of the magnetopause thickness we may refer to the works [2008]. Therefore, it is quite sufficient to present quasi-stationary expressions of the distribution of the magnetic field over the meridional magnetopause and the boundary layer thickness ($'$ means the time derivative)

$$1)\ \lambda_m = \lambda_{0m} e^{-\frac{t}{\tau_0}}$$

$$\frac{H_y}{H_0} = \left(1 - \frac{x}{\delta_H}\right) + \lambda_{0m}^{-1} e^{\frac{t}{\tau_0}} \left[\left(\frac{\delta_H'}{\delta_H^{\,2}} \frac{x^3}{6} - \frac{\delta_H'}{6} x \right) + \alpha \left(\frac{x^3}{6\delta_H} - \frac{\delta_H}{6} x \right) \right] \tag{9}$$

$$\delta_H = (3\lambda_{0m}\alpha^{-1})^{1/2} \left[e^{-\alpha t} + \left(1 - \frac{1}{\alpha\tau_0}\right)^{-1} \left(e^{-\frac{t}{\tau_0}} - e^{-\alpha t} \right) \right]^{1/2}, \tag{10}$$

$$2)\ \lambda_m = \lambda_{0m}(1 - e^{-\frac{t}{\tau_0}})$$

$$\frac{H_y}{H_0}=(1-\frac{x}{\delta_H})+\lambda_{0m}^{-1}\left((1-e^{-\frac{t}{\tau_0}})\right)^{-1}\left[(\frac{\delta'_H}{{\delta_H}^2}\frac{x^3}{6}-\frac{\delta'_H}{6}x)+\alpha(\frac{x^3}{6\delta_H}-\frac{\delta_H}{6}x)\right], \quad (11)$$

$$\delta_H=(3\lambda_{0m}\alpha^{-1})^{1/2}\left[\left(1-e^{-\alpha t}\right)+\left(1-\frac{1}{\alpha\tau_0}\right)^{-1}\left(e^{-\frac{t}{\tau_0}}-e^{-\alpha t}\right)\right]^{1/2}. \quad (12)$$

The existence of the magnetopause is provided by the global surface DCF current, which screens the geomagnetic field from the solar wind. In this way the correctness in regard to the general image of the flow around of the magnetosphere, according to which the magnetopause is the magnetic boundary layer, will be proved. For model 1) we have $\delta_H=\left(3\lambda_{0m}\alpha^{-1}\right)^{1/2}$ when $t=0$, according to (10). So, Earth's magnetic boundary layer a priori has a certain thickness in this case, as opposed to case 2) for which $\delta_H=0$ when $t=0$. It means that we may use physical analogy at the hydrodynamic boundary layer, inside of which for assessment of the energy changes there are two effective parameters: the thickness of the boundary layer and the thickness of loss of the mechanical impulse. For the MHD boundary layer, as the analogy of these parameters, two characteristics were used: 1) δ_a - the thickness of displacement of magnetic field induction; 2) δ_b - the thickness of magnetic energy displacement [4,11]. According to the explanation the thickness of displacement of magnetic field induction shows the thickness of the induction flow loss by means of comparing the distribution of the magnetic field to the corresponding distribution of the ideal profile in the latitudinal section of the magnetopause. In addition, the thickness of the energy loss of the magnetic field shows the thickness of the lost energy layer by comparing it to the ideal distribution. Generally, these parameters are defined by the following expressions

$$\delta_a=\int_0^{\infty\delta_H}\left(1-\frac{H}{H_0}\right)dx, \quad (13)$$

$$\delta_b=\int_0^{\infty\delta_H}\left(1-\frac{H^2}{H_0^2}\right)dx. \quad (14)$$

Therefore, it is logical to consider the one of the thicknesses (10), (12), (13) and (14) as the linear scale necessary for quantitative assessment of the MG wave parameters. It is obvious that in (9) and (11) expressions the role of the second approximation is much less compared to the first one. It is obvious that parameters C_H and C'_p will change according to the time as well as transversally to the magnetopause. Consequently, for assessment of the magneto-gradient wave velocity and the Rossby magnetic parameter it is sufficient to consider that the distribution of the magnetic field in the magnetopause is approximated by the linear terms of the expression (9) and (11). Thus, the phase velocities will be defined by the first approximation of Schwec. It means that we may use the following simple expressions for the magneto-gradient wave and the Rossby wave constituent of the expressions (1) and (2)

$$|C_H|=\frac{c}{4\pi en}\cdot\frac{H_0}{\delta_H}, \qquad C'_p=\frac{eH_0}{Mc\delta_H k_z^2}. \quad (15)$$

These formulas included δ_H as the linear scale and H_0 as a characteristic value of the magnetic field in the magnetopause. Thus, we can have characteristic values of the phase velocities of in the quasi-stationary magnetopause, the thickness of which is determined by the variation in time of the magnetic viscosity of the plasma. Let us use the following parameters of an average disturbed solar wind plasma near the magnetosphere boundary: $\lambda_m=10^{14}\text{cm}^2\text{s}^{-1}$ and $n=20\,\text{particle.cm}^{-3}$. The characteristic value $H_0=2\cdot10^{-4}$ gauss corresponds to the unperturbed value of the geomagnetic dipole at the low boundary of the magnetopause. Now, we can determine

the value of the wave number by means of the minimal linear scale of the stagnation zone boundary $-l \approx 10^8$ cm, i.e. $k_y = 2\pi \cdot 10^{-8} cm$ [8]. Let us consider the characteristic time of the magnetospheric substorm development – 500s as the characteristic scale of the τ_0 time. By means of these parameters the following characteristic values are defined: $C_H \approx 5 \cdot 10^8$cm.s^{-1} and $C_H^l \approx 2 \cdot 10^8$cm.s^{-1}. Therefore it becomes possible to define the velocities of the fast and slow magneto-gradient waves, after which we recieve the frequency spectrum characteristic of the magneto-gradient waves by means of expressions: $\omega_+ = k_y C_+$ and $\omega_- = k_y C_-$. As a matter of fact, there is not a great difference between these values, due to which in the equatorial magnetopause an overlap of the frequency spectrum of the fast and slow magneto-gradient waves will take place

1) $\lambda_m = \lambda_{0m} e^{-\frac{t}{\tau_0}}$;

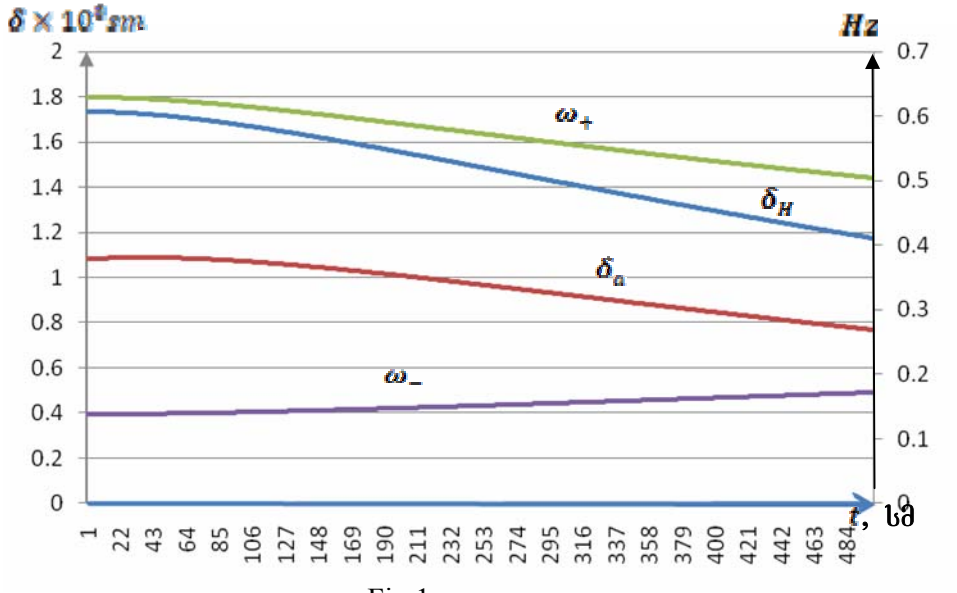

Fig.1

2) $\lambda_m = \lambda_{0m}(1 - e^{-\frac{t}{\tau_0}})$

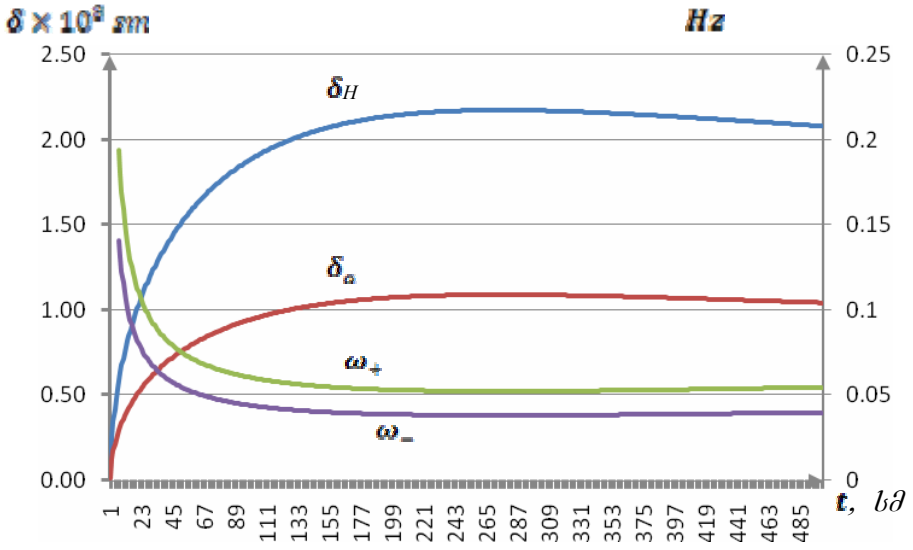

Fig.2

The figures 1-2 show the scheme of variation of the ω_+ parameter and the schemes of the δ_H and δ_a parameters during the characteristic time interval for both models of magnetic viscosity. Thus, in case of $\lambda_m = \lambda_{0m} e^{-t/\tau_0}$ the characteristic value of ω_+ is almost constant- 0.5Hz. However, when $\lambda_m = \lambda_{0m}(1 - e^{-t/\tau_0})$ we have the characteristic spectrum value of the ω_+ (0.2-0.05)Hz. For comparison we may use value $\omega_* \approx 5 \cdot 10^{-3}$ Hz, which was obtained in the approximation of the minimal size stagnation zone in the paper [8]. It is obvious that in case we use the δ_a as a characteristic linear scale instead of the δ_H there will not be much difference in quantitative results.

Thus, in the limits of the above presented model in the equatorial magnetopause a significant change of the frequency spectrum of the magneto-gradient waves characteristic of the stagnation zone may occur. It may be caused by the change in the thickness of the magnetopause and the specification of the distribution of the magnetic field in it due to variation in time of the magnetic viscosity of the solar wind. It is noteworthy that in such a case the frequency spectrum characteristic of the stagnation zone contains the frequencies of short and middle period geomagnetic pulsations.

Acknowledgements:

This project was carried out with support of the Shota Rustaveli National Science Foundation grant (contract № 12/70).
Noncommercial edition

References

[1] Parker E.N. Comments on the reconnection rate of magnetic fields. J. Plasma Physics, 1973, v.9. p.1,pp.49-63.
[2] Pudovkin M.L.,Semenov V.S. The reconnection theory and interaction of solar wind with the Earth's magnetosphere. Moscow,"Nauka", 1985, 125p. (in Russian)
[3] Kereselidze Z. Kirtskhalia V., Chkhitunidze M., Kalandadze I. On Modeling of Magnetic Boundary Layer on the Dayside Magnetosphere. Georgian International Journal of Sci. and Teq.,2008,ISSN1939-5925,vol.1№3,pp.249-256.
https://www.novapublishers.com/catalog/product_info.php?products_id=13354
[4] M. Chkhitunidze, N. Dzhondzoladze. The Magnetic Boundary Layer of the Earth as an Energy-supplying Channel for the Processes inside the Magnetosphere. J. Georgian Geophys.Soc.,Issue (B), Phys. of Atmosphere, Ocean and Space Plasma, 2012 v.15, pp.95-108.
[5] Хантадзе А.Г. Гидромагнитные градиентные волны в динамо-области ионосферы.Сообщ. АН ГССР, 1986, т.123, №1 с.69-71.
[6] Tolstoy I. Hydromagnetic gradient waves in the ionospere. J. Geophys.Res.,1967, V.47. №5, p.1435-1442.
[7] Хантадзе А.Г., Кереселидзе З.А., Гогатишвили Я.М. Геомагнетизм и Аэрономия.1980,т.xx, №6, с.1047-1052.
[8] Aburjania G.D., Kereselidze Z.A., Khantadze A.G., Chkhitunidze M.S..Large-Scale LF lectromagnetic Waves in the Earth's magnetosheath.Geomagnetism and Aeronomy, 2007, #5, pp.548-554.
[9] Абурджания Г.Д., Хантадзе А.Г. Особенности распространения УНЧ-планетарных электромагнитных волн в земной ионосфере, обусловленные кривизной геомагнитного поля. Гомагнетизм и Аэрономия, том.45, №5, с.673-681,2005.
[10] Shwec M.O. About of approximate solution of same task of hydrodynamic boundary layer. Appl.Math. and Mech. 1949, vol. 3, Issue XII, pp.253-266.
[11] Kereselidze Z.A. MHD Effects of finite electric conductivity of solar wind near the Earth's Magnetosphere. Tbilisi,State Univ. Press.,1986, 122p. (in Russian).

[12] Dorelli J.C., Hesse M., Kuznetsova M.M., Rastaetter L. A new look at driven magnetic reconnection at the terrestrial subsolar magnetopause. J. of Geophys. Res., 2010, v.109, A12216,doi:10.1029/2004JA01045

მაგნიტოგრადიენტული ტალღების სიხშირეთა სპექტრის მოდელირება ეკვატორიალურ მაგნიტოპაუზაზე მზის ქარის პლაზმის ცვლადი ელექტრული გამტარებლობის შემთხვევაში

მ. ჩხიტუნიძე, ზ. კერესელიძე

რეზიუმე

ცნობილია, რომ გარდამავალ არეში მაგნიტოსფეროს დღის მხარის წინ დარტყმითი ტალღის შემდეგ მზის ქარის დინება შენელებულია. შესაბამისად, მზის ქარში ვითარდება ანომალური ელექტრული წინაღობა, რაც პლაზმის მაგნიტური სიბლანტის ზრდას იწვევს. ეს ეფექტი განსაკუთრებით საგრძნობია გარდამავალი არის ფოკალურ ნაწილში (მაგნიტოსფეროს წინამდებარე სტაგნაციის ზონა), სადაც, განსხვავებით პერიფერიული არეებისაგან, ჩვენი შეხედულებით სამართლიანი აღარ არის ერთსითხოვანი მაგნიტური ჰიდროდინამიკის (მჰდ) მიახლოება. ეს განსაკუთრებით ეხება სტაგნაციის ზონის ფუძეს, ანუ დედამიწის მაგნიტური სასაზღვრო ფენის (მაგნიტოპაუზა) ცენტრალურ ნაწილს. ამიტომ აქ კორექტულია სასრული ელექტრული გამტარებლობის მქონე მზის ქარის პლაზმის მსხვილმასშტაბოვანი მოძრაობის აღწერა ორსითხოვანი მაგნიტური ჰიდროდინამიკის განტოლებათა სისტემით. საზოგადოდ, მაგნიტური ველისა და სიჩქარეთა ველის თვითშეთანხმებული ანალიზური ამონახსნის მიღება, განსაკუთრებით მარტივი შემთხვევების გარდა, შეუძლებელია მათემატიკური გართულებების გამო. თუმცა, მაგნიტოსფეროს გარსდენის შემთხვევაში, მზის ქარის მკვეთრი დამუხრუჭების გამო, არსებობს გამოსავალი: გარდამავალი არის ფოკალურ ნაწილში შესაძლებელია დინების ტოპოლოგიის განსაზღვრა კინემატიკურ მიახლოებაში. ასეთი ხერხი შესაძლებელს ხდის მაგნიტოპაუზის შესაბამისი, მჰდ განტოლებათა სისტემის შემადგენელი, მაგნიტური ინდუქციის განტოლების ამოხსნას მიახლოებითი ანალიზური მეთოდით. მაგნიტოსფეროს კრიტიკული წერტილის მახლობლად მზის ქარის დამუხრუჭების პროცესის აღმწერ სხვადასხვა კინემატიკურ მოდელებს შორის განსაკუთრებული სიმარტივით გამოირჩევა პარკერის ბრტყელი (ორ განზომილებიანი) კინემატიკური მოდელი უკუმშვადი გარემოსათვის. მოცემულ ნაშრომში ეს მოდელი გამოყენებულია ეკვატორიალურ მაგნიტოპაუზაზე როსბის პლანეტერული ატმოსფერული ტალღების ტიპის მაგნიტოგრადიენტული ტალღების მახასიათებელი პარამეტრების მისაღებად. ამისათვის, გამოყენებული იყო მზის ქარის მაგნიტური სიბლანტის დროში იმპულსური ცვლილების მოდელები და შვეცის მიმდევრობითი მიახლოებების ანალიზური მეთოდი. განისაზღვრა მაგნიტოგრადიენტული ტალღების ფაზური სიჩქარის მახასიათებელი სიდიდე და მოხდა მათი სიხშირეთა უწყვეტი (კვაზისტაციონარული) სპექტრის მოდელირება, რომელიც მოიცავს მოკლე და საშუალო პერიოდიანი რეგულარული გეომაგნიტური პულსაციების დიაპაზონს.

Моделирование спектра частот магнитоградиентных волн на экваториальной магнитопаузе в случае переменной электропроводности плазмы солнечного ветра

М.Чхитунидзе, З. Кереселидзе

Резюме

Известно, что в переходном слое, на дневной стороне магнитосферы, после прохождения фронта ударной волны, происходит торможение течения солнечного ветра. Соответственно, в солнечном ветре развивается аномальное электрическое сопротивление, что вызывает увеличение его магнитной вязкости. Этот эффект находится в фокальной части переходного слоя (застойная зона перед магнитосферой), где в отличие от периферийных областей, по нашему мнению, одножидкостное приближение магнитной гидродинамики (МГД) является несправедливым. Такое замечание особенно относится к основанию застойной зоны т.е. к центральной части (магнитопаузы) магнитного пограничного слоя Земли. Поэтому, тут для описания крупномасштабного движения плазмы солнечного ветра, имеющей конечную электрическую проводимость, пользуются уравнениями двухжидкостной магнитной гидродинамики. Вообще, получение самосогласованного аналитического решения магнитного поля и поля скоростей, кроме особенно простых случаев, является невозможным из-за математических осложнений. Однако, в случае обтекания магнитосферы, из-за резкого торможения солнечного ветра, существует выход - топологию течения в фокальной части переходного слоя можно определить в кинематическом приближении. Такой способ позволяет одну из составляющих системы МГД уравнений магнитопаузы (в частности, уравнение магнитной индукции) найти преближенным методом. Среди различных кинематических моделей, которые описывают процесс торможения солнечного ветра вблизи критической точки магнитосферы, особой простотой выделяется плоская (двухмерная) кинематическая модель Паркера для несжимаемой среды. В данной работе, эта модель используется для определения характерных параметров магнитоградиентных волн Россби на экваториальной магнитопаузе. Для этого были использованы модели импульсного изменения магнитной вязкости солнечного ветра и аналитический метод последовательных приближений Швеца. Были определены характерные величины фазовой скорости магнитоградиентных волн, при помощи которых было проведено моделирование непрерывного (квазистационарного) спектра частот, который включает диапазон регулярных средне и коротка периодных геомагнитных пульсаций.

Journal of the Georgian Geophysical Society,
Issue B. Physics of Atmosphere, Ocean, and Space Plasma, v.16b, 2013, pp. 47-52

Assessment of the WKB method error by the Gratton kinematic model for the Earth's magnetic boundary layer task

[1]Marina Chkhitunidze, [1]I.Khvedelidze, [2]Nino Dzhondzoladze

[1]*I.Javakhishvili Tbilisi State University, M.Nodia Institute of Geophysics,1 Aleqsidze str.,0171,Tbilisi*
[2]*I.Gogebashvili Telavi State University*

Abstract

The work touches the flat model of the magnetic boundary layer corresponding to the meridional section of the magnetosphere. It solves the single-component equation of the magnetic induction, which matches so-called Zhigulevs's first order the magnetic boundary layer, in which field of speed is given by the modified Gratton's kinematic model for the compressible solar wind. The work also describes the obtained exact numerical solution to the above mentioned equation and approximate analysis solution by the Wentzel-Kramers-Brillouin (WKB) method. The boundary conditions correspond to the area containing critical points at the dayside and night side of the magnetosphere, i.e. in the plasmasphere. It defines the error (≈ 1%) of the WKB method and the linear size of the use area(1-0,6) of this method. It assesses the compressibility effect of the solar wind, which must be influencing on the topological image of the magnetic field distribution in the magnetopause and the area alongside the plasmapause.

During the interaction of the solar wind and the geomagnetic field a special structure is formed. It is the magnetopause, which by its features resembles the boundary layer. The mathematical modeling of this formation must be done on the basis of magneto-hydrodynamic (MHD) equations. Namely, as a result of their simplification so called Zhigulev's equations for the magnetosheath of I and II order are received. These equations appeared to correspond to the main sections of the Earth's magnetosphere: I order system corresponds to the meridional section of the magnetosphere, and II order system – to the equatorial one. The main problem for the magnetopause modeling is self-consistency of the solar wind flow and the geomagnetic field that appeared impossible for a general case. In order to prevent this problem we used different kinematic models of the velocity field. In the gasodynamic approximation these models give an image of the cosmic plasma flow near the critical point of the magnetosphere [1-3]. The most popular among these models appeared the Parker kinematic model and its modifications, by means of which the main parameters of the magnetopause were analytically obtained: thickness and profiles of the magnetic field [4]. The advantage of these solutions is the physical obviousness, though they have a significant lack: the defects of analytical solution are mainly caused by two factors:

I. *errors of the approximation analysis methods (e.g. the Shwets method);*
II. *shortage of measures in the use area of the Parker kinematic model (the focal area containing the critical point).*

Therefore the work [5] described the flat modification of so called Gratton kinematic model. This method obviously more matches the solar wind flow in the central area of the

magnetosheath, which is in fact a maximum size focal area. Hereby, let us note that, apart the day side of the magnetosphere, the Gratton model is admissible for the night side (the magnetosphere tail) as well. Namely, according to the topology of the geomagnetic field force lines, there is a critical point at the night side of the plasmasphere. Consequently, there is a focal area, which is formed during convective motion directed from the neutral layer to the sun. Such special cases are recorded by scientific satellites during strong perturbations of the solar wind when reconnection of the geomagnetic field bounding the plasmic layer takes place in the magnetosphere tail [6].

The goal of the work is determination of topological image of the geomagnetic field distribution in the meridional section and assessment of the errors of the approximation analysis solution of the magnetic field induction equation in case we use Gratton's flat compressible kinematic model. This task has a practical value in the viewpoint of modeling of the magnetopause immediately as well as for the assessment of the meridional magnetopause parameter errors obtained by the second order magnetic boundary layer equation. This error is caused by the Parker kinematic model and the Shwets sequence approximation model, precision of which was assessed earlier in regard to several accurate solutions and is approximately 15-20% [7]. At the same time, below, within the framework of our task, we have assessed the error of the Wentzel-Kramers-Brillouin (WKB) method. It is known that this method is especially effective for the solution of second order differential equations with varying coefficients of the following type:

$$y'' + f(t)y' + g(t)y = 0. \qquad (1)$$

In the case of just some coefficients it is impossible to obtain an exact solution for (1) equation. This fact is a limitation for the physical task. Namely, we have such a situation in the case of meridional magnetopause modeling, which is quite observable if we use the Gratton model:

$$\begin{cases} V_x = -U_0\left(1 - e^{-\frac{U_0}{\nu}x}\right), \\ V_y = U_0 \cdot K_y \cdot \gamma \cdot e^{-\frac{U_0}{\nu}x}, \end{cases} \qquad (2)$$

where U_0 is a velocity characteristic of the solar wind, ν - magnetic viscosity, K_y - a reverse value of the linear scale. Here a coordinate system with its origin in the critical point is used: X axis is either directed toward the sun (in the case of the day side of the magnetosphere) or opposite to the sun (at the night side of the magnetosphere); Y axis determines the direction of the extreme line of the geomagnetic field. In regard to Z axis the model is homogenous as the compressibility of the solar wind plasma is postulated. From the continuity equation we will receive

$$div\vec{V} = \frac{\partial V_x}{\partial x} + \frac{\partial V_y}{\partial y} = -U_0 \cdot \frac{U_0}{\nu} e^{-\frac{U_0}{\nu}x} + U_0 K_y e^{-\frac{U_0}{\nu}x} = \theta t, \qquad (3)$$

where a notation $t = e^{-\frac{U_0}{\nu}x}$ is used.

If we disregard the curvature of the geomagnetic field it will be sufficient to look at the equation of the single-component magnetic field induction, which corresponds to the meridional magnetic boundary layer:

$$H_y \frac{\partial}{\partial y} V_y - V_x \frac{\partial}{\partial x} H_y - H_y \theta e^{-\frac{U_0}{\nu}x} = -\nu \frac{\partial^2 H_y}{\partial x^2}. \qquad (4)$$

It is quite obvious that (4) equation does not change during the variation in the magnetic field force line direction. This means that the equation really corresponds to the day side as well as the night side of the magnetosphere. If we refer to a new variable: $t = e^{-\frac{U_0}{\nu}x}$ and take into account

that $\frac{dH_y}{dx} = \frac{dH_y}{dz}\frac{dz}{dx} = \left(-\frac{v_0}{v}\right)\frac{dH_y}{dz}t$, $\frac{d^2H_y}{dx^2} = \frac{v_0^2}{v^2}\left(\frac{d^2H_y}{dz^2}t^2 + \frac{dH_y}{dz}t\right)$ by simple transformations we will receive the equation of (1) equation type

$$\frac{d^2H_y}{dt^2} + \frac{dH_y}{dt} + \frac{1}{t}H_y = 0. \qquad (5)$$

The exact numerical solution to the equation requires boundary conditions, which are similar to each other in the cases of both the magnetopause and the plasmasphere of the magnetosphere night side

$$H_y = H_0 , \quad \text{when } t=1, \qquad \frac{dH_y}{dt} = 0. \qquad (6)$$

where H_0 is the value characteristic of the geomagnetic field at the lower boundary of the magnetopause or the night side of the plasmapause. The second criterion of (6) equation physically means that there is disregard of the surface magnetospheric DCF- current effect, which always exists in the magnetopause, whereas is absent in the plasmapause. This limitation is not significant for our task as it is always possible to indirectly take into consideration the magnetic effect of the DCF- current in the way of varying the value characteristic of the geomagnetic field.

As we have mentioned above (5) equation may be solved also by the WKB approximation analysis method. By the scheme of WKB the equation (5) gives the following equation:

$$V'' + h(t)V = 0 , \qquad (7)$$

V is connected with H_y, and $h(t)$ coefficient is determined by means of the coefficients of (5) equation [8]. Namely, in our case $h(t) = \frac{1}{t} - \frac{1}{4}$.

For the solution, according to the WKB method, let us have $V = e^{i\Phi(t)}$ notation. Consequently, we will receive a nonlinear equation as follows:

$$-(\Phi')^2 + i\Phi'' + h = 0 . \qquad (8)$$

In the first approximation, i.e. when the number with an imaginative coefficient is disregarded, from (8) equation we will receive

$$\Phi' = \pm\sqrt{h} , \quad \text{i.e.} \quad \Phi = \pm\int\sqrt{h}dt . \qquad (9)$$

It is natural that such a supposition is correct only in the case the following condition is fulfilled:

$$|\Phi''| \approx \frac{1}{2}\left|\frac{h'}{\sqrt{h}}\right| << h . \qquad (10)$$

If we use the expression $h(t) = \frac{1}{t} - \frac{1}{4}$, it will be quite obvious that condition $\left(\frac{1}{2}\left|\frac{h'}{\sqrt{h}}\right| \le h\right)$ is roughly satisfied only in this interval $t \in (1-0{,}6)$, and not in the whole interval

(1-0). The approximation next to Φ is searched by the iteration, for which in (8) equation let us suppose that $\Phi'' \approx \pm h^{-\frac{1}{2}} \cdot \frac{h'}{2}$. In this case we will have

$$(\Phi')^2 \approx h \pm \frac{i}{2}\frac{h'}{\sqrt{h}}, \qquad (11),$$

from which

$$\Phi' \approx \pm\sqrt{h} + \frac{i}{4}\frac{h'}{h}, \qquad (12),$$

i.e. there is

$$\Phi(t) \approx \pm\int\sqrt{h(t)}dt + \frac{i}{4}\ell nh(t), \qquad (13),$$

from which

$$V \approx \frac{1}{h^{1/4}}\left\{C_+ e^{i\int\sqrt{h}dt} + C_- e^{-i\int\sqrt{h}dt}\right\}. \qquad (14)$$

If we correspond (5) equation to (1) general equation we receive that $f = 1$. Consequently, according to the WKB method $H_y = V(t)e^{-\frac{ikx}{\varepsilon}}$. Thus, for the magnetic field we have the following general expression

$$H_y \approx \frac{e^{-\frac{ikx}{\varepsilon}}}{\left(\frac{k}{\varepsilon}-\frac{k}{a}\right)^{1/4}} H_0\left\{C_+ e^{i\int\sqrt{\left(\frac{k}{\varepsilon}-\frac{k}{a}\right)}dx} + C_- e^{-i\int\sqrt{\left(\frac{k}{\varepsilon}-\frac{k}{a}\right)}dx}\right\}. \qquad (15)$$

The constants C_+ and C_- are determined by two algebraic equations that are received by the boundary conditions (6). Finally, we have

$$C_+ \approx -3.4086 + 0.2896i,$$
$$C_- \approx -3.4086 - 0.2896i. \qquad (16)$$

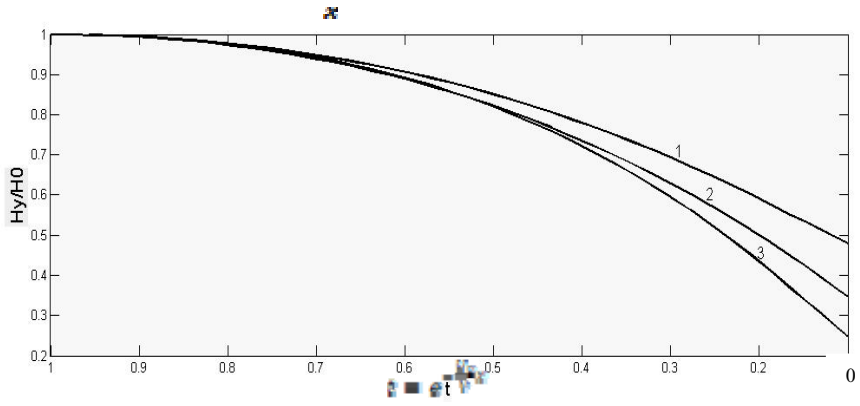

Fig.1

Fig.1 shows the algebraic normalized solution of (5) equation (line.1), the curve corresponding to (15) expression (line.2) and the numerical solution to the same equation in the case of non-compressible medium (θ=0) (line.3). It is obvious that between the exact numerical solution and the approximate analysis solution there is quite a good consistency in the some interval of $t \in (1-0,6)$ $(x \in (0,\infty))$. This means that if we refer to the initial coordinate system the exact and approximate solutions give in fact identical results of the magnetic field distribution near the critical point. The difference between (1) and (2) these solutions becomes significant after the point, from which the criterion (10) is not fulfilled $t = 0,6$. Its position in space is determined by parameter $\frac{y_0}{\gamma}$, the value of which depends on the quality of the solar wind perturbation.

Conclusion

Thus, we may conclude that within the framework of our task the error of the WKB method does not exceed 1%, which is quite acceptable for the approximate analysis method. At the same time, it is noteworthy that according to our model the compressibility effect must by quite significantly influencing on the topological image of the magnetic field distribution.

This project was carried out with support of the Shota Rustaveli National Science Foundation grant (contract № 12/70).
Noncommercial edition

References

[1] Pudovkin M.L.,Semenov V.S. The reconnection theory and interaction of solar wind with the Earth's magnetosphere. Moscow,"Nauka", 1985, 125p. (in Russian)
[2] Kereselidze Z.A. MHD Effects of finite electric conductivity of solar wind near the Earth's Magnetosphere. Tbilisi,State Univ. Press.,1986, 122p. (in Russian)
[3] Parker E.N. Comments on the reconnection rate of magnetic fields. J. Plasma Physics, 1973, v.9. p.1,pp. 49-63.
[4] Kereselidze Z., Kirtskhalia V., Chkhitunidze M., Kalandadze I. On Modeling of Magnetic Boundary Layer on the Dayside Magnetosphere. Georgian International Journal of Sci. and Teq.,2008, ISSN 1939-5925,vol.1№3,pp.249-256. https://www.novapublishers.com/catalog/product_info.php?products_id=13354
[5] Chkhitunidze M. DCF- current Magnetic Effect in the Focal Area of the Magnetosphere and the Gratton Model Modification in a Compressible Medium. Bulleting the Georgian academy of sciences. 2013, v.7, №3
[6] Sergeev V.A., Ciganenko N.A. Magnetosphere of Earth. M., Science, 1980, 174 p.(in Russian)
[7] Buznikova L.I. Iotkovsky B.G., Kirillov. About applicability of a method of consecutive approximations for interface calculation at a magnetohydrodynamic current in channels. Publishing house Academy of Sciences of the USSR, 1969, I, p.143-148. (in Russian)
[8] J. Metyuz, R. Walker. Mathematical methods of physics. Publishing house, Moscow "Atomizdat ",1972, 401p. (in Russian)

ვკბ მეთოდის ცდომილების შეფასება გრატონის კინემატიკური მოდელის გამოყენებით დედამიწის მაგნიტური სასაზღვრო ფენის ამოცანისათვის

მ.ჩხიტუნიძე, ი.ხვედელიძე, ნ. ჟონჟოლაძე

რეზიუმე

განხილულია დედამიწის მაგნიტური სასაზღვრო ფენის ბრტყელი მოდელი, რომელიც შეესაბამება მაგნიტოსფეროს მერიდიონალურ კვეთას. ამოხსნილია ე.წ. ჟიგულევის პირველი გვარის მაგნიტური სასაზღვრო ფენის შესაბამისი მაგნიტური ინდუქციის ერთკომპონენტიანი განტოლება, რომელშიც სიჩქარეთა ველი მოცემულია კუმშვადი მზის ქარისათვის მოდიფიცირებული გრატონის კინემატიკური მოდელით. მიღებულია ამ განტოლების ზუსტი რიცხვითი ამონახსნი და მიახლოებითი ანალიზური ამონახსნი ვკბ მეთოდით. სასაზღვრო პირობები შეესაბამება კრიტიკული წერტილების შემცველ არეს მაგნიტოსფეროს დღის მხარეზე და ღამის მხარეზე, ანუ პლაზმოსფეროზე. განსაზღვრულია ვკბ მეთოდის ცდომილება (≈ 1%) და ამ მეთოდის გამოყენების არის ხაზოვანი ზომა. შეფასებულია მზის ქარის კუმშვადობის ეფექტი, რომელიც მაგნიტოპაუზაზე და პლაზმოპაუზის მიმდებარე არეში საკმაო გავლენას უნდა ახდენდეს მაგნიტური ველის განაწილების ტოპოლოგიურ სურათზე.

Оценка ошибки метода WKB с помощью кинематическиой модели Гратона для задачи магнитного пограничного слоя Земли

М. Чхитунидзе, И. Хведелидзе, Н. Джонджоладзе

Резюме

В данной работе рассмотрена плоская модель магнитного пограничного слоя Земли, которая соответствует меридиональному сечению магнитосферы. Решено однокомпонентное уравнение магнитной индукции, соответствующее уравнению I первого рода Жигулева магнитного пограничного слоя Земли, в котором поле скоростей дано модиффицированной моделью Гратона для сжимаемого солнечного ветра. Получено точное численное решение этого уравнения и приближённое аналитическое решение методом Вентцел-Крамер-Брилвена. Граничные условия соответствуют области, содержащей критической точке на дневной и ночной сторонах магнитосферы, то есть на плазмосфере. Определены ошибка метода ВКБ (≈ 1 %) и линейный размер области использования этого метода. Оценен эффект сжимаемости солнечного ветра, который существено должен влиять на топологическую кортину распределения магнитного поля на магнитопаузе и в области плазмопаузы.

Journal of the Georgian Geophysical Society,
Issue B. Physics of Atmosphere, Ocean, and Space Plasma, v.16b, 2013, pp. 53-76

Generation of zonal flow and magnetic field by coupled Rossby – Alfvén – Khantadze waves in the Earth's ionospheric E – layer

T. D. Kaladze[1, 2]*, W. Horton[3], L. Z. Kahlon[1], O. Pokhotelov[4] and O. Onishchenko[4]

[1]*Physcis Department, GC University, Lahore 54000, Pakistan*
[2]*I. Vekua Institute of Applied Mathematics, Tbilisi State University, 2 University str., 0186 Tbilisi, Georgia*
[3]*Institute for Fusion Studies, The University of Texas at Austin, Austin, Texas, USA*
[4]*Institute of Physics of the Earth, 10 B. Gruzinskaya Str., 123995 Moscow, Russia*

Abstract

It is shown that in the Earth's weakly ionized ionospheric E-layer with the dominant Hall conductivity new type of coupled Rossby – Alfvén – Khantadze (CRAK) electromagnetic (EM) planetary waves attributable by latitudinal inhomogeneity of both the Earth's Coriolis parameter and the geomagnetic field can exist. Under such coupling new type of dispersive Alfvén waves is revealed. Generation of sheared zonal flow and magnetic field by CRAK EM planetary waves is investigated. The nonlinear mechanism of the instability is based on the parametric excitation of zonal flow by interacting four waves leading to the inverse energy cascade in the direction of longer wavelength. A 3D set of coupled equations describing the nonlinear interaction of pumping CRAK waves and zonal flow is derived. The growth rate of the corresponding instability and the conditions for driving them are determined. It is found that growth rate is mainly stipulated by Rossby waves but the generation of the intense mean magnetic field is caused by Alfvén waves.

PACS numbers: 52.35.Mu, 92.10.hf, 94.20.wc

Keywords: Zonal flow, Ionospheric E-layer, Rossby – Alfvén – Khantadze waves, Nonlinear instability.

1. Introduction

Large-scale wave motions have the significant influence on energy balance in the Earth's atmospheric circulation [1, 2]. However, the presence of charged particles in the electrically conductive weakly ionized ionosphere substantially enriches the conditions for propagation of different nature low-frequency wave modes. Numerous ground-based and satellite observations [3 – 20] show that planetary-scale (with wavelengths $\lambda \geq 10^3\, km$ and several days period) wave perturbations of electromagnetic (EM) origin regularly exist in different ionospheric layers. Increasing interest to the planetary-scale ultra-low-frequency (ULF) wave perturbations is caused by the fact that many ionospheric phenomena from the same frequency range can play the role of ionospheric precursors of some extraordinary phenomena

Corresponding author, *< E-mail address: tamaz_kaladze@yahoo.com> (Tamaz Kaladze).
(earthquakes, volcano eruptions, etc.) [21 – 23] and also appear as the ionospheric response to the anthropogenic activity [24 – 27]. Forced oscillations of that kind under the impulsive impacts on the ionosphere and during magnetospheric storms were also observed [21].

In recent years increasing number of theoretical and experimental investigations was devoted to the investigation of dynamics of Rossby type waves (induced by the spatial inhomogeneity of the Coriolis parameter) in the Earth's ionosphere. Dokuchaev [28] first indicated the necessity of accounting for interaction of induced electric current with the Earth's magnetic field on the winds dynamics. The next step was done by Tolstoy [29] pointed out the importance of other global factor, acting permanently in the ionosphere - space inhomogeneity of the geomagnetic field on the dynamics of Rossby type waves in the Earth's ionospheric E-layer. The waves were entitled hydromagnetic gradient (HMG) waves. It was also shown that HMG waves can couple with the Rossby waves in the E-layer heights. He suggested that HMG waves may appear as traveling perturbations of the S_q current system producing from a few to several tenths of *nT* strong variations of the geomagnetic field.

Recently, in [30 – 34] was established new type of waves propagating in the ionospheric E-layer. They can be considered as the generalization of tropospheric Rossby waves by the spatially inhomogeneous geomagnetic field $\mathbf{B}_0$. As distinct from HMG waves, these waves do not cause the Earth's magnetic field significant perturbation and are produced by the dynamo electric field $\mathbf{E}_d = \mathbf{v} \times \mathbf{B}_0$. Note that in addition these waves are caused by the Hall conductivity in the E-layer. The waves of such different from HMG waves nature were termed "magnetized Rossby (MR) waves" [32].

Both HMG and MR waves compose so called slow long-period group of planetary waves having quite low phase velocities of the order of the local ionospheric winds (1 – 100 m/s). At middle – latitudes, their wavelengths ~ 10^3 *km* and longer, but the wave period alter from 2 h to 14 days. Correspondingly, the frequency falls in the range of $10^{-4} – 10^{-6}$ s^{-1}. In the experiments [3 – 5, 9, 10, 14, 20] some characteristics of these waves are observed.

Under the space (latitudinal) inhomogeneity of the geomagnetic field and Hall effect new type of waves, so called fast large-scale EM perturbations in the middle-latitude ionosphere also can propagate. In contrast to the slow waves, the fast modes are associated with oscillations of the ionospheric electrons frozen in the geomagnetic field and are connected with the large-scale internal vortical electric field generation in the ionosphere, i.e. $\mathbf{E}_v = \mathbf{V}_D \times \mathbf{B}_0$, where $\mathbf{V}_D = \mathbf{E} \times \mathbf{B}_0 / B_0^2$ is an electron drift velocity. The fast EM waves propagate along the parallels against the mean-zonal flow to the east as well as to the west. In E-region the phase velocity of fast waves is sufficiently high $|c_B| \approx 2 – 20$ kms^{-1}. Due to the dependence of c_B on the density of the charged particles the appropriate frequency of fast waves ($\omega \approx k_x c_B$) also changes almost by one order of magnitude during daytime and nighttime. As compared to the slow waves fast modes have relatively high frequency in the range 10^{-1}- 10^{-4} s^{-1} with the corresponding periods from 4 *min* to 6 *h* and the wavelength $\geq 10^3$ *km*. In contrast to the slow modes, fast EM planetary waves give rise to strong pulsations of the geomagnetic field 20 – 80 *nT*. Such new type of large – scale ULF wave EM perturbations in the ionospheric E - and F - regions first was theoretically revealed in [35 – 37], where the first classification of the EM planetary waves into fast and slow waves also is given. Such fast EM planetary waves are called Khantadze waves and were recorded in the middle and moderate latitudes during the launching of spacecrafts [18] and fixed by the ionospheric and magnetic world network observations [9, 19, 38].

Extensive analysis of the planetary EM waves in the ionospheric E - and F - layers is given in [39 – 41]. It was shown that large-scale waves are weakly damped. New type of coupled Rossby waves with Alfvén waves first was revealed in [42], where the possibility of existence of the new spatially isolated joint Alfvén – Rossby nonlinear vortical structures in the Earth's ionosphere is also shown. We believe that the further investigation of the nonlinear dynamics of ULF planetary EM waves is so necessary.

In the given paper, we show that the action of the latitudinal inhomogeneity of both the Coriolis parameter and the geomagnetic field through the vertically propagating geomagnetic field perturbations lead to the coupled propagation of EM Rossby – Alfvén – Khantadze modes. By this fact the initial equations describing the appropriate nonlinear dynamics becomes 3D. The aim of the present paper is to investigate the possibility of mean zonal – flow and magnetic field generation by the EM coupled Rossby – Alfvén – Khantadze (CRAK) planetary waves in the ionospheric E - layer.

Ground - based and satellite observations [1, 2] confirm the permanent existence of large-scale azimuthally symmetric band – like sheared zonal flows surrounding the globe at different layers of the Earth's ionosphere and propagating along the parallels with inhomogeneous velocities along the meridians (see, e.g. [43]). Thus, the Earth's ionosphere represents the dynamical system of different nature waves and zonal flows. Under such favorable conditions for nonlinear interactions different EM nonlinear stationary solitary structures can appear [42, 44].

According to the one existing idea spatially inhomogeneous zonal winds (shear flows) can be produced by nonuniform heating of the atmospheric layers by solar radiation. First in [45] was suggested the generation mechanism of zonal flows by tropospheric Rossby waves in neutral atmosphere invoking parametric instability in terms of the kinetic equation for wave packets. The investigation of zonal – flow generation problem by Rossby waves was further developed in [46, 47] using the parametric instabilities mechanism on the basis of a monochromatic four – wave resonant nonlinear interaction. In these papers it was shown that zonal flows in a non – uniform rotating neutral atmosphere can be excited by finite – amplitude Rossby waves. Accordingly, these papers study the interaction of pump waves (Rossby waves), a sheared flow and two satellites of the pump wave (side – band waves). This approach is an alternative to the standard weak turbulence approach used by [45]. The driving mechanism of this instability is due to the Reynolds stresses, which are inevitably inherent for finite – amplitude small – scale Rossby waves. Owing to this essential nonlinear mechanism, spectral energy transfers from small – scale Rossby waves to large – scale enhanced zonal flows (inverse cascade) in the Earth's neutral atmosphere. In addition, the zonal - flow generation was considered within a simple model of Rossby wave turbulence, using the classical nonlinear two – dimensional Charney equation. It was found that the necessary condition for zonal flow generation is similar to the Lighthill criterion for modulation instability in nonlinear optics [48]. By the numerical simulation of sheared zonal flow interaction with Rossby waves in the Earth's neutral atmosphere [49] is shown that new solitary structures arise to produce the structural turbulence.

Further [50] revealed the new mechanism for the problem of zonal flow generation by the drift waves in magnetized plasmas adding a scalar nonlinearity of Korteweg – de Vries type to the generalized Hasegawa – Mima equation containing the vector nonlinearity also. It was shown that in this case zonal – flow generation always exists and needs no criterion fulfillment.

Investigation of the mean zonal flow generation problem in the Earth's electrically conducting ionosphere was firstly undertaken in [51 – 54], where the excitation of zonal flow by MR waves in the ionospheric E - layer was considered.

However, the investigation of another very important nonlinear process, viz., the generation of mean zonal flows and magnetic field by EM planetary waves in the ionospheric layers was started recently. Nonlinear dynamics of coupled Rossby – Khantadze and coupled internal – gravity and Alfvén EM planetary waves in the weakly ionized ionospheric E – layer was investigated by [55, 56]. It was shown that such EM planetary waves along with mean zonal flows can generate intense mean magnetic fields also. In the present paper, we will focus our attention on the Earth's weakly ionized, conductive ionospheric gas of the E - layer ($\approx 90 - 150\ km$ from the Earth's surface) and will consider the generation of mean zonal flow and magnetic field by coupled Rossby – Alfvén – Khantadze (CRAK) EM planetary waves. Developed in [57, 58] techniques for the case of EM waves will be used. The paper is organized as follows: In Sec. 2, basic equations modeling the nonlinear propagation of EM CRAK planetary waves in the ionospheric E - layer are obtained. Linear propagation properties of the EM coupled Rossby – Alfvén – Khantadze waves are given in detail in Sec. 3. Using the modified parametric approach, a set of coupled equations describing the nonlinear interaction of pumping EM CRAK planetary waves with an arbitrary spectrum and zonal flows is derived in Sec. 4. In the same section zonal flow dispersion relation is also obtained. In Secs. 5 and 6 it is shown that the system of equations obtained in Sec. 4 is unstable to a three wave parametric instability, whereby a coherent, monochromatic pumping Rossby – Alfvén – Khantadze waves can drive a band of modes and associated zonal flow and magnetic field generation. Namely, in Sec. 5 zonal flow growth rate is analyzed in detail. In Sec. 6, magnetic field generation dynamics is investigated in detail. Our discussion and conclusions are presented in Sec. 7.

2. Physical modeling for ionospheric E – layer

We consider the weakly ionized ionospheric E – layer plasma comprising of electrons, ions, and neutral (molecules) particles. Due to the condition $n / N << 1$, where n and N are the equilibrium number densities for

the charged particles and neutrals, respectively and strong collisional coupling between the ions and neutrals the dynamics of such ionospheric E – layer gas is largely determined by its massive neutral component. Attributable by the existence of charged particles Ampere force plays the significant role in the problem set along with the effects of the latitudinal inhomogeneity of the vertical component of the Earth's angular rotation $\mathbf{\Omega}$ and of the geomagnetic field $\mathbf{B}_0(\mathbf{x})$ [55]. We also introduce the local Cartesian coordinates (x, y, z) system with the x - axis directed from the west to the east, y - axis directed from the south to the north and the z - axis along with the local vertical direction. The following relations for latitude λ and longitude ϕ are valid: $y = (\lambda - \lambda_0)R$ and $x = \phi R \cos\lambda_0$, where R is the distance from the Earth's center. In the defined local coordinate system, the components of the geomagnetic field vector are $\mathbf{B_0} = (0, B_{0y}, B_{0z}) = (0, B_{eq}\cos\lambda, -2B_{eq}\sin\lambda)$, where B_{eq} is the equatorial value of the geomagnetic field at a distance R from the Earth's center. As to the Earth's angular velocity $\mathbf{\Omega}$, we have $\mathbf{\Omega} = (0, \Omega_{0y}, \Omega_{0z}) = (0, \Omega_0\cos\lambda, \Omega_0\sin\lambda)$ [55].

According to [33], we can construct the following single-fluid momentum equation which describes the dynamics of the electrically conducting weakly ionized ionospheric E – layer plasma

$$\frac{\partial \mathbf{v}}{\partial t} + (\mathbf{v}\cdot\nabla)\mathbf{v} + \frac{\nabla p}{\rho} - \frac{1}{\rho}\mathbf{j}\times\mathbf{B} + 2\mathbf{\Omega}\times\mathbf{v} - \mathbf{g} = 0, \qquad (1)$$

where $\mathbf{v}$ is the incompressible $(\nabla\cdot\mathbf{v} = 0)$ neutral gas velocity, $\rho = Nm_N$ is the gas mass density, p is the gas pressure of the neutral gas and g is the gravitational acceleration. In Eq. (1) along with the Coriolis force the following Ampere force

$$\mathbf{F}_A = \frac{1}{\rho}\mathbf{j}\times\mathbf{B} = \frac{1}{\rho\mu_0}\nabla\times\mathbf{B}\times\mathbf{B}, \qquad (2)$$

is taken into account, where μ_0 is the permeability of free space, and $\mathbf{B} = \mathbf{B_0} + \mathbf{b}$ is the total magnetic induction.

From Eq. (1) follows the following equation for vorticity $\boldsymbol{\zeta} = \nabla\times\mathbf{v}$:

$$\frac{\partial \boldsymbol{\zeta}}{\partial t} - (\boldsymbol{\zeta}\cdot\nabla)\mathbf{v} + (\mathbf{v}\cdot\nabla)\boldsymbol{\zeta} - \frac{1}{\rho\mu_0}\left[(\mathbf{B}\cdot\nabla)\nabla\times\mathbf{B} - (\nabla\times\mathbf{B}\cdot\nabla)\mathbf{B}\right] + 2\left[(\mathbf{v}\cdot\nabla)\mathbf{\Omega} - (\mathbf{\Omega}\cdot\nabla)\mathbf{v}\right] = 0. \qquad (3)$$

By using the plasma conditions in the ionospheric E – layer we may simplify the generalized Ohm's law expression. First, the condition $\omega_{ci}/\nu_i << 1$ ($\omega_{ci} = eB/m_i$ is the ion cyclotron frequency, and ν_i is the ion – neutral collision frequency) allows to consider unmagnetized ions. Due to the high values of ν_i we can suppose $\mathbf{v}_i = \mathbf{v}$, which means that the ions are completely dragged by the ionospheric winds. As to electrons they are magnetized, $\omega_{ce}/\nu_e >> 1$ (ω_{ce} is the electron cyclotron frequency and ν_e is the electron – neutral collision frequency). It means that electrons are frozen in the external magnetic field and they only experience drift perpendicular to the magnetic field, i.e $\mathbf{v}_e = \mathbf{v}_E = \mathbf{E}\times\mathbf{B}/B^2$. Under such conditions generalized Ohm's law for the ionospheric E- layer is [55]

$$\mathbf{E} + \mathbf{v}\times\mathbf{B} = \frac{1}{en}\mathbf{j}\times\mathbf{B} = \frac{\rho}{en}\mathbf{F}_A, \qquad (4)$$

where the right-hand side reflects Hall effect [39]. Then from the Faraday's law $\nabla\times\mathbf{E} = -\frac{\partial \mathbf{B}}{\partial t}$ we can find the following equation for the magnetic induction $\mathbf{B}$ [55]:

$$\frac{\partial \mathbf{B}}{\partial t} + \frac{1}{en\mu_0}\left[(\mathbf{B}\cdot\nabla)\nabla\times\mathbf{B} - (\nabla\times\mathbf{B}\cdot\nabla)\mathbf{B}\right] - (\mathbf{B}\cdot\nabla)\mathbf{v} + (\mathbf{v}\cdot\nabla)\mathbf{B} = 0. \qquad (5)$$

In contrast to the ordinary frozen in condition for a conducting fluid this equation contains the second term which is caused by the action of the Ampere force on the ionized plasma component (the Hall effect).

Eqs. (3) and (5) constitute our initial general equations. In the ionospheric E – layer, the large-scale wave motions are basically two – dimensional, i.e. $\mathbf{v} = (\mathrm{v}_x, \mathrm{v}_y, 0)$ and by using the incompressibility condition $\nabla \cdot \mathbf{v} = 0$, we can introduce the stream function $\psi(x, y, z)$, so that $\mathrm{v}_x = -\partial\psi / \partial y$, and $\mathrm{v}_y = \partial\psi / \partial x$. Further we will consider sufficiently high latitudes in the northern hemisphere, assuming that the geomagnetic field $\mathbf{B}_0 = B_{0z}(y)\mathbf{e}_z$ and the Earth's angular velocity $\mathbf{\Omega} = \Omega_{0z}(y)\mathbf{e}_z$. Let us suppose that the magnetic induction perturbation is also two – dimensional, i.e. $\mathbf{b} = (b_x, b_y, 0)$ and according to the condition $\nabla \cdot \mathbf{B} = 0$, we can introduce the magnetic function $A(x, y, z)$, so that $b_x = \partial A / \partial y$, and $b_y = -\partial A / \partial x$. Then from Eq. (3) we get

$$\frac{\partial \Delta_\perp \psi}{\partial t} + \beta \frac{\partial \psi}{\partial x} + J(\psi, \Delta_\perp \psi) = -\frac{B_{0z}}{\rho\mu_0}\frac{\partial \Delta_\perp A}{\partial z} + \frac{1}{\rho\mu_0} J(A, \Delta_\perp A). \tag{6}$$

Here, $\beta = \partial f / \partial y = 2\partial\Omega_{0z} / \partial y$, $\Delta_\perp = \partial_x^2 + \partial_y^2$ is the two – dimensional (2D) Laplacian and $J(a,b) = \partial_x a \, \partial_y b - \partial_y a \, \partial_x b$ is the the vector nonlinearity called Jacobian (Poisson bracket). Note that in Eq. (6) we neglected the term containing $\partial B_{0z} / \partial y$ compared with the first term on the right – hand side.

To transform magnetic induction Eq. (5) we consider its x – and y – components in terms of magnetic function A:

$$\frac{\partial^2 A}{\partial t \partial y} + \frac{B_{0z}}{en\mu_0}\frac{\partial^3 A}{\partial x \partial z^2} - c_B \frac{\partial^2 A}{\partial x \partial y} + B_{0z}\frac{\partial^2 \psi}{\partial y \partial z} + J(\psi, \frac{\partial A}{\partial y}) - J(A, \frac{\partial \psi}{\partial y}) = 0, \tag{7}$$

$$\frac{\partial^2 A}{\partial t \partial x} - \frac{B_{0z}}{en\mu_0}\frac{\partial^3 A}{\partial y \partial z^2} - c_B \frac{\partial^2 A}{\partial x^2} + B_{0z}\frac{\partial^2 \psi}{\partial x \partial z} + J(\psi, \frac{\partial A}{\partial x}) - J(A, \frac{\partial \psi}{\partial x}) = 0, \tag{8}$$

where $c_B = \beta_B / en\mu_0$, $\beta_B = \partial B_{0z} / \partial y$. In Eqs. (7), and (8) we neglected the terms ~ A^2 / L^4 in comparison with $A\psi / L^3$, where L is the scale-length for planetary waves.

Let's integrate Eqs. (7), and (8) by y, and x, respectively. We get

$$\frac{\partial A}{\partial t} + \frac{1}{en\mu_0}\int dy B_{0z}(y)\frac{\partial^3 A}{\partial x \partial z^2} - c_B \frac{\partial A}{\partial x} + \int dy B_{0z}(y)\frac{\partial^2 \psi}{\partial y \partial z} + J(\psi, A) = F_1(x, z), \tag{9}$$

$$\frac{\partial A}{\partial t} - \frac{B_{0z}}{en\mu_0}\int dx \frac{\partial^3 A}{\partial z^2 \partial y} - c_B \frac{\partial A}{\partial x} + B_{0z}\frac{\partial \psi}{\partial z} + J(\psi, A) = F_2(y, z). \tag{10}$$

Here, F_1 and F_2 are arbitrary functions of integration. Let us represent in Eqs. (9) and (10) $B_{0z}(y) \approx B_{0z}(y_0) + y\,\partial B_{0z} / \partial y$, then we get

$$\begin{aligned} &\frac{\partial A}{\partial t} + \frac{B_{0z}(y_0)}{en\mu_0}\int dy \frac{\partial^3 A}{\partial x \partial z^2} + c_B \int dy y \frac{\partial^3 A}{\partial x \partial z^2} - c_B \frac{\partial A}{\partial x} + B_{0z}(y_0)\frac{\partial \psi}{\partial z} \\ &+ \frac{\partial B_{0z}}{\partial y}\int dy y \frac{\partial^2 \psi}{\partial y \partial z} + J(\psi, A) = F_1(x, z), \end{aligned} \tag{11}$$

$$\frac{\partial A}{\partial t} - \frac{B_{0z}}{en\mu_0}\int dx \frac{\partial^3 A}{\partial z^2 \partial y} - c_B \frac{\partial A}{\partial x} + B_{0z}(y_0)\frac{\partial \psi}{\partial z} + J(\psi, A) = F_2(y, z). \tag{12}$$

For the consistency of Eqs. (11), and (12), we choose:

$$F_1(x, z) = \frac{B_{0z}(y_0)}{en\mu_0}\int dy \frac{\partial^3 A}{\partial x \partial z^2} + c_B \int dy y \frac{\partial^3 A}{\partial x \partial z^2} + \frac{\partial B_{0z}}{\partial y}\int dy y \frac{\partial^2 \psi}{\partial y \partial z}, \tag{13}$$

$$F_2(y,z) = -\frac{B_{0z}(y_0)}{en\mu_0}\int dx \frac{\partial^3 A}{\partial z^2 \partial y}. \quad (14)$$

Then we get the following common equation

$$\frac{\partial A}{\partial t} - c_B \frac{\partial A}{\partial x} + B_{0z}(y_0)\frac{\partial \psi}{\partial z} + J(\psi, A) = 0. \quad (15)$$

Equations (6) and (15) compose the initial system of equations for our problem and describe the nonlinear dynamics of the EM planetary low – frequency wave perturbations in the ionospheric E – layer. From Eqs. (6) and (15), we can obtain the following temporal conservation law of energy $\mathcal{E}$

$$\frac{\partial \mathcal{E}}{\partial t} = \frac{\partial}{\partial t}\left\{\frac{1}{2}\int[\rho(\nabla_\perp \psi)^2 + \frac{1}{\mu_0}(\nabla_\perp A)^2]dxdy\right\} = 0. \quad (16)$$

3. Linear EM planetary waves

Linear dispersion relation for EM CRAK waves can be readily obtained from Eqs. (6) and (15)

$$(\omega + \frac{k_x}{k_\perp^2}\beta)(\omega + k_x c_B) = k_z^2 \mathrm{v}_A^2, \quad (17)$$

where ω is the wave frequency, $\mathrm{v}_A^2 = B_{0z}^2/\mu_0\rho$ is the squared Alfvén velocity, and $k_\perp^2 = k_x^2 + k_y^2$, k_x, k_y, and k_z are the components of the wave vector $\mathbf{k}$ along the x-, y-, and z- axes. When $k_x = 0$ we get the Alfvén branch of oscillations with the dispersion relation $\omega = \pm k_z \mathrm{v}_A$; when $k_z = 0$ we get the additional two branches of oscillations: 1) $\omega = -k_x\beta/k_\perp^2$, which describes the Rossby waves (slow waves), and 2) $\omega = -k_x c_B$, which describes the Khantadze waves (fast waves). Thus the dispersion relation (17) describes the propagation of EM CRAK waves in the ionospheric E – layer.

The solution of the dispersion equation (17) by taking into account the velocity $c_B < 0$

$$\omega_{1,2} = \frac{k_x}{2}\left[|c_B| - \frac{\beta}{k_\perp^2} \pm \sqrt{\left(|c_B| + \frac{\beta}{k_\perp^2}\right)^2 + 4\frac{k_z^2}{k_x^2}\mathrm{v}_A^2}\right]. \quad (18)$$

Eq. (18) represents that EM coupled Rossby – Alfvén – Khantadze waves have two branches of oscillations, one branch of oscillation ω_1 (with "+" sign before the radical) and other one ω_2 (with "–" sign before the radical).

Eq. (18) for the case of small $k_\perp^2 << 1$ reads as follows

$$\omega_1 = k_x(|c_B| + k_\perp^2 \frac{k_z^2 \mathrm{v}_A^2}{\beta k_x^2}), \quad (19)$$

and

$$\omega_2 = k_x(-\frac{\beta}{k_\perp^2} - k_\perp^2 \frac{k_z^2 \mathrm{v}_A^2}{\beta k_x^2}). \quad (20)$$

As to the case of large $k_\perp^2 >> 1$, we get from Eq. (18)

$$\omega_{1,2} = \frac{k_x}{2}\left\{|c_B| - \frac{\beta}{k_\perp^2} \pm \sqrt{c_B^2 + 4\frac{k_z^2}{k_x^2}\mathrm{v}_A^2}\left[1 + \frac{|c_B|\beta}{k_\perp^2\left(c_B^2 + 4\frac{k_z^2}{k_x^2}\mathrm{v}_A^2\right)}\right]\right\}. \quad (21)$$

Here we consider $k_z^2 \mathrm{v}_A^2 / k_x^2 c_B^2 \sim 1$ to obtain Eqs. (19) – (21).

Thus the branch ω_1 reprsents the Khantadze waves imposed by the action of both the latitudinal inhomogeneity of the Coriolis force and magnetic field perturbations, while the branch ω_2 represents the Rossby waves imposed by the same factors. Under the action of these factors Khantadze waves are propagating eastward with the increased phase velocity ω_1 / k_x, while the phase velocity of westward propagating Rossby waves is also increasing.

The case of small $k_x^2 << 1$, also can be described from Eq. (18)

$$\omega_{1,2} = \pm k_z \mathrm{v}_A \left[1 + k_x^2 \frac{\left(|c_B| + \frac{\beta}{k_\perp^2} \right)^2}{8 k_z^2 \mathrm{v}_A^2} \right] + \frac{k_x}{2} \left(|c_B| - \frac{\beta}{k_\perp^2} \right). \tag{22}$$

These are Alfvén waves branch imposed by the action of latitudinal inhomogeneity of Coriolis force and latitudinal inhomogeneity of the geomagnetic field.

We can represent in the β - plane approximation [33] the Coriolis parameter as

$$f = 2\Omega_{0z} = 2\Omega_0 \sin\lambda = f_0 + \beta y, \tag{23}$$

with

$$\beta = \frac{\partial f}{\partial y} = \frac{2\Omega_0 \cos\lambda_0}{R} > 0, \tag{24}$$

and the geomagnetic field as

$$B_{0z} = -2B_{eq} \sin\lambda = \gamma_0 + \beta_B y, \tag{25}$$

with

$$\beta_B = \frac{\partial B_{0z}}{\partial y} = -\frac{2B_{eq} \cos\lambda_0}{R} < 0. \tag{26}$$

By introducing the dimensionless variables $k^* = k |c_B|^{1/2} / \beta^{1/2}$, and $\omega^* = \omega / \beta^{1/2} |c_B|^{1/2}$, we can rewrite the dispersion relation (18) as

$$y_{1,2} = \frac{1}{2x^2} \left(x^2 - 1 \pm \sqrt{(x^2+1)^2 + 4x^4 \alpha} \right), \tag{27}$$

where $y = \omega^* / k_x^*$, $x^2 = k_\perp^{*2}$, and $\alpha = k_z^2 \mathrm{v}_A^2 / k_x^2 c_B^2$. For the ionospheric E – layer parameters $B_{eq} \sim 0.5 \times 10^{-4} T$, $2\Omega_0 \sim 10^{-4} rad/s$, $n/N \sim 10^{-8} - 10^{-6}$, $\rho = (10^{-7} - 10^{-8}) kgm^{-3}$, we can find that $|c_B| \sim (1-10) km/s$, $\mathrm{v}_A \sim (0.1-1) km/s$. In Fig. 1, the dependence of dimensionless phase velocity y of coupled Rossby – Alfvén – Khantadze branches of oscillations on wave number x for the different values of $\alpha = 0$; 1; 5 is shown. A and B curves correspond to "+" and "–" signs before the radical in Eq. (27), respectively. Thus A and B curves correspond to ω_1 and ω_2 branches of oscillations in Eqs. (19) – (21), respectively.

We can find the following behavior of $y_{1,2}$:

a) when $x \to 0$,

$$y_1 = 1 + x^2 \alpha, \qquad \text{and} \qquad y_2 = -\frac{1}{x^2} - x^2 \alpha. \tag{28}$$

b) when $x \to \infty$

$$y_{1,2} = \frac{1}{2}\left[1 - \frac{1}{x^2} \pm \left(\sqrt{1+4\alpha} + \frac{1}{x^2\sqrt{1+4\alpha}}\right)\right]. \quad (29)$$

In Eqs. (28) and (29) y_1 and y_2 correspond to Khantadze and Alfvén waves, respectively.

4. Nonlinear interaction of coupled Rossby – Alfvén – Khantadze EM planetary waves and zonal flow dispersion relation

To find the possibility for the zonal flow generation by the EM CRAK planetary waves in the ionospheric E – layer we will consider the initial nonlinear Eqs. (6) and (15). Existing in this equations the nonlinear Jacobian terms allows to consider a standard four - wave nonlinear interaction, in which the coupling between the pump $\tilde{X} = (\tilde{\psi}, \tilde{h})$ EM planetary waves and two side - band $\hat{X} = (\hat{\psi}, \hat{h})$ modes drives low - frequency large - scale $\overline{X} = (\overline{\psi}, \overline{h})$ zonal flows with variation only along the y – axis. Accordingly, the total perturbed quantities $X = (\psi, h)$ are decomposed in three components,

$$X = \tilde{X} + \hat{X} + \overline{X}, \quad (30)$$

where

$$\tilde{X} = \sum_{\mathbf{k}} \left[\tilde{X}_+(\mathbf{k}) \exp(i\mathbf{k}\cdot\mathbf{r} - i\omega_{\mathbf{k}} t) + \tilde{X}_-(\mathbf{k}) \exp(-i\mathbf{k}\cdot\mathbf{r} + i\omega_{\mathbf{k}} t)\right], \quad (31)$$

describes pump EM planetary modes spectrum ($\tilde{X}_-(\mathbf{k}) = \tilde{X}_+^*(\mathbf{k})$, where $*$ means the complex conjugate),

$$\hat{X} = \sum_{\mathbf{k}} \left[\hat{X}_+(\mathbf{k}) \exp(i\mathbf{k}_+\cdot\mathbf{r} - i\omega_{\mathbf{k}_+} t) + \hat{X}_-(\mathbf{k}) \exp(i\mathbf{k}_-\cdot\mathbf{r} - i\omega_{\mathbf{k}_-} t) + c.c.\right] \quad (32)$$

describes sideband modes spectrum, and

$$\overline{X} = \overline{X}_0 \exp(-i\Omega t + iq_y y) + c.c. \quad (33)$$

describes the zonal - flow modes varying only along meridians. Within the local approximation the amplitude of the zonal flow mode $\overline{X}_0 = (\overline{\psi}_0, \overline{h}_0)$ is assumed constant. The energy and momentum conservations $\omega_\pm = \Omega \pm \omega_{\mathbf{k}}$ and $\mathbf{k}_\pm = q_y \mathbf{e}_y \pm \mathbf{k}$ are fulfilled, and the pairs $(\omega_{\mathbf{k}}, \mathbf{k})$ and $(\mathbf{\Omega}, q_y \mathbf{e}_y)$ represent the frequency and wave vector of the EM planetary pump and zonal - flow modes, respectively. In the sequel we will omit the index $\mathbf{k}$ at ω for simplicity.

Substituting Eqs. (30) - (33) into (6) and (15), and according to the standard quasilinear procedure ignoring the small nonlinear term in the relations for the high frequency but not for the low frequency zonal flow modes we get for the EM planetary modes

$$\begin{cases} (\omega k_\perp^2 + \beta k_x)\tilde{\psi}_\pm = \dfrac{B_{0z}}{\rho\mu_0} k_z k_\perp^2 \tilde{A}_\pm, \\ (\omega + c_B k_x)\tilde{A}_\pm = B_{0z} k_z \tilde{\psi}_\pm. \end{cases} \quad (34)$$

From this homogeneous system the dispersion relation (17) for EM planetary modes follows.

Substituting Eqs. (30) – (33) into (6) and (15) to obtain the relations for the amplitude of the zonal flow modes and averaging out over the fast small – scale fluctuations, we get [57, 58]

$$-i\Omega\overline{\psi}_0 = R_\perp, \quad (35)$$

and

$$-i\Omega\overline{A}_0 = R_\parallel, \quad (36)$$

where $R_\perp$ and $R_\parallel$ are the mixture of Reynolds and electromotive forces, defined by

$$R_{\perp} = -\left\langle \frac{\partial \tilde{\psi}}{\partial x}\frac{\partial \hat{\psi}}{\partial y} + \frac{\partial \hat{\psi}}{\partial x}\frac{\partial \tilde{\psi}}{\partial y} \right\rangle + \frac{1}{\rho\mu_0}\left\langle \frac{\partial \tilde{A}}{\partial x}\frac{\partial \hat{A}}{\partial y} + \frac{\partial \hat{A}}{\partial x}\frac{\partial \tilde{A}}{\partial y} \right\rangle, \tag{37}$$

and

$$R_{\parallel} = iq_y \left\langle \tilde{\psi}\frac{\partial \hat{A}}{\partial x} + \hat{\psi}\frac{\partial \tilde{A}}{\partial y} \right\rangle, \tag{38}$$

where $\langle \cdots \rangle$ represents the average over fast oscillations. Using the Fourier series (31) and (32), we can write these quantities as

$$R_{\perp} = -\sum_{\mathbf{k}} k_x r_{\perp}(\mathbf{k}), \tag{39}$$

and

$$R_{\parallel} = q_y \sum_{\mathbf{k}} k_x r_{\parallel}(\mathbf{k}), \tag{40}$$

where

$$\begin{aligned} r_{\perp}(\mathbf{k}) &= q_y(\tilde{\psi}_{-}\hat{\psi}_{+} - \tilde{\psi}_{+}\hat{\psi}_{-}) + 2k_y(\tilde{\psi}_{-}\hat{\psi}_{+} + \tilde{\psi}_{+}\hat{\psi}_{-}) \\ &- \frac{1}{\rho\mu_0}[q_y(\tilde{A}_{-}\hat{A}_{+} - \tilde{A}_{+}\hat{A}_{-}) + 2k_y(\tilde{A}_{-}\hat{A}_{+} + \tilde{A}_{+}\hat{A}_{-})], \end{aligned} \tag{41}$$

and

$$r_{\parallel}(\mathbf{k}) = \tilde{\psi}_{+}\hat{A}_{-} - \tilde{\psi}_{-}\hat{A}_{+} + \hat{\psi}_{+}\tilde{A}_{-} - \hat{\psi}_{-}\tilde{A}_{+} = \tilde{\psi}_{-}\hat{\lambda}_{+} - \tilde{\psi}_{+}\hat{\lambda}_{-}. \tag{42}$$

Here we used Eq. (34) for $\tilde{A}_{\pm}$ to construct the following auxiliary side – band amplitudes

$$\hat{\lambda}_{\pm} = \frac{k_z B_{0z}}{\omega + k_x c_B}\hat{\psi}_{\pm} - \hat{A}_{\pm}. \tag{43}$$

To calculate the functions $r_{\perp}$ and $r_{\parallel}$, we need to define the side – band amplitudes $\hat{\psi}_{\pm}$ and $\hat{A}_{\pm}$. According to Eqs. (6) and (15), these amplitudes satisfy the following system [57, 58]

$$\begin{cases} (\omega_{\pm}k_{\perp\pm}^2 \pm k_x\beta)\hat{\psi}_{\pm} \mp k_z k_{\perp\pm}^2 \dfrac{B_{0z}}{\rho\mu_0}\hat{A}_{\pm} = \mp ik_x q_y(k_{\perp}^2 - q_y^2)\tilde{\psi}_{\pm}\bar{\psi}_0 \\ \qquad \pm i\dfrac{q_y}{\rho\mu_0}(k_{\perp}^2 - q_y^2)\dfrac{k_x k_z B_{0z}}{\omega + k_x c_B}\tilde{\psi}_{\pm}\bar{A}_0, \\ \pm k_z B_{0z}\hat{\psi}_{\pm} - (\omega_{\pm} \pm k_x c_B)\hat{A}_{\pm} = \pm ik_x q_y \tilde{\psi}_{\pm}\bar{A}_0\left(\dfrac{k_z B_{0z}}{\omega + k_x c_B}\dfrac{\bar{\psi}_0}{\bar{A}_0} - 1\right). \end{cases} \tag{44}$$

We can find the following solutions of the system (44)

$$\begin{aligned} \hat{\psi}_{\pm} = \frac{ik_x q_y}{D_{\pm}}\tilde{\psi}_{\pm}\Bigg\{ &\bar{\psi}_0\left[\mp(k_{\perp}^2 - q_y^2)(\omega_{\pm} \pm k_x c_B) - \frac{k_z^2 \mathrm{v}_A^2 k_{\perp\pm}^2}{\omega + k_x c_B}\right] \\ &+ \bar{A}_0\frac{k_z B_{0z}}{\rho\mu_0}\left[\pm\frac{k_{\perp}^2 - q_y^2}{\omega + k_x c_B}(\omega_{\pm} \pm k_x c_B) + k_{\perp\pm}^2\right] \end{aligned} \tag{45}$$

and

$$\hat{A}_{\pm} = \pm\frac{ik_x q_y}{D_{\pm}}\tilde{\psi}_{\pm}\left\{\overline{\psi}_0\left[-\frac{k_z B_{0z}}{\omega + k_x c_B}(\omega_{\pm}k_{\perp\pm}^2 \pm k_x\beta) \mp k_z B_{0z}(k_{\perp}^2 - q_y^2)\right]\right.$$
$$\left. + \overline{A}_0\left[\omega_{\pm}k_{\perp\pm}^2 \pm k_x\beta \pm \frac{k_{\perp}^2 - q_y^2}{\omega + k_x c_B}k_z^2 \mathrm{v}_A^2\right]\right\}, \tag{46}$$

where

$$D_{\pm} = (\omega_{\pm}k_{\perp\pm}^2 \pm k_x\beta)(\omega_{\pm} \pm k_x c_B) - k_z^2\,\mathrm{v}_A^2\,k_{\perp\pm}^2. \tag{47}$$

Applying Eqs. (45) and (46), the expression (43) for the auxiliary side – band amplitudes takes the following form

$$\hat{\lambda}_{\pm} = \frac{ik_x q_y}{D_{\pm}}\tilde{\psi}_{\pm}\overline{A}_0\left\{\mp\frac{\Omega(k_{\perp}^2 - q_y^2)}{\omega + k_x c_B}\left[\frac{\overline{\psi}_0}{\overline{A}_0}k_z B_{0z} - \frac{k_z^2\mathrm{v}_A^2}{\omega + k_x c_B}\right]\right.$$
$$\left. + \left(1 - \frac{k_z B_{0z}}{\omega + k_x c_B}\frac{\overline{\psi}_0}{\overline{A}_0}\right)\left[-2q_y\Omega k_y + \frac{k_x}{k_{\perp}^2}\beta q_y^2 \pm 2q_y k_y\beta\frac{k_x}{k_{\perp}^2} \mp \Omega(k_{\perp}^2 + q_y^2)\right]\right\}. \tag{48}$$

We assume that $q_y / k_{\perp} \sim \Omega/\omega << 1$, which is valid in the existing theory of zonal – flow generation [45]. Then, from Eq. (48) follows the distinguished fact that the main contributions of the "magnetic" and "stream function" side – band amplitudes to the evolution equation of the mean magnetic field mutually cancel each other [see Eqs. (36), (38), (40), and (42)]. If we use the superscripts "(1), (2), …" to show the order of magnitudes with respect to q_y and Ω, then Eq. (47) can be written as follows

$$D_{\pm} = \pm D^{(1)} + D^{(2)} \pm D^{(3)} + D^{(4)}, \tag{49}$$

where

$$D^{(1)} = 2q_y k_y\omega(\omega + k_x c_B) + (\omega + k_x c_B)k_{\perp}^2\Omega + \Omega(\omega k_{\perp}^2 + k_x\beta) - 2q_y k_y k_z^2\mathrm{v}_A^2,$$
$$D^{(2)} = -q_y^2 k_z^2\mathrm{v}_A^2 + \Omega^2 k_{\perp}^2 + 2q_y k_y\Omega(\omega + k_x c_B) + \omega q_y^2(\omega + k_x c_B) + 2q_y k_y\omega\Omega,$$
$$D^{(3)} = 2q_y k_y\Omega^2 + \Omega q_y^2(\omega + k_x c_B) + \omega\Omega q_y^2,$$
$$D^{(4)} = \Omega^2 q_y^2. \tag{50}$$

If we keep in Eq. (48) only first two terms over the named above small parameters q_y and Ω we get

$$\hat{\lambda}_{\pm} = \hat{\lambda}_{\pm}^{(1)} + \hat{\lambda}_{\pm}^{(2)}, \tag{51}$$

where

$$\hat{\lambda}_{\pm}^{(1)} = -i\frac{k_x q_y}{D^{(1)}}\tilde{\psi}_{\pm}\overline{A}_0\left[\frac{\Omega k_{\perp}^2}{\omega + k_x c_B}\left(\frac{\overline{\psi}_0}{\overline{A}_0}k_z B_{0z} - \frac{k_z^2\mathrm{v}_A^2}{\omega + k_x c_B}\right)\right.$$
$$\left. + \left(1 - \frac{k_z B_{0z}}{\omega + k_x c_B}\frac{\overline{\psi}_0}{\overline{A}_0}\right)\left(-2q_y k_y\beta\frac{k_x}{k_{\perp}^2} + \Omega k_{\perp}^2\right)\right], \tag{52}$$

$$\hat{\lambda}_{\pm}^{(2)} = \pm i\frac{k_x q_y}{D^{(1)}}\tilde{\psi}_{\pm}\overline{A}_0\left[\frac{D^{(2)}}{D^{(1)}}\frac{\Omega k_{\perp}^2}{\omega + k_x c_B}\left(\frac{\overline{\psi}_0}{\overline{A}_0}k_z B_{0z} - \frac{k_z^2\mathrm{v}_A^2}{\omega + k_x c_B}\right)\right.$$
$$\left. + \left(1 - \frac{k_z B_{0z}}{\omega + k_x c_B}\frac{\overline{\psi}_0}{\overline{A}_0}\right)\left(-2q_y\Omega k_y + \frac{k_x}{k_{\perp}^2}\beta q_y^2 - 2k_y q_y\frac{k_x}{k_{\perp}^2}\beta\frac{D^{(2)}}{D^{(1)}} + \Omega k_{\perp}^2\frac{D^{(2)}}{D^{(1)}}\right)\right]. \tag{53}$$

We can prove that the contribution of $\hat{\lambda}_{\pm}^{(1)}$ in Eq. (42) is zero. Thus, we get

$$r_{\parallel}(\mathbf{k}) = \tilde{\psi}_{-}\hat{\lambda}_{+}^{(2)} - \tilde{\psi}_{+}\hat{\lambda}_{-}^{(2)}, \tag{54}$$

where for $\hat{\lambda}_{\pm}^{(2)}$ we can obtain

$$\begin{aligned}\hat{\lambda}_{\pm}^{(2)} = \pm i\frac{k_x q_y}{D^{(1)2}}\tilde{\psi}_{\pm}\overline{A}_0\Omega\Bigg\{ & D^{(2)}\frac{k_\perp^2}{\omega + k_x c_B}\left(\frac{\overline{\psi}_0}{\overline{A}_0}k_z B_{0z} - \frac{k_z^2 \mathrm{v}_A^2}{\omega + k_x c_B}\right) \\ & + \left(1 - \frac{k_z B_{0z}}{\omega + k_x c_B}\frac{\overline{\psi}_0}{\overline{A}_0}\right)\left[-4k_x\beta k_y q_y\Omega + q_y^2\frac{k_x\beta}{k_\perp^2}(\omega k_\perp^2 + k_x\beta - 4k_y^2\omega) + \Omega^2 k_\perp^4\right]\Bigg\}.\end{aligned} \tag{55}$$

Consequently, we can transform Eq. (54) to

$$r_{\parallel}(\mathbf{k}) = i\frac{k_x q_y \Omega}{D^{(1)2}} I_{\mathbf{k}}(f_{\parallel}^{\psi}\overline{\psi}_0 + f_{\parallel}^{A}\overline{A}_0), \tag{56}$$

where

$$\begin{aligned} f_{\parallel}^{\psi} = & \frac{k_z B_{0z}}{\omega + k_x c_B}\Bigg\{-k_x\beta q_y^2\Bigg(2\omega + k_x c_B + \frac{k_x\beta}{k_\perp^2} \\ & - 4\frac{k_y^2}{k_\perp^2}\omega\Bigg) + 2k_y q_y\Omega[2k_x\beta + k_\perp^2\omega + k_\perp^2(\omega + k_x c_B)]\Bigg\}, \end{aligned} \tag{57}$$

$$\begin{aligned} f_{\parallel}^{A} = & \frac{1}{\omega + k_x c_B}\Bigg\{\Omega^2 k_\perp^4\left(k_x c_B - \frac{k_x\beta}{k_\perp^2}\right) \\ & + q_y\Omega k_y\left[-4k_x\beta(\omega + k_x c_B) - 2k_\perp^2 k_z^2 \mathrm{v}_A^2 - 2\omega k_\perp^2\left(\omega + \frac{k_x\beta}{k_\perp^2}\right)\right] \\ & + q_y^2\frac{k_x\beta}{k_\perp^2}(\omega + k_x c_B)\left[\omega k_\perp^2 + k_x\beta - 4k_y^2\omega + k_\perp^2\left(\omega + \frac{k_x\beta}{k_\perp^2}\right)\right]\Bigg\}. \end{aligned} \tag{58}$$

In Eq. (56) we introduced the intensity of pumping waves

$$I_{\mathbf{k}} = 2\tilde{\psi}_{+}\tilde{\psi}_{-}. \tag{59}$$

Analogously we can transform Eq. (41). To this end, we represent the solution (45) as the expansion

$$\hat{\psi}_{\pm} = \hat{\psi}_{\pm}^{(0)} + \hat{\psi}_{\pm}^{(1)}, \tag{60}$$

where

$$\hat{\psi}_{\pm}^{(0)} = \pm\frac{ik_x q_y k_\perp^2}{D^{(1)}}\tilde{\psi}_{\pm}\left\{-\overline{\psi}_0\left[(\omega + k_x c_B) + \frac{k_z^2 \mathrm{v}_A^2}{\omega + k_x c_B}\right] + 2\overline{A}_0\frac{k_z B_{0z}}{\rho\mu_0}\right\}, \tag{61}$$

$$\begin{aligned}\hat{\psi}_{\pm}^{(1)} = & \frac{ik_x q_y}{D^{(1)}}\tilde{\psi}_{\pm}\Bigg\{\overline{\psi}_0\left[-k_\perp^2\Omega - 2q_y k_y\frac{k_z^2 \mathrm{v}_A^2}{\omega + k_x c_B} + \frac{D^{(2)}}{D^{(1)}}k_\perp^2\left(\omega + k_x c_B + \frac{k_z^2 \mathrm{v}_A^2}{\omega + k_x c_B}\right)\right] \\ & + \overline{A}_0\frac{k_z B_{0z}}{\rho\mu_0}\left(\frac{k_\perp^2\Omega}{\omega + k_x c_B} + 2q_y k_y - 2k_\perp^2\frac{D^{(2)}}{D^{(1)}}\right)\Bigg\}.\end{aligned} \tag{62}$$

Similarly for Eq. (46) we have the expansion

$$\hat{A}_{\pm} = \hat{A}_{\pm}^{(0)} + \hat{A}_{\pm}^{(1)}, \tag{63}$$

where

$$\hat{A}_{\pm}^{(0)} = \pm i \frac{k_x q_y}{D^{(1)}} \tilde{\psi}_{\pm} \left[-\overline{\psi}_0 k_z B_{0z} \left(\frac{\omega k_\perp^2 + k_x \beta}{\omega + k_x c_B} + k_\perp^2 \right) + \overline{A}_0 \left(\omega k_\perp^2 + k_x \beta + \frac{k_\perp^2 k_z^2 \mathrm{v}_A^2}{\omega + k_x c_B} \right) \right], \tag{64}$$

$$\hat{A}_{\pm}^{(1)} = i \frac{k_x q_y}{D^{(1)}} \tilde{\psi}_{\pm} \left\{ \overline{\psi}_0 k_z B_{0z} \left[-\frac{\Omega k_\perp^2 + 2 q_y k_y \omega}{\omega + k_x c_B} + \frac{D^{(2)}}{D^{(1)}} \left(\frac{\omega k_\perp^2 + k_x \beta}{\omega + k_x c_B} + k_\perp^2 \right) \right] + \overline{A}_0 \left[\Omega k_\perp^2 + 2 q_y k_y \omega - \frac{D^{(2)}}{D^{(1)}} \left(\omega k_\perp^2 + k_x \beta + \frac{k_\perp^2 k_z^2 \mathrm{v}_A^2}{\omega + k_x c_B} \right) \right] \right\}. \tag{65}$$

Accordingly, for Eq. (41) we get

$$r_\perp(\mathbf{k}) = \frac{i k_x q_y}{D^{(1)^2}} I_{\mathbf{k}} \left(f_\perp^{\psi} \overline{\psi}_0 + f_\perp^{A} \overline{A}_0 \right), \tag{66}$$

where

$$f_\perp^{\psi} = \frac{8 k_y^3 k_z^2 \mathrm{v}_A^2 q_y^2 k_x c_B}{\omega + k_x c_B} \left(-\omega + \frac{k_z^2 \mathrm{v}_A^2}{\omega + k_x c_B} \right) + q_y \Omega \left[8 k_y^2 \omega k_\perp^2 \frac{k_z^2 \mathrm{v}_A^2}{\omega + k_x c_B} + 4 k_y^2 k_\perp^2 (\omega + k_x c_B)^2 - k_\perp^4 (\omega + k_x c_B)^2 - k_\perp^4 k_z^2 \mathrm{v}_A^2 - 12 k_y^2 (\omega k_\perp^2 + k_x \beta) \frac{k_z^2 \mathrm{v}_A^2}{\omega + k_x c_B} + k_z^2 \mathrm{v}_A^2 \frac{(\omega k_\perp^2 + k_x \beta)^2}{(\omega + k_x c_B)^2} + k_\perp^2 k_z^2 \mathrm{v}_A^2 \frac{\omega k_\perp^2 + k_x \beta}{\omega + k_x c_B} \right], \tag{67}$$

$$f_\perp^{A} = \frac{k_z B_{0z}}{\rho \mu_0} \left\{ 8 k_y^3 q_y^2 \left[\omega k_x c_B - k_z^2 \mathrm{v}_A^2 + \frac{\omega k_z^2 \mathrm{v}_A^2}{\omega + k_x c_B} \right] + q_y \Omega \left[4 k_y^2 \omega k_\perp^2 \frac{k_z^2 \mathrm{v}_A^2}{(\omega + k_x c_B)^2} - 2 k_\perp^2 k_z^2 \mathrm{v}_A^2 \frac{\omega k_\perp^2 + k_x \beta}{(\omega + k_x c_B)^2} + 2 k_\perp^4 (\omega + k_x c_B) - 4 k_y^2 k_\perp^2 (\omega + k_x c_B) + 4 k_y^2 k_\perp^2 \frac{k_z^2 \mathrm{v}_A^2}{\omega + k_x c_B} - 12 k_\perp^2 k_y^2 \omega + 8 k_y^2 (\omega k_\perp^2 + k_x \beta) \right] + 4 \Omega^2 k_\perp^2 k_y k_x \frac{\beta - k_\perp^2 c_B}{\omega + k_x c_B} \right\}. \tag{68}$$

Using Eqs. (39), (40), (56), and (66), we can reduce Eqs. (35) and (36) to the following form:

$$\begin{cases} \overline{\psi}_0 = I_\perp^{\psi} \overline{\psi}_0 + I_\perp^{A} \overline{A}_0, \\ \overline{A}_0 = I_\parallel^{\psi} \overline{\psi}_0 + I_\parallel^{A} \overline{A}_0, \end{cases} \tag{69}$$

where

$$I_{\perp}^{\psi}=\sum_{\mathbf{k}}\frac{k_x^2q_yI_{\mathbf{k}}}{\Omega D^{(1)2}}\Bigg\{8\frac{k_x^2k_y^3}{k_{\perp}^2}k_z^2\mathrm{v}_A^2q_y^2\frac{\beta c_B}{\omega+k_xc_B}$$

$$+q_y\Omega\Bigg[(\omega+k_xc_B)^2k_{\perp}^2(4k_y^2-k_{\perp}^2)+\left(1-12\frac{k_y^2}{k_{\perp}^2}\right)(\omega k_{\perp}^2+k_x\beta)^2 \tag{70}$$

$$-k_{\perp}^4k_z^2\mathrm{v}_A^2+8k_y^2\omega(\omega k_{\perp}^2+k_x\beta)+\frac{(\omega k_{\perp}^2+k_x\beta)^3}{k_{\perp}^2(\omega+k_xc_B)}\Bigg]\Bigg\},$$

$$I_{\perp}^{A}=\sum_{\mathbf{k}}\frac{k_x^2q_y}{\Omega D^{(1)2}}I_{\mathbf{k}}\frac{k_zB_{0z}}{\rho\mu_0}\Bigg\{-8k_y^3q_y^2\frac{k_x^2\beta c_B}{k_{\perp}^2}$$

$$+q_y\Omega\Bigg[4k_y^2\omega\frac{\omega k_{\perp}^2+k_x\beta}{\omega+k_xc_B}+2(\omega+k_xc_B)k_{\perp}^2(k_{\perp}^2-2k_y^2)+12k_y^2k_x\beta \tag{71}$$

$$-2\frac{(\omega k_{\perp}^2+k_x\beta)^2}{\omega+k_xc_B}\Bigg]+4\Omega^2k_{\perp}^2k_y\left(-k_{\perp}^2+\frac{\omega k_{\perp}^2+k_x\beta}{\omega+k_xc_B}\right)\Bigg\},$$

$$I_{\parallel}^{\psi}=-\sum_{\mathbf{k}}\frac{k_x^2q_y^2}{D^{(1)2}}I_{\mathbf{k}}\frac{k_zB_{0z}}{\omega+k_xc_B}\Bigg\{-k_x\beta q_y^2\left(2\omega+k_xc_B+\frac{k_x\beta}{k_{\perp}^2}-4\frac{k_y^2}{k_{\perp}^2}\omega\right) \tag{72}$$

$$+2k_yq_y\Omega\Big[2k_x\beta+k_{\perp}^2(2\omega+k_xc_B)\Big]\Bigg\},$$

$$I_{\parallel}^{A}=-\sum_{\mathbf{k}}\frac{k_x^2q_y^2}{D^{(1)2}}I_{\mathbf{k}}\frac{1}{\omega+k_xc_B}\Bigg\{\Omega^2k_{\perp}^4\Bigg[\omega+k_xc_B-\frac{1}{k_{\perp}^2}(\omega k_{\perp}^2+k_x\beta)\Bigg]$$

$$-q_y\Omega k_y\Big[4k_x\beta(\omega+k_xc_B)+2k_{\perp}^2k_z^2\mathrm{v}_A^2+2\omega(\omega k_{\perp}^2+k_x\beta)\Big] \tag{73}$$

$$+2q_y^2\frac{k_x\beta}{k_{\perp}^2}(\omega+k_xc_B)(\omega k_{\perp}^2+k_x\beta-2k_y^2\omega)\Bigg\}.$$

In Eqs. (70) – (73)

$$D^{(1)}=(\Omega-q_yV_g)\Big[k_{\perp}^2(\omega+k_xc_B)+\omega k_{\perp}^2+k_x\beta\Big], \tag{74}$$

where V_g is the zonal – flow group velocity given by

$$V_g=\frac{\partial\omega}{\partial k_y}=2\frac{k_x\beta k_y(\omega+k_xc_B)}{k_{\perp}^2(2\omega k_{\perp}^2+k_{\perp}^2k_xc_B+k_x\beta)}. \tag{75}$$

From the system of Eqs. (69), we get the following zonal – flow dispersion relation:

$$1-(I_{\perp}^{\psi}+I_{\parallel}^{A})+I_{\perp}^{\psi}I_{\parallel}^{A}-I_{\perp}^{A}I_{\parallel}^{\psi}=0. \tag{76}$$

Further we will show that in the most interesting case this biquadratic with respect to $\Omega-q_yV_g$ zonal flow dispersion relation can be reduced to a quadratic one.

Let us consider the monochromatic wave packet case of the primary modes, which means a single wave vector on the right – hand sides of Eqs. (70) – (73). Because the values $I_{\parallel}^{\psi}$ and $I_{\parallel}^{A}$ are of the order of $O(q_y^2)$,

while $I_{\perp}^{\psi}$ and $I_{\perp}^{A}$ are of $O(1)$, we conclude that the right – hand sides of these equations will match only if the value $\Omega - q_y V_g$ is also a small parameter. Therefore the zonal – flow dispersion relation (76) reduces to

$$1 = I_{\perp}^{\psi}, \tag{77}$$

or,

$$(\Omega - q_y V_g)^2 = -\Gamma^2, \tag{78}$$

where Γ^2 means the squared zonal – flow growth rate defined by

$$\begin{aligned}\Gamma^2 = &-\frac{k_x^2 q_y^2 I_{\mathbf{k}}}{(\omega + k_x c_B)\left[(2\omega + k_x c_B)k_{\perp}^2 + k_x\beta\right]}\left\{4k_x k_y^2 k_z^2 \mathrm{v}_A^2 \frac{c_B}{\omega + k_x c_B}\right. \\ &+ \frac{(\omega + k_x c_B)}{\left[(2\omega + k_x c_B)k_{\perp}^2 + k_x\beta\right]}\left[k_{\perp}^2(\omega + k_x c_B)^2(4k_y^2 - k_{\perp}^2) - 12\frac{k_y^2}{k_{\perp}^2}(\omega k_{\perp}^2 + k_x\beta)^2\right. \\ &\left.\left. - k_{\perp}^4 k_z^2 \mathrm{v}_A^2 + 8k_y^2\omega(\omega k_{\perp}^2 + k_x\beta) + (\omega k_{\perp}^2 + k_x\beta)^2 + \frac{(\omega k_{\perp}^2 + k_x\beta)^3}{k_{\perp}^2(\omega + k_x c_B)}\right]\right\}.\end{aligned} \tag{79}$$

5. Generation of zonal flow

The most suitable case to analyze the zonal flow growth rate is $k_y = 0$. Therefore for this case the zonal flow growth rate (79) takes the form

$$\begin{aligned}\Gamma^2 = &\frac{q_y^2 I_{\mathbf{k}} k_x}{\left[(2\omega + k_x c_B)k_x + \beta\right]^2} \\ &\times\left[(\omega + k_x c_B)^2 k_x^3 + k_x^3 k_z^2 \mathrm{v}_A^2 - (\omega k_x + \beta)^2 k_x - \frac{(\omega k_x + \beta)^3}{(\omega + k_x c_B)}\right].\end{aligned} \tag{80}$$

By using the solution (18), Eq. (80) becomes

$$\Gamma^2 = \frac{2q_y^2 I_{\mathbf{k}} k_x^2 (k_x^2 |c_B| + \beta)}{k_x^2 |c_B| + \beta \mp \sqrt{(k_x^2 |c_B| + \beta)^2 + 4k_x^4 c_B^2 \alpha}}, \tag{81}$$

Here, $\alpha = k_z^2 \mathrm{v}_A^2 / k_x^2 c_B^2$, the upper (minus) sign before the radical belongs to Khantadze branch ω_1, and the lower one to Rossby branch ω_2.

It is seen from Eq. (81) that Khantadze waves give no contribution ($\Gamma^2 < 0$) to the generation of zonal flow, but the maximum growth rate is achieved by Rossby waves having the dispersion $\omega = -\beta / k_x$ at $\alpha = 0$. In this case

$$\Gamma^2 = q_y^2 k_x^2 I_{\mathbf{k}}. \tag{82}$$

This value coincides with the maximum value of growth rate achieved in the problem [54, 55].

If we introduce the dimensionless variables x and y used for Eq. (27), we rewrite Eq. (81) as follows

$$\gamma = \frac{\Gamma^2}{K} = \frac{2x^2(x^2 + 1)}{x^2 + 1 \mp \sqrt{(x^2 + 1)^2 + 4x^4 \alpha}}, \tag{83}$$

where the normalization constant $K = q_y^2 I_{\mathbf{k}} \beta / |c_B|$. In Fig. 2, the dependence of the function γ on wave number x for the different values of α is shown. *A* and *B* curves correspond to "–" and "+" signs before the radical in Eq. (83), respectively.

6. Magnetic field generation

From Eq. (69) it follows that

$$\frac{\overline{A}_0}{\overline{\psi}_0} = \frac{I_{\parallel}^{\psi}}{1 - I_{\parallel}^{A}}, \tag{84}$$

or taking into account that $I_{\parallel}^{A} \sim O(q_y^2)$, we get

$$\frac{\overline{A}_0}{\overline{\psi}_0} = I_{\parallel}^{\psi}. \tag{85}$$

Thus the value of the generated mean magnetic field is the order of q_y^2 in comparison with the mean zonal flow value. Using Eqs. (78) and (79) we get at $\Omega = q_y V_g$ (use also Eq. (75) for V_g):

$$\frac{\overline{A}_0}{\overline{\psi}_0} = q_y^2 k_x k_z B_{0z} \beta \frac{M}{N}, \tag{86}$$

where

$$M = 2\omega k_{\perp}^2 + k_{\perp}^2 k_x c_B + k_x \beta - 4k_y^2 \omega - 4k_y^2 (\omega + k_x c_B) - 4k_y^2 k_x \beta \frac{\omega + k_x c_B}{2\omega k_{\perp}^2 + k_{\perp}^2 k_x c_B + k_x \beta}, \tag{87}$$

$$\begin{aligned} N = {} & 4k_x k_y^2 k_z^2 \mathrm{v}_A^2 k_{\perp}^2 c_B \frac{2\omega k_{\perp}^2 + k_{\perp}^2 k_x c_B + k_x \beta}{\omega + k_x c_B} + k_{\perp}^6 (\omega + k_x c_B)^3 \left(4\frac{k_y^2}{k_{\perp}^2} - 1 \right) \\ & - k_{\perp}^6 k_z^2 \mathrm{v}_A^2 (\omega + k_x c_B) + 8k_y^2 \omega k_{\perp}^4 k_z^2 \mathrm{v}_A^2 - 12k_y^2 k_{\perp}^2 k_z^2 \mathrm{v}_A^2 (\omega k_{\perp}^2 + k_x \beta) \\ & + k_{\perp}^4 k_z^2 \mathrm{v}_A^2 (\omega k_{\perp}^2 + k_x \beta) + (\omega k_{\perp}^2 + k_x \beta)^3. \end{aligned} \tag{88}$$

Thus, when $k_x k_z B_{0z} \beta \neq 0$ mean magnetic field is also generated along with the mean zonal flow generation.

As in the case of Eq. (80) we consider $k_y = 0$, then from Eq. (86) we get

$$\frac{\overline{A}_0}{\overline{\psi}_0} = q_y^2 \frac{k_z}{k_x} B_{0z} \beta \frac{P}{Q}, \tag{89}$$

where

$$\begin{aligned} P &= 2\omega k_x + k_x^2 c_B + \beta, \\ Q &= -k_x^3 (\omega + k_x c_B)^3 - k_x^3 k_z^2 \mathrm{v}_A^2 (\omega + k_x c_B) + k_x^2 k_z^2 \mathrm{v}_A^2 (\omega k_x + \beta) + (\omega k_x + \beta)^3 \\ &= -(k_x^2 c_B - \beta)\left[(2\omega + k_x c_B) k_x + \beta \right]^2. \end{aligned} \tag{90}$$

Then

$$\frac{\overline{A}_0}{\overline{\psi}_0} = q_y^2 \frac{k_z}{k_x} \frac{B_{0z} \beta}{(\beta - k_x^2 c_B)[(2\omega + k_x c_B) k_x + \beta]}. \tag{91}$$

Substituting the solution (18), we get

$$\frac{\overline{A}_0}{\overline{\psi}_0} = \pm q_y^2 \frac{B_{0z} \beta |c_B|}{\mathrm{v}_A} \frac{\sqrt{\alpha}}{(\beta + k_x^2 |c_B|)[(|c_B| k_x^2 + \beta)^2 + 4k_x^4 \alpha c_B^2]^{1/2}}. \tag{92}$$

For the evaluation order we get

$$\frac{\overline{A}_0}{\overline{\psi}_0} \approx \pm \frac{q_y^2 B_{0z} |c_B|}{\mathrm{v}_A \beta} \sqrt{\alpha}. \tag{93}$$

In the dimensionless variables x and y used for Eq. (27), we get from Eq. (92)

$$\frac{\overline{A}_0}{\overline{\psi}_0} = \pm \frac{q_y^2 B_{0z} |c_B|}{\mathrm{v}_A \beta} \frac{\sqrt{\alpha}}{(1 + x^2)[(1 + x^2)^2 + 4x^4 \alpha]^{1/2}}. \tag{94}$$

In Fig. 3 the dependence of the function $\lambda = \frac{\bar{A}_0}{\bar{\psi}_0} \frac{\mathrm{v}_A \beta}{q_y^2 B_{0z} |c_B|}$ on wave number x for the values α = 1; 5 is shown. *A* and *B* curves correspond to "+" and "–" signs in Eq. (94).

7. Discussions and conclusions

In this paper, the nonlinear generation of large – scale, and low – frequency zonal flows and magnetic fields by relatively small – scale ULF EM coupled Rossby – Alfvén – Khantadze (CRAK) planetary waves is investigated in the Earth's ionospheric E – layer. The importance of latitudinal non-homogeneity of both Coriolis parameter and the geomagnetic field along with the prevalent effect of Hall conductivity for CRAK is shown. In addition, accounting of the vertically directed propagation of the perturbations under the consideration leads to the *z*-dependence and the problem becomes essentially three-dimensional. As a result, owing to the existence of magnetic field perturbations, Alfvén waves also became incorporated in the dynamics of problem. Action of these effects leads to the coupled propagation of EM Rossby – Alfvén – Khantadze modes, which are described by the system of nonlinear Eqs. (6) and (15). Due to such coupling dispersion of both Alfvén and Khantadze waves appeared. Note that the long-lived (compared to linear wave packets) nonlinear structures can be formed under the condition when the waves dispersion is compensated by their nonlinearity.

The dispersion relation for the linear EM CRAK is obtained [see Eq. (17)] and analyzed in detail in Sec. 3. The mode is composed by two branches ω_1 and ω_2. For small values of perpendicular wave number $k_\perp$ the frequencies ω_1 and ω_2 can be described analytically by Eqs. (19) and (20) while for large values of $k_\perp$ by Eq. (21). Analytical expression for the corresponding new type of Alfvén waves is given by Eq. (22). All branches of oscillations are mutually influenced. Depending on the perpendicular wave number the appropriate behavior of phase velocities $\omega_{1,2}/k_x$ for the different values of parameter $\alpha = k_z^2 \mathrm{v}_A^2 / k_x^2 c_B^2$ is given in Fig. 1 (Curves *A* belong to ω_1 and *B* ones to ω_2). It is clarified that in case of small $k_\perp$ the phase velocity of the branch ω_1 tends to the finite value $\omega_1 / k_x = |c_B|$ and corresponds to Khantadze waves, while for the branch ω_2 it tends to the $-\infty$, which corresponds to Rossby waves. For the large values of $k_\perp$ the phase velocity of the branch ω_1 tends to the finite value $\omega_1 / k_x = \frac{1}{2}|c_B|(1+\sqrt{1+4\alpha})$ which is more then $|c_B|$. Thus the existence of Alfvén waves causes the increase of the phase velocity of Khantadze waves as compared with the case $\alpha = 0$. As to the case of Rossby waves for the large values of the perpendicular wave number $k_\perp$ the phase velocity of the branch ω_2 tends to the finite value $\omega_2 / k_x = \frac{1}{2}|c_B|(1-\sqrt{1+4\alpha}) < 0$. Thus in this case Alfvén waves cause the increase of the phase velocity of Rossby waves as compared with the case $\alpha = 0$. Note that in case of $k_x > 0$ the branch of Khantadze waves (ω_1) propagates along the latitude circles eastward, while the branch of Rossby waves (ω_2) along the latitude circles westward against a background of mean zonal wind.

$\alpha = 1 \quad \alpha = 5 \quad \alpha = 0$

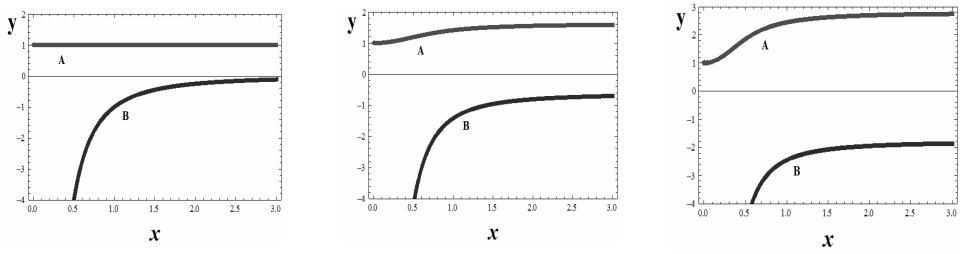

Fig. 1. Dependence of phase velocity of coupled Rossby – Alfvén – Khantadze modes on wave number x at different values of α .

Dealing with zonal flows and magnetic fields generation problem by EM CRAK modes in the weakly ionized ionospheric E-layer gas we have used the modified parametric approach [58] and the spectrum of primary modes is assumed to be arbitrary [see Eq. (31)]. Then, instead of the side-band amplitude for a single wave vector $\boldsymbol{k}$, we have dealt with a spectrum of such amplitudes [see Eq. (32)] and as a consequence the appropriate driving forces are presented as summation (or integration) over the spectrum of the primary modes [see Eq. (39) and (40)]. The developed method can be effectively used for different types of primary modes having arbitrary spectrum broadening. To describe the nonlinear dynamics of the zonal flows and magnetic fields generation by EM CRAK waves the appropriate system of coupled equations is obtained [see Eqs. (35) and (36)]. We have shown that these equations are unstable to four wave parametric instability and the coherent, monochromatic CRAK waves can drive a band of modes and corresponding zonal flow and magnetic field unstable. Thus, we have investigated the interaction of a pump CRAK modes, two their satellites (side-band waves) and a sheared zonal flow. For the monochromatic wave packet the instability [see Eq. (78)] is of the hydrodynamic type. The nonlinear instability mechanism is driven by the vorticity advection leading to the inverse energy cascade toward the longer wavelength. Consequently, short wavelength turbulence of CRAK waves is unstable causing the excitation of low-frequency and large-scale perturbations of the zonal flow and magnetic field. It is shown that in the system of Eqs. (35) and (36) controlling the evolution of zonal flow and magnetic field the driving mechanism of the instability is associated with the mixture of mean Reynolds and Maxwell stresses $R_{\perp}$ [see Eq. (37)] and mean electromotive force $R_{\parallel}$ [see Eq. (38)], respectively.

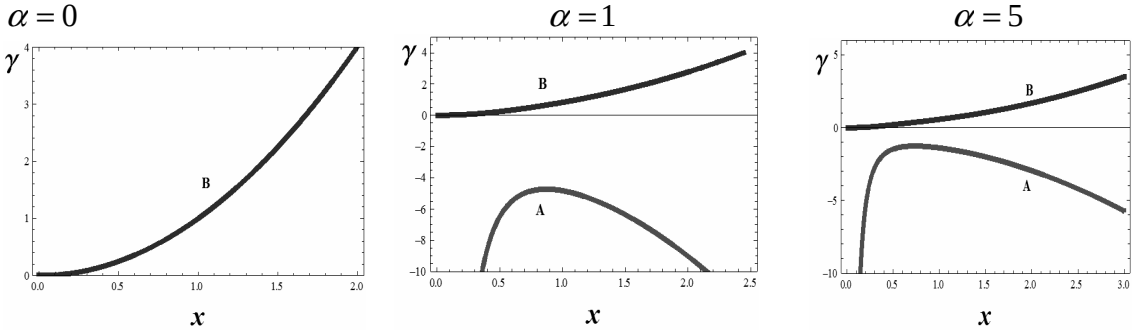

Fig. 2. Dependence of the function γ on wave number x at different values of α .

We studied the propagation of zonal flow along the geographical parallels when the corresponding mean flow velocity depends only on the meridional *y*-coordinates. From our investigations it is seen that the maximum growth rate of the zonal flow generation is achieved at $k_y = 0$, when the group velocity $V_g = 0$ [see Eq. (75)] and therefore the real part of oscillations for zonal flow becomes zero. In this case the excitation of zonal flow is stipulated only by Rossby waves and the corresponding growth rate is (see Eq. (82))

$$\Gamma \approx \left| q_y k_x r_R^3 \beta \tilde{\psi}_+ \right|, \tag{95}$$

which is equal to the maximum growth rate achieved in the problems [Kaladze et al. 2009, 2012]. In Eq. (95) the stream function $\tilde{\psi}_+$ of pump modes is normalized by $\mathrm{v}_R r_R$, where $\mathrm{v}_R = \beta r_R^2$ is the Rossby velocity and $r_R = c_s / f$ (c_s is the equivalent sound speed in the ionospheric *E*-layer) is the Rossby radius, respectively. Here for this regime, we have $q_y r_R \sim 0.1$, $k_x r_R \sim 10$, $r_R \approx 10^6 m$, $\beta \approx 10^{-11} m^{-1} s^{-1}$, and $\tilde{\psi}_+ \sim 10^{-2}$. Then, the numerical value for the zonal flow growth rate becomes $\Gamma \approx 10^{-7} s^{-1}$. This estimation is consistent with existing observations, and conducted investigations provide the essential nonlinear mechanism for the driving spectral energy from short-scale CRAK waves to large-scale reinforced zonal flows in the Earth's ionosphere.

In Fig.2 the dependence of the squared dimensionless growth rate γ on the wave number *x* (see Eq. (83)) for the different values of α is shown (curves A belong to the branch ω_1 and *B* ones to ω_2). It is seen that Khantadze waves (ω_1) don't contribute in the generation of zonal flow, for them $\gamma \le 0$. The maximum growth rate is achieved for the Rossby waves branch ω_2 at $\alpha = 0$. This is the case when Alfvén waves also don't contribute in the growth rate. Thus the generation of zonal flow is mainly stipulated by Rossby waves. With increase of α the growth rate is decreasing in accordance with Eq. (83).

Here, the mean magnetic field excitation has the special attention and its dynamics is described with detail in Sec. 6. Generated magnetic field is of the order q_y^2 with respect to the excited mean zonal flow and is caused only by the existence of Alfvén waves. Excited mean magnetic field has the prevalent component b_y (as in the calculations we gave the priority to $k_y = 0$ consideration) and as the zonal flow is sheared in the meridional *y*-direction. It is found that the ratio of the mean magnetic function $\overline{A}_0$ to mean zonal flow $\overline{\psi}_0$ strongly depends on the pumping wave branches of ω (see Eq. (91)). After the substitution of ω from Eq. (18), we get Eq. (92), which shows that both Rossby (ω_2) and Khantadze (ω_1) branches give symmetric by sign contributions in the generation of the magnetic field component b_y. The following estimation for the generated magnetic field (see Eq. (93)) is valid

$$\left|\overline{b}_y\right| \approx \frac{q_y^2 B_0 \left|c_B\right|}{\mathrm{v}_A \beta r_R} \sqrt{\alpha}\overline{\psi}_0, \tag{96}$$

where the Rossby radius r_R is chosen as the characteristic scale-length. Numerically, to approximate this value, we consider $\left|c_B\right| \sim (1-10)\,km/s$, $\mathrm{v}_A \sim (0.1-1)\,km/s$, $B_0 \sim 0.5\times 10^{-4} T$, $\beta \approx 10^{-11} m^{-1} s^{-1}$, and consider $\overline{\psi}_0 \approx \overline{\mathrm{v}}\mathrm{r}_R$ (where $\overline{\mathrm{v}} = (1\text{-}100)\mathrm{m/s}$) is the local ionospheric mean wind's velocity). Then, the values for the excited mean magnetic field becomes $\left|\overline{b}_y\right| = (10^2 - 10^3) nT$. Consequently, the intensification of the geomagnetic field perturbed pulses takes place.

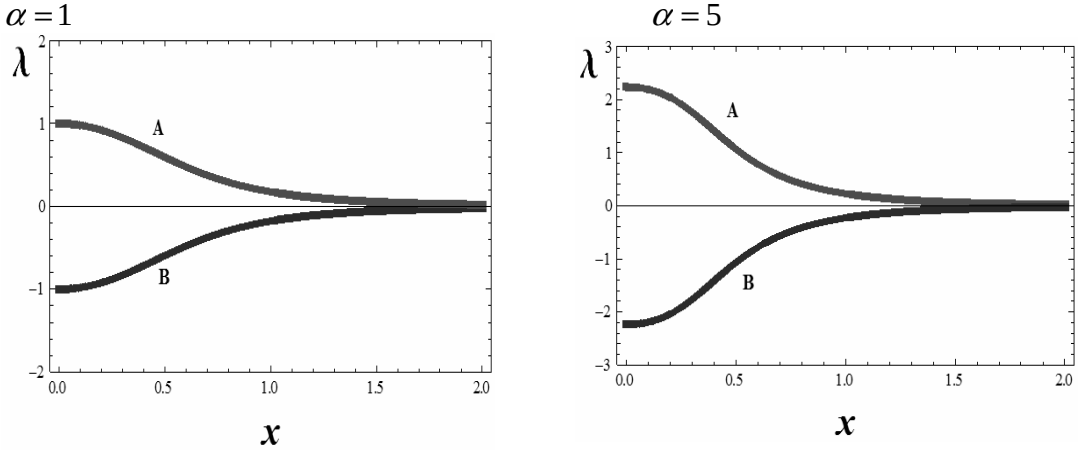

Fig. 3. Dependence of the function λ on wave number *x* at different values of α.

In Fig.3 the dependence of the dimensionless ratio (see Eq. (94)) on wave number *x* for the values $\alpha = 1;5$ is shown. The curve *A* belongs to Khantadze waves contribution, while the curve *B* to Rossby waves contribution.

Note that for the large latitude in the northern hemisphere our consideration has been limited to the nearly constant dipole geomagnetic field.

Placed on the solid ground magnetometer chains register large-scale variations of exposed origin in δB. However, the incoming values are much lower than those in the *E*-layer since δB falls off exponentially below the conductive slab (e.g., [59]), i.e. $\delta B \propto \exp(-2\pi d/\lambda)$, where $d \approx 150km$ is the characteristic scale at the *E*-layer heights. For the discussing planetary wavelengths $\lambda \approx 10^3 km$ and the estimated damping rate is of order unity. We would like to note that studied in the given paper theoretically ULF electromagnetic modes in the *E*-layer are not adequately studied experimentally and further experimental studies are required.

Thus, in this paper the conducted investigation shows that parametric instability becomes a sufficient nonlinear mechanism to drive large-scale zonal flows and intense mean magnetic field in the weakly ionized ionosphere *E*-layer.

Acknowledgments. The authors are grateful for the partial financial support from the International Space Science Institute (Bern, Switzerland) through the grant Large – scale vortices and zonal winds in planetary atmospheres/ionospheres: Theory vs. observations.

It would be worth to mention the JGGS vice-ed.'s attention to the work.

References

[1] Pedlosky J. 1987 Geophysical Fluid Dynamics *Springer*

[2] Satoh M. 2004 Atmospheric Circulation Dynamics and General Circulation Models *Springer*

[3] Cavalieri D.J., Deland R.J., Poterna J.A. and Gavin R.F. 1974 The correlation of VLF propagation variations with atmospheric planetary-scale waves *J. Atmos. Terr. Phys.* **36** 561- 574

[4] Cavalieri D.J. 1976 Traveling planetary-scale waves in the E-region *J. Atmos. Terr. Phys.* **38** 965-974

[5] Manson A.H., Heek C.E. and Gregory J.B. 1981 Winds and waves (10 min-30 day) in the mesosphere and lower thermosphere at Saskatoon (52 °N, 107 °W, L = 4.3) during the year, October 1979 to July 1980 *J. Geophys. Res.* **86** 9615-9625

[6] Hirooka, T. and Hirota I. 1985 Normal Mode Rossby Waves Observed in the Upper Stratosphere. Part II: Second Antisymmetric and Symmetric Modes of Zonal Wavenumbers 1 and 2 *J. Atmos. Sc.* **42** 536-548

[7] Randel W. J. 1987 A study of planetary waves in the southern winter troposphere and stratosphere. Part I: Wave structure and vertical propagation *J. Atmos. Sc.* **44** 917-935

[8] Sorokin V.M. 1988 Wavy processes in the ionosphere related to the geomagnetic field *Izv. Vuz. Radiofis.* **31** 1167-1179

[9] Sharadze Z.S., Japaridze G.A., Kikvilashvili G.B. et al. 1988 Wavy disturbances of non- acoustical nature in the middle-latitude ionosphere *Geomag. Aeron.* **28** 446-451

[10] Sharadze Z.S., Mosiashvili N.V., Pushkova G.N. and Yudovich L.A. 1989 Long-period- wave disturbances in E-region of the ionosphere *Geomag. Aeron.* **29** 1032-1035

[11] Williams C.R. and Avery S.K. 1992 Analysis of long-period waves using the mesosphere-stratosphere-troposphere radar at Poker Flat Alaska *J. Geophys. Res.* **97** 20855-20861

[12] Forbes J.M. and Leveroni S. 1992 Quasi 16-day oscillation in the ionosphere *Geophys. Res. Lett.* **19** 981-984

[13] Bauer T.M., Baumjohann W., Treumann R.A. et al. 1995 Low-frequency waves in the near-earth plasma sheet *J. Geophys. Res.* **100A** 9605-9617

[14] Zhou Q.H., Sulzer M.P. and Tepley C.A. 1997 An analysis of tidal and planetary waves in the neutral winds and temperature observed at low-latitude E-region heights *J. Geophys. Res.* **102** 11491-11505

[15] Lastovicka, J. 1997 Observations of tides and planetary waves in the atmosphere-ionosphere system *Adv. Space Res.* **20** 1209-1222

[16] Smith A.K. 1997 Stationary Planetary Waves in Upper Mesospheric Winds *J. Atmos. Sci.*, **54** 2129-2145

[17] Lawrence A.R. and Jarvis M.J. 2003 Simultaneous observations of planetary waves from 30 to 220 km *J. Atmos. Solar – Terr. Phys.* **65** 765-777

[18] Burmaka V P., Lysenko V.N., Chernogor L.F. and Chernyak Yu.V. 2006 Wave-like processes in the ionospheric F region that accompanied rocket launches from the Baikonur Site *Geomagn. Aeron.* **46** 742-759
[19] Alperovich L.S. and Fedorov E.N. 2007 Hydromagnetic Waves in the Magnetosphere and the Ionosphere *Springer*
[20] Fagundes P.R., Pillat V.G., Bolzan M.J. et al. 2005 Observations of F layer electron density profiles modulated by planetary wave type oscillations in the equatorial ionospheric anomaly region *J. Geophys. Res.* **110** A12302
[21] Haykowicz L. A. 1991 Global onset and propagation of large-scale traveling ionospheric disturbances as a result of the great storm of 13 March 1989 *Planet. Space Sci.* **39** 583-593
[22] Liperovsky V.A., Pokhotelov O.A. and Shalimov S.L. 1992 Ionospheric Earthquake Precursos *Nauka Moscow*
[23] Cheng K.Y. and Huang N. 1992 Ionospheric disturbances observed during the period of Mount Pinatubo eruptions in June 1991 *J. Geophys. Res.* **97** 16995-17004
[24] Pokhotelov O.A., Parrot M., Fedorov E.N., Pilipenko V.A., Surkov V.V. and Gladychev V.A. 1995 Response of the ionosphere to natural and man-made acoustic sources, *Ann. Geophys.* **13** 1197-1210
[25] Shaefer L.D., Rock D.R., Lewis J.P. et al. 1999 Lawrence Livermore Laboratory *Livermore* CA 94550
[26] Burmaka V.P., Chernogor L.F. 2004 Clustered-instrument studies of ionospheric wave disturbances accompanying rocket launches against the background of nonstationary natural processes *Geomagn. Aeron.* **44**(3) 518-534
[27] Burmaka V.P., Taran L.F., Chernogor L.F. 2005 Results of investigations of the wave disturbances in the ionosphere by noncoherent scattering *Adv. Mod. Radiophys.* **3** 4-35
[28] Dokuchaev V.P. 1959 Influence of the earth's magnetic field on the ionospheric winds, Izvestia AN SSSR *Seria Geophysica* **5** 783-787
[29] Tolstoy I. 1967 Hydromagnetic gradient waves in the ionosphere *J. Geophys. Res.* **72** 1435-1442
[30] Kaladze T.D. and Tsamalashvili L.V. 1997 Solitary dipole vortices in the Earth's Ionosphere, *Phys. Lett. A* **232** 269-274
[31] Kaladze T.D. 1998 Nonlinear vortical structures in the Earth's ionosphere *Phys. Scripta* **T75** 153-155.
[32] Kaladze T.D. 1999 Magnetized Rossby waves in the Earth's ionosphere, *Plasma Phys. Reports* **25** 284-287
[33] Kaladze T.D., Aburjania G.D., Kharshiladze O.A., Horton W., and Kim Y. – H. 2004. Theory of magnetized Rossby waves in the ionospheric E layer *J. Geophys. Res.* **109** A05302 doi: 10.1029/2003JA010049
[34] Kaladze T.D. and Horton W. 2006 Synoptic-scale nonlinear stationary magnetized Rossby waves in the ionospheric E-layer *Plasma Phys. Reports* **32** 996-1006
[35] Khantadze A.G. 1986 Hydromagnetic gradient waves in dynamo region of the ionosphere *Bull. Acad. Sci. Georgian SSR* **123** 69-71

[36] Khantadze A.G. 1999 On the electromagnetic planetary waves in the Earth's ionosphere *J. Georgian Geophys. Soc.* **4B** 125-127
[37] Khantadze A.G. 2001. A new type of natural oscillations in conducting atmosphere *Dokl. Akad. Nauk*, **376** 250-252
[38] Sharadze Z.S. 1991 Phenomena in the Middle – Latitude Ionosphere *PhD Thesis Moscow*.
[39] Kaladze T.D., Pokhotelov O.A., Sagdeev R Z., Stenflo L., and Shukla, P.K. 2003 Planetary electromagnetic waves in the ionospheric E-layer *J. Atmos. Solar – Terr. Phys.* **65** 757-764
[40] Kaladze T.D. 2004 Planetary electromagnetic waves in the ionospheric E-layer, *Proceedings of the First Cairo Conference on Plasma Physics & Applications: CCPPA 2003* (Cairo, Egypt, October 11 – 15, 2003). *Shriften des Forschungszentrums Jülich, Bilateral seminars of the International Bureau* **34** 68-74 (Eds. H. - J. Kunze, T. El – Khalafawy, H. Hegazy, German – Egyptian Cooperation)

[41] Khantadze A.G., Jandieri G.V., Ishimaru A., Kaladze T.D. and Diasamidze Zh.M. 2010 Electromagnetic oscillations of the Earth's upper atmosphere (review) *Ann. Geophys.* **28** 1387- 1399
[42] Kaladze T.D. and Tsamalashvili L.V. 2001 Nonlinear Alfven-Rossby vortical structures in the Earth's ionosphere *Phys. Lett. A* **287**, 137-142
[43] Petviashvili V.I. and Pokhotelov O.A. 1992 Solitary Waves in Plasmas and in the Atmosphere *Reading, PA: Gordon and Breach Science Publishers*
[44] Pokhotelov O.A., Stenflo L. and Shukla P.K. 1996 Nonlinear structures in the Earth's magnetosphere and atmosphere *Plasma Phys. Reports* **22** 852-863
[45] Smolyakov A.I., Diamond P.H. and Shevchenko V.I. 2000 Zonal flow generation by parametric instability in magnetized plasmas and geostrophic fluids *Phys. Plasmas* **7** 1349-1351
[46] Shukla P.K. and Stenflo L. 2003 Generation of zonal flows by Rossby waves *Phys. Lett. A* **307** 154-157
[47] Onishchenko O.G., Pokhotelov O.A., Sagdeev R.Z., Shukla P.K. and Stenflo L. 2004 Generation of zonal flows by Rossby waves in the atmosphere *Nonlin. Proc. Geophys.* **11** 241- 244
[48] Lighthill M. J. 1965 Group velocity *J. Inst. Math. Appl.* **1** 1-28
[49] Kaladze T.D., Pokhotelov O.A., Stenflo L., Rogava J., Tsamalashvili L.V. and Tsiklauri M. 2008 Zonal flow interaction with Rossby waves in the Earth's atmosphere: A numerical simulation, Phys. Lett. A, **372**, 5177-5180
[50] Kaladze T.D., Wu D.J., Pokhotelov O.A., Sagdeev R.Z., Stenflo L., and Shukla P. K. 2005 Drift wave driven zonal flows in plasma *Phys. Plasmas* **12** 122311(1-6)
[51] Kaladze T.D., Wu D.J., Pokhotelov O.A., Sagdeev R. Z., Stenflo L. and Shukla P. K. 2007 Zonal flow generation by magnetized Rossby waves in the ionospheric E-layer, // Mathematical Physics, Proceedings of the 12th Regional Conference, slamabad Pakistan 27 March-1 April 2006 p. 237-251 Eds. M. Jamil Aslam, Faheem Hussain, Asghar Qadir, Riazuddin, Hamid Saleem, *World Scientific Publishing*
[52] Kaladze T.D., Wu D.J., Pokhotelov O.A., Sagdeev R.Z., Stenflo L., and Shukla P. K. 2007 Rossby-wave driven zonal flows in the ionospheric E-layer *J. Plasma Phys.* **73** 131-140
[53] Kaladze T.D., Wu D.J., Tsamalashvili L.V. and Jandieri G.V. 2007 Localized magnetized Rossby structures under zonal shear flow in the ionospheric E-layer *Phys. Lett. A* **365** 140-143
[54] Kaladze T.D., Shah H.A., Murtaza G., Tsamalashvili L.V., Shad M., and Jandieri G. V. 2009 Influence of non-monochromaticity on zonal-flow generation by magnetized Rossby waves in the ionospheric E-layer *J. Plasma Phys.* **75** 345-357
[55] Kaladze T.D., Kahlon L.Z. and Tsamalashvili L.V. 2012 Excitation of zonal flow and magnetic field by Rossby–Khantadze electromagnetic planetary waves in the ionospheric E-layer *Phys. Plasmas* **19** 022902 (1-12)

[56] Kaladze, T.D., Kahlon L.Z., Tsamalashvili L.V. and Kaladze D.T. 2012 Generation of zonal flow and magnetic field by coupled internal-gravity and alfvén waves in the ionospheric E-layer *J. Atmos. Solar – Terr. Phys.* **89** 110-119
[57] Mikhailovskii A.B., Smolyakov A.I., Kovalishen E.A., Shirokov M.S., Tsypin V. S., Botov P.V. and Galvão R.M.O. 2006 Zonal flows generated by small-scale drift-Alfven modes *Phys. Plasmas* **13** 042507
[58] Kaladze T.D., Wu D.J. and Yang L. 2007 Small-scale drift-Alfven wave driven zonal flows in plasmas *Phys. Plasmas* **14** 032305
[59] Pokhotelov O.A., Khruschev V., Parrot M., Senchenkov S. and Pavlenko V.P. 2001 Ionospheric Alfven resonator revisited: feedback instability *J. Geophys. Res.* **106**, 25813-25824, doi: 10.1029/2000JA000450

(Received in final form 20 December 2013)

Генерирование зонального течения и магнитного поля сцеплёнными волнами Россби-Альфвена-Хантадзе в Е-слое ионосферы Земли

Т. Д. Каладзе, В. Хортон, Л. З. Кахлон, О. Похотелов, О. Онищенко

Резюме

Показано, что в слабоионизированном Е-слое ионосферы Земли, где преобладает холловская проводимость плазмы, может существовать новый тип сцеплённых электромагнитных (ЭМ) планетарных волн Россби-Альфвена-Хантадзе (СРАХ), обусловленных широтной неоднородностью кориолисова параметра Земли и геомагнитного поля. Под воздействием такого сцепления возбуждается новый тип диспергирующих волн Альфвена. Исследуется генерирование сдвигового зонального течения и магнитного поля под действием СРАХ ЭМ планетарных волн. Нелинейный механизм неустойчивости основывается на параметрическом возбуждении зонального течения посредством взаимодействия четырёх волн, ведущих к инверсионному каскаду энергии в сторону более длинных волн. Выведена система 3D сцеплённых уравнений, описывающих нелинейное взаимодействие накачивающих СРАХ волн и зонального течения. Определены скорость роста соответствующей неустойчивости и условиядля их управления. Обнаружено, что рост скорости главным образом обусловлен волнами Россби, а генерация магнитного поля средней интенсивности вызывается волнами Альфвена.

დედამიწის E–ფენაში ზონალური დინების და მაგნიტური ველის გენერირება როსბი–ალფვენ–ხანთაძის გადაბმული ტალღების მეშვეობით

თ. კალაძე, ვ. ხორტონი, ლ. ზ. კაჰლონი, ო. პოხოტელოვი, ო. ონიშჩენკო

რეზიუმე

ნაჩვენებია, რომ დედამიწის იონოსფეროს სუსტად იონიზირებულ E–ფენაში, სადაც ბატონობს ქოლის გამტარობა, გენერირდება ახალი ტიპის როსბი–ალფვენ–ხანთაძის (გრახ)

გადაბმული პლანეტარული ელექტრომაგნიტური ტალღები განპირობებული დედამიწის კორიოლისის პარამეტრის და გეომაგნიტური ველის განედური არაერთგვაროვნებების არსებობით. ტალღების ამგვარი გადაბმულობის გამო აღიძვრება ახალი ტიპის ალფვენის ტალღები. შეისწავლებაზონალური დინების წანაცვლების და (გრახ ემ) პლანეტარული ტალღების წარმოშობა. არამდგრადობის არაწრფივი მექანიზმი ეყრდნობა ზონალური ნაკადის პარამეტრულ აღძვრას ოთხი ტალღის ურთიერთქმედებით, რომელსაც მივყავართ ენერგიის ინვერსიულ კასკადისკენ უფრო გრძელი ტალღების მიმართულებით. გამოყვანილია 3D გადაბმულ განტოლებათა სისტემა, რომელიც აღწერს მქაჩავი (გრახ) ტალღების არაწრფივ ურთიერთობას ზონალურ დინებასთან. განსაზღვრულია სათანადო არამდგრადობის ზრდის სიჩქარე და მისი მართვის პირობები. მიღებულია, რომ სიჩქარის ზრდა ძირითადად განისაზღვრება როსბის ტალღების მოქმედებით, ხოლო მაგნიტური ველის წარმოშობა – ალფვენის ტალღების მოქმედებით.

Journal of the Georgian Geophysical Society,
Issue B. Physics of Atmosphere, Ocean, and Space Plasma, v.16b, 2013, pp. 76-81

Appearance of lower thermosphere and ionosphere F2 region dynamical coupling caused by tidal motions over Abastumani

Nikoloz Gudadze, Goderdzi G. Didebulidze, Giorgi Sh. Javakhishvili

E. Kharadze Abastumani Astrophysical Observatory at Ilia State University; K. Cholokashvili Ave 3/5; Tbilisi 0162; GEORGIA
guda@iliauni.edu.ge; didebulidze@iliauni.edu.ge; javakhishvili@iliauni.edu.ge

Abstract. The presence of planetary scale motion characteristic variations in the Earth's upper atmosphere is shown in the intensities of the nightglow mesopause hydroxyl OH(8-3) band, the lower thermosphere oxygen green OI 557.7nm line and the ionosphere F2 region red OI 630.0 nm line, observed from Abastumani(41.75N, 42.82E). There is demonstrated the simultaneous observation for the mentioned intensities characterized by vertical propagation of 4-8 hour tidal motions, which are considered as the manifestation of the lower and upper atmosphere-ionosphere F2 layer dynamical coupling in the Caucasus region.
It is shown that in the considered cases, for terdiurnal tidal motions, is possible to estimate the wavelength of the vertical propagation, which is equal to the distance between luminous layers (about 130-150 km) or its multiple values (65-75, 32-37 km). The profile of the electron content is necessary to reveal smaller wavelengths.

1. Introduction

Tidal motions are mainly planetary scale dynamical processes [2] and play an essential role in the climatology of the mesosphere and thermosphere regions of the Earth's atmosphere [3, 4]. The main source of the thermal tidal motions is the periodical absorption of the Solar electromagnetic radiation by Earth's surface and atmosphere during daily rotation of the planet. In the upper atmosphere, such thermal tidal movements can be characterized by periods of 24 and 12 hours [2], and also with a low periods of 4-8 hours [12]. Tidal motions are important processes for the dynamical coupling between lower and upper atmosphere under various helio-geophysical conditions in the given region of the globe. The interest of this kind investigations increases in the last decade [1, 6, 8, 11].

The dynamical coupling between lower and upper atmosphere is shown in the mesosphere-thermosphere-ionosphere interaction and the simultaneous observations and monitoring on the airglow intensities for mentioned atmosphere regions are important to study the development of this processes.

In this paper the nightly variations of the intensities of the mesosphere hydroxyl OH(8-3) band (maximum luminous layer about 87 km), the lower thermosphere green OI 557.7 nm line (maximum luminous layer about 95 km) and the ionosphere F2 region red OI 630.0 nm line (with maximum luminous layer about 230-280 km) are considered, where the 4-8 hours period tidal characteristic changes occurs simultaneously. Mention phenomenon

will be considered as a manifestation of importance of the tidal motions in the lower and upper atmosphere-ionosphere dynamical coupling processes. Its investigation is important to manifest the characteristic parameters of the tidal motions in the (Caucasus) region, which source could be as at the near Earth surface as well *in situ* generation in the atmosphere.

2. Tidal variations in the hydroxyl OH band, the green 557.7 nm and the red 630.0 nm line nightglow intensities

The systematic simultaneous photometrical observations of the nightglow intensities of the mesosphere hydroxyl OH bands, the lower thermosphere green OI 557.7 nm line and the ionosphere F2 region red OI 630.0 nm line are carrying out in Abastumani Astrophysical Observatory from 1957 year. These data is important to investigate dynamical and structural processes in the Caucasus region of the upper atmosphere during different helio-geophysical conditions [3, 4]. The brightest object of the nightglow spectrum of these observations is hydroxyl OH(8-3) band, which is mainly emitted from the coolest region of the atmosphere - mesopause. Main process for OH(8-3) band excitation is the reaction $O_3+H=OH+O_2$ and its volume emission rate ε_{OH} [10]

$$\varepsilon_{OH} \propto [H][O_3] \qquad (1)$$

where $[O_3]$ and $[H]$ are densities of the O_3 ozone molecule and the H atoms of hydrogen in the emitted region of the mesosphere. These parameters change during the seasons and during the night as well. They are sensitive to vertical flux changes of neutral components in the mesosphere and lower thermosphere, which can be induced by tidal motions.

The source of the upper atmosphere tidal motions sometimes is in the lower atmosphere and it propagates to the lower thermosphere and the ionosphere F2 region [7]. The nightglow intensity of the green 557.7 nm line $(O(^1S) \xrightarrow{557.7nm} (^1D))$ in the lower thermosphere is also sensitive on mention atmospheric disturbances. The green line in the lower thermosphere is excited during the Barth two step mechanism [9] and its volume emission rate ε_{5577}

$$\varepsilon_{5577} \propto [O]^3 \qquad (2)$$

where $[O]$ is atomic oxygen density. Atomic Oxygen O, eq.1, Ozone O_3 and Hydrogen atom H, eq.2, are small components of the atmosphere and their changes significantly could be modulated by atmospheric tidal motions. Their changes are mutually coupled. For example the relative part of ozone increases during increase of vertical flux which in turn increases luminosity of hydroxyl *OH(8-3)* band (eq.1). Also, the green line intensity decreases caused by decreasing in the relative part of atomic oxygen density in the same region. The picture is vice versa when the stream is downward - the increase in the green line intensity is accompanying with decreasing in the hydroxyl OH bands intensity. This phenomenon occurs in most seasons of the year and gives additional information on characteristic periods of tidal motions and on their vertical distribution as well.

We are using the nightly behavior of the red OI 630.0 nm line intensity emitted from the ionosphere F2 region beside the green 557.7 nm line and hydroxyl OH(8-3) band intensities to illustrate the propagation of the tidal motions to the heights of mentioned region. The volume emission rate of the red line intensity ε_{6300} [3]

$$\varepsilon_{6300} \propto \frac{[O_2](h)Ne(h,t)}{1+\frac{d_D}{A_D}} \qquad (3)$$

here *[O2](h)* is the height distribution of the density of oxygen molecules and *Ne(h,t)* is the time varying height profile of the F2 layer electron density, d_D is the rate of the collisional deactivation of $O(^1D)$ atoms with the dominant neutrals (*O, N2, O2*) [5] in the same region. Note, that the electron density *Ne* behavior is sufficiently determined by vertical motion of the neutrals and also on changes in horizontal wind velocity [3] which in turn is characteristic for tidal motions and comparatively less noticeable for the hydroxyl *OH* bands and the green line intensities, eq.1-2.

The tidal motions and its horizontal and vertical velocities and their vertical propagation can be described by the following equation [2]:

$$V_{tid} = (U,W)\cdot e^{\frac{z}{2H}}\cdot\cos\left[\frac{2\pi}{T}t-\frac{2\pi}{\lambda_z}z+\psi\right] \qquad (4)$$

here U and W are the horizontal and vertical component of tidal velocity, respectively; t is time (in hours) and T corresponds to period of tidal motion which is 4-8 hour (the terdiurnal type tides) in our case; $z=h-h_0$ is the difference between actual and some initial height and H is the atmospheric scale height; λ_z is the vertical wavelength and ψ corresponds to some initial phase of tidal velocity.

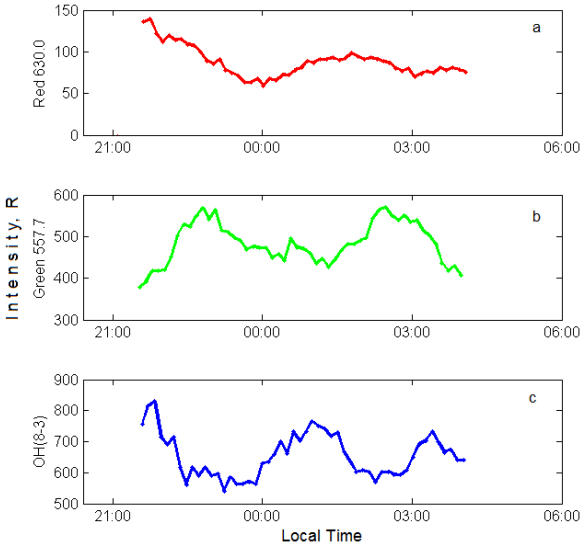

Figure 1

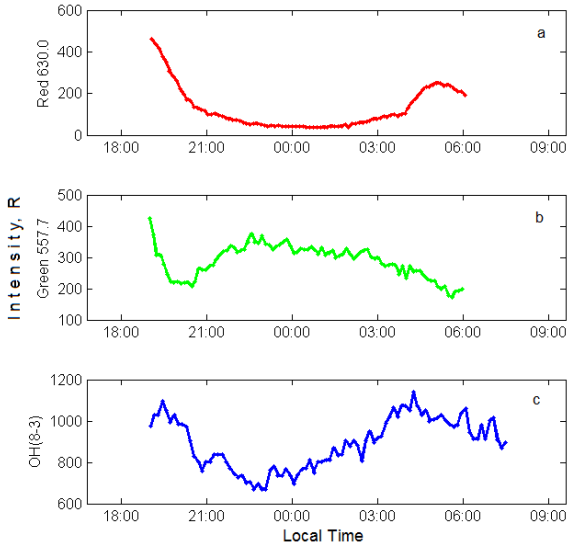

Figure 2

The night behavior of the Hydroxyl OH(8-3) band (panels c), OI 557.7 nm line (panels b) and red OI 630.0 nm line (panels a) observed column intensities from Abastumani (41.75N, 42.82E) for 2-3 September 1989 (Figure 1) and 13-14 January 1991 (Figure 2).

The Figures 1 and 2 shows an existence of the 4-8 hour periods tidal type disturbances in the mesosphere-thermosphere regions and their propagation to the ionosphere F2 region

heights. The Figure 1 and 2 corresponds to different phase of development of the same kind of tidal motions.

The propagated disturbance in the ionosphere corresponds to decrease of neutral wind vertical component (W), eq. (4), or increase of northward wind (U) phase on the Figure 1. Another plot (Figure 2) shows the similar process in case of 4 hour dallying of phase, when electron density Ne is decreased during the vertical downward neutral wind ($W<0$) or increase in northward wind velocity ($U>0$) in the ionosphere F2 region which corresponds the downward flux in the lower thermosphere (the intensity of the green line increases and hydroxyl intensity decreases).

Note, that the demonstrated observations correspond to geomagnetically quiet conditions (the values of daily Ap index 8 and 12 corresponds to demonstrated observation for 02-03 September of 1989 and 13-14 January of 1991) and other planetary scale disturbances then tidal motions are less supposed.

3. Conclusion

The existence of the planetary scale characteristic motions in the Earth's upper atmosphere by the mesopause region hydroxyl OH(8-3) band, the lower thermosphere green OI 557.7 nm line and the ionosphere F2 region OI 630.0 nm line intensities observed from Abastumani, has been shown. There was demonstrated the simultaneous observation for the mentioned intensities characterized by vertical propagation of 4-8 hour tidal motions during the geomagnetically quiet conditions, which are considered as the manifestation of coupling between the lower and upper atmosphere in the Caucasus region. The wavelength of the terdiurnal motion vertical distribution could be equal to the distance between 557.7 nm and 630.0 nm lines luminous layers (about 130-150 km) or its multiple values (65-75, 32-37 km) in the considered cases. The source of these tidal motions could be at the Earth surface or *in situ* generated in the lower and upper atmosphere.

Acknowledgment. This study is supported by Georgian Shota Rustaveli National Science Foundation grant No 13/09 and No 39/56.

Reference

[1] Chang, L. C., C.-H. Lin, J.-Y. Liu, N. Balan, J. Yue, and J.-T. Lin, J. Geophys. Res. Space Physics, 2013, v.118, pp.2545–2564;

[2] Chapman, S. and Lindzen, R.S., *D.Reidel Press, Dordrecht, Holland*, 1970, 200 pp.;

[3] Didebulidze, G.G., Chilingarashvili, S.P., Toroshelidze, T.I., *J. Atmos. Sol.-Terr. Phys.*, 2002, v.64, pp.1105-1116;

[4] Fishkova, L.M., *Metsniereba Press, Tbilisi*, 1983 (in Russian);

[5] Gudadze, N. B., Didebulidze, G. G., Javakhishvili, G. Sh., Shepherd, M. G., and Vardosanidze, M. V., *Can. J. Phys.*, 2007, v85, pp189–198;

[6] Guharay, A., P.P. Batista, B.R. Clemesha, S. Sarkhel, R.A. Buriti, *J. Atmos. Sol.-Terr. Phys.*, 2013, v.104, pp.87–95;

[7] Luan, X., Dou,, X. Lei, J., Jiang, G., *JGR*, 2012, 117(A11). DOI: 10.1029/2012JA018199;

[8] Mthembu, S.H., V.Sivakumar, N.J.Mitchell, S.B.Malinga, *J. Atmos. Sol.-Terr. Phys.*, 2013, v.102, pp.59–70;
[9] McDade, I.C., Murtagh, D.P., Greer, G.H., Dickinson, P.H.G., Witt, G., Stegman, J., Thomas, I., Jenkins, D.B., *Planetary and Space Science*, 1986, v.34, pp.789–800;
[10] Mcdade, I.C., Llewellin, E.J., Murtagh, D.P., Greer, G.H., *Planetary and Space Science*, 1987, v. 35 (9), pp.1137–1147;
[11] Yue Jia, Jiyao Xu, Loren C.Chang, Qian Wu, Han-Li Liu, Xian Lu, James RussellIII, *J. Atmos. Sol.-Terr. Phys.*, 2013, v.105-106, pp.191–198;
[12] Zhao, G., Liu, L., Ning, B., Wan, W., and Xiong, J., Earth Planets Space, 2005, v.57, pp.393–398.

ქვედა თერმოსფეროსა და იონოსფეროს F2 არის მიმოქცევითი მოძრაობებით გამოწვეული ზოგიერთი დინამიური კავშირები აბასთუმანთან

ნიკოლოზ გუდაძე, გოდერძი გ. დიდებულიძე, გიორგი შ. ჯავახიშვილი

რეზიუმე

ნაჩვენებია დედამიწის ზედა ატმოსფეროში პლანეტარული მასშტაბის მოძრაობებისათვის დამახასიათებელი ცვლილებების არსებობა აბასთუმნიდან (41.75N, 42.82E) დამზერილი მეზოპაუზის ჰიდროქსილის OH(8-3) ზოლის, ქვედა თერმოსფეროს მწვანე OI 557.7 ნმ ხაზის და იონოსფეროს F2 არის წითელი OI 630.0 ნმ ხაზის ღამის ცის ნათების ინტენსივობებში. დემონსტრირებულია მათ ინტენსივობებში 4-8 საათიანი მიმოქცევითი მოძრაობების ვერტიკალური გავრცელებისათვის დამახასიათებელი ერთდროული დაკვირვებები, რომლებიც განხილულია კავკასიის რეგიონში ქვედა და ზედა ატმოსფეროს კავშირების გამოვლინებად. ნაჩვენებია, რომ მსგავს შემთხვევებში შესაძლებელია შეფასდეს მიმოქცევითი მოძრაობების (8საათიანი პერიოდით) ვერტიკალური გავრცელების ტალღის სიგრძე, რომელიც დემონსტრირებულ შემთხვევაში მნათ ფენებს შორის მანძილის ტოლი (დაახლოებით 120-140 კმ) ან ჯერადია (60-70, 30-35 კმ-ია). უფრო მცირე ტალღის სიგრძეებისათვის ამ კავშირების გამოვლენა საჭიროებს ელექტრონების კონცენტრაციის პროფილს.

Выявление динамисческой связи между нижней термосферой и ионосферной F2 областями с помощью приливного движения над Абастумани

Николз Гудадзе, Годердзи Г. Дидебулидзе, Гиорги Ш. Джавахишвили

Резюме

По наблюдениям из Абастумани (41.75N, 42.82E) интенсивности излучения собственного свечения ночного неба, в частности, полосы гидроксила OH(8-3) из области мезопаузы, линий атомного кислорода OI 557.7 нм из нижней термосферы и OI 630. 0нм из ионосферной F2 области, выявлены характерные вариации движения планетарных масштабов в верхней атмосфере Земли.

Продемонстрированы данные одновременных наблюдений указанных интенсивностей, с характерными приливными движениями и вертикальным распространением продолжительностью 4-8 часов, что рассматривается как проявление динамической связи между нижней и верхней атмосферой и ионосферой в Кавказском регионе.

Показано, что в рассматриваемых случаях, для приливных движений (с периодом около 8 часов), возможно оценить длину волны вертикального распространения приливного движения, которая приблизительно равна расстоянию между слоями излучения (приблизительно 130-150 км) или их частным величинам (65-75, 32-37 км).

Journal of the Georgian Geophysical Society,
Issue B. Physics of Atmosphere, Ocean and Space Plasma, v.16b, 2013, pp 82-88

Galactic cosmic rays flux and geomagnetic activity coupling with cloud covering in Abastumani

Maya Todua and Goderdzi Didebulidze

Abastumani Astrophysical Observatory
Ilia State University

Abstract

The analysis of long-term observations in Abastumani (41.75° N, 42.82° E) revealed differences in the seasonal variations of Galactic Cosmic Rays (GCRs) flux and geomagnetic activities at cloudless days and cloudless nights. Particularly, in summer, the inter-annual distributions of the planetary geomagnetic Ap index and Sudden Storm Commencement (SSC) exhibited minima for cloudless days and maxima for cloudless nights, where GCR flux showed deep minimum. This feature in the case of SSC was demonstrated for the first time. The long-term trends of Ap index during summer time also revealed various meanings for cloudless day and night. These results can be regarded as the effect of cosmic factors on cloud covering in Abastumani, which in turn may have an influence on climatic variations.

1. Introduction

During the last decade the problem of impact of cosmic factors on cloud cover and its consequences on global climate has become of an increasing interest [1]. The solar wind, as well as Galactic Cosmic Rays (GCR) flux, modulated by it, effect the structure of the atmosphere. GCRs are the main source of ionization in the troposphere and lower stratosphere and they can initiate cloud condensation nuclei (CCN) [2, 3]. Geomagnetic storms also affect atmospheric structure and GCR flux [4]. Thus, there should be the interconnection between solar activity, GCR flux and geomagnetic disturbances.

The active processes on the Sun, like energetic proton events, coronal mass ejections (CME), solar flares, etc., are followed by decrease of GCR flux in the heliosphere [5, 6]. Since the active processes happen more often during solar maximum, then in minimum phase, the variations of the GCR flux are in antiphase with the 11-year solar cycle: it's decrease is greater during solar maximum, then during minimum phase [7].

According to Svensmark and Friis-Christensen [2], the lower level cloud covering correlates with the 11-year cycle of GCR flux and can cause variations of the ion numbers produced by it, which in turn affect the changes in the amount of CCN [8]. The cloud covering process is also connected to the temperature and seasonal changes of the atmosphere, in general.

Various seasonal atmospheric conditions can also influence differently the variations of the CCN produced by GCR. Therefore, there is a possibility that the inter-annual changes impact the cloud covering. At the same time, geomagnetic disturbances accompany active processes on the Sun and modulate GCR flux, which may be reflected on the cloud covering processes.

The goal of this paper is to reveal possible influence of cosmic factors on the cloud covering, considering inter-annual and long-term variations of GCR flux, solar activitiy, geomagnetic Ap index and Sudden Storm Commencement and their relationships, at cloudless days and cloudless nights in Abastumani.

2. Inter-annual variations of the planetary geomagnetic Ap index, SSC, GCR and solar radio $F_{10.7}$ fluxes at cloudless days and nights in Abastumani

To reveal the influence of cosmic factors on cloud covering we consider the inter-annual variations of planetary geomagnetic Ap index, Sudden Storm Commencement (SSC), GCR flux and solar radio flux $F_{10.7}$ at cloudless days and nigths in Abastumani.

Fig.1 demonstrates mean seasonal values of Ap index for moderate geomagnetic disturbances (Ap≤49), as well as corresponding normalized GCR flux and solar radio $F_{10.7}$ flux in Abastumani during 1957-1993, for cloudless days (white circles) and nights (black circles). GCR values X (at days with Ap≤49) are normalized to their mean $\overline{X}$: $X_n = (X - \overline{X}) / \overline{X}$.

Fig.1a demonstrates that, for cloudless nights, in addition to the Ap's well-known semi-annual variations with greatest values in spring and fall [9], it also reveals maximum in summer. This indicates the influence of cosmic factors on cloud covering. For the same cloudless nights GCR flux drops in summer as well. This decrease can cause reduction of ionization in the lower atmosphere and, consequently, the decrease of the amount of cloud formation nuclei, which in turn results in more cloudless nights.

The reduction of GCR flux in Summer is even more evident for strong geomagnetic disturbances (Ap≥50), which is often accompanied by Forbush decrease of GCR [6, 10]. The GCR effect on cloud covering appears even stronger since solar radio flux changes (at Ap≤49) in summer for cloudless nights are insignificant.

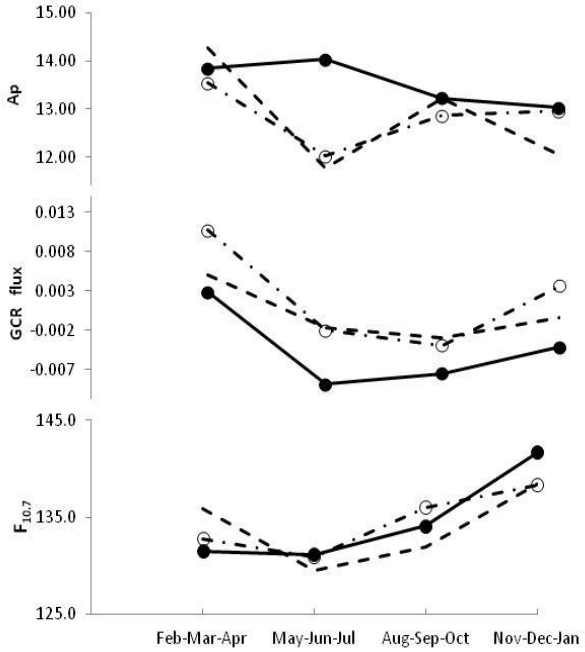

Fig. 1. The inter-annual distributions of seasonal mean values of the following quantities at the planetary geomagnetic Ap≤49: (top panel) *Ap* index; (middle panel) the normalized GCR flux observed by Tbilisi neutron monitor during 1964-1993 and (bottom panel) solar radio flux $F_{10.7}$. Dashed lines are for all day-night periods, dash-dotted lines and white circles – for cloudless days, and solid lines and dark circles – for cloudless nights at Abastumani in 1957-1993.

We considered the inter-annual distributions of monthly mean values of relative monthly numbers of Sudden Storm Commencement (SSC) and normalized GCR flux observed by Tbilisi neutron monitor during 1964-1993, for all, cloudless days and cloudless nights (Fig.2). Relative monthly numbers of SSC (characteristic frequency of SSC occurence) is a ratio of number of days (nights) with SSC to number of days (nights), for every month, summed during 1957-1993. Similar to above case, for cloudless nights, the sharp maximum of SSC in June is accompanied by the deep minimum of GCR flux.

The observed different sensitivity of cloud covering to the cosmic factors during day and night should affect the radiation balance on the Earth's surface and possibly the climate. To reveal the influence of cosmic factors on climate change we will consider the long-term trends of geomagnetic index for cloudless days and nights in the next chapter.

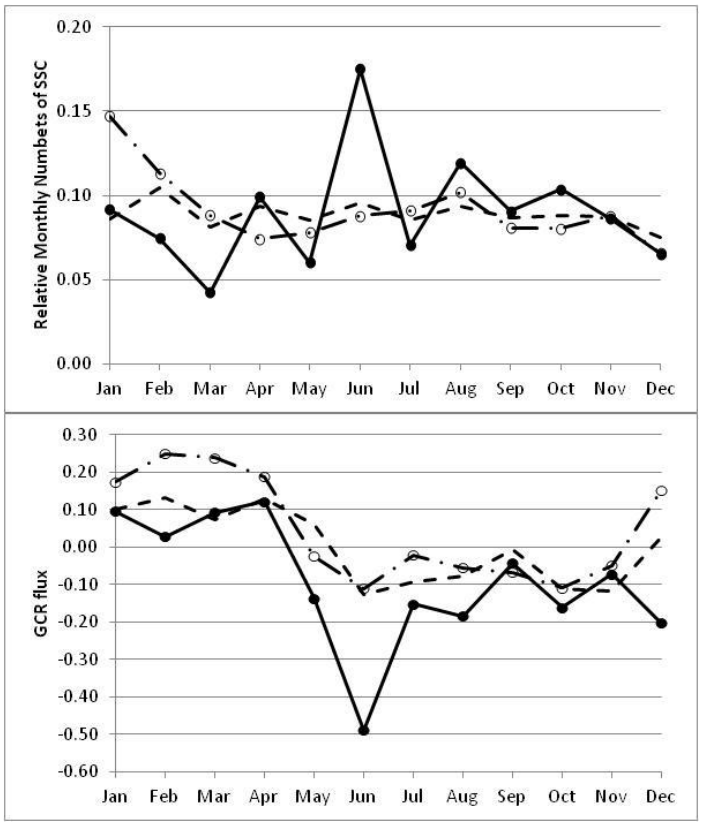

Fig. 2. The inter-annual distributions of monthly mean values of the following quantities: (top panel) relative monthly numbers of Sudden Storm Commencement; (bottom panel) the normalized GCR flux observed by Tbilisi neutron monitor during 1964-1993. Dashed lines are for all day-night periods, dash-dotted lines and white circles – for cloudless days, and solid lines and dark circles – for cloudless nights at Abastumani in 1957-1993.

3. Long-term trends of the planetary geomagnetic Ap index for cloudless days and nights

Like solar activity, the number of geomagnetic disturbances and thus planetary geomagnetic Ap index undergo changes with 11-year, secular and possibly other long-term periods, typical for solar variabilities. The considered dataset covers three 11-year solar cycles [11]. In Abastumani, the monthly and seasonal long-term trends (during 1957-93) in the red line of nightglow intensity were determined [12]. For this period the annual mean values of Ap index experience a minor positive trend. Almost the same values are obtained for cloudless days and nights. On Fig.3 the trend values of Ap for cloudless days, nights and all day-nights at moderate geomagnetic disturbances ($Ap \leq 49$) are demonstrated.

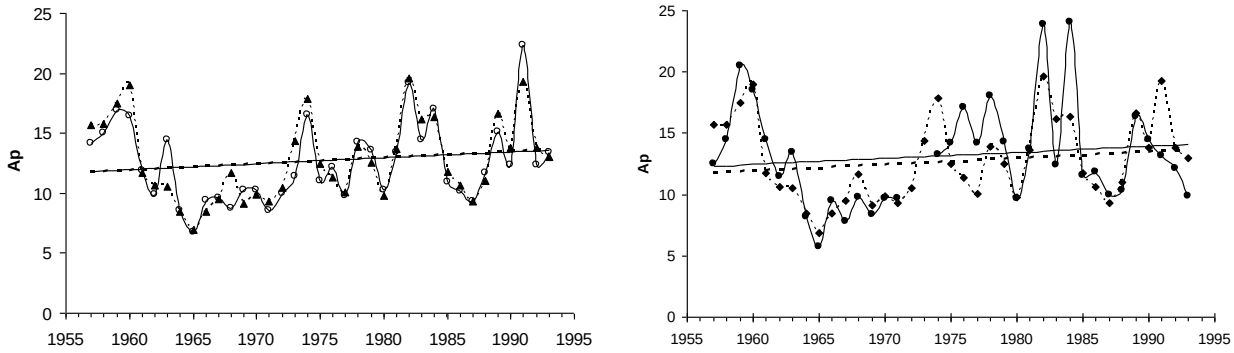

Fig. 3. Long-term variations of the mean annual planetary geomagnetic *Ap* index with *Ap≤49* for all day-nights (dashed lines and triangles), cloudless days (left fig., white circles), cloudless nights (right fig., dark circles) and their linear long-term trends during 1957-1993.

However, for seasonal mean Ap the trends are significantly different in case of cloudless nights. In the table, Ap seasonal trends (year^{-1}) and errors in 95% confidence are presented for all day-nights, cloudless days and cloudless nights.

	All Ap		Cloudless days Ap		Cloudless nights Ap	
	trend	±95% c.i.	trend	±95% c.i.	trend	±95% c.i.
Feb-Mar-Apr	0.092	0.017	0.136	0.036	0.178	0.065
May-Jun-Jul	0.009	0.014	0.008	0.023	-0.104	0.044
Aug-Sep-Oct	0.056	0.016	0.058	0.024	0.091	0.038
Nov-Dec-Jan	0.070	0.015	0.034	0.033	0.072	0.056

For cloudless days and nights these trend values are significantly different in summer (May-Jun-Jul): 0.008±0.023 and -0.104±0.044, respectively, with statistically significant negative number for nights. This negative trend for cloudless nights indicates the decrease of number of magnetically disturbed cloudless nights and thus the reduction of loss of infrared radiation emitted by the Earth's surface. This phenomenon may indicate the impact of cosmic factors on climate change.

4. Conclusion

We obtained different inter-annual variations of planetary geomagnetic Ap index (Ap≤49) and Sudden Storm Commencement at cloudless days and nights in Abastumani. For cloudless nights, mean seasonal Ap and SSC are the greatest in summer, while it is the smallest for cloudless days. In the case of SSC, this feature is demonstrated for the first time in the present paper. So, the effect for weak and moderate geomagnetic disturbances (Ap≤49) and strong ones are similar. The GCR flux decrease is also the greatest in summer.

We obtained that for summer season, the long-term trend of Ap for cloudless nights is significantly different from the one for cloudless days.

The obtained different seasonal sensitivity of cloud covering process to geomagnetic activity and GCR flux changes indicates the impact of cosmic factor on radiation balance on the Earth's surface. This fact, as well as different long-term trends of geomagnetic disturbances for cloudless days and nights, also point on possible cosmic factor influences on climatic variations.

Acknowledgment. This study is supported by Georgian Shota Rustaveli National Science Foundation grant No. 13/09.

Referencecs

[1] Gray, L. J., et al. *Rev. Geophys.*, 2010, 48, RG4001.
[2] Svensmark, H., Friis-Christensen, E., *Journal of Atmospheric and Solar-Terrestrial Physics*, 1997, 59, 1225–1232.
[3] Tinsley, B.A., Zhou, L., Plemmons, A., *Atmos. Res.*, 2006, 79, 266-295.
[4] Laštovička, J., *Journal of Atmospheric and Terrestrial Physics*, 1996, 58, 831–843.
[5] Kniveton, D.R., *Journal of Atmospheric and Solar-Terrestrial Physics*, 2004, 66, 1135-1142.
[6] Kudela, K., Brenkus, R., *Journal of Atmospheric and Solar-Terrestrial Physics*, 2004, 66, 1121-1126.
[7] Pudovkin, M.I., Veretenenko, S.V., *Advances in Space Research***,** 1996, v.17, Issue 11, 161–164.
[8] Marsh, N.D., Svensmark, H., *Physical Review Letters*, 2000, 85, 5004-5007.
[9] Russell, C.T., McPherron, R.L., *Journal of Geophysical Research*, 1973, 78(1), 92-108.
[10] Todua, M., Didebulidze, G.G. *Acta Geophysica*, 2013, 62, Issue 2, pp.381-399
[11] Megrelishvili, T. G., Fishkova, L. M., *Izvestiia, Fizika Atmosfery i Okeana*, 1982, 18, p. 1114-1120.
[12] Didebulidze, G. G.; Lomidze, L. N.; Gudadze, N. B.; Pataraya, A. D.; Todua, M., International *Journal of Remote Sensing*, 2011, v.32, issue 11, pp. 3093-3114.

Связь потока галактических космических лучей и геомагнитной активности с облачностью в Абастумани

Майя Тодуа и Годердзи Дидебулидзе

Абастуманская Астрофизическая Обсерватория
Государственный Университет Илии

Резюме

Анализ продолжительных наблюдений в Абастумани выявил различия сезонных вариаций потока галактических космических лучей (GCR) и геомагнитной активности для ясных дневных и ночных времен суток. В частности, в летнее время, годовые распределения планетарного геомагнитного индекса Ap и внезапного начала бури (SSC) имеет минимальное значение во время ясных дней и максимальное во время ночей. В то же время, в случае ясных ночей, поток GCR имеет глубокий минимум. Для SSC эта особенность была

продемонстрирована впервые. Продолжительные тренды Ap индекса также выявили различные значения в летнее время для ясных дней и ночей. Полученные результаты могут быть проявлением влияния космических факторов на облачность в Абастумани, которое, в свою очередь, может иметь воздействие на климатические изменения.

გალაქტიკური კოსმოსური სხივების ნაკადისა და გეომაგნიტური აქტივობის კავშირი ღურბელდაფარვასთან აბასთუმანში

მაია თოდუა და გოდერძი დიდებულიძე

აბასთუმნის ასტროფიზიკური ობსერვატორია
ილიას სახელმწიფო უნივერსიტეტი

რეზიუმე

აბასთუმანში წარმოებული გრძელვადიანი დაკვირვებების ანალიზმა აჩვენა, რომ გალაქტიკური კოსმოსური სხივების (GCR) ნაკადისა და გეომაგნიტური აქტივობების სეზონური ყოფაქცევა უღრუბლო დღეებისა და უღრუბლო ღამეების შემთხვევაში განსხვავებულია. კერძოდ, ზაფხულში, პლანეტური გეომაგნიტური Ap ინდექსისა და ქარიშხლების უეცარი დაწყების (SSC) შიდაწლიური განაწილებები უღრუბლო დღეების შემთხვევაში მინიმალური, ხოლო უღრუბლო ღამეების დროს მაქსიმალური მნიშვნელობებით ხასიათდება. ამავე დროს, უღრუბლო ღამეების შემთხვევაში, GCR-ის ნაკადმა მკვეთრი მინიმუმი გამოავლინა. SSC-ის შემთხვევაში ეს თავისებურება პირველადაა დაფიქსირებული. Ap ინდექსის გრძელვადიანი ტრენდები ზაფხულის პერიოდში ასევე განსხვავებული აღმოჩნდა უღრუბლო დღეებისა და ღამეებისათვის. ეს შედეგები შესაძლოა მიუთითებდეს კოსმოსური ფაქტორების გავლენას ღრუბელთდაფარვაზე აბასთუმანში, რაც, თავის მხრივ, შესაძლოა აისახოს კლიმატის ცვლილებებზე.

Journal of the Georgian Geophysical Society,
Issue B. Physics of Atmosphere, Ocean and Space Plasma, v.16b, 2013, pp 89-110.

Evolution of weather forming ULF electromagnetic structures in the ionospheric shear flows

G. Aburjania[1,2], Kh. Chargazia[1,2], O. Kharshiladze[2] and G. Zimbardo[3]

[1] I. Vekua Institute of Applied Mathematics,
Tbilisi State University, 2 University str., 0143 Tbilisi, Georgia;

[2] M. Nodia Institute of Geophysics,
Tbilisi State University, 1 Aleqsidze str., 0193 Tbilisi, Georgia

[3] Physics Department, University of Calabria,
Ponte P. Bucci, Cubo 31 C , 87036 Rende, Italy

E-mail: khatuna.chargazia@gmail.com;

Abstract

This work is devoted to study of transient growth and further linear and nonlinear dynamics of planetary electromagnetic (EM) ultra-low-frequency internal waves (ULFW) in the rotating dissipative ionosphere due to non-normal mechanism, stipulated by presence of inhomogeneous zonal wind (shear flow). Planetary EM ULFW appears as a result of interaction of the ionospheric medium with the spatially inhomogeneous geomagnetic field. An effective linear mechanism responsible for the generation and transient intensification of large scale EM ULF waves in the shear flow is found. It has been shown that the shear flow driven wave perturbations effectively extract energy of the shear flow and temporally algebraic increasing own amplitude and energy (by several orders). With amplitude growth the nonlinear mechanism of self-localization is turned on and these perturbations undergo self organization in the form of the nonlinear solitary vortex structures due to nonlinear twisting of the perturbation's front. Depending on the features of the velocity profiles of the shear flows the nonlinear vortex structures can be either monopole vortices, or dipole vortex, or vortex streets and vortex chains. From analytical calculation and plots we note that the formation of stationary nonlinear vortex structure requires some threshold value of translation velocity for both non-dissipation and dissipation complex ionospheric plasma. The space and time attenuation specification of the vortices is studied. The characteristic time of vortex longevity in dissipative ionosphere is estimated. The long-lived vortex structures transfer the trapped particles of medium and also energy and heat. Thus the structures under study may represent the ULF electromagnetic wave macro turbulence structural element in the ionosphere.

Keywords: *ULF electromagnetic wave, Inhomogeneous geomagnetic field, Shear flow, non-modal approach, Nonlinear solitary vortex structures.*

PACS: 52.35. Mw, 52.35.We, 94.20.W

1. Introduction

In the work presented here, we continue to study a special type of internal waves, which appear in the ionosphere under the influence of the spatially inhomogeneous geomagnetic field and the Earth's rotation velocity (Aburjania *et al* 2002, 2003, 2004, 2007). So, we are interested in large-scale (planetary) ultra-low-frequency (ULF) electromagnetic (EM) slow and fast wave motions in the ionospheric medium (consisting of electrons, ions and neutral particles), which have a horizontal linear scale L_h of order 10^3 km and higher, a vertical scale L_v of altitude scale order H ($L_v \approx H$). In the mid-latitude E-layer, slow ULF waves have phase velocities of 1-100 m/s along the parallels, and period variations from several hours to tens of days, i.e. they have the frequencies in the range of $(10^{-4} - 10^{-6})$ s^{-1}, as it is obvious from the long-term observations (Cavalieri et al. 1974; Manson et al. 1981; Sharadze et al. 1989; Zhou et al. 1997). In contrast to conventional planetary Rossby waves, they give rise to a perturbation of the geomagnetic field (a few nanoteslas (nT)) – a

circumstance that gives evidence of their electromagnetic nature. These waves are generated by the electrostatic dynamo electric field of polarization $\mathbf{E_d} = \mathbf{V} \times \mathbf{H}_0 / c$, where $\mathbf{H}_0$ is the strength of the geomagnetic field, $\boldsymbol{V}$ is velocity, c is light speed. Observations also show, that at temperate and mid-latitudes of the ionospheric E-region there are large-scale, relatively fast planetary electromagnetic wave perturbations, which propagate along the parallels with velocity of order of 2-20 km/s, their periods vary from several of minutes to a few hours, i.e. they have the frequencies in the range of $(10^{-1} - 10^{-4})$ s^{-1}, and an amplitude from hundreds to thousand of nT, as it is obvious from the observations (Al'perovich et al. 1982; Sharadze et al. 1988; Burmaka et al. 2004; Georgieva et al. 2005). Fast waves are generated by the latitudinal gradient of the geomagnetic field and the Hall effect and represent a variation of the vortical electric field – $\mathbf{E_v} = \mathbf{V_D} \times \mathbf{H}_0 / c$, where $\mathbf{V_D} = \mathbf{E} \times \mathbf{H}_0 \, \mathrm{c} / \mathrm{H}_0^2$ is an electron drift velocity. The fast waves are caused by the oscillations of electrons, completely frozen in the geomagnetic field. The phase velocities of these perturbations differ by magnitude at daily and nightly conditions in the E-layer of the ionosphere. In the mid-latitude F-layer the fast planetary electromagnetic wave perturbations propagate east-west along lines of constant latitude with a phase velocity of several units-tens of km/s; the periods range from a few seconds to several minutes, i.e. they have the frequencies in the range of $(10^{1} - 10^{-3})$ s^{-1}and accompanied by strong pulsation of the geomagnetic field ($20 - 10^{3}$ nT), as it is obvious from the observations (Sorokin, 1988; Sharadze et al. 1988; Burmaka et al. 2004; Georgieva et al. 2005; Fagundas et al. 2005). The phase velocity of the fast magneto-ionospheric wave perturbations in the F-layer does not vary noticeably on the period of a day, but depends on the ionospheric ionization levels.

These perturbations represent the eigen oscillations of the E and F-regions of the ionosphere and they are responsible for ionospheric electromagnetic weather formation. Such forced oscillations are observed at impulse action on the ionosphere from above - at magnetic storms (Haykowicz, 1991), from bellow – at seismic activity, volcano eruption and anthropogenic activities (Pokhotelov et al. 1995; Shaefer et al. 1999). So, at external influences these oscillations will be excited or amplified first in the ionosphere as eigen modes of the ionospheric resonator. Thus, these waves may be represented also ionospheric electromagnetic response on natural and artificial activities.

Observations (Gershman, 1975; Gossard and Hooke, 1975; Kamide and Chian, 2007) show also, that spatially inhomogeneous zonal winds (shear flows), produced by nonuniform heating of the atmospheric layers by solar radiation, permanently exist in the atmosphere and ionosphere layers. Herewith, investigation of the problem of generation and evolution of ionospheric EM ULF electromagnetic waves at interaction with the inhomogeneous zonal wind (shear flow) becomes important.

2. The governing equations

We choose our model as a two-dimensional $\beta-$plane with sheared flow. Since the length of planetary waves ($\lambda \geq 10^3$ km) is comparable with the Earth's radius R, we investigate such notions in approximation of the $\beta-$plane, which was specially developed for analysis of large-scale processes (Pedlosky, 1978), in the "standard" coordinate system. In this system, the x-axis is directed along the parallel to the east, the y-axis along the meridian to the north and the z-axis – vertically upwards (the local Cartesian system). For simplicity, the equilibrium velocity $\boldsymbol{V}_0$, geomagnetic field H_0, perturbed magnetic field $\mathbf{h}$ and frequency of Earth's rotation $\boldsymbol{\Omega}_0$ are given by $\boldsymbol{V}_0 = \mathrm{V}_0(\mathrm{y})\,\mathbf{e_x}$, $\boldsymbol{H}_0\,(0, 0, -\mathrm{H_p}\cos\theta)$, $\boldsymbol{h}\,(0, 0, h_z)$, $\Omega_0\,(0, 0, \Omega_0\cos\theta)$. Here and elsewhere $\mathbf{e}\,(\mathbf{e_x}, \mathbf{e_y}, \mathbf{e_z})$ denotes a unit vector, $\mathrm{H_p} = 5\times10^{-5}$ T is the value of geomagnetic field strength in the pole and we suppose that geomagnetic colatitude θ coincides with a geographical colatitude θ'. In the ionosphere the large-scale motions are quasi-horizontal (two-dimensional) (Aburjania et al. 2002; 2003; 2006) and hydrodynamic velocity of the particles $\mathbf{V} = (\mathrm{V_{x,}}, \mathrm{V_y}, 0)$. The fluid is assumed to be incompressible and therefore a stream function ψ can be defined trough $\boldsymbol{V} = [\nabla\boldsymbol{\psi}, \boldsymbol{e_z}]$. Medium motion is considered near the latitude $\varphi_0 = \pi/2 - \theta_0$.

Not considering any more detail in the new under review branches of planetary waves (see Aburjania et al , (2002-2004, 2007)) we would like to note that beginning with the altitude of 80 km and higher, the upper atmosphere of the Earth is a strongly dissipative medium. Often when modelling large-scale processes for this region of the upper atmosphere, effective coefficient of Rayleigh friction between the ionospheric layers is

introduced. The role of the ion friction rapidly increases at the altitudes above 120 km (Kelley, 1989, Kamide and Chian, 2007) and its analytical expression coincides with the Rayleigh friction formula (Aburjania and Chargazia, 2007). Therefore, often during a study of large-scale $(10^3 - 10^4)$ km, ULF $(10 - 10^{-6})\mathrm{s}^{-1}$ wavy structures in the ionosphere, we will apply the well-known Rayleigh formula to dissipative force $\boldsymbol{F} = -\Lambda \boldsymbol{V}$, assuming the altitudes above $(80 - 130)$ km $\Lambda \approx 10^{-5}$ s^{-1} (Dickinson, 1969; Gosard and Hooke, 1975), and the altitudes above 130 km $\Lambda = N\nu_{in}/\mathrm{N_n}$, where N and N_n denote concentrations of the charged particles and neutral particles, ν_{in} is frequency of collision of ions with molecules (Gershman, 1974; Kelley, 1989; Al'perovich and Fedorov, 2007).

The governing equations of the considered problem are the closed system of magnetohydrodynamic equations of the electrically conducting ionosphere (Gershman, 1974; Kelley, 1989; Aburjania et al. 2004; 2007; Al'perovich and Fedorov, 2007). The solution of the temporal evolution of inhomogeneously sheared flow reduces to solution of the set of nonlinear partial differential equations for ψ and magnetic field perturbation, h_z (see Aburjania et al. 2002):

$$\left(\frac{\partial}{\partial t} + V_0(y)\frac{\partial}{\partial x}\right)\Delta\psi + \left(\beta - V_0^{''}\right)\frac{\partial\psi}{\partial x} + C_H\frac{\partial h}{\partial x} + \Lambda\Delta\psi = J(\psi, \Delta\psi), \tag{1}$$

$$\left(\frac{\partial}{\partial t} + V_0(y)\frac{\partial}{\partial x}\right)h - \beta_H\frac{\partial\psi}{\partial x} + \delta\cdot C_H\frac{\partial h}{\partial x} = J(\psi, h). \tag{2}$$

Here

$$\beta = \frac{\partial 2\Omega_0}{\partial y} = -\frac{1}{R}\frac{\partial}{\partial\theta}(2\Omega_0) = \frac{2\Omega_0\sin\theta_0}{R},$$

$$\beta_H = \frac{eN}{\rho c}\frac{\partial H_{0z}}{\partial y} = -\frac{N}{N_n}\frac{eH_p}{MRc}\sin\theta_0 < 0, \quad V_0^{''}(y) = \frac{d^2V_0(y)}{d^2y},$$

$$h = \frac{eN}{N_nMc}h_z, \quad C_H = \frac{c}{4\pi eN}\frac{\partial H_{0z}}{\partial y} = -\frac{cH_p}{4\pi eNR}\sin\theta_0 < 0,$$

$$\Delta = \frac{\partial^2}{\partial x^2} + \frac{\partial^2}{\partial y^2}, \quad J(a,b) = \frac{\partial a}{\partial x}\cdot\frac{\partial b}{\partial y} - \frac{\partial a}{\partial y}\cdot\frac{\partial b}{\partial x}. \tag{3}$$

$\rho = N_nM$ is density of neutral particles; m and M are masses of electrons and ions (molecules); e is the magnitude of the electron charge; c is the light speed. Further we consider a motion in neighborhood of fixed latitude ($\theta = \theta_0$). The dimensionless parameter δ is introduced here for convenience. In the ionospheric E region $(80 - 150)$ km, where the Hall effect plays an important role, this parameter is equal to unity ($\delta = 1$). In the F region $(200 - 600)$ km, where the Hall effect is absent, δ turns to zero ($\delta = 0$).

The system of Eqs. (1), (2), at corresponding initial and boundary conditions, describes nonlinear evolution of the spatial two-dimensional large-scale ULF electromagnetic perturbations in sheared incompressible ionospheric E- and F-regions.

From the equations (1), (2) we determine the temporal evolution of the energy of wavy structures, $E(x,y,t)$

$$\frac{\partial E}{\partial t} = \int V_0^{'}(y)\frac{\partial\psi}{\partial x}\frac{\partial\psi}{\partial y}dxdy - \Lambda\int|\nabla\psi|^2dxdy, \tag{4}$$

where

$$E = \frac{1}{2}\left(|\nabla\psi| + k\,|h|\right)dxdy, \quad V_0^{'}(y) = \frac{dV_0(y)}{dy}, \quad k_0^2 = \frac{N}{N_n}\frac{\omega_{\mathrm{Pi}}^2}{c^2}, \quad \omega_{\mathrm{Pi}}^2 = \frac{4\pi e^2N}{M}; \tag{5}$$

and the potential enstrophy Q of wave perturbations:

$$\frac{\partial Q}{\partial t} = \frac{\partial}{\partial t}\left[\frac{1}{2}\int\left(|\Delta\psi|^2 + \frac{|\nabla h|^2}{k_0^2}\right)dxdy\right] = -\int V_0^{'}\frac{\partial h}{\partial x}\frac{\partial h}{\partial y}dxdy - \int V_0^{'''}\frac{\partial\psi}{\partial x}\frac{\partial\psi}{\partial y}dxdy - \Lambda\int|\Delta\psi|^2dxdy. \tag{6}$$

We note that in the absence of zonal flow ($V_0 = 0$) and Rayleigh friction ($\Lambda = 0$) the wavy structure energy and enstrophy are conserved.

Therefore, the existence of sheared zonal flow can be considered as the presence of an external energy source. One can see, that presented zonal shear flow (term with $V_0(y)$ in (4)) feeds the medium with external source of energy for generation of the wave structures (development of the shear flow instability). In this case it is necessary the velocity of the shear flow to have at least the first derivative according to meridional coordinate different from zero ($V_0'(y) \neq 0$). This conclusion can be made by virtue of above used modal (local - spectral) approach, which can't give much information about the features of the shear flow instability. But this doesn't mean that such instability always arises and remains in such form. This is exactly due to non-adequacy of modal approach at investigation of the features of shear flows, which is already considered in the introduction. In shear flows the modal approach can detect only possibility of instability. But for investigation of instability generation conditions and its temporal development in the ionosphere an alternative approach, namely, non-modal mathematical analysis becomes necessary. As it will be shown in the section 4 on the basis of more adequate method for such problems –nonmodal approximation, shear flows can become unstable transiently till the condition of the strong relationship between the shear flows and wave perturbations is satisfied (Chagelishvili et al. 1996; Aburjania et al. 2006), e. i. the perturbation falls into amplification region in the wave number space. Leaving this region, e. i. when the perturbation passes to the damping region in the wave vector space, it returns an energy to the shear flow and so on (if the nonlinear processes and self-organization of the vortex structure will not develop before) (Aburjania et al. 2006). The experimental and observation data shows the same (Gossard and Hooke, 1975; Pedlosky, 1979; Gill, 1982). Thus, non-uniform zonal wind or shear flow can generate and/or intensify the internal gravity waves in the ionosphere and provoke transient growth of amplitude, i.e. transient transport the medium into an unstable state. In the section 4 we confirm this view by using a different, more self-consistent method for the shear flow.

3. Local dispersion relation

Equations (1) and (2) are partial differential equations the variable coefficients of which depend on the spatial coordinate y. An analysis of the existence of nontrivial solutions by direct expansion of the physical quantities in Fourier integrals it is impossible even for the initial stage of the evolution of wave perturbations. This is why we have to use a local approximation by assuming that the coefficients of Eqs. (1) and (2) are locally uniform (constant), ($v_0 = const$). This approach justifies the use of the Fourier expansion in spatial and time variables to analyze the spectrum of the perturbations described by these equations (Mikhailovskii, 1974).

We represent the solution to Eqs. (1) and (2) in terms of the spatiotemporal Fourier expansion of the wave perturbations:

$$[\psi(x,y,t),h(x,y,t)] = \int [(\psi(k_x,k_y),h(k_x,k_y)] \exp\left\{i\left[k_x x + k_y y - \omega t\right]\right\} dk_x dk_z , \qquad (7)$$

where $\boldsymbol{k}$ is the wave vector and ω is the frequency. Substituting representation (7) into Eqs. (1) and (2) yields the dispersion relation

$$\tilde{\omega}^2 + \left(\frac{k_x}{k^2}\beta - \delta \cdot k_x C_H + i\Lambda\right)\tilde{\omega} - \delta \cdot \frac{k_x C_H}{k^2}\left(k_x\beta + i\Lambda k^2\right) - \frac{k_x^2}{k^2} C_H \beta_H = 0 . \qquad (8)$$

Here $\tilde{\omega} = \omega - k_x V_0$. Assuming that the wave number $k = \left(k_x^2 + k_y^2\right)^{1/2}$ is real, and the frequency is complex, $\tilde{\omega} = \omega_0 - k_x V_0 + i\gamma = \omega_1 + i\gamma$, $|\gamma| << \omega_0$, and taking in to account that the velocity $C_H < 0$ and $\beta_H < 0$, we obtain from dispersion relation (8) the spectrum of linear perturbations

$$\omega_1^2 + \left(\delta \cdot k_x |C_H| + \frac{k_x}{k^2}\beta\right)\omega_1 + \frac{k_x^2}{k^2}|C_H|[\delta \cdot \beta - |\beta_H|] = 0 . \qquad (9)$$

where $\omega_1 = \omega_0 - k_x V_0$, and the damping rate

$$\gamma = -\frac{(\delta \cdot k_x |C_H| + \omega_1)\Lambda}{\left(2\omega_1 + \frac{k_x\beta}{k^2} + \delta \cdot k_x |C_H|\right)} . \qquad (10)$$

From formula (9) we can determine two wave branches:

$$\omega_0^{(1,2)} = k_x V_0 + \frac{k_x}{2k^2}\left\{-\delta|C_H|k^2 - \beta \pm \left[\left(\delta|C_H|k^2 + \beta\right)^2 - 4k^2|C_H|\left(\delta\beta - |\beta_H|\right)\right]^{1/2}\right\} . \qquad (11)$$

(i) *E-region* $(\delta = 1)$.

For E region of the ionosphere, where the Hall effect plays an essential role $(\delta = 1)$, the equations (11) and (10) obtain the following form respectively:

$$\frac{\omega_0^{(1,2)}}{k_x} = V_0 - \frac{|C_H|k^2 + \beta}{2k^2} \pm \frac{1}{2k^2}\left\{\left(|C_H|k^2 + \beta\right)^2 - 4|C_H|k^2\beta'\right\}^{1/2}, \tag{12}$$

$$\gamma = -\frac{(k_x|C_H| + \omega_1)\Lambda}{\left(2\omega_1 + \frac{k_x\beta}{k^2} + k_x|C_H|\right)} \tag{13}$$

Here $\beta' = \beta - |\beta_H|$.

Equation (12) describes the propagation ULF planetary electromagnetic waves in the ionospheric E-layer having two branches of oscillations fast $\omega_0^{(1)}$ (with "+" sign before the radical) and slow $\omega_0^{(2)}$ (with "$-$" sign before the radical). The fast and slow mode (12) is an eigen oscillation of E-region of the ionospheric resonator. Wave is of electromagnetic origin and can exist in the presence of latitudinal gradient of the equilibrium geomagnetic field. It is seen that at $\beta \approx |\beta_H|$, the first branch $\omega_0^{(1)} = k_x V_0$ and for second branch we get

$$\omega_0^{(2)} = k_x V_0 - k_x|C_H| - \frac{k_x\beta}{k^2}. \tag{14}$$

In case long wave-length perturbations $k^2 \ll \beta/|C_H|$, we get from (12) and (13)

$$\omega_0^{(1)} = k_x V_0 - k_x\left[|C_H| - \frac{|C_H\cdot\beta_H|}{\beta} - \frac{k^2C_H^2|\beta_H|}{\beta^2}\left(1 - \frac{|\beta_H|}{\beta}\right)\right], \quad |\gamma^{(1)}| = \frac{k^2|C_H\beta_H|}{\beta^2}\Lambda \ll \Lambda, \tag{15}$$

and

$$\omega_0^{(2)} = k_x V_0 - k_x\left[\frac{\beta}{k^2} + \frac{|C_H\cdot\beta_H|}{\beta} + \frac{k^2C_H^2|\beta_H|}{\beta^2}\left(1 - \frac{|\beta_H|}{\beta}\right)\right], \quad \gamma^{(2)} = -\Lambda. \tag{16}$$

From these expressions we see that depending on the sign of $(\beta - |\beta_H|)$, fast $\omega_0^{(1)}$ waves can propagate both westward and eastward virtually without damping, while slow $\omega_0^{(2)}$ waves are propagating only westward and are damping substantially (but for more large-scale waves the damping can be weak).

In case of relatively short wave-length perturbations $k^2 \gg \beta/|C_H|$, we get

$$\omega_0^{(1)} = k_x V_0 - \frac{k_x}{k^2}\left[\beta - |\beta_H| + \frac{|\beta_H|}{|C_H|k^2}\left(\beta - |\beta_H|\right)\right], \quad \gamma^{(1)} = -\Lambda, \tag{17}$$

and

$$\omega_0^{(2)} = k_x V_0 - k_x\left[|C_H| + \frac{|\beta_H|}{k^2} - \frac{2|\beta_H|}{|C_H|k^4}\left(\beta - |\beta_H|\right)\right], \quad |\gamma^{(2)}| \approx \frac{|\beta_H|}{k^2|C_H|}\Lambda \ll \Lambda. \tag{18}$$

As before, we see that depending on the sign $(\beta - |\beta_H|)$, slow $\omega_0^{(1)}$ waves can propagate both westward and eastward and are damping substantially, while fast $\omega_0^{(2)}$ waves are propagating only westward without damping.

(ii) *F-region* ($\delta = 0$).

For F-region of the ionosphere, where the Hall effect is absent ($\delta = 0$), from (11) and (10) we obtain following solutions:

$$\omega_0^{(1,2)} = k_x V_0 + \frac{k_x}{2k^2}\left[-\beta \pm \left(\beta^2 + 4k^2 \left|C_H \cdot \beta_H\right|\right)^{1/2}\right], \tag{19}$$

and

$$\gamma^{(1,2)} = -\frac{\omega_I^{(1,2)}}{2\omega_I^{(1,2)} + k_x \beta / k^2}\Lambda. \tag{20}$$

In case long wave-length perturbations $k^2 \ll \beta^2 / \left|C_H \cdot \beta_H\right|$, we get from (19) and (20)

$$\omega_0^{(1)} = k_x V_0 + \frac{k_x \left|C_H \cdot \beta_H\right|}{\beta}\left[1 - \frac{\left|C_H \cdot \beta_H\right|}{\beta^2}k^2\right], \quad \left|\gamma^{(1)}\right| \approx \frac{k^2 \left|C_H \beta_H\right|}{\beta^2}\Lambda \ll \Lambda, \tag{21}$$

and

$$\omega_0^{(2)} = k_x V_0 - k_x\left[\frac{\beta}{k^2} + \frac{\left|C_H \cdot \beta_H\right|}{\beta}\left(1 - \frac{k^2 \left|C_H \cdot \beta_H\right|}{\beta^2}\right)\right], \left|\gamma^{(2)}\right| \approx \frac{\beta^2}{4k^2\sqrt{C_H \beta_H}}\Lambda \ll \Lambda. \tag{22}$$

From these expressions we see that fast $\omega_0^{(1)}$ waves can propagate only eastward virtually without damping, while slow $\omega_0^{(2)}$ waves are propagating only westward and are damping substantially.

In case of relatively short wave-length perturbations $k^2 \gg \beta^2 / \left|C_H \cdot \beta_H\right|$, we get

$$\omega_0^{(1)} = k_x V_0 + \frac{k_x}{k}\left\{\sqrt{C_H \beta_H} - \frac{\beta}{2k} + \frac{\beta^2}{8\sqrt{\left|C_H \beta_H\right|}k^2}\left(1 - \frac{\beta^2}{16\left|C_H \beta_H\right|k^2}\right)\right\}, \quad \left|\gamma^{(1)}\right| = \frac{\Lambda}{2}, \tag{23}$$

and

$$\omega_0^{(2)} = k_x V_0 - \frac{k_x}{k}\left\{\sqrt{C_H \beta_H} + \frac{\beta}{2k} + \frac{\beta^2}{8\sqrt{\left|C_H \beta_H\right|}k^2}\left(1 - \frac{\beta^2}{16\left|C_H \beta_H\right|k^2}\right)\right\}, \quad \left|\gamma^{(1)}\right| = \frac{\Lambda}{2}. \tag{24}$$

We see that $\omega_0^{(1)}$ waves can propagate only eastward, while $\omega_0^{(2)}$ waves are propagating only westward. These waves are weakly damping.

The wave branches (15) and (18) represent the dispersion relations for fast EM planetary waves stipulated by Hall conductivity ($\delta = 1$) and the permanently acting factors in the E-region of the ionosphere – latitudinal gradient of the geomagnetic field and angular velocity of the Earth's rotation. The wave branches (21), (23) and (24) represent also fast EM planetary waves caused by the global factors, acting permanently in the F-region of the ionosphere – inhomogeneity of the geomagnetic field and angular velocity of the Earth's rotation. As to the wave branches (16), (17) and (22), they are of slow magnetized Rossby (MR)-type. In the dispersion of the slow waves (16), (17) and (22) along with the latitudinal gradient of the Earth's angular velocity latitudinal gradient of the geomagnetic field plays the important role, which reduces the phase velocity. The same for the fast waves (15), (18), (21), (23) and (24) – non-uniform nature of the angular velocity of the Earth rotation stipulates the mutual coupling of the fast and slow waves, which causes intensification of the dispersion of the fast waves. Without such couplings, for example, the fast waves (15), (23) and (24) become non-dispersive.

4. Non-modal analysis of the linear evolution of disturbances

In deriving dispersion relations (8)-(11), we used a local approximation; i.e., we assumed that the quantities V_0 and V_0'' are locally uniform (as well as β, β_H and C_H, as is usually done in the β-plane approximation) and expanded the physical quantities in Fourier integrals. The applicability of the local approximation to nonuniform medium and sheared flows is limited (Mikhailovskii, 1974). The results obtained by using this

approximation are valid only for the initial stage of the evolution of perturbations. In particular, when the background flow is spatially nonuniform in the meridional direction, applying the Fourier expansion in the y coordinate is unjustified. According to (Reddy et al. 1993; Trefenthen et al. 1993; Chagelishvili et al, 1996; Aburjania et al. 2006), a more adequate approach to investigating the evolution of wave perturbations in sheared flows in the linear stage is provided by a nonmodal (rather than modal, i.e., direct Fourier expansion) mathematical analysis.

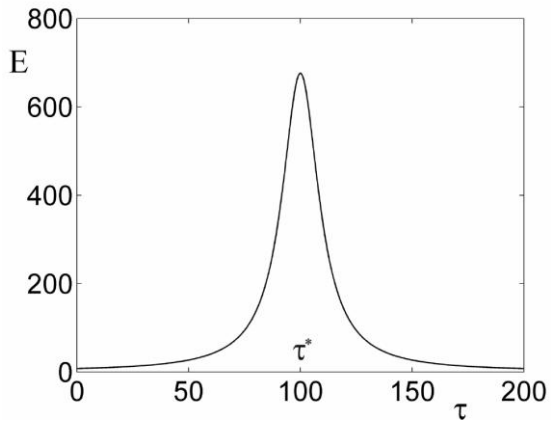

Fig. 1. Evolution of the non-dimensional energy density $E(\tau)$ (formulae (45)) to the initial parameters: $|\beta_H| = 0.1$, $\beta = 0.06$, $k_x = 0.01$, $k_y(0) = 0.1$, $S = 0.1$, $C_H = 1$.

Therefore, for adequate description of the dynamics of ULF waves interaction with inhomogeneous ionospheric winds on the basis of dynamical equations (1), (2), the non-modal mathematical analysis will be used below, which accounts non self-adjointness of the operators in this equations and non-orthogonality of the corresponding eigen-functions (Aburjania et al. 2006).

In this section, for definiteness, we choose the velocity profile of the sheared flow (nonuniform wind) to have the simplest form $V_0(y) = A \cdot y$, where $A > 0$ is the constant parameter of the wind shear, which we take to be positive and independent of y. The non-modal approach begins with a transformation to the convective coordinates $x_1 = x - v_0(y)t,\ y_1 = y,\ t_1 = t,$ that are the coordinates in the local rest frame of the mean flow.

In our problem, this is equivalent to the following change of variables:

$$x_1 = x - Ayt, \quad y_1 = y, \quad t_1 = t, \tag{25}$$

or

$$\frac{\partial}{\partial t} = \frac{\partial}{\partial t_1} - Ay\frac{\partial}{\partial x_1}, \quad \frac{\partial}{\partial x} = \frac{\partial}{\partial x_1}, \quad \frac{\partial}{\partial y} = \frac{\partial}{\partial y_1} - At_1\frac{\partial}{\partial x_1}. \tag{26}$$

In terms of the new variables, Eqs. (1) and (2) read

$$\frac{\partial}{\partial t_1}\left\{\left[\frac{\partial^2}{\partial x^2} + \left(\frac{\partial}{\partial y_1} - At_1\frac{\partial}{\partial x_1}\right)^2\right]\psi\right\} + \beta\frac{\partial\psi}{\partial x_1} + C_H\frac{\partial h}{\partial x_1} + \nu\left\{\frac{\partial^2}{\partial x^2} + \left(\frac{\partial}{\partial y_1} - At_1\frac{\partial}{\partial x_1}\right)^2\right\}\psi = 0, \tag{27}$$

$$\frac{\partial}{\partial t_1}h - \beta\frac{\partial\psi}{\partial x} + C_H\frac{\partial h}{\partial x} = 0. \tag{28}$$

The coefficients of the initial set of linear equations (1) and (2) depend on the spatial coordinate y. Having made the above charge of variables, we switch from this spatial nonuniformity Eqs. (1) and (2) to the temporal nonuniformity in Eqs.(27) and (28).

Hence, we have reduced the boundary-value problem to the Cauchy problem. Since the coefficients of Eqs. (8) and (9) are now independent of the spatial coordinates x_1 and y_1, we can apply the Fourier expansions in the spatial variables x_1 and y_1 to the equations, without using any local approximations and can independently consider the time evolution of the SFHs:

$$\begin{Bmatrix}\psi(x_1,y_1,t_1)\\ h(x_1,y_1,t_1)\end{Bmatrix}=\int\int_{-\infty}^{\infty}\int dk_{x_1}dk_{z_1}\begin{Bmatrix}\tilde{\psi}(k_{x_1},k_{y_1},t_1)\\ \tilde{h}(k_{x_1},k_{y_1},t_1)\end{Bmatrix}\times exp(ik_{x_1}x_1+ik_{y_1}z_1). \quad (29)$$

Here, quantities with tilde (e.g., $\tilde{\psi}$]) denote the SFHs of the corresponding physical quantities.

We substitute representation (29) into Eqs. (27) and (28), omit the tilde from the Fourier harmonics of the physical quantities, and switch to the dimensionless variables

$$\tau\Rightarrow\omega_0 t_1;\quad (x,y)\Rightarrow\frac{(x_1,y_1)}{R};\quad \psi\Rightarrow\frac{\tilde{\psi}}{\omega_0 R^2};\qquad h\Rightarrow\frac{\tilde{h}}{\omega_0};$$

$$S\Rightarrow\frac{A}{\omega_0};\quad k_{x,y}\Rightarrow k_{x_1,y_1}R;\quad k_z=k_z(0)-k_xS\tau;\quad k^2(\tau)=k_x^2+k_z^2(\tau);$$

$$\nu\Rightarrow\frac{\Lambda}{\omega_0 R^2};\quad \beta\Rightarrow\beta\frac{R}{\omega_0};\quad C_H\Rightarrow\frac{C_H}{\omega_0 R};\quad \Phi=k^2(\tau)\psi(\tau); \quad (30)$$

As a result, for each SFH of the perturbed quantities, in the non-dissipative case $(\nu=0)$, we obtain the equations

$$\frac{\partial\Phi}{\partial\tau}-\beta k_x\frac{\Phi}{k^2(\tau)}-ik_xC_Hh=0, \quad (31)$$

$$\frac{\partial h}{\partial\tau}-ik_x\beta\frac{\Phi}{k^2(\tau)}+ik_xC_Hh=0. \quad (32)$$

The closed set of Eqs. (31) and (32) describes the linear interaction of a ULF PEW with a sheared flow and the evolution of the related perturbations in an ionospheric medium. After the above manipulations, the wave vector of the perturbations, $\boldsymbol{k}\,(k_x,k_y(t))$ becomes time-dependent, $k_y(\tau)=k_y(0)-k_xS\cdot\tau;k^2(\tau)=(k_x^2+k_y^2(\tau))$, that is, the wave vector is subject to a linear drift in wave-number space. Because of the time variation of the wave vector (i.e., the separation of the perturbation scales in the linear stage), the interaction even between the perturbations that occur initially on very different characteristic scales is highly pronounced (Aburjania et al . 2006).

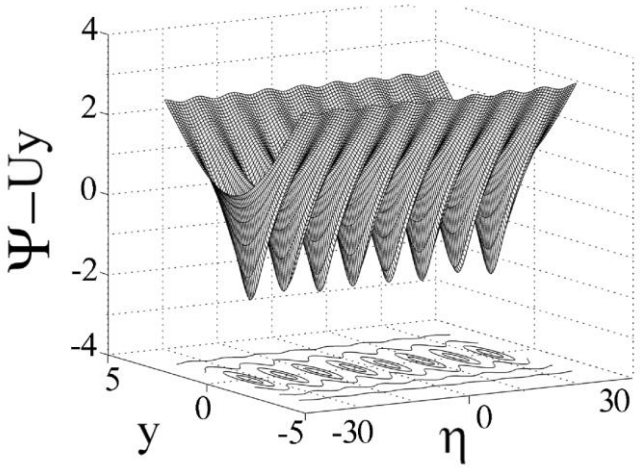

Fig. 2. Relief and level lines in the rest frame of the vortices $\Psi(\eta,y)-Uy$, calculated from formula (55) for $\psi_0^0=1$, $k=1$, $æ_0=0.5$ (the longitudinal vortex street).

In wave number space, the total dimensionless energy density E of the wave perturbations, SFHs of which are determined by Eqs. (31) and (32), has the form

$$E[k(\tau)]=\frac{1}{2}\left[|\Phi(\tau)|^2+\frac{|h(\tau)|^2}{k_0^2}\right]. \quad (33)$$

Correspondingly, from Eq. (4) we can see that, in the presence of a zonal flow with the velocity $V_0(y)$, the energy density of the SFHs evolves according to law

$$\frac{dE(\tau)}{d\tau} = V_0' \frac{\partial \psi}{\partial x}\frac{\partial \psi}{\partial y} = -SV_x(\tau)V_y(\tau). \tag{34}$$

In the absence of a sheared flow ($S = 0$), the total energy density of the wave perturbations in the ionosphere is conserved, $dE(\tau)/d\tau = 0$.

Let us now turn to Eq. (34) to find out what is the result of the evolution of the energy of a wave perturbation: is it an increase or a decrease in its energy? To do this, we must calculate the right-hand side of Eq. (34), a task that requires solving Eqs. (31) and (32). In this way, differentiating Eq. (31) with respect to time and using Eq. (32), we arrive at the following second-order equation for the generalized stream function $\Phi = k^2(\tau)\psi(\tau)$:

$$\frac{d^2\Phi}{d\tau^2} + P_1(\tau)\frac{d\Phi}{d\tau} + P_2(\tau)\Phi = 0, \tag{35}$$

where

$$P_1(\tau) = ik_x\left(C_H - \frac{\beta}{k^2(\tau)}\right), \qquad P_2(\tau) = \frac{k_x^2}{k^2(\tau)}\left[C_H\beta' - 2iS\frac{k_y(\tau)}{k^2(\tau)}\beta\right], \quad \beta' = \beta + \beta_H. \tag{36}$$

Equation (35) can be simplified by introducing a new variable (Magnus 1976). Setting

$$\Phi = Y\,exp\left[-(1/2)\int P_1(\tau')d\tau'\right], \tag{37}$$

we can transform Eq. (35) to the equation of a linear oscillator with time-dependent parameters

$$\ddot{Y} + \Omega^2(\tau)Y = 0. \tag{38}$$

Here, the prime denotes the derivative with respect to time and

$$\ddot{Y} = \frac{d^2Y}{d\tau^2}; \qquad \Omega^2(\tau) = P_2(\tau) - \frac{1}{2}\dot{P}_1(\tau) - \frac{1}{4}P_1^2(\tau) \approx$$

$$\approx \frac{k_x^2C_H^2}{4}\left(1 - \frac{\beta}{k^2(\tau)C_H}\right)^2 + \frac{k_x^2}{k^2(\tau)}\left(C_H\beta' - iS\frac{k_y(\tau)}{k^2(\tau)}\beta\right). \tag{39}$$

We solve Eq. (38) in the adiabatic approximation (Zel'dovich and Myshkis, 1973) by assuming that the quantity $\Omega(\tau)$ varies adiabatically with time:

$$\left|\dot{\Omega}(\tau)\right| << \left|\Omega^2(\tau)\right|. \tag{40}$$

Under this assumption, homogeneous equation (38) can be solved approximately. For a flow with $S << 1$, condition (40) is satisfied for a wide range of wave numbers, $\left|k_y(\tau) = k_y(0) - k_xS\tau\right|$. In other words, when the time variation of $\left|k_y(\tau)\right|$ is due to the linear drift of the wave vector in wave number space, condition (40) is valid throughout the entire evolution of the SFHs. The approximate solution to Eq. (38) can then be represented as

$$Y = \frac{C}{\sqrt{\Omega(\tau)}}exp\left[-i\int_0^\tau \Omega(\tau')d\tau'\right], \tag{41}$$

where $C = const$. Substituting representation (41) into formulas (37) and (30), we can construct the solutions to Eqs. (31) and (32):

$$\psi(\tau) = \frac{\Phi(\tau)}{k^2(\tau)} = \frac{C}{k^2(\tau)\sqrt{\Omega(\tau)}}exp\left[-i\phi(\tau)\right], \tag{42}$$

$$h(\tau) = -\frac{k^2(\tau)\psi(\tau)}{k_xC_H}\left[\Omega(\tau) + \frac{k_xC_H}{2}\left(1 + \frac{\beta}{k^2(\tau)C_H}\right)\right], \tag{43}$$

Here, with allowance for the obvious inequality $\left|C_H\right| >> \left|\beta'/k^2(\tau)\right|$, we assume that

$$\Omega(\tau)=\frac{k_x C_H}{2}\left(1+\frac{\beta+2\beta_H}{k^2(\tau)C_H}\right),\ \phi(\tau)=k_x C_H\tau+\frac{\beta_H}{k_x S}\left[arct\frac{k_y(\tau)}{k_x}-arct\frac{k_y(0)}{k_x}\right]. \qquad (44)$$

Inserting formulas (42)-(44) into expression (33) and taking into account the inequalities $k_0^2=4\pi^2\times10^{-6}<<1$, $|\beta_H|\geq\beta$, $\beta>0$, $\beta_H<0$, $C_H<0$, we arrive at the following expression for the normalized energy density of the Fourier harmonics:

$$E(\tau)\approx1+\left|\frac{6|\beta_H|-|\beta|}{8\left[k_x^2+\left(k_y(0)-Sk_x\tau\right)^2\right]C_H}\right|. \qquad (45)$$

In the initial evolutionary stage such that $k_y(0)/k_x>0$ (when $k_y(\tau)>0$), the denominator in expression (45) decreases with time τ, $0<\tau<\tau^*=k_y(0)/(Sk_x)=100$ and, accordingly, the energy density of the SFHs increases monotonically and reaches its maximum (which is several times higher than its initial value) at $\tau=\tau^*=100$. On longer time scales, $\tau^*<\tau<\infty$, the energy density decreases (when $k_y(\tau)<0$) and monotonically approaches a value approximately equal to the initial density. In other words, in the initial evolutionary stage, when $k_y(\tau)>0$ and the SFHs of the perturbations are in the amplification range in wave number space, the perturbations temporarily extract energy from the sheared flow to increase their amplitude several times on the time interval $0<\tau<\tau^*=k_y(0)/(Sk_x)$; in the subsequent stage, when $k_y(\tau)<0$, and the SFHs of the perturbations are in the damping range in wave number space, the perturbations return the energy back to the sheared flow on time scales $\tau^*<\tau<\infty$ (Figure 1), provided that nonlinear processes have not come into play and no self-organization of the wave structures has occurred prior to this stage. In a medium with a sheared flow, such an energy transient redistribution is caused by the fact that the wave vectors of the perturbations become time-dependent, $k=k(\tau)$; that is, the scales of the perturbations are partitioned and the structures occurring on comparable scales efficiently interact with each other, thereby sharing the free energy of the system among themselves.

So, within a time interval $\tau\leq\tau^*$ EM ULF wave disturbances redistribute the mean shear flow energy – draw energy from the main flow (the shear energy) and significantly grow (by several orders).

5. Shear flow driven nonlinear solitary vortex structures

It was shown in previous section, at the zonal flow velocity inhomogeneity, at interaction with the wind the EULF wave perturbations can sufficiently increase own amplitude and energy and in their dynamics the nonlinear effects will be appeared. As a rule, considering nonlinearity, steepness of the wave front increase leading to its breaking or formation of shock wave. However, as it is well known, shock waves do not arise spontaneously in the ionosphere. This indicates that in the real ionosphere for the planetary-scale motions when dissipative forces can be neglected, nonlinear effects of the medium must be essential (Aburjania et al. 2003, 2007). As a result, before breaking the wave must disintegrate either into separate nonlinear waves or into the vortex formations. If nonlinear increase of steepness of wave front will be exactly compensated by dispersion spreading, then stationary vortex structures will appear in the ionosphere. The more so, as experimental data and observations show (Bengtsson and Lighthill, 1982; Cmyrev et al, 1991; Petviashvili and Pokhotelov, 1992; Nezlin, 1994; Aburjania, 2006) that the nonlinear solitary vortex structures may exist in the different layers of Earth's atmosphere. Thus, the shear flow energy accumulation in the ionospheric disturbances may be results in the formation of nonlinear vortex structures. So, the ionosphere medium with sheared flow creates a favorable condition for formation of the nonlinear stationary solitary wave structures.

5.1. The stationary vortex streets in the nondissipative ionosphere

Vortex streets of various shapes can be generated in conventional liquid and plasma media with a sheared flow as a result of the nonlinear saturation of the Kelvin-Helmholtz instability (Gossard and Hooke, 1975; Kamide and Chian, 2007).

Thus, we will seek the solution of the nonlinear dynamic equations (1), (2) (in nondissipative stage, when $\Lambda\approx0$) in the form $\psi=\psi_0(\eta,y)$, $h=h(\eta,y)$, where $\eta=x-U\tau$, i.e. the stationary solitary structures,

propagating along x-axis (along the parallels) with velocity $U = const$ without changing its' shape. In accordance to Aburjania and Chargazia (2007), system of equation (1), (2) has the solution

$$h(\eta, y) = \frac{\beta_H}{C_H - U}\Psi\,, \tag{46}$$

$$\Delta\psi_0 - v_0^{'}(y) - \frac{C_H\beta^{'} - U\beta}{C_H - U}y = F(\psi_0 - \int^{y} v_0(y)dy - Uy)\,, \tag{47}$$

with $F(\xi)$ being an arbitrary function of its argument and $\Delta = \partial^2/\partial\eta^2 + \partial^2/\partial y^2$.Vortex streets have complicated topology and can occur when the function $F(\xi)$ in Eq. (47) is nonlinear (Petviashvili and Pokhotelov, 1992, Aburjania, 2006).

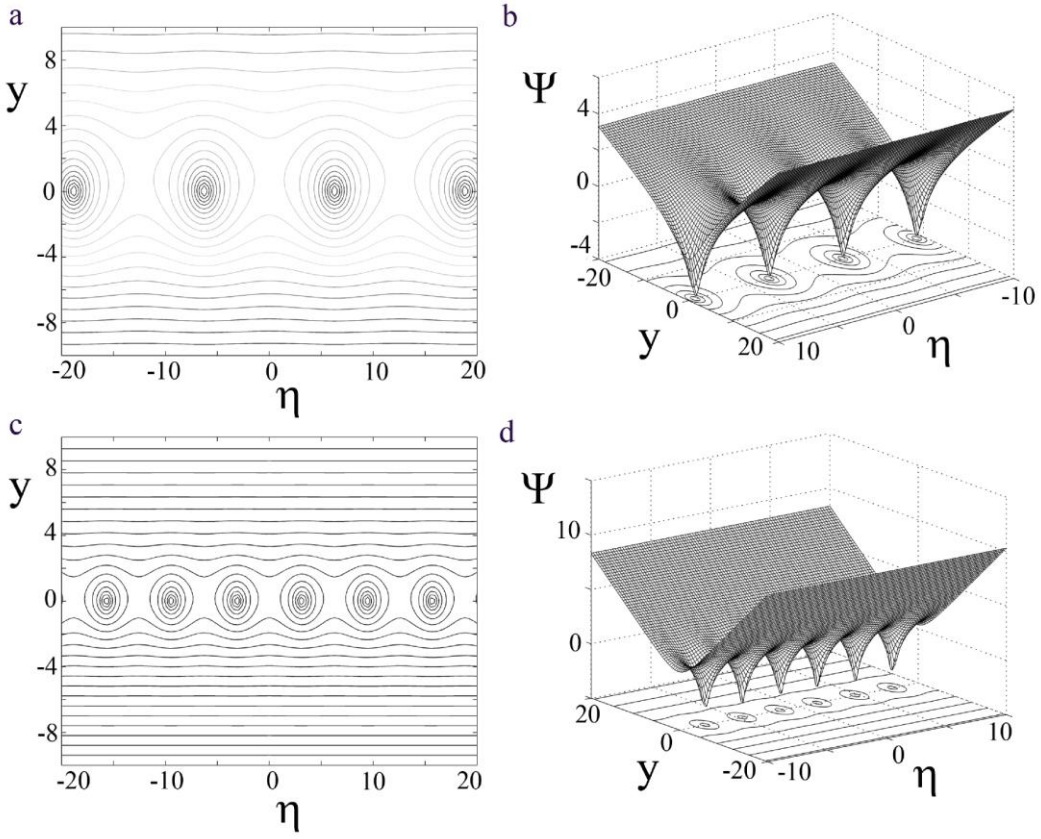

Figure 3. The level lines and relief of the stream function of vortex solution (55) in the moving system of coordinates to the parameters: a). $\psi_0^0 = 1$, $U = 0.1$, $æ_0 = 0.2$, $\kappa = 0.5$; b). $\psi_0^0 = 1$, $U = 0.1$, $æ_0 = 0.2$, $\kappa = 1$; c). $\psi_0^0 = 1$, $U = 0.1$, $æ_0 = 0.2$, $\kappa = 0.5$; d). $\psi_0^0 = 1$, $U = 0.1$, $æ_0 = 0.2$, $\kappa = 1$.

In (47) we assume that a nonlinear structure propagates with the velocity U satisfying the condition

$$U = \frac{\beta^{'}}{\beta}C_H\,. \tag{48}$$

For this case, choosing F to be a nonlinear function, $F(\xi) = \psi_0^0\kappa^2(exp(-2\xi/\psi_0^0)$ (Petviashvili and Pokhotelov, 1992; Aburjania, 2006), we can reduce Eq. (47) to

$$\Delta(\psi_0 - Uy) = \psi_0^0 k^2\, exp\left[-2(\psi_0 - Uy)/\psi_0^0\right]\,. \tag{49}$$

Then we introduce the new stream function

$$\Psi_0(\eta, y) = \Phi_0(y) + \psi_0(x, y)\,, \tag{50}$$

and the velocity potential $\Phi_0(y)$ of the background sheared zonal flow,

$$V_0(y) = \frac{d\Phi_0(y)}{dy}\,. \tag{51}$$

The stream function of the background sheared flow $\Phi_0(y)$ can be chosen to have the form

$$\Phi_0(y) = Uy + \psi_0^0 \ln(æ_0 y). \tag{52}$$

Here, ψ_0^0 is the amplitude of the vortex structure, $2\pi/\kappa$ kappa is its characteristic size, and $2\pi/æ_0$ is the nonuniformity parameter of the background sheared flow.

Taking into account formula (50) and using stream function (52), we can write vortex equation (49) as

$$\Delta\psi_0 = \psi_0^0 æ_0^2 \left[\frac{\kappa^2}{æ_0^2} e^{-2\psi_0/\psi_0^0} - 1 \right]. \tag{53}$$

This equation has the solution (Mallier and Maslowe, 1993)

$$\psi_0(\eta, y) = \psi_0^0 \ln\left[\frac{ch(\kappa y) + \sqrt{1-æ_0^2}\cos(\kappa\eta)}{ch(æ_0 y)} \right], \tag{54}$$

which describes a street of oppositely circulating vortices. Substituting solution (54) and stream function (52) into formula (50), we arrive at the final solution

$$\Psi_0(\eta, y) = Uy + \psi_0^0 \ln[ch(\kappa y) + \sqrt{1-æ_0^2}\cos(\kappa\eta)]. \tag{55}$$

Formulas (54), (52), and (51) yield the following expressions for the velocity components of the medium and sheared flow:

$$V_x(\eta, y) = U + \psi_0^0 \kappa \frac{sh(\kappa y)}{ch(\kappa y) + \sqrt{1-æ_0^2}\cos(\kappa\eta)}, \tag{56}$$

$$V_y(\eta, y) = \psi_0^0 \kappa \frac{\sqrt{1-æ_0^2}\sin(\kappa\eta)}{ch(\kappa y) + \sqrt{1-æ_0^2}\cos(\kappa\eta)}, \tag{57}$$

$$V_0(y) = U + \psi_0^0 æ_0 th(æ_0 y). \tag{58}$$

For $æ_0 = 1$, solution (56) describes a background flow of the type of sheared zonal flow with velocity (58). For $æ_0^2 < 1$, a street of cyclonic-type vortices forms in the middle of the zonal flow with velocity (58) (Figure 2). A solution like that described by formulas (56) and (57), with closed current lines in the form of cat's eyes, was for the first time obtained by Kelvin.

The vortex structures move with velocity (48). If we take into account that $\beta_H < 0$, $\beta' = \beta - |\beta_H| < 0$ as far as $|\beta_H| > \beta > 0$, $C_H < 0$ from expression (48) follows $U > 0$. For E-region the characteristic parameters $\mathrm{N/N}_n = 5\times10^{-7}$, $\Omega_H = eH_p/(Mc) \approx 10^3\ \mathrm{s}^{-1}$, $\mathrm{R} = 6.4\times10^6 m$, $2\Omega_0 \cong 10^{-4} rad\cdot s^{-1}$, we get that $\beta = 2\Omega_0 \sin\theta_0 / R \approx 0.8\times10^{-11} m^{-1}s^{-1}$, $|C_H| \approx 10\ km\cdot s^{-1}$, $|\beta_H| = (N/(N_n R))\Omega_H \sin\theta_0 \approx 4\times10^{-11} m^{-1}s^{-1}$. Thus, the vortices move with velocity $U \approx 4|C_H| > |C_H|$ along the parallels to the east. Therefore, this velocity is greater than the phase one of the corresponding linear periodic waves $U > |C_H| \approx 10\ \mathrm{km\cdot s}^{-1}$. So, the vortices don't come into resonance with the linear waves and don't loose energy on their excitation (Stepanyants and Fabrikant 1992).

For estimation of the linear scale of the vortex structures let's remember the general formal relation between the dispersion equation of the linear waves and with so-called modified dispersion equation of the nonlinear structures (Petviashvili and Pokhotelov, 1992; Aburjania, 2006). This is coupling of the phase velocity of linear wave $V_p = \omega/k$ with motion velocity of the nonlinear structures $U \coloneqq -\omega/k \to U$; relation of the wave vector k of the linear disturbances with the characteristic linear scale of the vortex d : $-k \to d^{-1}$. Taking into account this fact for characteristic scale of the fast vortex structures from (14) we get:

$$d^f = \left(\frac{|C_H|}{\beta} \right)^{1/2}. \tag{59}$$

And for the slow Rossby type vortex structures from the equations (16), (17) we get:

$$d^s = \left(\frac{U}{\beta}\right)^{1/2}. \qquad (60)$$

Substituting in these expressions the typical for the Earth's ionosphere numerical values $|C_H| \approx 10$ km s^{-1}, $\beta \approx 10^{-11} m^{-1} s^{-1}$, we find for fast structures $d^f \approx 10^4 km$. For slow Rossby-type vortices $U \approx 10$ m s^{-1} and we can obtain $d^s \approx 10^3 km$.

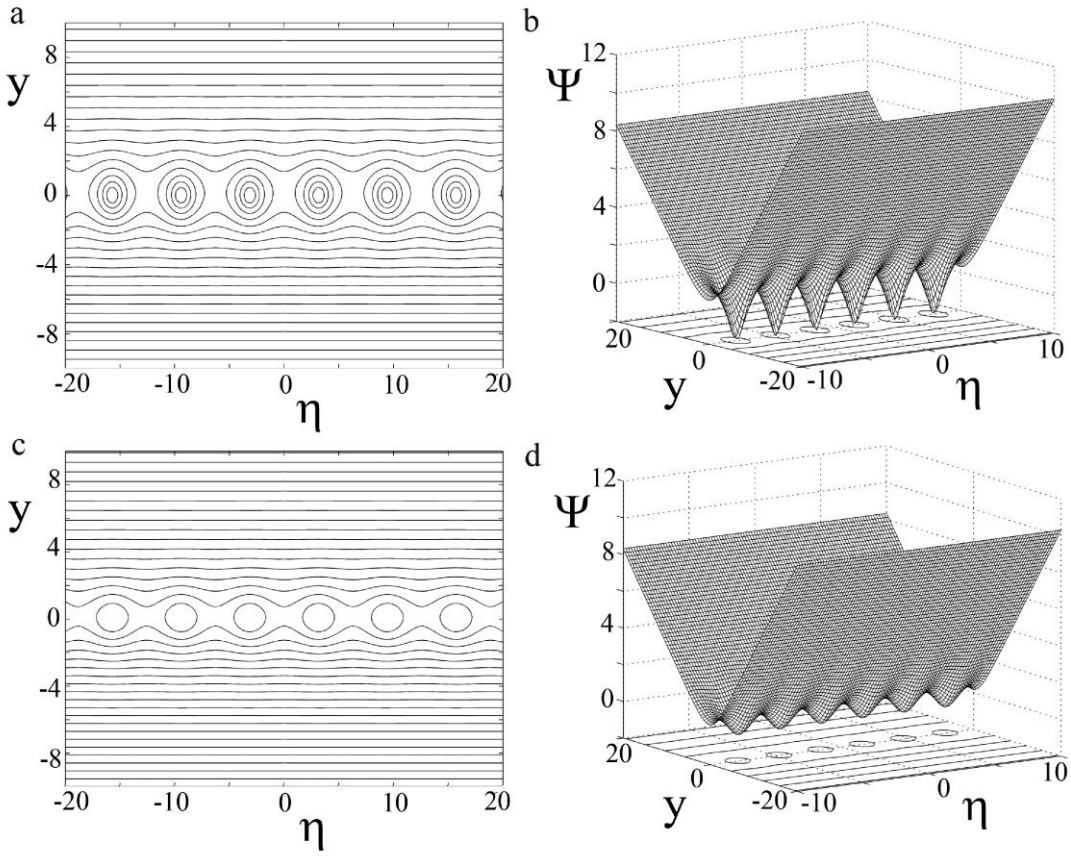

Figure 4. The level lines and relief of the stream function of vortex solution (55) in the moving system of coordinates to the parameters: a). $\psi_0^0 = 1$, U = 0.1, æ$_0$ = 0.5, κ = 1; b). $\psi_0^0 = 1$, U = 0.1, æ$_0$ = 0.5, κ = 1; c). $\psi_0^0 = 1$, U = 0.1, æ$_0$ = 0.9, κ = 1; d). $\psi_0^0 = 1$, U = 0.1, æ$_0$ = 0.9, κ = 1;

For magnetic field perturbation from (46) and (55), we can obtain the following estimation:

$$|h| \approx |\beta_H| \cdot d\,, \qquad (61)$$

valid for both the fast and slow modes. For the ionospheric conditions $|\beta_H| \approx 4 \times 10^{-11} m^{-1} s^{-1}$, thus using the estimations to carried out above, we my conclude that fast vortical motion generate magnetic pulsations $h^f \approx 10^{-4} T$, while in case slow Rossby-type vortical motions – $h^s \approx 10^{-5} T$.

Note that nonlinear stationary equation (47) also has an analytic solution in the form of a Larichev-Reznik cyclone-anticyclone dipole pair and other class of solitary solutions by different profiles of background shear flows (Petviashvili and Pokhotelov, 1992; Jovanovich et al. 2002; Aburjania, 2006; Aburjania et al. 2003; 2004; 2007).

5.2. Attenuation of the vortex streets in the dissipative ionosphere

In the dissipative approximation ($\Lambda \neq 0$), we switch to the above self-similar variables (η and y) and take into account the relationship $\partial / \partial \tau = -U \partial / \partial \eta$, which then holds. As a result, we can write Eqs. (1) and (2) as

$$-U \frac{\partial}{\partial \eta} \Delta \Psi + \beta \frac{\partial \Psi}{\partial \eta} + C_H \frac{\partial h}{\partial \eta} + \Lambda \Delta \psi - J(\Psi, \Delta \Psi) = 0\,, \qquad (62)$$

$$(C_H - U)\frac{\partial h}{\partial \eta} - \beta_H \frac{\partial \Psi}{\partial \eta} - J(\Psi, h) = 0. \tag{63}$$

Equation (63) has the solution

$$h(\eta, y) = \frac{\beta_H}{C_H - U}\Psi. \tag{64}$$

Substituting solution (64) into Eq. (62), take into account the expression (48) and rearranging the term, we arrive at a single nonlinear equation:

$$\left(D_\eta + \frac{\Lambda}{U}\right)\Delta\Psi = 0, \tag{65}$$

where

$$D_\eta = \frac{\partial}{\partial \eta} + \frac{1}{U}\left(\frac{\partial \Psi}{\partial \eta}\frac{\partial}{\partial y} - \frac{\partial \Psi}{\partial y}\frac{\partial}{\partial \eta}\right).$$

The equation (65) yield a solution as

$$\Psi = \Psi_0 \cdot \exp\left(-\frac{\Lambda}{\mathrm{U}}\eta\right). \tag{66}$$

Here the zero[th] order Ψ_0 is identified with solution (55) (Figure 2). The incorporation of dissipation effects has modified the solution of the dynamical non-linear differential equation. It can be seen from (66) that friction (or collision) is responsible for exponential decay of stationary nonlinear vortex structures in space. This street of vortices can be studied by plotting the stream line function $\Psi(\eta, y)$(Eqs. (66) and (55)). We have free parameters Ψ_0^0, κ and $æ_0$, and the velocity of movement of the structures U will be determine by (48).

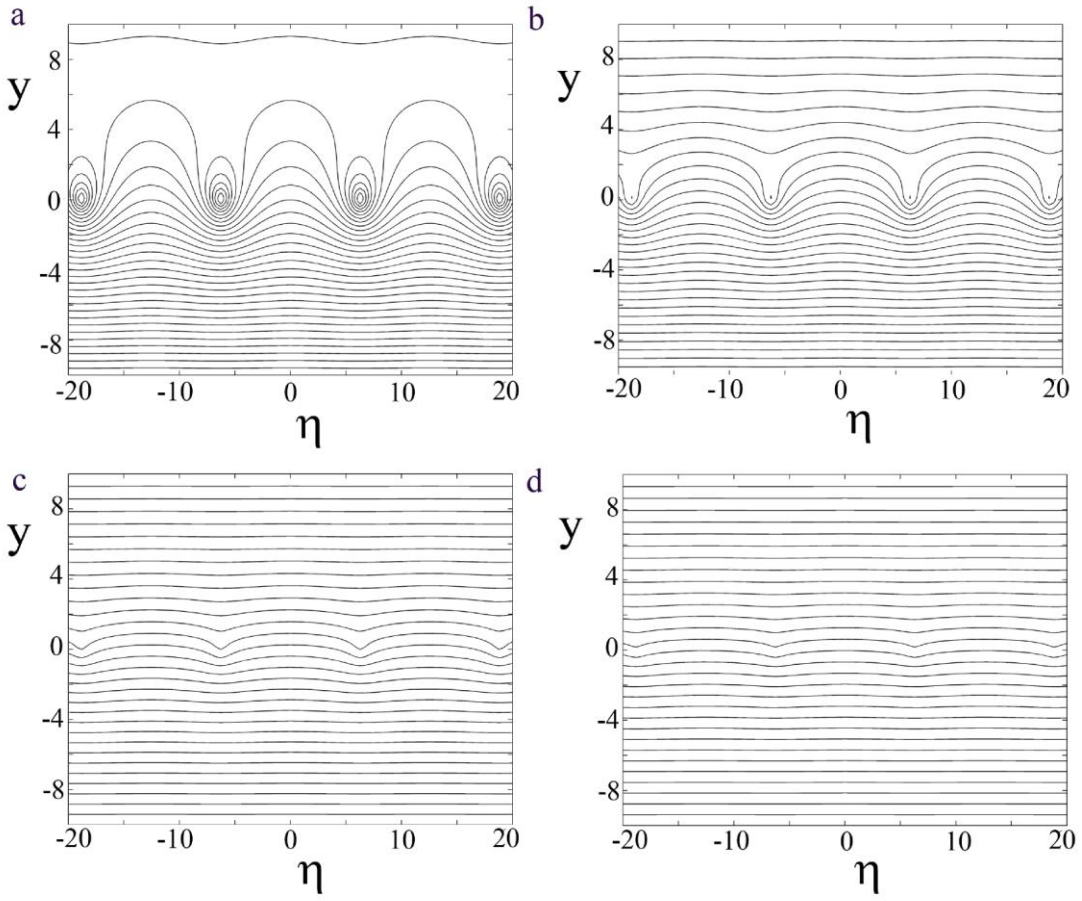

Figure 5. The level lines and relief of the stream function of vortex solution (55) in the moving system of coordinates to the parameters: a). $\psi_0^0 = 1$, $\mathrm{U} = 0.6$, $æ_0 = 0.2$, $\kappa = 0.5$; b). $\psi_0^0 = 1$, $\mathrm{U} = 1.5$, $æ_0 = 0.2$, $\kappa = 0.5$; c). $\psi_0^0 = 1$, $\mathrm{U} = 5$, $æ_0 = 0.2$, $\kappa = 0.5$; d). $\psi_0^0 = 1$, $\mathrm{U} = 10$, $æ_0 = 0.2$, $\kappa = 0.5$;

Figure3a shows the $\kappa = 0.5$ case and $\Psi_0^0 = 1$, $U = 0.1$, $æ_0 = 0.2$, while Figure 3c shows the $\kappa = 1$ case. Three dimensional plots for the same parameters are shown in Figure 3b and 3d. At decrease of the linear scales of the vortices (with increase of κ) the number of the vortices will increase in the given area of the medium and their amplitudes will decrease (Figure 3c, 3d).The reduction in κ causes a reduction in number of vortices, e.g., the $\kappa = 1$stream function plots six vortices (Figure 3c, 3d). We, therefore, note that the number of vortices increases with increasing κ, e.g. the formation of nonlinear structures is attributed to low frequency mode.

At decrease of the linear scale of the background wind inhomogeneity (increasing $æ_0$) the linear scales, amplitudes and steepness of peaks of the vortices decrease accordingly (Figure 4).

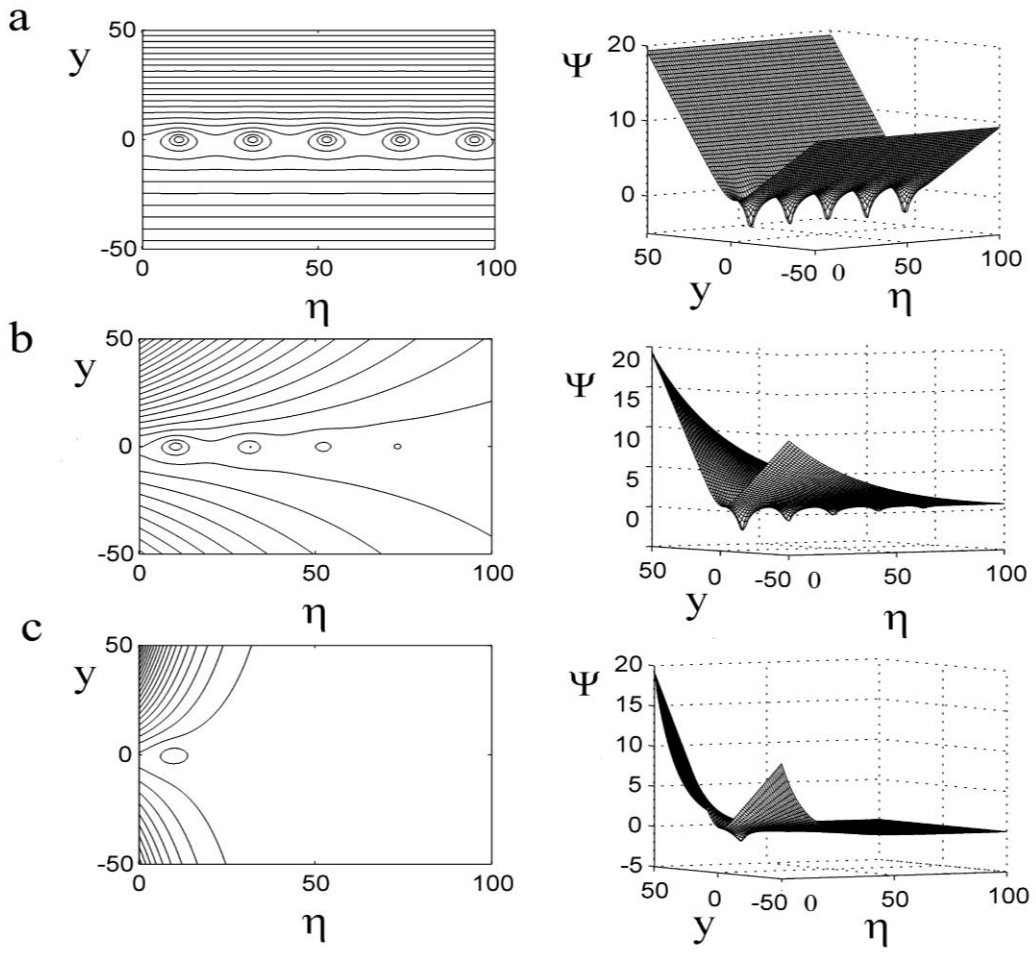

Figure 6. Spatial damping of the vortex structures (the level lines and relief of the stream function), calculated from formula (66) to the parameters: a). $\psi_0^0 = 1$, $U = 0.1$, $æ_0 = 0.2$, $\kappa = 0.3$, $\Lambda = 0.0000$; b). $\psi_0^0 = 1$, $U = 0.1$, $æ_0 = 0.2$, $\kappa = 0.3$, $\Lambda = 0.0025$; c). $\psi_0^0 = 1$, $U = 0.1$, $æ_0 = 0.2$, $\kappa = 0.3$, $\Lambda = 0.0100$;

The street of vortices is in almost stationary frame of reference, it disappears for higher frame velocity ($U > 1$), i.e. the contribution of logarithmic and hyperbolic trigonometric functions are no longer overcome by the contribution of linear term viz. Uy in (55) and, therefore, vortex formation is replaced by straight stream lines (Figure5). Due to increase of the translation velocity (U) of the structures and the background flows the scales and amplitudes of the generated vortices will decrease. In case of comparably high velocity background wind ($U > 1$) the vortex will not be generated at all and only the background flow will remain in the medium (Figure 5). Further, due to the nonlinear term, the velocity of dispersive waves must be greater than the phase velocity of a wave which resulted in a bending of the wave front and hence vortices start to form.

The street of vortex disappears in the space for high dissipation rate Λ (or collision frequency) (Figure 6). We credence that the dissipation effect has not permitted the vortex formation, but the topography of stream line function has been modified (Figure 6).

5.3. Relaxation of the vortex structures in the ionosphere

The real mechanism of dissipation in the atmosphere against the background of baroclinic, nonlinear and dispersive effects generates in the ionosphere moving spatial structures representing the equilibrium stationary solutions (54) and (55) of the governing magneto-hydrodynamic equations (1) and (2). For qualitative estimation of the evolution and the temporal relaxation of stationary vortex structures in the ionosphere, built in previous paragraphs, the dynamic equations (1) and (2) can be approximately written as the following Helmholtz's vortex transfer equation:

$$\frac{\partial}{\partial t}\nabla\times\boldsymbol{V} = \boldsymbol{P} - \Lambda(\nabla\times\boldsymbol{V}), \tag{67}$$

which describes the generation of nonzero vorticity $\nabla\times\boldsymbol{V}$ ($(\nabla\times\boldsymbol{V})_z = \Delta\Psi$) in the ionosphere under the action baroclinic vector $\boldsymbol{P}$ (source function) taking in to account the temperature contrasts in the form of advection of warm and cold, medium dispersion and influence of small nonlinearity. According to the observations (Gill, 1982; Pedlosky, 1982), vector $\boldsymbol{P}$ for low-frequency disturbances is a slowly varying function of time. In this case the vortex Eq. (67), with the initial conditions of Cauchy $\nabla\times\boldsymbol{V}\big|_{t=0} = 0$ (at the initial moment in the atmosphere there no vortices) has the bounded solution:

$$\nabla\times\boldsymbol{V} = \frac{\boldsymbol{P}}{\Lambda}\left(1-\boldsymbol{e}^{-\Lambda t}\right). \tag{68}$$

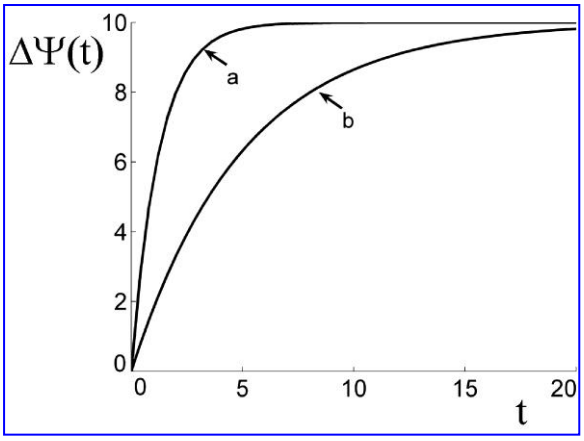

Figure 7. Relaxation of the vorticity of perturbations, calculated from formula (68) to the parameters: a). $\Lambda = 0.8$, $P/\Lambda=10$; b). $\Lambda = 0.2$, $P/\Lambda=10$.

Dissipative effects have an accumulative nature and its action becomes perceptible only after a certain interval. From Eq. (68) it follow that vorticity will increase linearly with time only at small time intervals ($t \ll 1/\Lambda$) under the action of baroclinicity and some other effects. After a certain time, when the dissipation effect reaches a specific value, vortex growth speed decreases (the vorticity growth rate decreases) and for the large intervals of time ($t \gg 1/\Lambda$) it tends to constant (equilibrium) value $\boldsymbol{P}/\Lambda$ (Figure 7).The value of dimensional time $T = 1/\Lambda \approx 10^5 s \geq 24$ hour can be called a relaxation time of non-stationary vortex street. Indeed, for the lower atmosphere relaxation time is of the order of twenty-four hours (Gossard and Hooke, 1975; Pedlosky, 1982) and consequently here large scale vortices must be long-lived. Stationary solution describes the equilibrium between baroclinicity and the dissipation effects ($\boldsymbol{P} = \Lambda(\nabla\times\boldsymbol{V})$). As a result, the dissipative structure is generated in the ionosphere in the form of stationary street of cyclones and anticyclones.

6. Conclusions

Thus, in the present article we have obtained the simplified system of nonlinear dynamical equations describing linear and nonlinear interaction of planetary electromagnetic ultra-low-frequency fast and slow wavy structures with zonal shear flow in the Earth's dissipative ionosphere. Along with the prevalent effect of Hall conductivity for such waves, the latitudinal inhomogeneity of both the angular velocity of the Earth's rotation and the geomagnetic field becomes essential. Due to spatial inhomogeneity of the Earth's rotation velocity fast and slow waves can be coupled. Such coupling results in an appearance of strong dispersion of these waves. Note that,

without this coupling the fast branches in the both ionospheric E and F-regions lose the dispersion property for both large and short wave-length perturbations.

Effective linear mechanisms are revealed, which account the transient pumping of shear flow energy into wave disturbance energy, an extreme intensification (by several orders) of wavy processes, self-organization of generated wavy disturbances into the nonlinear solitary vortex structures, dissipation relaxation of vortices and finally the conversion of perturbation energy to heat. A remarkable feature of the sheared flow is a reduction in the scales of wave perturbations in the linear regime due to the variation of the wave vector of the perturbations with time $k = k(\tau)$ and also due to the linear drift of the SFHs of the perturbations in wave number space and, accordingly, the energy transfer into small scales, i.e., into the dissipative region. The Linear intensification of EM ULF wave may take place temporarily, for certain values of the parameters of the medium, shear and waves. This makes an unusual way of shear flow heating in the ionosphere: waves draw up the shear flow energy and pump it through the linear drift of spatial Fourier-harmonics (SFH) in the space of wave numbers (subdivision of disturbance scales) to the damping domain. Finally, the friction, viscosity and inductive damping may convert this pumped energy to heat. The process is permanent and may lead to a strong heating of the medium. The heating intensity depends on the initial disturbance level and shear flow parameters.

The generation of the slow electromagnetic linear waves in the ionospheric E-region by the gradient of both geomagnetic field's, angular velocities of the Earth's rotation and inhomogeneous zonal wind was shown. Slow wave propagate in E-region along the latitudinal circles westward and eastward against a background of mean zonal wind and are the waves of Rossby type. The frequency of the slow waves vary in the diapason of $(10^{-4} \div 10^{-6})\,\mathrm{s}^{-1}$; period of these waves vary in the range from 2 hour to 14 day; wavelength is about 10^3 km and longer, the phase velocity has the same order as the local winds' do from a few to hundred of $\mathrm{m \cdot s^{-1}}$ ($V_p^s \approx (1 \div 100)\ \mathrm{m \cdot s^{-1}}$). The slow waves experience the strong attenuate by Rayleigh friction between the layers of the local atmosphere and the damping factor is $|\gamma^s| = \Lambda \sim 10^{-5}\, s^{-1}$. Though the attenuation would be weaker for longer large-scale waves with wavelength of about 10^4 km and the timescale of a week or longer. The linear slow waves perturb the magnetic field, which has the order of $h^s \approx \left|4\pi e N V_p^s \xi\right| / c$ (ξ - transversal shift of the charged particles). For the value of the phase velocity $V_p^s = 50\ m \cdot s^{-1}$ and $\xi = 1$ km, we have $h^s \approx 1$ nT. Perturbed magnetic field strength increases up to 20 nT, if transversal displacement of the system ξ =10 km and the phase velocity $V_p^s \sim 10^2\ \mathrm{m \cdot s^{-1}}$. Thus, the linear slow electromagnetic waves in the dynamo-region are accompanied by the noticeable micro-pulses of the geomagnetic field and have the same order as the micro-pulses caused by S_q currents in the same region. The slow waves are generated by the dynamo electric field $\boldsymbol{E_d} = \boldsymbol{V} \times \boldsymbol{H}_0 / c$. These waves, on seen, were observed in the experiments (Cavalieri et al. 1974; Manson et al. 1981; Sharadze et al. 1989; Zhou et al. 1997).

Generation of the linear fast planetary electromagnetic waves in the ionospheric E-region by the gradient of geomagnetic field, the Hall's effect and inhomogeneous zonal wind was established. These waves propagate along the latitude against a background of the zonal-mean flow westward and eastward at the speed of a few $\mathrm{km \cdot s^{-1}}$ ($V_p^f \approx (1 \div 7)\, km \cdot s^{-1}$) in the dynamo-region. The waves have the frequency of order of $(10^{-1} \div 10^{-4})\mathrm{s}^{-1}$; the periods are in the interval from 4 minutes to 6 hours; wavelength of about 10^3 km and longer. They attenuate weakly and $|\gamma^f| \sim 0.01\Lambda \sim 10^{-7}\, s^{-1}$. The essential micro-pulses of the geomagnetic field caused by the fast waves equal to $h^f \approx \left|2eNC_H \lambda^f\right| / c \sim 10^3$nT. They could be assumed as a new mode of the own oscillations in E-region of ionosphere. Frequencies and phase speeds of fast waves depend on density of the charged particles. Therefore, the phase velocities of fast disturbances in E-region of the ionosphere differ almost by one order of magnitude for daytime and nighttime conditions. High phase velocities, as well as their strong change between day and night preclude the identification of these disturbances with MHD waves. The fast waves are caused by oscillations of the electrons, completely frozen-in the geomagnetic field and are generated by the vortex electric field $\boldsymbol{E_v} = \boldsymbol{V_D} \times \boldsymbol{H}_0 / c$. These waves were observed in the experiments (Al'perovich et al. 1982; Sharadze et al, 1988; Burmaka et al, 2004; Georgieva et al, 2005).

It is established, that in the ionospheric F-region inhomogeneity of the geomagnetic field and inhomogeneous zonal wind generates fast planetary electromagnetic wave, propagating along the latitude circles to the east or to the west with phase velocity $V_p^f \approx (5 \div 50)$ km $\mathrm{s^{-1}}$. Frequency of waves is in limits

$(10 \div 10^{-3})s^{-1}$ and the waves are weakly damped with decrement $|\gamma^f| \approx 10^{-6} s^{-1}$. The period of perturbations varies in a range $(1 \div 110)$ s. Amplitude of geomagnetic micro pulsations, generated by these waves, is about $h^f \approx 10^3$ nT. These waves are new modes of eigen oscillations of F-region of the ionosphere. Such waves as magneto-ionospheric wave perturbations have been found out in experiments (Sharadze *et al* 1988, Sorokin 1988, Bauer *et al* 1995, Burmaka *et al* 2004, Georgieva *et al* 2005, Fagundas *et al* 2005).

The frequencies of the investigated waves vary in the band ω~ (10- 10^{-6}) s^{-1} and occupy both infrasound and ULF bands. Wavelength is λ~ (10^3 -10^4) km, period of oscillation is $T \sim 1\ \text{s} - 14$ days. The electromagnetic perturbations from this band are biological active (Kopitenko et al. 1995). Namely, they can play an important role as a trigger mechanism of the pathological complications in people having the tendency to hyper tensional and other diseases. Thus, these waves deserve great attention, as they are to be the significant source of the electromagnetic pollution of environment.

It is show, that at interaction with the inhomogeneous local wind the EM ULF wave perturbations can sufficiently increase own amplitude and energy and in their dynamics the nonlinear effects will be appeared. Dynamical competition of the nonlinear and the dispersion effects at the different layers of the ionosphere creates a favorable condition for self-organization of the EM ULF disturbances into nonlinear vortex structures. The self-localization of the planetary ULF waves into the long-lived solitary vortex streets in the non-dissipative ionosphere is proved in the basis of the analytical solution of the governed nonlinear dynamic equations. The exact stationary solution of these nonlinear equations has an asymptote $\psi \sim exp(-\kappa r)$ at $r \to \infty$, so the wave is strongly localized along the Earth surface. The translation velocity U of ULF EM vortices is very crucial which in turn depends on parameters β and β_{H}. From analytical calculation and plots we note that the formation of stationary nonlinear vortex street require some threshold value of translation velocity U (48) for both nondissipation and dissipation complex ionospheric plasma. For some large value of the background wind's spreading velocity ($U \geq 10$) the vortex structures may not be raised at all and only the background wind will be preserved in the medium (Figure 5). Number of vortices in generated nonlinear structures and a value of amplitudes of these vortices essentially depend on the size of the background wind's inhomogeneity – decreasing the latter – generated vortex's size and amplitude will automatically decrease (Figure 4). It's shown that the space and time attenuation can't resist the formation of the vortex structures, but affect the topographic features of the structures (Figure 6, Figure 7). The generated nonlinear vortex structures are enough long-live (> 24 hour) in dissipative ionosphere.

Depending on the type of velocity profile of the zonal shear flow (wind), the generated nonlinear long-lived vortex structures maybe represent monopole solitary anticyclone or cyclone, the cyclone – anticyclone pair, connected in a certain manner and/or the pure dipole cyclone – anticyclone structure of equal intensity, and/or the vortex street, or the vortex chains, rotating in the opposite direction and moving along the latitudinal circles (along the parallels) against a background of the mean zonal wind (see also - (Jovanovich et al. 2002, Aburjania et al. 2003; 2006; 2007)).

The nonlinear large-scale vortices generate the stronger pulses of the geomagnetic field than the corresponding linear waves. Thus, the fast vortices generate the magnetic field $h^f \approx 10^5\ nT$, and the slow vortices form magnetic field $h^s \approx 10^4\ nT$. The formation of such intensive perturbations could be related to the specific properties of the considering low frequency planetary structures. Indeed, they trap the environmental particles, and the charged particles in E- and F-regions of the ionosphere are completely or partially frozen into the geomagnetic field. That's why, the formation of these structures indicates at the significant densification of the magnetic force lines and, respectively, the intensification of the disturbances of the geomagnetic field in their location. Since, the number of the capture parcels is the order of the passed-by (transient), the perturbation of the magnetic field in the stronger faster vortices would be the same order as of the background field. On the earth surface located R_0 (($\sim (1 \div 3) \cdot 10^2$ km) below the region of the researching wave structure, the level of the geomagnetic pulses would be less by $exp(-R_0/\lambda_0)$ factor. λ_0 is the characteristic length of the electromagnetic perturbations. Since $\lambda_0 \sim (10 \div 10^2) R_0 >> R_0$ the magnetic effect on the earth would be less then in E- and F-regions, but in spite of this they are easily registered too.

We have defined the velocity diapason of propagation for vortical structures and show that vortices move faster than the corresponding linear waves. This means that if the source (for example, the above mentioned nonlinear vortex structure) moves along parallels at a velocity greater than V_p^{max}, the source does not come in resonance with the corresponding linear waves. Nonlinear vortices moving faster than the corresponding linear

waves can retain their non-linear amplitude, as far as they do not lose energy by radiation of linear waves. It means, that these sources can not excite a linear wave due to Cherenkov mechanism, and can retain its initial energy (Stepanyants and Fabrikant, 1992). Thus, these vortex structures can be generated, self-sustained and propagated with velocity $|U| > V_p^{max}$ along the horizontal in any direction.

The motion of medium particles in studied nonlinear vortex structures is characterized by nonzero vorticity $\nabla \times \boldsymbol{V} \neq 0$, i.e. the particle rotate in vortices. The characteristic velocity of this rotation U_c is of order of the vortex velocity U, $U_c \geq U$. In this case the vortex contains the group of trapped particles (the number of these particles is approximately the same as the number of transit particles); rotating, these particles move simultaneously with the vortex structure. Therefore, being long-lived objects, non-linear planetary-scale electromagnetic vortex structures may play an important role in transporting matter, heat, and energy, and also in driving the macroturbulence of the ionosphere (Aburjania, 1990; 2011). In particular, the vortex structures that play the role of "turbulent agents" can be treated as elements of the horizontal macroscopic turbulent exchanges in global circulation processes in the ionospheric E and F-layers. The coefficient of the horizontal turbulent exchange can be estimated from the Obukhov-Richardson formula (Monin and Yaglom, 1967): $K_T \approx 10^{-2} d^{4/3} m^2 s^{-1}$. Thus, for vortices with dimensions of about $d \sim 10^3 km$ at latitudes of about $\varphi = 50°$-55°, we obtain $K_T \approx 3 \times 10^6 m^2 s^{-1}$. This estimate (which can be regarded as an upper one) shows that, in the global exchange processes between high and low latitudes, the meridional heat transport from north to south in the ionospheric E and F-layers should be of macro turbulence nature (recall that, in the ionosphere, the polar regions are warmer than the equatorial region).

The fast and slow electromagnetic planetary waves are own degree of freedom of the E and F-regions of the ionosphere. Thus, first of all, the impact on the ionosphere from top or the bottom (magnetic storm, earthquake, artificial explosions and so on) induces (or intensify) the wave structures of these modes (Aburjania and Machabeli, 1998). At the certain strength of the source, the nonlinear solitary vortices would be generated (Aburjania, 1996), which is proved by the observations (Bengtsson and Lighthill, 1982; Chmyrev et al. 1991, Nezlin, 1999; Shaefer et al. 1999).

Hence, inhomogeneity of the Earth's rotation along the meridian, geomagnetic field and zonal prevailing flow (wind) can be considered among the real sources generating planetary ULF waves and vortex structures of an electromagnetic nature in the ionosphere. Such nonlinear structures can arise permanently and finally may constitute the strong vortical (or structural) turbulence in the medium (Aburjania, 1990; 2011; Aburjania et al . 2009).

Acknowledgements. The research leading to these results has received funding from the European Union Seventh Framework Programme [FP7/2007-2013] under grant agreement № 269198 - Geoplasmas (Marie Curie International Research Staff Exchange Scheme) and Shota Rustaveli National Science Foundation's Grant no 31/14.

Authors thank and honour the memory of George Aburjania and Archil Khantadze for their tremendous contribution to the development and solving of these problems.

References

[1] Aburjania, G. 2011, Formation of strong Stationary vortex turbulence in the terrestrial magnetosheat. Geomagn. Aeron. 51, 6, 720-729.

[2] Aburjania, G., Chargazia, Kh., Zelenyi, L. and Zimbardo, G. 2009, Model of strong stationary vortical turbulence in space plasmas. Nonlin. Proc. Geophys., 16, 11-22.

[3] Aburjania, G. and Chargazia, Kh. 2007, Dynamics of the large-scale ULF electromagnetic wave structures in the ionosphere. J. Atmos. Sollar-Ter. Physics, 69, 2428-2441.

[4] Aburjania, G., Khantadze, A. and Kharshiladze, O. 2006, Mechanism of planetary Rossby wave amplification and transformation in t he ionosphere with an inhomogeneous zonal smooth shear wind. J. Geophys. Res., 111 A09304 doi: 10.1029/2005JA01/567.

[5] Aburjania, G. 2006, Self-Organization of Nonlinear Vortex Structures and Vortex Turbulence in Dispersive Media. KomKniga, Moscow (in Russian).

[6] Aburjania, G., Chargazia, Kh., Jandieri, G., Khantadze, A. and Kharshiladze, O. (2004). On the new modes of planetary-scale electromagnetic waves in the ionosphere. Ann. Geophys., 22, 4, 508-517.

[7] Abururjania, G., Jandieri, G. and Khantadze, A. (2003). Self-organization of planetary electromagnetic waves in E-region of the ionosphere. J. Atmos. Sollar-Ter. Physics, 65, 661- 671.
[8] Aburjania, G., Khantadze, A. and Kharshiladze, O. (2002). Nonlinear planetary electromagnetic vortex structures in the ionosphere F-layer. Plasma Phys. Rep., 28, 7, 586-591.
[9] Aburjania, G. and Machabeli, G. (1998). Generation of electromagnetic perturbations by acoustic waves in the ionosphere. J. Geophys. Res. A, 103, 9441-9447.
[10] Aburjania, G. (1996). Self-organization of acoustic-gravity vortices in the ionosphere before earthquake. Plasma Phys. Rep., 22, 10, 954-959.
[11] Aburjania, G. (1990). Structural turbulences and diffusion of plasmas in the magnetic traps. Plasma Phys. Rep., 16, 1, 70-76.
[12] Al'perovich, L. and Fedorov, E. (2007). Hydromagnetic Waves in the Magnetosphere and the ionosphere. Sprimger.
[13] Al'perovich, L., Drobgev, V., Sorokin, V. et al. (1982). On the midlatitude oscillations of thegeomagnetic field and its connection to the dynamical processes in the ionosphere. Geomag. Aeron., 22, 5, 797-802.
[14] Bengtsson, L. and Lighthill, J. (Edits.). (1982). Intense Atmospheric Vortices. Springer-Verlag, Berlin –Heidelberg.
[15] Burmaka, V. and Chernogor, L. (2004). Clustered-instrument studies of ionospheric wave disturbances accompanying rocket launches against the background of non-stationary natural processes. Geomagn. Aeron., 44, 3, 518-534.
[16] Cavalieri, D., Deland, R., Poterna, J. et al. (1974). The correlation of VLF propagation variations with atmospheric planetary-scale waves. J. Atmos. Terr. Phys., 36, 561-574.
[17] Chagelishvili, G., Rogava, A. and Tsiklauri, D. (1996). The effect of coupling and linear transformation of waves in shear flows. Phys. Rev. E, 53, 6028-6031.
[18] Cmyrev, V., Marchenco, V., Pokhotelov, O. et al. (1991). Vortex structures in the ionosphere and magnetosphere of the Earth. Planet Space Sci., 39, 1025-1030.
[19] Fagundes, P., Pillat, V., Bolzan, J. et al. (2005). Observation of F-layer electron density profiles modulated by planetary wave type oscillations in the equatorial ionospheric anomaly region. J. Geophys. Res., 110 A, 1302.
[20] Georgieva, K., Kirov, B., Atanasova, D. and Boneta, A. (2005). Impact of magnetic clouds on the middle atmosphere and geomagnetic disturbances. J. Atmos. Sollar-Terr. Phys., 67, (1,2), 163-176.
[21] Gershman, B. N. (1974). Dynamics of the Ionospheric Plasma. Nauka, Moscow (in Russian).
[22] Gill, E.: Atmosphere-Ocean Dynamic. Academic Press, New York, London, Paris.
[23] Gossard, E. and Hooke, W. (1982). Waves in Atmosphere. Elsevier, Amsterdam 1975.
[24] Haykovicz, L. A. (1991). Global onset and propagation of large-scale traveling ionospheric disturbances as a result of the great storm of 13 March 1989. Planet Space Sci., 10, 583- 593.
[25] Jovanovich, D., Stenflo, L. and Shukla, P.K. (2002). Acoustic-gravity nonlinear structures. Nonl. Proc. Geophys., 9, 333-339.
[26] Kamide, Y. and Chian, C.-L. (2007). Handbook of the Solar-Terrestrial Environment. Springer-Verlag, Berlin-Heidelberg.
[27] Kelley, M. C. (1989). The Earth's Ionosphere, Plasma Physics and Electrodynamics. Academic Press Inc., San Diego, California.
[28] Kopitenko, Yu. A., Komarovskikh, M. I., Voronov, I. M. and Kopitenko, E. A. (1995). Connection between ULF electromagnetic litospheric emission and extraordinary behavior of biological system before the earthquake. Biofizika, 40, 1114-1119 (in Russian).
[29] Magnus, K. (1976). Schwingungen, Teubner, Stuttgart.
[30] Mallier, R. and Maslowe, S. A. (1993). A row of counter-rotating vortices. Phys. Fluids., 5, 1074-1075.
[31] Manson, A. H., Heek, C. H. and Gregory, J. B. (1981). Winds and waves (10min-30day) in the mesosphere and lower thermosphere at Saskatoon. J. Geophys. Res., 86, 10, 9615-9625.
[32] Monin, A. S. and Iaglom, A. N. (1967). Statistical Hydrodynamics V 2. Nauka, Moscow (in Russian).
[33] Nezlin, M. V. (1999). Rossby solitary vortices on giant planets and in the laboratory. CHAOS, 4, 187-202.
[34] Pedlosky, J. (1982). Geophysical Fluid Dynamics. Springer-Verlag, New York.
[35] Petviashvili, V. I. and Pokhotelov, O. A. (1992). Solitary Waves in Plasma and in the Atmosphere. Gordon and Breach Reading.

[36] Pokhotelov, O. A., Parrot, M., Pilipenko, V. A. et al. (1995). Response of the ionosphere to natural and man-made acoustic sources. Ann.Geophys., 13, 1197-1210.
[37] Reddy, S. C., Schmid, P. J. and Hennigston, D. S. (1993). Pseudospectra of the Orr-Sommerfeld operator. SIAM J. Appl. Math., 53, 15-23.
[38] Shaefer, L. D., Rock, D. R., Lewis, J. P. et al. (1999). Detection of Explosive Events by Monitoring Acousticaly-Induced Geomagnetic Perturbations. Lawrence Livermore Laboratory.
[39] Sharadze Z S, Mosashvili N V, Pushkova G N and Yudovich L A, 1989 Long-period wave disturbances in E-region of the ionosphere *Geomagn. Aeron.* 29 (6) 1032-1034
[40] Sharadze, Z. S., Japaridze, G. A., Kikvilashvili, G. B. et al. (1988). Wavy disturbances of non-acoustical nature in the midlatitude ionosphere. Geomagn. Aeron., 27, 3, 446-451.
[41] Sorokin, V. M. (1989). Wave processes in the ionosphere associated with geomagnetic field. Izv. Vuzov. Radiofizika, 31, 10, 1169-1179 (in Russian).
[42] Stepanyants, Y. A. and Fabrikant, A. L. (1992). Features of the Cherenkov emisión of drift waves in hydrodynamics and in plasma. Sov. Phys. JETP, 102, 5, 1512-1523.
[43] Trefenthen, L. N., Trefenthen, A. E., Reddy, S. C. and Driscoll, T. A. (1993). Hydrodynamic stability without eigenvalues. Science, 261, 578-584.
[44] Zel'dovich, Ya. B. and Mishkis, A. D. (1972). Elements of Applied Mathematics. Nauka, Moscow (in Russian).
[45] Zhou, Q. H., Sulzer, M. P. and Tepley, C. A. (1997). An analysis of tidal and planetary waves in the neutral winds and temperature observed at low-latitude E-region heights. J. Geophys. Res., 102, 11, 491-505.

(Received in Final Form 26 June 2013)

ამინდის შემქმნელი ულტრა დაბალი სიხშირის ელექტრომაგნიტური სტრუქტურები წანაცვლებით დინებიან იონოსფეროში

ოლეგ ხარშილაძე, ხათუნა ჩარგაზია

აბსტრაქტი

ნაშრომი ეძღვნება ულტრადაბალი სიხშირის ელექტრომაგნიტური ტალღური სტრუქტურების ტრანზიენტულ ზრდას და შემდგომ წრფივ და არაწრფივ დინამიკას მბრუნავ დისიპაციურ იონოსფეროში, რომელიც განპირობებულია არაერთგვაროვანი ზონალური ქარების (წანაცვლებითი დინება) არსებობით. პლანეტარული უდს ელექტრომაგნიტური ტალღები გენერირდებიან იონოსფერულ გარემოსა და სივრცით არაერთგვაროვანი გეომაგნიტური ველის ურთიერთქმედებით. ნაპოვნია დიდმასშტაბიანი უდს ელექტრომაგნიტური ტალღების გენერაციის და შემდგომი გაძლიერების ეფექტური წრფივი მექანიზმი წანაცვლებით დინებებში. ნაჩვენებია, რომ ეს ტალღური შეშფოთებები ეფექტურად ქაჩავენ ენერგიას წანაცვლებითი დინებებისგან და ზრდიან საკუთარ ენერგიას და ამპლიტუდას (რამდენიმე რიგით) დროის მიხედვით ალგებრული წესით. ამპლიტუდის ზრდასთან ერთად ირთვება თვითლოკალიზების მექანიზმი და ეს შეშფოთებები თვითორგანიზდებიან არაწრფივი განმხოლოებული, ძლიერად ლოკალიზებული უდს ელექტრომაგნიტური გრიგალური სტრუქტურების სახით, განპირობებული შეშფოთებათა პროფილის არაწრფივი გრეხით. წანაცვლებითი ქარის სიჩქარის პროფილზე დამოკიდებულებით არაწრფივი უდს ელექტრომაგნიტური სტრუქტურები შეიძლება იყოს მონოპოლური, გრიგალური ჯაჭვი ან გრიგალური ბილიკი არაერთგვაროვანი ზონალური ქარის ფონზე.

ანალიზური და რიცხვითი გამოთვლებიდან ნათელი ხდება, რომ სტაციონარული გრიგალური სტრუქტურების წარმოსაქმნელად საჭიროა სიჩქარის გადატანის რაიმე ზღვრული მნიშვნელობა ორივე დისიპაციური და არადისიპაციური იონოსფერული პლაზმისათვის. შესწავლილია გრიგალების ჩაქრობის დროითი და სივრცითი მახასიათებლები. შეფასებულია გრიგალის არსებობის მახასიათებელი დრო დისიპაციური იონოსფეროში. ხანგრძლივ გრიგალურ სტრუქტურებს გადააქვთ ჩაჭერილი ნაწილაკები, სითბო და ენერგია. ამრიგად, განსახილველი სტრუქტურები შეიძლება წარმოადგენდნენ უდს ელექტრომაგნიტურ ტალღურ მაკროტურბულენტობის სტრუქტურულ ელემენტებს იონოსფეროში.

Ультранизкочастотные электромагнитные погодаобразующие структуры в ионосфере со сдвиговым течением

Олег Харшиладзе, Хатуна Чаргазиа

Абстракт

Работа посвящена изучению транзиентного нарастания и дальнейшей линейной и нелинейной динамике ультранизкочастотных (УНЧ) планетарных электромагнитных (ЭМ) волн в диссипативной врашающейся ионосфере в присутствии неоднородного зонального ветра (сдвигового течения). Планетарные ЭМ УНЧ волны генерируются при взаймодействии ионосферной среды с пространственно неоднородным геомагнитным полем. Анализируется эффективный линейный механизм генерации и усиления планетарных ЭМ волн в сдвиговых течениях. Показано, что эти волны эффективно черпают энергию сдвигового течения и существенно увеличивают свою амплитуду и энергию по алгебрайческому закону. С увеличением амплитуды возмущений включается нелинейный механизм самолокализации и эти возмущения самоорганизуются в виде сильнолокализованных УНЧ ЭМ нелинейных уединенных вихревых структур, обусловленных нелинеыным укручением профиля возмущения. В зависимости от вида профиля скорости сдвигового течения нелинейные структуры могут быть как чисто монопольным вихрем, так и вихревой дорожкой и вихревой цепочкой на фоне неоднородного зонального ветра. Как показывают аналитические и численные исследования, для формирования стационарных нелинейных вихревых структур необходима опредиленное значение скорости переноса как в диссипативной так и в недисипативной ионосферной плазме. Изучена временные и пространственные характеристики затухания вихрей. Дана оценка характерного времени затухания вихря в диссипативной ионосфере. Долгоживущие вичревые структуры переносят захваченные частици, тепло и энергию в среде. Таким образом рассмотренные структуры могут быть структурными элементами УНЧ ЭМ макротурбулунтности в ионосфере.

Journal of the Georgian Geophysical Society,
Issue B. Physics of Atmosphere, Ocean and Space Plasma, v.16b, 2013, pp 111-117

Concerning Issue of Substance Radiation

O. Lomaia

M. Nodia Institute of Geophysics

Abstract

In the article are examined tests, conducted for study of the phenomenon "of quantum behavior" of the electrons in experimental physics.

Has been expressed a supposition that any type radiation of the substance, including light, comprises of two constituent parts: radial and wave radiation. They are variants of qualitative matter and energy, which spread in space with a great speed without mingling in each other. Radiation doesn't comprise of charged particles having mass of immobility. Their occurrence takes place during propagation of radiation in space.

Electron is a particle and not a wave-particle as this is stated by leading scientists of quantum mechanics.

As it is known, a substance being in a certain state, has ability to radiate energy, field having electromagnetic qualities or substance stream (or simultaneously both) and also in a different conditions – to absorb energy and modify.

All good of the modern civilization (radio transistor, television, computer, metro and all transport facilities working on current and other) became possible after was ascertained that electromagnetic forces transmit in space by means of fields and variable magnetic field causes variable electric fields in space (and vice-versa).

Modern physics, in the theory of elementary particles, ascertained that even when neither particle is found in space, vibrations of electromagnetic field take place; in the vacuum appear and disappear elementary, so called virtual particles, which in certain conditions have ability to transform into real particles. And modern quantum electrodynamics already describes a process of light radiation and absorption by the electrons being in the atom composition.

Did physics come to such important result? As it is known light represents a minor, but an important part of broad spectrum of substance radiation.

During several centuries the scientists were trying to determine what does light represent – corpuscles or waves. Over the time of the entire history of science development opinion concerning nature of light was periodically changing. M. Planck's discovery of quantum of energy and action at the frontier of XX century to a certain extent changed opinions on light, but dualism in this issue has not been exterminated to the end. Corpuscules were changed by light quantum - photons. Scientists could examine events concerning propagation of light only from the wave standpoint and light influence on substance (photoeffect, Compton event) was being defined only on the basis of opinion concerning corpuscules and photons [1. 2].

Photon is a quantum of electromagnetic field – elementary particle, participating only in electromagnetic interaction and does not participate in a weak and strong interaction. Thus, a certain unusual picture is obvious: one and same object (light or γ radiation) simultaneously

behaves as a particle so as a wave. De Broglie supposed: as light waves have qualities of the particles, it's possible that particle electron has a wave quality, i.e. it, as light, is characterized by dualism [3]. Many physicists accepted a wave-particles reality. Though it wasn't easy because as we know, wave is indeterminable in space and a particle is concentrated at the point. But, it was evident that these incompatible modes together were giving a full reflection of microworld reality [2].

There appeared a standpoint that quantum event doesn't subordinate to the ordinary logic. Heinzerberg in the theories reflecting microworld brought in algebra of matrix graphs, on which is written probability of events and not any values reflecting an event. He relied on the conception of electron as a particle and processes, as quantum interruptibility [2]. E. Schrodinger selected another way. He created wave mechanics for the microworld, which he described by ordinary order of mechanics description: he was conceiving an electron as a wave and vibrations - as continuous process.

Exists standpoint concerning quantum mechanics that by using probability we beautify our personal uncertainty in circumstances and ignorance of nature history. And nature itself really knows to absolute precision. Classical physics never had doubt about it. [4]

Nils Bohr in scientific disputes with the colleagues often indicated: "It's time to come to an agreement that we do not understand something important!" [4]. By bringing in a complementation (complementarity) principle to the microworld physics, N. Bohr attempted to make incomprehensible clear. He stated that from the classical standpoint, qualities with difficulty connecting with the reality do not exclude but fill each other.

And Heinzerberg with the same purpose mathematically deduced a law of correlation of ambiguity, which is equal to the statement that nature is not at all exact [2. 3].

Author of the present article considers that he has enough solid foundation to express the following opinion: it's the physicists' opinion on existence of wave particles in nature, in particular, conception of electron as of wave-particle, does not correspond to the facts, as they rely on the incorrect analysis of the experimental results, which is caused by difficult theory existing on light nature. We shall attempt, to the extent possible, to confirm this consideration. We consider that at the initial stage, for this will be enough to consider many tests conducted by the physicists in the past with the purpose of study of the electron behavior and conclusions inferred proceeding from them. "Feynman's lectures on physics" will assist us in this [5]. Chapter 37 of the book under the title "Quantum behavior" starts with detailed examination of the tests conducted by bullets, waves and electrons and analysis of the received results. Physicists believed that for comprehension of the electron behavior is necessary to opposite with them a behavior of solid particles and water waves. That is why they used first one then second conception to ascertain what would happen in certain conditions.

Common scheme of the above mentioned tests was as follows. Researchers in different experiments used sources of solid particles, waves and electrons (machine gun in case of solid particles, water launder and waves "source" – object which vibrates by means of small engine in perpendicular direction of the water surface and causes sphere waves in it – in case of water waves and electronic ejector – in case of electrons). Proper flows received from them were preceded by impermeable wall; in the middle part it had two clefts of identical size situated not so far from each other, in which flow, coming from the source, ran without obstacles. An absorbing structure was placed after the wall. In the test conducted by the bullets, the role of the absorber was fulfilling breastwork, in the experiment conducted on water waves – sand bar, in electrons test – metal plate. A detector (sand box, waves' height (intensity) measurer and

particles counter (for instance Geiger counter) was fastened to them. It was possible to move a detector along the wall and ascertain probability of hit of the substances under research in points, distant from its centre by various distances. (In case of water waves was interesting determination of distribution of the waves' intensity on the axle).

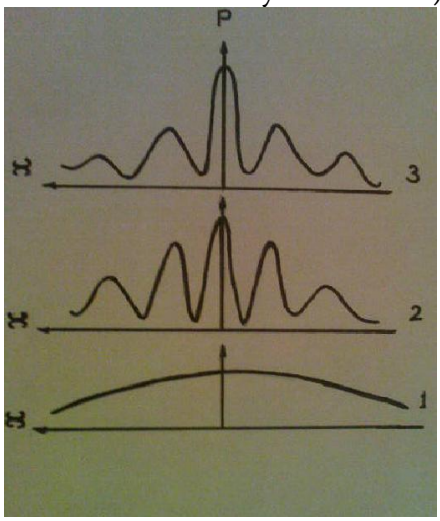

Fig. 1

On figure 1 are given results of the conducted research – received corresponding curves.

Received curves apply to two types; first type curve is received in case when interference does not have place in the test. Second type curve (2) in case of water waves is received when after the waves come through two clefts takes place diffraction and interference. Curve 3 received in the issue of the test conducted with electrons turned out to be similar of the waves and curve received in case of the waves is similar of the curve 2, i.e. electrons revealed wave nature and gave us interference picture. On the basis of the examined result was made conclusion that electron is "wave-particle". After much discussions, concerning how could electrons give received picture of distribution on absorbing surface, the test was repeated with the slight difference that behind the first wall, between two clefts, was placed a source of strong light so that to precise ways of electrons movement. It is known that electric charge has a quality to disperse light fallen on it. That is why light dispersed by electron falls in to the observer's eye and the latter will see where the electron passed. Was received unexpected result: curve 3 changed type and resembled curve 1. When lamp was turned off, again appeared interference picture, curve 3 resembled curve 2. Was made a conclusion that electron, when it is observed, behaves in other way and it is possible that "electron is something very delicate". "It is not within our power to explain how it works" – says Feynman, "we just can tell you what did the tests show" [5].

Heinzerberg admitted that in the discussed test is revealed a principle of indefiniteness. Feynman writes in his lectures: "Complete theory of quantum mechanics, which we use today during description of atoms and i.e. entirely substances, depends on correctness of a principle of indefiniteness, but, if anytime we will be given a possibility "to destroy it, quantum mechanics will start giving non-agreed results and we will be forced to exclude it from the row of correct, proper theories on nature events". And one more pessimistic conclusion "from the lectures": "no one has yet found solution of this puzzle (here are supposed results of the last examined test, author's note). Thus, now we are forced to limit ourselves by probability calculation. We say "today", but doubt is serious that all this is already constant and cracking this nut is not within the power of a human's teeth as such is nature of the objects".

Partially differing author's opinion is offered in this article for consideration concerning

the nature of light, also the events related to light and some puzzles resulting from the aforementioned experiments, in particular the behavior of electrons, which "is not like anything" according to the physicians' opinion.

In classical science it was considered that physics studies the events, where "the essence of substance is not changed", although, yet in the seventeenth century I. Newton in his "optics" together with other significant views was paying attention to the issue of light and substance interaction, he wrote: "can light turn into substance and vice versa ?". As for modern physics, it studies the events, during occurrence of which "the essence of substance" is changed more deeply, than during chemical reactions. Such is a transformation of electromagnetic radiation into particle, which has non-zero immobility mass. The test has shown that the photon of significantly fast (more than the determined amount) vibration is transformed into a substance - positive and negative electrode.

On the basis of the considered in the article experiments, and taking into account the opinions, stated by the leading scientists of classical and modern physics concerning the nature of light and related to it events, it is possible to draw a conclusion as follows.

Any kind of radiation of substance, and inclusive of light, is of a difficult composition. It contains two parts simultaneously: radial and wavy radiation. They represent two different kinds of matter and energy. They include some charged particle of immobility mass, therefore it is proper to talk about double character of radiation - wavy and radial.
Radiation is spread in the space at the known speed c=300 000 km/sec.

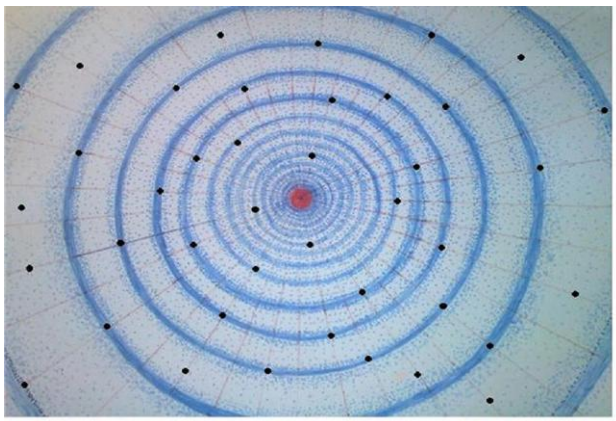

Fig. 2

Schematic figure of light waves and rays.

On the figure 2 is given the aforementioned scheme of propagation of light. At those points of the space, where the ray crosses the ridge of wave, which possesses maximal meaning of energy, by adding of these two energies (radial and maximal wavy) are created the conditions, in order to originate a solid, charged particle (or through hardening a virtual particle, or through discharging an electrode from any atom). Probably, they would not have an initial speed (or it would be smaller than the speed of light), and they would be easily gripped by the ridge of light wave (like a rake on the ridge of sea wave) . Therefore, the trajectory of electron movement will get a wave form, i.e. the electron will reveal the feature, which it does not possess as usual. This can explain a diffractional picture of the electrode movement after passing two gaps, obtained in the aforementioned tests. Therefore, the conclusion is drawn as

follows: an electron is a particle and it is not "a wave-particle" or as it has been called by the scientists "microcentaur", which surprised the physicians of the twentieth century by its incomprehensible movement.

E. Schrodinger stated that "a moving particle is nothing but foam on wavy radiation". It is difficult not to remember the issues, which were considered by N. Bore due to the definition of "wave-particle", brought in physics: "may be the nature does not need certain initial conditions for its existence on the micro-level?" and one more - "aren't they "coordinate-void"?". The famous physicians in their debates and discussions tried to approach the truth about the movement of those charged particles, which showed up in the related to light events.

Let's remember I. Newton's idea on the nature of light: "I think that light is something that is differently propagated from luminous body. We can assume that light is a material emanation or movement, or an impulse, which causes movement, or something else... I admit only, that light consists of rays, which are different from each other by circumstances, amount, form or strength, as well as sand granules and lake waves differ". By the contemporaries' presenting of I. Newton, light atoms differ from substance atoms only by "rapidity" and "smallness". As S. I. Pavlov informs us, later I. Newton put forward a compromise hypothesis using the priorities of emissive and wavy ideas. I.E. Newton's true conception on light was the merging of corpuscle and wave faces. Modern physics has come to an analogical conclusion; light represents the merging of photons and waves. Thereby, the ideas stated by us concerning the nature of light should not be unacceptable for the modern physicians.

Taking into account all the aforementioned opinions, let's consider the experiment conducted for studying the behavior and nature of electrons, the result of which has created a big puzzle for the physicians and led them to the conclusion that we will never explain why is happening the event, which has occurred during the test: why was changing the curve, reflecting the allocation of electrons, on the electrons absorbing plate as a result of the bulb's switch on and off , and why was it receiving the face, characterizing sometimes solid particles and sometimes waves.

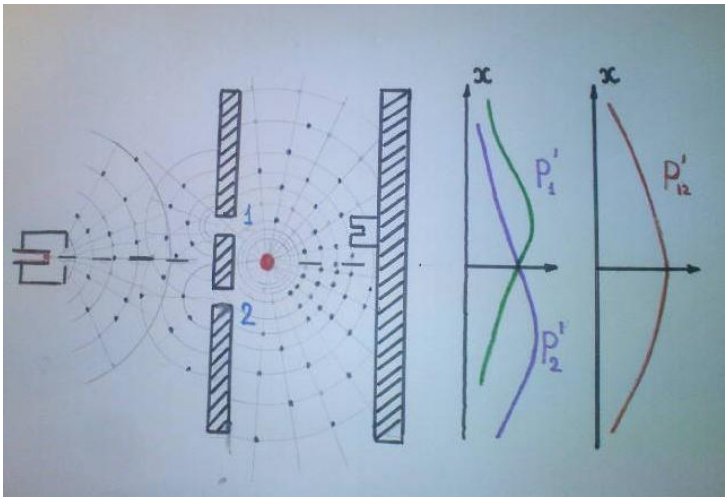

Fig. 3

The picture, depicting the scheme and the renewed results' analysis of the experiments, conducted for studying the behavior of electrons.

On the figure 3 is given the scheme of these experiments. It represents a tungsten wire, placed in the metal box, which is warmed by current. The front side of the box has a hole. Negative current is led to the wire, and positive current is led to the box. As the experimentators assume, the wire radiates electrons upon its heating, which by affecting the box walls obtain rapidity and some of them break out of the hole. Electrons have got a certain speed, at which they move and when they approach the front wall of the box with two holes, they break out of them and reach a detector, i.e. the counter of charged particles. As it was mentioned above, the curve of electrons allocation on X axis appeared to be depicting the interference.

According the aforementioned assumption, in the electron weapon from the tungsten wire, upon its shot, will radiate light as waves and rays, and not electrons. They appear in the space upon propagation of light on the ridge of wave and move together with this ridge. Thus, along their X axis, the curve of allocation will receive a face of wave, i.e. it will be depicting the interference.

When the aforementioned experiment was repeated with the difference that between the gaps and the absorbing walls was placed the source of strong light, it showed own picture of electrons' allocation on the absorbing walls by its radiation and emerged electrons. As the light waves did not break into two different gaps, they did not undergo interference and non-interferential picture was obtained. The second source of light was stronger that the first one, it was better than the first one and covered the interferential picture, received from it. Moreover, the direction of the propagation of lights waves and rays in the space, existing between the first and second sources, is opposite to each other and thus the electrons, coming from the first source could possibly not reach the counter.

Hopefully, on the basis of the aforementioned hypothesis it would be possible to explain the results of a number of other experiments and to formulate a new theory on the nature of light.

The fact that the substance, existing in a certain condition radiates energy, which in its turn, upon propagating in the space, affects the virtual particle, emerging from vacuum, and creates a new solid particle possessing charge and immobility mass - electron, really deserves the physicians' attention. It is not excluded that better studying of these events will lead us to the source of origin of world and evolution.

References

[1] Ф.Э.С. Изд. “Советская Энциклопедия” М. 1962
[2] Мигдал А. Б. “Квантовая физика для больших и маленьких“ Изд “Наука“, М. 1989
[3] В. Крейчи, “Мир глазами современной физики“ Изд. “Мир“, М. 1984
[4] Д. Данин, “Годы сбывщихся надежд “. В кн. “Пути в незнаемое“. Изд. “ Советский писатель“ М. 1987
[5] Р. Фейнман, Р Лейтон, М. Сэндс, “Фейнмановские лекции по физике“ Изд. “Мир“, М. 1976
[6] ივანე ვაშაკიძე, გივი ნიკობაძე. „თანამედროვე ფიზიკა ყველასთვის“. თბ. უნივერს. გამომცემლობა. თ. 1999.
[7] С. И. Вавилов, “Исаак Ньютон“ Изд. АН СССР М. 1961.
[8] С. И. Вавилов, “Ньютон и Современность“. В сб. “Исаак Ньютон“ М. 1943.

ნივთიერების გამოსხივების საკითხისადმი

ო. ლომაია

რეზიუმე

სტატიაში განხილულია ექსპერიმენტულ ფიზიკაში ელექტრონების „კვანტური ქცევის“ ფენომენის შესასწავლად ჩატარებული ცდები.

გამოთქმულია ვარაუდი, რომ ნივთიერების ნებისმიერი სახის გამოსხივება, და მათ შორის სინათლე, შეიცავს ორ შემადგენელ ნაწილს: სხივურ და ტალღურ გამოსხივებებს. ისინი ნატიფი მატერიისა და ენერგიის ნაირსახეობებია, რომლებიც ვრცელდება სივრცეში დიდი სიჩქარით ერთმანეთთან შეურევლად. გამოსხივება არ შეიცავს დამუხტულ, უძრაობის მასის მქონე ნაწილაკებს. მათი წარმოქმნა ხდება სივრცეში გამოსხივების გავრცელებისას.

ელექტრონი არის ნაწილაკი და არა ტალღა-ნაწილაკი, როგორც ამას აცხადებენ კვანტური მექანიკის წამყვანი მეცნიერები.

К вопросу о природе излучения

О. Ломая

Резюме

В статье рассмотрены опыты, проведенные в экспериментальной физике с целью изучения "квантового поведения" електронов. Высказано предположение о том, что всякого вида излучение и в том числе свет, состоит из двух составляющих частей: лучевого и волнового излучения. Они представляют собой два различных вида тонкой материи и энергии. Они распространяются в пространстве с большой скоростью не смешиваясь друг с другом. Излучение не содержит в себе заряженных, имеющих массу покоя частиц. Они возникают при распространении излучений в пространстве. Электрон является частицей, а не волно- частицей, как это объявляют ведущие ученые квантовой механики.

Journal of the Georgian Geophysical Society,
Issue (B) Physics of Atmosphere, Ocean, and Space Plasma, v. 16, 2013, pp.118-127

On the one-dimensional two-phase/many-component convective flows in different geophysical mediums: laboratory method of modeling of fluids bubble boiling

Anzor Gvelesiani

Iv. Javakhishvili Tbilisi State University, M. Nodia Institute of Geophysics
1, Alexidze Str., 0171 Tbilisi, Georgia,
e-mail: <anzor_gvelesiani@yahoo.com>

Abstract

Today, research of different geophysical medium shells' stability is one of the actual problems. We paid our attention to the vertical motions of different fluids heated from below: in the first part there are theoretical aspects of the problem, in the second, experimental part, – original fluid bubble boiling method of modeling of vertical one-dimensional two-phase flow. Supposed laboratory method considers vertical motion of heated from below fluids – main element of convection, which plays important role in extraordinary natural phenomena (thunderstorms, volcanoes, gazer, mantle-plumes, tectonic motions, ionosphere continued waves, solar wind, magnetic storms etc.), and named by us as "bubble boiling method of fluids". Preliminary experiments of modeling of fluid convective motions were successfully conducted at the base of Institute's thermobarochamber. Results were many times repeated and controlled in detail. Graphic and table materials represent in next paper of this issue. Because the convective motions presents in all geophysical shells and analogically the subjects, practical and theoretical activity of the Institute collaborators are connected with each other, perhaps it will be possible to develop and expand it further together.

1. Introduction

This paper focuses on some cases of instability processes taking place in nature, laboratory, and technique. Laminar flows in porous materials and turbulence are similar in the sense that full detailed description of their motion analytically is impossible, and in case of porous materials are added the difficulties connected with the complexity of the geometry [1-18].

The purpose of study of both abovementioned problems consists in mathematical description of flows by means of properly averaged variables. The "theory" of currents in the porous materials essentially is based on generalization of Darcy's empirical observations [1, 4]. We paid our attention to the vertical motions of different fluids heated from below: in the first part there are theoretical aspects of the problem, in the second, experimental part, – original fluid bubble boiling method of modeling of vertical one-dimensional two-phase flow. Supposed laboratory method considers vertical motion of heated from below fluids – main element of convection, which plays important role in extraordinary natural phenomena (thunderstorms, volcanoes, gazer, mantle-plumes, tectonic motions, ionosphere continued waves, solar wind, magnetic storms etc.), and named by us as "bubble boiling method of fluids" [5-18]. Preliminary experiments of modeling of fluid convective motions were successfully conducted at the base of Institute's thermobarochamber.

2. Convection of magnetized, non-conducting fluid [2]

Magnetized liquid is colloidal suspension of suspended particles in fluid-carrier **(**water, kerosene, transformer fluid and others). In Oberbeck–Boussinesq approximation, the equations of complex gravitational and magnetic convection are following [2]:

$$\frac{\partial \vec{v}}{\partial t} + (\vec{v}\cdot\nabla)\vec{v} = -\frac{1}{\rho_0}\nabla p + \nu\nabla^2\vec{v} + [1-\alpha(T-T_0)]\vec{g} + \frac{\mu_0}{\rho_0}M(T,H)\nabla H\,,$$

$$\nabla\cdot\vec{v} = 0\,,\ \frac{\partial T}{\partial t} + \vec{v}\cdot\nabla T = a\nabla^2 T\,,\ \nabla\times\vec{H} = 0\,,\ \nabla\cdot\left(\left(1+\frac{M(T,H)}{H}\right)\vec{H}\right) = 0,$$

$$\rho = \rho_0[1-\alpha(T-T_0)],\quad M = M_0 - K(T-T_0) + \chi(H-H_0), \qquad (2.1)$$

where $\vec{v}$, p, T, T_0, α, a, $\vec{g}$, H, μ_0 are respectively the vector of velocity, pressure, temperature, temperature at which $\rho = \rho_0$, coefficient of volume expansion, coefficient of heat conduction, acceleration due to gravity, magnetic field, magnetic permeability, $M_0 = M(T_0, H_0)$, M is an intensity of magnetization of fluid, $K = \partial M(T_0, H_0)/\partial T$, is pyromagnetic coefficient, $\chi = \partial M(T_0, H_0)/\partial H$ is a susceptibility of fluid, $\rho_0 = \rho(T_0)$, the model is correct at small changing of the temperature and magnetic field near T_0 and H_0, respectively. The term $M\nabla H$ is conditioned by magnetic properties of the fluid and characterizes its interaction with the magneto-gradient field. At M = 0 or $\nabla H = 0$ the system (2.1) coincides with the model of usual natural convection model.

3. Convection of conducting fluids [3]

Let us consider case when the **direction** of the impressed **magnetic field** coincides with the **vertical**. The relevant equations are:

$$\frac{\partial\theta}{\partial t} = \kappa\nabla^2\theta + \beta w\,,\ \frac{\partial h_z}{\partial t} = \eta\nabla^2 h_z + H\frac{\partial w}{\partial z}\,,$$

$$\frac{\partial\xi}{\partial t} = \eta\nabla^2\xi + H\frac{\partial\zeta}{\partial z}\,,\ \frac{\partial\zeta}{\partial t} = \nu\nabla^2\zeta + \frac{\mu H}{4\pi\rho}\frac{\partial\xi}{\partial z}\,,$$

$$\frac{\partial}{\partial t}\nabla^2 w = g\alpha\left(\frac{\partial^2\theta}{\partial x^2} + \frac{\partial^2\theta}{\partial y^2}\right) + \nu\nabla^4 w + \frac{\mu H}{4\pi\rho}\frac{\partial}{\partial z}\nabla^2 h_z\,,$$

where θ, w, ζ , ξ/4π, κ, η, ν are the temperature, vertical velocity, vorticity, current density, temperature conductivity, electrical resistivity, kinematic viscosity, respectively.

4. Kelvin-Helmholtz instability in porous media: the Darcian flow [4]

Laminar flows in porous materials and turbulence are similar in the sense that full detailed description of their motion analytically is impossible, and in case of porous materials are added the difficulties connected with the complexity of the geometry [1-12].

The purpose of study of both abovementioned problems consists in mathematical description of flows by means of properly averaged variables. The "theory" of currents in the porous materials essentially is based on generalization of Darcy's empirical observations [1, 4].

Consider parallel flow of two immiscible fluids in an infinite, fully saturated, uniform, homogeneous, and isotropic porous media with constant porosity (φ) and constant permeability (λ). The two fluids are incompressible and have constant properties.

$$\frac{\partial p_i}{\partial x} = -\frac{\rho_i}{\phi}\frac{\partial v_{x,i}}{\partial t} - \frac{\mu_i}{\lambda} v_{x,i} + \rho_i g \sin\alpha,$$
$$\nabla \cdot \vec{v} = 0.$$

After linearization of these equations and neglecting nonlinear terms for typical normal mode of wavenumber k in the x direction in the real part of potential of velocity and the disturbed interface the resulting equation for ω is slightly more general than the characteristic equation obtained by [5] is

$$\omega^2 A + \omega B + i\omega k C + ikD + k^2 E = 0,$$

$$A = \rho_1 + \rho_2,\ B = \frac{\phi}{\lambda}(\mu_1 + \mu_2),\ C = \frac{\rho_1 U_1 + \rho_2 U_2}{\phi},\ D = \frac{\mu_1 U_1 + \mu_2 U_2}{\lambda},$$
$$E = (\sigma + \sigma_M)k + (1/k)g(\rho_2 - \rho_1)\cos\alpha,$$

here in general ω is the complex number $\omega = \omega_R + i\omega_I$.

Is it possible to consider Kelvin-Helmholtz instability as a trigger mechanism of light earthquakes? When heating of considered medium from below and Kelvin-Helmholtz instability happen concurrently we must know the numerical value of the Rayleigh number $Ra \geq 10^3$ (for turbulence).

5. Subvertical accumulation of earthquakes hypocenters – seismic "nets" [5]

Having studied data of JMA catalogues of Japan earthquakes, Vadkovsky obtained compact (in space and time) accumulation of earthquakes centres (see Figs. 1a, 1b). Because of distinctive vertically oriented cylinders form Vadkovsky named them seismic "nets".

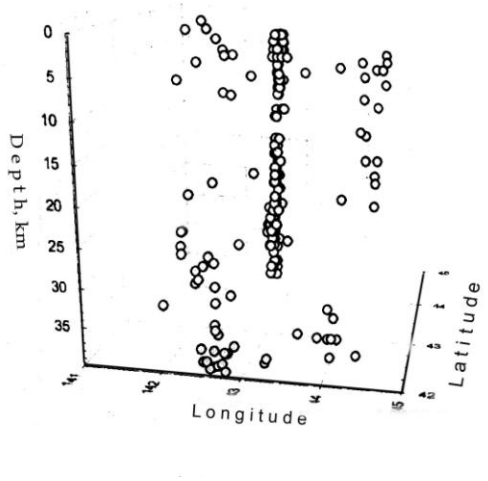

Fig. 1a. Formation of the seismic "net" in region of the Island Hokkaido, [5].

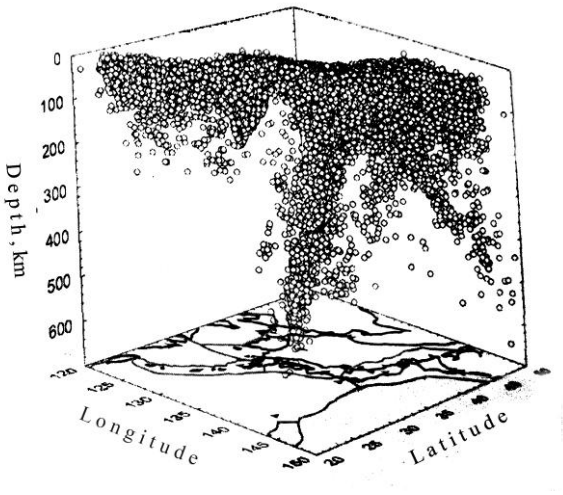

Fig. 1b. Formation of the seismic "net" in region of the Island Hokkaido, [5].

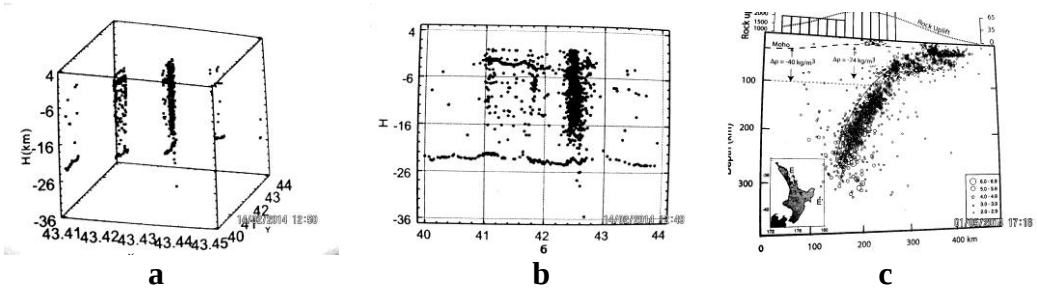

a **b** **c**

Fig. 2 Distribution of hypocenters of earthquakes: **(a)** in Caucasus (3d view under angle of vision 45^0), [6]; **(b)** in Caucasus (vertical plate), [6].

.

Similar investigations were made for Georgia, too, and obtained on the base of great number of data of light earthquakes both 3D structure of distribution of hypocenters of earthquakes and subvertical seismic "nets"(see Figs. 2a, 2b).

That seismic "nets" will attract very serious attention of scientists, working on the problem of convective motion because of striking likeness between the vertical distribution of hypocenters of weak earthquakes and vertically oriented chain of air bubbles moving upwards in boiling water (see Figs. 4-). In search of seismic "nets", the 3D, visual, analytical methods of grouping of the earthquakes, technique of investigation Markov's chains, and fractals multitude were used. The data time interval (7 years) is too small one to tell with confidence in space-time characteristics of the "nets". Nevertheless, geometry and speed of formation latter enable to judge on the possible **role of fluids in the process of their formation,** since neither melt nor, of course, any solid phase cannot have such high mobility.

It is possible to say, that the seismic "nets" phenomenon one can with confidence include them into a group of one-dimensional vertical flows, studying by supposed below fluid bubble boiling method (see).

6. Neotectonics: Remarkable plates convergence [7, 8].

Following fragment from [8] is interesting not only for geologists.

"Recent geodynamics of Georgia and adjacent territories of the Black Sea-Caspian Sea region, as a whole, are determined by its position between the **still-converging** Eurasian and Africa-Arabian plates" (Fig. 3a). Analogical picture of block rotation rates, volcanic arcs, and distribution of epicentres and hypocenters of earthquakes in Australia (Fig. 3b) (as result of interaction between the Australian plate and the Pacific plate (Fig. 3c)).

Furthermore, according to geodetic data of Caucasus, the order of **rate** this **convergence** is ~ 20-30 mm/yr (Fig. 3a). The same order convergence rates showed in Fig. 3b (the authors of [18], when interpreting of rotations represents following examples of there calculations: 200, 100, and 20 mm/yr for Japan, Ligurian Sea, and North Island, respectively).

All of these examples of natural extraordinary convective phenomena we consider only from the standpoint of vertically directed convective one-dimensional flows, caused by Archimedes' buoyancy force. It discoveries in the form of thermals in atmosphere and ocean, mantle plumes in the liquid core of the Earth, etc. We tried to visualize considered process of heating fluid below and illustrate this report correspondingly, as far as possible. Simultaneously, to describe it from new point of view we suggest experimental method. Proceeding from essential peculiarity of these extraordinary phenomena, we began to study peculiarities of bubble-boiling process of chemical solution (glucose) of different density. Method allowed obtain some important thermodynamical and thermochemical properties of boiling solutions, clearing and confirming some of natural facts. Therefore, the first was named by us "fluids bubble-boiling modelling laboratory method".

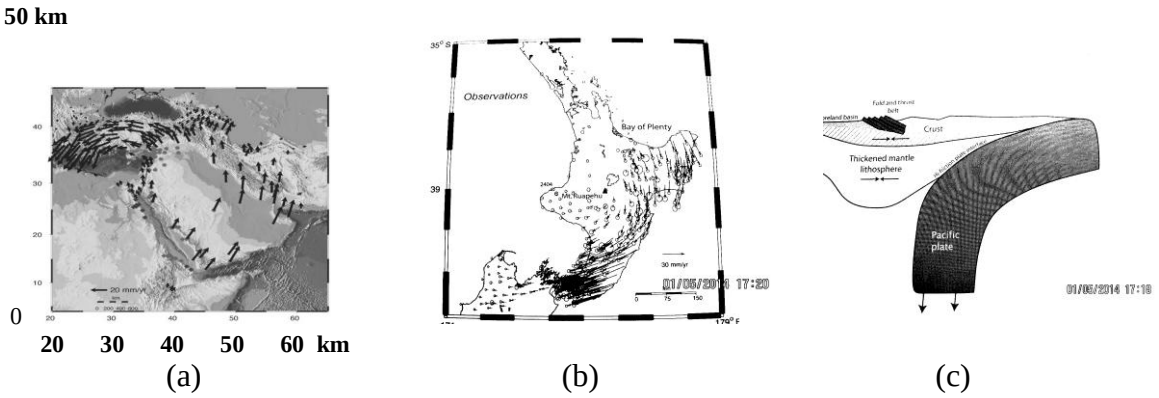

(a) (b) (c)

Fig. 3. Present-day GPS- derived station velocities: **(a)** – the zone of interaction of the African**,** Arabian, and Eurasian plates from data spanning the period 1988-2005, [7]; **(b)** GPS velocities field in the North Island and northwestern South Island based on a decade of observations [18]; **(c)** according to [18] beneath Wanganui Basin might be the general case of young active continental margin before back-arc extension and volcanism begin. It is noteworthy that this area (Fig. 3a) contains sites of the strongest Caucasian earthquakes – 1988 Spitak (Armenia) and 1991 Ratcha (Georgia) [8].

Continuing this phrase, we note that because of small Reynolds number there is possibility of laboratory modelling of such motions fluids in the mental (details of theory and experiment see in [14]). Then, for good reason one may contend that this **tectonic rate field is** directly / exactly **connected with molten mantle convective motion**. The latter was considered in detail in our article [14].

It is necessary to note that represented in Fig. 4b and Fig. 4c volcanoes in detail studied in the article [15]. There was calculated volume of materials discharged during the main phases of volcano's activity during the 1955-2009 (Kamchatka). Authors of [16] studied explosive activity with great variations in the frequency and energy of explosions; magma as it was moving along the conduit was stratified to form a set of vertical filaments; the leading explosive mechanism during that period was a fragmentation wave that was produced in a gas-charged, viscous, porous magma during decompression. One notices that the shape of some shock waves in air indicates the occurrence of air blasts above the crater (in our modeling bubble-projectile boiling of fluid (!)). The air blasts have been caused by combustible volcanic gases such as carbon monoxide and hydrogen (CO and H_2) which entered the atmosphere in sufficient amounts (see Fig. 4b).

a **b** **c**

Fig. 4. (a) – Subglacial volcanic eruption [17]; (b) – eruption of volcano Bezymyannyi [Internet]; (c) – eruption of volcano Kluchevskaya Sopka – [Internet].

Fig. 4c shows two interesting cases of independent convective thermals (plumes) – small cumulus cloud and volcano's first burning hot muddy-gas eruption, – the phenomena, which we model in laboratory by fluid bubble boiling method (see below).

II. Fluids bubble-boiling modelling laboratory method: intensive one-dimensional vertical convective motion (extraordinary phenomena of nature)

A. Purpose and scope of this method.

Preliminary experiments of laboratory modeling of fluid thermo-chemical convection were carrying out at Thermo-baro-chamber of Institute of Geophysics. There were observed and measured: (1) differentiation of solutions; (2) generation layers with boundaries containing high concentration of accumulated pollution; (3) thermodynamic parameters changing in space and time; T, Q, S, ρ, P, V, α, β, ν, κ, Ra; (4) the many-layer fluids system and (5) formation and velocity of Stokes' size bubbles at the bottom of heating vessel with water sugar solution, oil, (6) their fast vertical motions in the mass of slow ascending infinitesimal air bubbles; (photography and video-recording) They were photographed during bubble boiling of chemical solution.

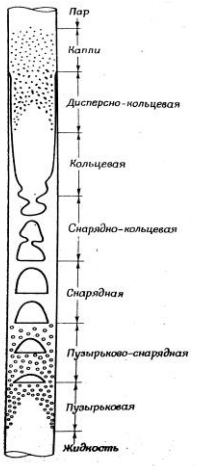

Fig. 5a. Structurs of fluid heated from below: fluid; bubble; bubble-slug; slug; slug-annular; annular; dispersed-annular; drops; vapor. Approximate sequence flow structures in vertical evaporator tube [9].

Fig.5b. A schematic illustration of the vertical directed main geothermal flows; hot gazer (left); main boiling fluid Na-Cl, pH neutral; hot steam, surface oxide, solutions; oxidation; zone of precipitation [10].

B. Calculated clouds. Computer calculations have correctly reflected the vertical one-dimensional two-phase flows of convective motions in nature (compare Figs. 6a-b and Figs. 7a-b), one of which is given in [12] (Emanuel (1989) [12])

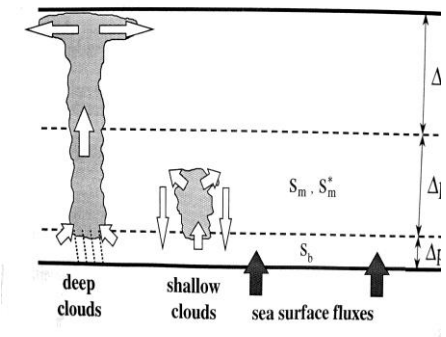

a

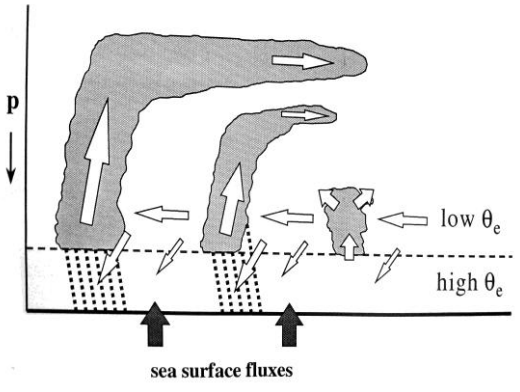

b

Fig. 6. Vertical structure of Emanuel's hurricane model: "**(a)** – **deep clouds** transfer mass from the subcloud layer to the top layer; **shallow clouds** exchange entropy between the lower troposphere and the subcloud layer without producing a net mass flux; **(b)** illustration of airflow in a developing Emanuel's tropical cyclone model; for a cyclone to spin up, lower tropospheric air above the boundary layer must flow inward; this air has a relatively low moist entropy, and if it were to ascend directly into the vortex core, the core entropy would reduce, the core would cool, and the cyclone would decay. Instead, the air descends within shallow clouds, within precipitating downdrafts, and outside of clouds because of Ekman suction. This descent of relatively dry air reduces the entropy of subcloud layer. The vortex core can become warmer than its environment only if the surface fluxes are large enough to offset this drying effect on the subcloud air parcels flow inward in the lower troposphere, sink downward in downdrafts , receive entropy from the ocean, and then ascend in deep convective clouds" [12].

C. Natural clouds (photographs, Tbilisi, Georgia. – by A.G.).

a b

Fig. 7. Convective clouds, thermals, moving slowly: (a) westward (Tbilisi, 14/08/13; 12:29); (b) eastward (Tbilisi, 11/08/13; 11:01).

Together Figs. 1-9 illustrate complete result of action of vertically oriented well-known Archimedes buoyancy force in nature.

a **b**

Fig. 8. Three-layer thermodynamic system – glucose syrup layer (bottom), thick intermediate bubbles and population (IP) layer, oil layer (it's well seen group of large air- bubbles), thin intermediate bubble and IP layer, and air-steam layer (top): **(a)** photograph shows oblique view of the solution topography; **(b)** photograph shows view from side (after 2 min).

Here and below photographs show side views of the solution in glass vessel.

a b

Fig. 9. Photographs show the same thermodynamic system as in Fig. 8, but here glucose solution colored by coffee: (a) it is well seen two large air bubbles fast vertically ascend upward (~ 40 cm/s); **(b)** large bubbles made their way through the thick intermediate bubbles and population (IP) layer (after 14 sec).

Conclusions

Here was used wide interval of solution density; thanks to suggested method of bubble boiling for laboratory investigation of thermo-chemical convection between existing layers were obtained intermediate layers with high concentration of accumulated pollution; discovery of second kind discontinuity of temperature-time dependence at the point $T_{bf}(t)$ of intensive infinitesimal air bubbles formation till the point $T_{bb}(t)$ of solution bubble boiling (note, that $T_0(t) - T_{bf}(t)$ is linear, and $T_{bf}(t) - T_{bb}(t)$ is near to parabolic). Analyze and discussion of physical aspects of this point and elliptic curve are given in our joint paper of this issue of JGGS/2013-2014. Preliminary experiments of modeling of fluid convective motions, which were successfully conducted at the base of Institute's thermobarochamber, must be continued.

Acknowledgment. Author thanks Cand. Phys.-Math. Sci. Nodar Tchiabrishvili for active participation and discussion of results of original laboratory experiments.

References

[1] Joseph D. D. Stability of fluid motions, I/II. Springer-Verlag, Berlin-Heidelberg-New York, 1976; M: Mir, 1981, 638 p.
[2] Berkovsky B. M., Polevikov V. K. Heat transfer and turbulent buoyant convection. Washington: Hemisphere Publ., 1977, pp. 443-455
[3] Chandrasekhar S. Hydrodynamic and hydromagnetic stability. Clarendon Press, Oxford, England, 1961, 652 p. 6
[4] Bau H. H. Kelvin-Helmholtz instability for parallel flow in porous media: A linear theory. Phys. Fluids, 1982, 25(10), October, pp. 1719-1722.
[5] Vadkovsky I. R.Subvertical accumulation of hypocenters of earthquakes – seismical "nails". Vestnik ONZ RAN, 2012, T. 4, NZ1001, doi:10.2205/2012NZ000110. 2012.
[6] Gamkrelidze N. P., Ghonghadze S. A., Mindeli P. Sh., Kiria D. K., Yavolovskaya O. V. The Physics of the Earth's Crust of the Territory of Georgia. Iv. Javakhishvili TSU, M. Nodia Institute of Geophysics: Tbilisi, 2012, 221 pp..
[7] Reilinger R. Kinematics and dynamics of active rifting of the Northern and Central Red Sea. RKL, 2006, EAR 03-05480.
[8] Adamia Sh., Mumladze T., Sadradze N., Tsereteli E., Tsereteli N., and O. Varazanashvili.

Late cenozoic tectonics and geodynamics of Georgia (SW Caucasus). Georgian Intern. J. Sci. Technol., 2008, v. 1, Is. 1, pp. 77-107.
[9] Wallis G. B. One-dimensional two-phase flow. McGraw-Hill Book Company. New York et al.), 440 pp.
[10] Zakharova O. K., Spichak V. V. Geothermal fields of Hengill Volcano, Iceland. Vulkanologia i Seismologia, 2012, N 1, pp. 3-18.
[11] Kopf A. J. (2002) Significance of mud volcanism. Rev. Geophys., 40(X), 1005, doi: 10.1029/2000RG000093, 2002.
[12] Smith R. K. The role of cumulus convection in hurricanes and its representation in hurricane models. Reviews of Geophysics, 38, 4 / November 2000, pp. 465-489.
[13] Gvelesiani A. I. On the convective motions in different layers of atmosphere. J.Georgian Geophys. Soc., 2010-2011, v.14B, pp. 161-182.
[14] Gvelesiani A. I**.** On the convective motions in different geophysical media. J. Georgian Geophys. Soc., 2012, v.15B, pp. 52-64.
[15] Zharinov N. A., Demyanchuk Yu. V. Assessing the volumes of material discharged by Bezymyannyi volcano during the 1955-2009 period. Vulkanologia i Seismologia, 2011, № 2, pp. 28-41.
[16] Firstov P. P., Fee D., Makhmudov E. R.The explosive activity of Karymskii volcano, Kamchatka: acoustic and Seismic observations. Vulkanologia i Seismologia, 2013, № 4, pp. 13-26.
[17] Roberts M. J. (2005) Jökulhlaups: A reassessment of floodwater flow through glaciers. Reviews of Geophysics, 43, RG1002, doi: 10.1029/2003RG000147.
[18] Stern T. A., Stratford W. R., Salmon M. L.(2006) Subduction evolution and mantle dynamics at a continental margin: central North Island, New Zealand. Rev. Geophys., 44, RG 4002 , doi: 10.1029/2005RG000171.

(Received in final form 30 November 2013)

Об одномерных двух-фазных/много-компонентных конвективных движениях жидкостей в различных геофизических средах: лабораторный метод моделирования пузырькового кипения жидкости

А. И. Гвелесиани

Резюме

В настоящей работе основное внимание сосредоточено на вертикальных конвективных движениях различных геофизических сред, подогреваемых снизу. Первая часть работы – теоретическая; вторая – экспериментальная. Предлагается новый метод лабораторного моделирования конвективных двух-фазных много-компонентных движений в естественных условиях (облака, вулканы, гейзеры, ментл-плюмс, тектонические сдвиги, ионосферные непрерывные волны, солнечные вспышки, магнитные бури и т.д.), названный нами методом пузырькового кипения жидкости. Получены обнадёживающие результаты предварительных экспериментов, проведённых на базе экспериментального комплекса термобарокамеры Института геофизики. Поскольку конвективные движения присутствуют во всех геофизических оболочках, а тематика, практическая и теоретическая деятельность сотрудников института прямо или косвенно связанаы с ними, то можно было бы начатые исследования совместно расширить и развить далее.

ერთგანზომილებიანი ორფაზოვანი /მრავალკომპონენტიანი სითხის მოძრაობა სხვადასხვა გეოფიზიკურ გარემოში: სითხის ბუშტოვანი დუღილის ლაბორატორიული მოდელირების მეთოდი

ანზორ გველესიანი

რეზიუმე

წინამდებარე სტატიაში მოკლედ განიხილება სხვადასხვა გეოფიზიკურ თხევად არეში ვერტიკალური კონვექციური მოძრაობების თავისებურებანი გამოწვეული მისი ქვემოდან გათბობის ან სხვა ბუნების ვერტიკალური არაერთგვაროვნების შემქმნელი მიზეზის გამო (ღრუბლები, ვულკანები, გეიზერები, მანტიის მენტლ–პლუმები, ტექტონიკური მოძრაობები, იონოსფერული უწყვეტი ტალღები, მზის პლაზმის ამოფრქვევები, მაგნიტური ქარიშხლები და სხვ.). პირველ ნაწილში სქემატურად მოცემულია პრობლემის ზოგიერთი თეორიული ასპექტი, მეორეში –კონვექციური მოძრაობის მოდელირების სითხის ბუშტოვანი დუღილის ლაბორატორიული მეთოდი. მოყვანილია პირველადი ცდების ზოგიერთი შედეგი. მოდელირების ექსპერიმენტები ჩატარებულია ინსტიტუტის თერმობაროკამერის ბაზაზე.

კონვექციურ მოვლენებს ადგილი აქვს პლანეტის ყველა გარსში და ისინი დაკავშირებული არიან ერთიმეორესთან. ინსტიტუტუტის სექტორულ–თემატიკური ფუნქციონირებაც ამგვარია. გამომდინარე აქედან, შეგვიძლია ვისურვოთ, ინსტიტუტის სათანადო სექტორების დაინტერესების შემთხვევაში, აღნიშნული კვლევების გაფართოება და განვითარება.

.

Journal of the Georgian Geophysical Society,
Issue(B), Physics of Atmosphere, Ocean and Space Plasma, v.16B, 2013 pp.128-136

Laboratory modeling of thermals generation in geophysical environments by means of fluid bubble boiling method

Anzor Gvelesiani, Nodar Chiabrishvili

Iv. Javakhishvili Tbilisi State University, Mikheil Nodia Institute of Geophysics,
1, M. Alexidze, 0171 Tbilisi, Georgia
e-mail: <anzor_gvelesiani@yahoo.com>

Abstract

It is used method of fluid bubble boiling with purpose of laboratory modeling of thermo-chemical convection in different geophysical mediums [1]. Preliminary experiments were carrying out in the abovementioned work. Here was used more wide interval of solution densities. Thanks to suggested method of bubble boiling for laboratory investigation of thermo-chemical convection were defined more precisely before obtained results: differentiation of solutions; generation layers with boundaries containing high concentration of accumulated pollution; second kind discontinuity of temperature-time dependence in the point of infinitesimal air bubbles formation, after which the straight line character of it turns into like parabolic one before achievement the bubble boiling point.

1. Introduction

In this report, on the base of the experimental complex – Thermobarochamber of Mikheil Nodia Institute of Geophysics – for the first time it is obtained new results on modeling of thermals origin and following formation of cumulus clouds in the atmosphere and other geophysical fluids, convective motions giving rise mantle plumes, volcanoes, thermal waters etc. Investigation of these thermo-chemical convective motions, connected with extraordinary phenomena of nature (thunderstorms, hailstorms, volcanoes, relative motion of plates, earthquakes etc.), is one of the most actual scientific and socioeconomic problems. Difficulties of numerous experimental, numerical, and theoretical studies of these processes have led scientists to the necessity of carrying of corresponding laboratory experiments [1]. Here was used wide interval of solution density; thanks to suggested method of bubble boiling for laboratory investigation of thermo-chemical convection between existing layers were obtained intermediate layers with high concentration of accumulated pollution; discovery of second kind discontinuity of temperature-time dependence at the point $T_{bf}(t)$ of intensive infinitesimal air bubbles formation till the point $T_{bb}(t)$ of solution bubble boiling (note, that function $T(t)$ in interval $T_0(t) - T_{bf}(t)$ is linear, and in $T_{bf}(t) - T_{bb}(t)$ is parabolic). All authors unanimously declared that appeal to the laboratory experiment is only right way for successful solution of the difficulties connected with this problem [1-10].

2. Scheme of device and characteristics of thermodynamic system

There are provided and analyzed results of joint laboratory experiments by method of fluid bubbly boiling in modeling of the process of thermals formation in different geophysical environment, in particular, of cumulus clouds, differentiation of under-cloud /over-cloud ranges etc.

Below, Fig. 1 shows the scheme of device for modeling of vertical one-dimensional two-phase thermal motion.

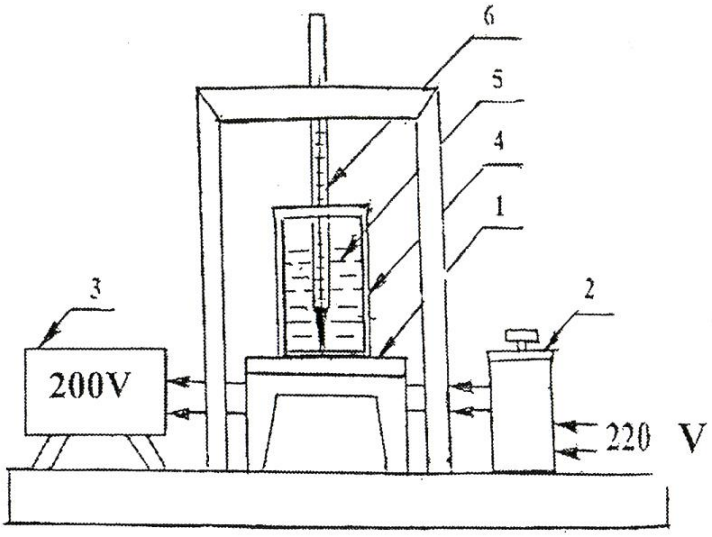

Fig. 1. Scheme of the experimental device: 1 – electrical heater;
2 – laboratory auto-connected transformer; 3 – voltmeter;
4 – chemical retort; 5 – glucose solution; 6 – thermometer.

Fig. 1 shows the minimum of necessary instruments to conduct experiments with high accuracy and completeness of information about all parameters of the system. Although, this scheme is very simple, however, as proved during careful and repeated experiments, we establish some important phenomena accompanying boiling process (reflected partly in the figures and tables).

III. Bubble-boiling method: Preliminary experimental results

In chemical retort, firstly, clear water (at initial temperature 10^0C, density $\rho_0 = 1.00$ g/cm^3) was used as object of investigation, and then – series of glucose solution with following values of density: $\rho_1 = 1.04$ g/cm^3, $\rho_2 = 1.08$ g/cm^3, $\rho_3 = 1.13$ g/cm^3, $\rho_4 = 1.18$ g/cm^3, $\rho_5 = 1.23$ g/cm^3, $\rho_6 = 1.29$ g/cm^3, $\rho_7 = 1.35$ g/cm^3, $\rho_8 = 1.41$ g/cm^3, $\rho_9 = 1.47$ g/cm^3.

Fig. 2 shows graphical dependence of temperature water (in ^{0}C) on time (in min.). It is evident two stages in the processes of heating both clear water and considered glucose solutions. One can see as straight lines in case of clear water, $\rho_0 = 1.00$ g/cm^3, just at temperature $T_{dc} = 80^0$C (Fig. 2a), and glucose solution of maximal density, $\rho_9 = 1.47$ g/cm^3, at temperature $T_{dc} = 40^0$C (Frig. 2b), undergo discontinuity of second kind, respectively. Shaded sectors show the degree of curves deviation from linearity, respectively. These two points of discontinuity, T_{dc}, are joined by straight line in Figs. 2a, b.

Table 1 contents results of measurements of temperature changing with time beginning heating of clear water ($\rho_0 = 1.0$ g/cm^3) and glucose solution ($\rho_9 = 1.47$ g/cm^3) from $T = 10^0$ C to the point of boiling $T = 100^0$ C. Difference is evident: in intervals of temperature $\Delta T = (10 - 50)^0$ C (first five cases of measuring) time of clear water heating is twice more than in case of glucose

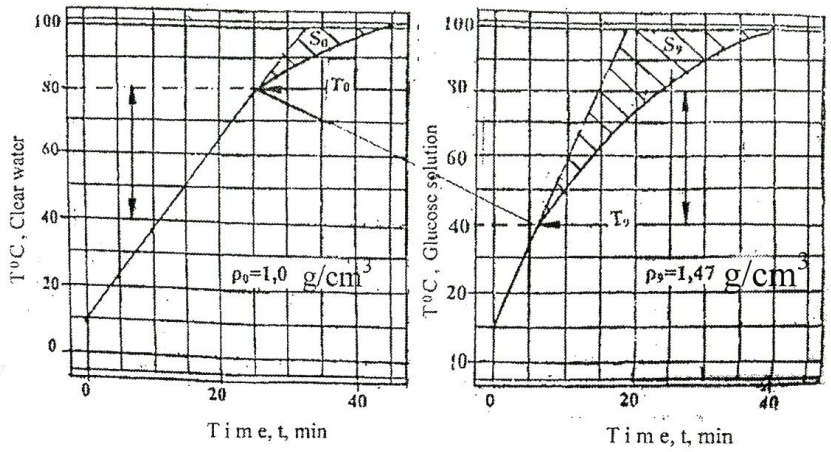

(a) **(b)**

Fig. 2. Temperature-time dependence of fluid heated below: (a) – clear water (ρ_0 = 1.0 g/cm^3); (b) – glucose solution (ρ_9 = 1.47 g/cm^3).

solution maximal density; then the values of these times approaches to each other, nevertheless, the difference between them remains and equals to Δt = 5 min at the boiling temperature T = 100^0 C. In the same relations are the quantity of clear water and the solution heat, respectively. Here also in the first five cases Q of the clear water twice more then Q of the glucose solution, these values approach to each other still the boiling point T = 100^0 C, where difference between them equals to ΔQ = 4500 cal.

Table 1. Dependence of temperature interval of clear water and glucose solution of maximal density on time and intensity of heating.

	Clear water, ρ_0 = 1.0 g/cm^3			Glucose solution, ρ_9 = 1.47 g/cm^3		
№ s	Temperature T^{0}C	Time t, min	Heat Q, cal	Temperature T^{0}C	Time t, min	Heat Q, cal
0	10	0	0	10	0	0
1	20	4	3600	20	2	1800
2	30	8	7200	30	4	3600
3	40	13	11700	40	6	5400
4	50	17	15300	50	9	8100
5	60	22	19800	60	14	12600
6	70	26	23400	70	18	16200
7	80	31	27900	80	24	21600
8	90	37	33300	90	30	27000
9	100	45	40500	100	40	36000

All 10 points of above mentioned solution densities represent in Fig. 3. It is well seen smooth passage of the curve from point to point before the point s = 6 (i.e. ρ_6 = 1.29 g/cm^3), after which the temperatures of discontinuity (T_{dc}), for last four values of density of sugar solution (ρ_6 = 1.29 g/cm^3,

ρ_7 = 1.35 g/cm^3, ρ_8 = 1.41 g/cm^3, and ρ_9 = 1.47 g/cm^3), coincide ($T_{dc,6} = T_{dc,7} = T_{dc,8} = T_{dc,9}$) and equal to 40^0 C.

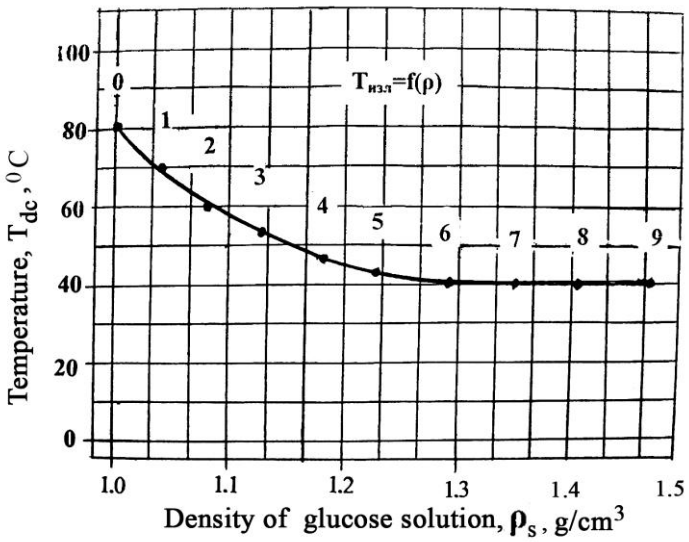

Fig. 3. Temperature of discontinuity, T_{dc}, dependence on the density of clear water (ρ_0 = 1.0 g/cm^3) and densities of glucose solution (ρ_S, g/cm^3), (S = 1, 2, …, 9).

Fig. 4 and 5 shows the maximal difference between clear water and glucose solution of density ρ_9 = 1.47 g/cm^3.

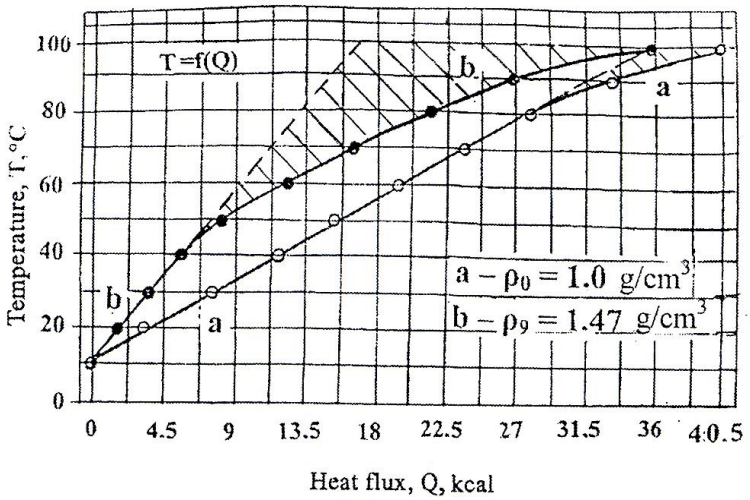

Fig. 4. Temperature dependence of glucose solution heated below upon heating flux: (a)– clear water (ρ_0 = 1.0 g/cm^3); (b) – glucose solution (ρ_9 = 1.47 g/cm^3); (circles denote temperatures of discontinuity, $T_{dc}(t)$, corresponding to ρ_S, (S = 0, 1, 2, . . . , 9).

Heat flux, Q kcal

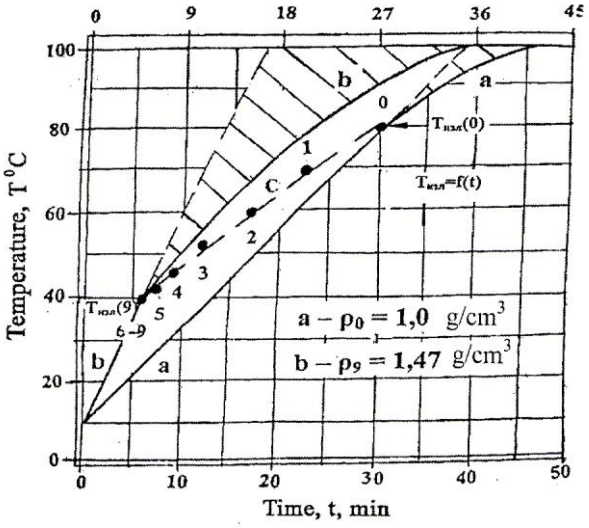

Fig. 5. Temperature-time and heat flux-time dependence at fixed density of solution ρ_S (solid lines): (a) corresponds to clear water (s = 0, ρ_0 = 1.0 g/cm^3); (b) – to maximal density of glucose solution (s = 9, ρ_9 = 1.47 g/cm^3); (c) - T_{dc} (t) temperature of discontinuity corresponds, including clear water, to all values of density, ρ_S, (S = 0, 1, 2, . . . , 9), (dashed line).

Table 2. Dependence of clear water and glucose solutions entropy for 10^0C of temperature intervals on the density, ρ_S, of solution.

№ s	Density of solution, ρ_S, g / cm^3	Intervals of temperature, ΔT, ^{0}C					
		40-50	50-60	60-70	70-80	80-90	90-100
		Entropy, ΔS = ΔQ / T, cal / ^{0}C					
0	1.0					630	900
1	1.04				450	585	810
2	1.08			495	495	630	720
3	1.13			405	504	675	900
4	1.18		360	405	450	580	900
5	1.23		360	405	450	630	900
6	1.29	360	360	360	450	640	900
7	1.35	270	270	370	450	675	900
8	1.41	360	360	60	450	630	900
9	1.47	315	360	405	450	540	900

Below, by construction of Fig. 6 we wish to sum up results of our preliminary experiments on modeling of convection process which are in any liquid and gaseous geophysical environment or, in

short, to describe whole process of heating and boiling glucose solution from beginning to the end. As concerns Table 3, it adds the data of Tables 1- 2 and Figs. 2-5, too.

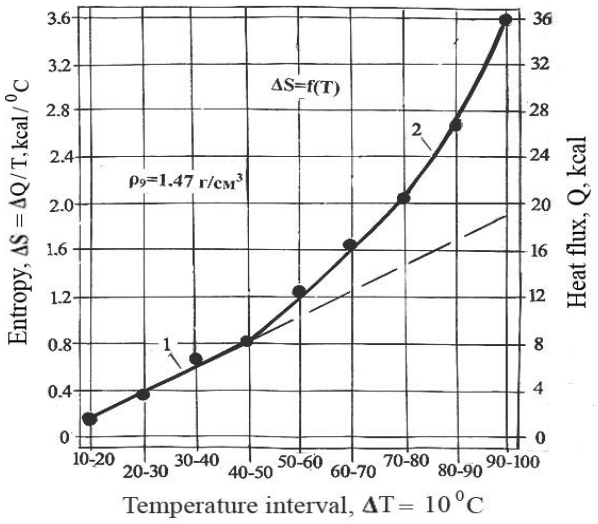

Fig. 6. Entropy-temperature graphic dependence of glucose solution with density ρ_9 = 1.47 g/cm^3 using $\Delta T = 10^0$C intervals. Dashed line shows deviation of the solid line from linearity after point (40-50, 0.8).

The graphic dependence between the entropy increase ($\Delta S = \Delta Q/T$) and selected from ((10-100) ^{0}C) range 10^0C-step temperature intervals is represented in Fig. 6.

Temperature intervals (10-20, …) along the abscissa axis correspond to the respective temperatures of discontinuity. Detailed analysis of the entropy growth dependence on temperature of the glucose solution with density ρ_9 = 1.47 g/cm^3 shows that the value of entropy is indicator of system's state at transfer from one condition to the following one. At that moment, corresponding to the temperature of discontinuity, T_{dc} , the system (solution) transfer from state of great number of least vapour bubbles, slowly ascending thermal-plumes (first stage – bubbly flow) to the state of bubble slug.

Table 3. Main heat characteristics of different density glucose solutions from the beginning of heating the glucose solutions to the bubbly boiling process.

№ sol	Temperature intervals, T, ^{0}C	Entropy, $\Delta S = \Delta Q / T$, kcal / ^{0}C	Correlation $\Delta S_{100}{}^0C / \Delta S_{20}{}^0C$	Correlation $\Delta S_{100}{}^0C / \Delta S_{40}{}^0C$
1	10-20	180	3600 / 180 =	
2	20-30	360	= 20	
3	30-40	540		3600 / 540 =
4	40-50	810		= 6.6
5	50-60	1260		
6	60-70	1620		
7	70-80	2115		
8	80-90	2700		
9	90-100	3600		

It is interesting to compare our results (Figs. 2-6 and Tables.) with Nukiyama's Fig. 7.

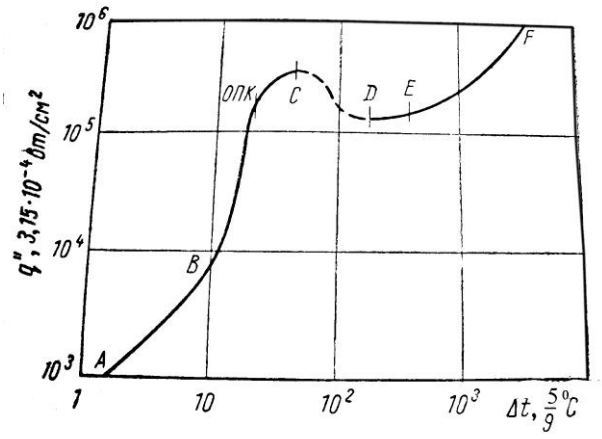

Fig. 7. Boiling of water at 100^0C on the electrically heated platinum wire. Maximal flux for bubbly boiling (Nukiyama (1934), see [3]).

Comparison and analysis of our results on clear water and nine cases of sugar solution densities (Figs. 2-6, Tables), and Nukiyama's (1934) ones (Fig.7) on only clear water, showed their accordance with each other. In both cases heat fluxes was the same order (~ 2.0 W/cm^2, in our case, against 3.14 W/cm^2 of Nukiyama (1934)); moreover, the angles of deviation from linearity between dashed and solid lines in Fig. 6 and between AB and BC parts of the curve of Fig. 7 are nearly the same.

Fig. 8. Photographs of convective clouds with individual towers (Tbilisi, Georgia).– by A. G.

Fig. 8 shows typical cumulus clouds over outskirts of Tbilisi: it is well seen as cloud towers visualize the atmospheric thermals – individual and groups of cloud towers; heat flux over the hilly partly wooded territory (and in the winter sea) is about ~ 100 W/m^2 [7-9]; our modeling heat flux equals to 2 W/cm^2; Parameters of convective clouds are following: vertical middle velocities of— about 3-5 m/sec, near the base of cloud dimensions.

Acknowledgments. The authors express gratitude to Dr. Sci. A. Amiranashvili for attention and kind consent to provide these experiments in the laboratory of Thermobarochamber of Mikheil Nodia Institute of Geophysics, to Dr. T. Bliadze and other participants of the seminar for discussion of some aspects of this problem.

References

[1] Gvelesiani A. I**.** On the one-dimensional two-phase/many-component convective flows in different geophysical mediums. J. Georgian Geophys. Soc., 2013-2014, v.16B, pp.118-127 .

[2] Wallis G. B. One-dimensional two-phase flow. McGraw-Hill Book Company. New York et al.), M.: Mir, 1972, 440 pp.

[3] Leppert G., K. Pitts. Boiling. In: Advances in heat transfer (eds. Irvine T. F., Hartnett J. P.), vol. I, 1964. Academic Press, New York-London), Problemy Teploobmena, M.: Atomizdat, 1967, pp. 142-199 (in Russian).

[4] Jellinek A. M., Manga M. Links between long-lived hot spots, mantle plumes, D″, and plate tectonics. Reviews of Geophysics, 2004, v. 42, RG3002, pp. 1-35.

[5] Gvelesiani A. I. On the convective motions in different layers of atmosphere. J. Georgian Geophys. Soc., 2010, v. 14B, pp. 161-182.

[6] Ratiani G. V., Shekriladze I. G. Investigation of the process of developed boiling of liquids. Problems of convective heat-exchange and cleanness of water steam. Tbilisi: Metsniereba, 1970, pp. 44-62.

[7] Smith R. K. The role of cumulus convection in hurricanes and its representation in hurricane models. Reviews of Geophysics, 38, 4 / November 2000, pp. 465-489.

[8] Pielke R. A. Sr. Influence of the spatial distribution of vegetation and soils on the prediction of cumulus convective rainfall. Reviews of Geophysics, 39, 2 / May 2001, pp. 151-177.

[9] Marshall J., Schott F. Open-ocean convection: Observations, theory, and models. Reviews of Geophysics, 37, 1 / February 1999, pp. 1-64.

(Received in final form 27 March 2014)

Лабораторное моделирование процесса термикообразования в атмосфере методом пузырькового кипения жидкости

А. И. Гвелесиани, Н. Г. Чиабришвили,

Резюме

В данной работе на базе комплекса Термобарокамеры Института геофизики впервые, методом пузырькового кипения жидкости, ставятся и анализируются совместные эксперименты по моделированию термохимической конвекции, процесса образования термиков в различных геофизических средах, в частности, образования кучевых облаков, расслоения подоблачной и облачной сред и пр. Исследование конвективных движений, связанных с экстраординарными явлениями природы (штормы, вулканы, движение тектонических плит, землетрясения и др.) является одним из самых актуальных научных и социоэкономических проблем. Трудности численных экспериментов, численных и теоретических исследований этих процессов привели учёных мира к признанию необходимости проведения соответствующих лабораторных экспериментов. Последние имеют не только прикладное, но и самостоятельное значение. Предложенным методом пузырькового кипения для лабораторного моделирования термохимической конвекции был получен ряд новых результатов (see [1]). Для широкого диапазона плотностей растворов в ходе кривых зависимости температуры T(t) и энтропии S(T) обнаружены точки разрыва непрерывности второго рода (в диапазоне $(40\text{-}80)^0$ C), после которой кривые отклоняются от начального линейного хода, изгибаются и параболически приближаются к точке кипения 100^0 C.

ატმოსფერული თერმიკების წარმოშობის ლაბორატორიული მოდელირება სითხის ბუშტისებრი დუღილის მეთოდის მეშვეობით

ა. გველესიანი, ნ. ჭიაბრიშვილი

რეზიუმე

ბუნების ექსტრაორდინარული მოვლენების სრული სახით აღწერა რიცხვითი ექსპერიმენტების, რიცხვითი და თეორიული მეთოდების გამოყენებით ჯერ–ჯერობით გადაულახავ ამოცანადაა გამოცხადებული მსოფლიო მეცნიერების მიერ, რამაც აიძულა ერთხმად ეღიარებინათ ლაბორატორიული ექსპერიმენტების /ანუ ლაბორატორიული მოდელირების აუცილებლობა.

შემოთავაზებული ბუშტისებრი დუღილის მეთოდით კონვექციური მოძრაობების

სხვადასხვა გეოფიზიკურ თხევად არეში, კერძოდ, გროვა ღრუბლების წარმოშობის მოდელირების მიზნით ჩატარებულია წინასწარი ლაბორატორიული ცდები. ცდები ტარდებოდა მრავალფენოვან ხსნარებზე [1]: წყალი–შაქრის ხსნარი–ზეთი–წყლის ორთქლი. შეისწავლებოდა ერთიდაიმავე მოცულობის მქონე წყლის შაქრის ხსნარების გათბობის დუღილამდე მიყვანის სრული პროცესი. პროცესის დროს მდუღარე სუფთა წყლის და ხსნარების სიმკვრივის ფართო დიაპაზონის მნიშვნელობებისათვის თერმოქიმიური კონვექციის წარმოშობის პირობებისა და აღმავალი ბუშტების (თერმიკების) წარმოშობის პირობების ვერტიკალური სიჩქარეების განსაზღვრისას გათვალისწინებულია განხილულ გარემოთა რეჟიმების სპეციფიკა. აღმოჩენილია T(t) და S(T) მრუდებზე უწყვეტობის მეორე რიგის დარღვევის წერტილები (დიაპაზონში (40–80)^0 C), რომლის მიღწევის შემდეგ (დასაწყისში წრფივი) მრუდი პარაბოლის გასწვრივ მიისწრაფვის დუღილის წერტილამდე 100^0 C. თერმოქიმიური კონვექციის დეტალები მოწმდებოდა კლასიკური კვლევების შედეგების ფონზე.

Journal of the Georgian Geophysical Society,
Issue B. Physics of Atmosphere, Ocean and Space Plasma, v.16, 2013, pp. 137-156

Numerical modeling of water dynamics of Russian zone of the Black Sea within the framework of operational oceanography tasks

Aleksandr. V. Grigoriev[1], Andrey. G. Zatsepin[2]

[1] *N. N. Zubov's State Oceanographic Institute, Kropotkinsky Lane 6, 119 034 Moscow, Russian Federation, e-mail: ag-privat@mail.ru*
[2] *Shirshov's Institute of Oceanology, Nakhimov's av.,36, 117997 Moscow, Russian Federation*

Abstract

Modeling of the Black Sea waters dynamics (Russian zone) was conducted within the framework of the European ARENA and ECOOP projects and Russian project JISWO on the basis of Princeton Ocean Model (POM). Nowcasting and three days forecasting of the Black Sea dynamics was carried out in a daily mode with horizontal resolution of ~1 km along the Russian coast of the basin. Examples of calculations are presented and their comparison with space remote sensing and in situ (hydrological measurements) data is fulfilled, results of model validation are discussed. Model data reproduce observed real dynamic structures. Increasing a spatial permit of processes allows reproduce in calculations the detail of hydrological structure, which do not principally find displaying in large-scale models (vortexes with horizontal spatial sizes ~10 km). The model and the observed vertical profiles are very similar. Synoptic eddies, reflected in the modeled salinity field show a high correspondence in the spatial size and horizontal location with satellite images. The comparison of modeled temperature field with satellite data also demonstrates their qualitative agreement. The conclusion that the proposed modeling technology can adequately monitor the variability of the waters of the region with the spatial and temporal resolution, unattainable using only field data, can prove important for operational oceanography.

1. Introduction

Numerical modeling of the Black and Caspian seas dynamics was fulfilled in the State Oceanographic Institute of Russian Federation (SOI) within the framework of European ARENA (2003-2007 years) and ECOOP project (European COastal-shelf sea OPerational observing and forecasting system, 2007-2010 years) and National project JISWO (Joint Information System on World Ocean) and has continued to the present.

A well-known numerical Princeton Ocean Model (Blumberg and Mellor, 1987, 1991), adapted for the regional conditions, was used. As is known, the POM model is based on full system of the equations of hydrodynamics of the ocean with a free surface and Boussinesq, hydrostatics, liquids incompressibility approximations (vertical sigma-coordinate). The turbulence model with level 2.5 closure, based on the turbulence hypotheses of Rott-Kolmogorov generalized by Mellor and Yamada (1982) for the stratificated stream is used for vertical mixing parameterization. For horizontal diffusivity - the scheme of Smolarkevich is used.

The purpose of the paper is a description of automated system of nowcasting and forecasting of hydrophysical parameters which built during ECOOP and estimation of quality of modeled fields. The system output in the Russian part of the Black Sea is described. These results were obtained in close co-operation with other participants of the project, particularly with the Marine Hydrophysical Institute of National Academy of Sciences of Ukraine, Sevastopol (MHI). The comparison of observations and modeled fields is also presented below.

2 Russian zone of Black Sea forecasting system

A first version of the Black Sea coastal forecasting system has been developed in the framework of Europian ARENA project (Kubryakov et al., 2006-2011; Kordzadze et al., 2008, 2011), Fig.1. The formal parameters of the numerical regional model in this case were the following: the grid for calculation which covered the Russian zone of the sea had dimension 305x105 points and lay in borders of 44.0°-45.16° northern latitude and 36.33°-41.0° east longitude. The horizontal grid step was equal ~1200 m. The 25 vertical layers were thickening exponentially from the middle layers to the surface and to the bottom of the sea for the best resolution of the surface and bottom border layers. At the task of boundary conditions, nested grid technology (one-way nested grid model without a feedback) was used (Kubryakov, 2004), see below. Thus, necessary data on the open liquid borders of area were delivered by a basin-scale model of circulation of MHI (Demyshev and Korotaev, 1996), (Dorofeev and Korotaev, 2004).

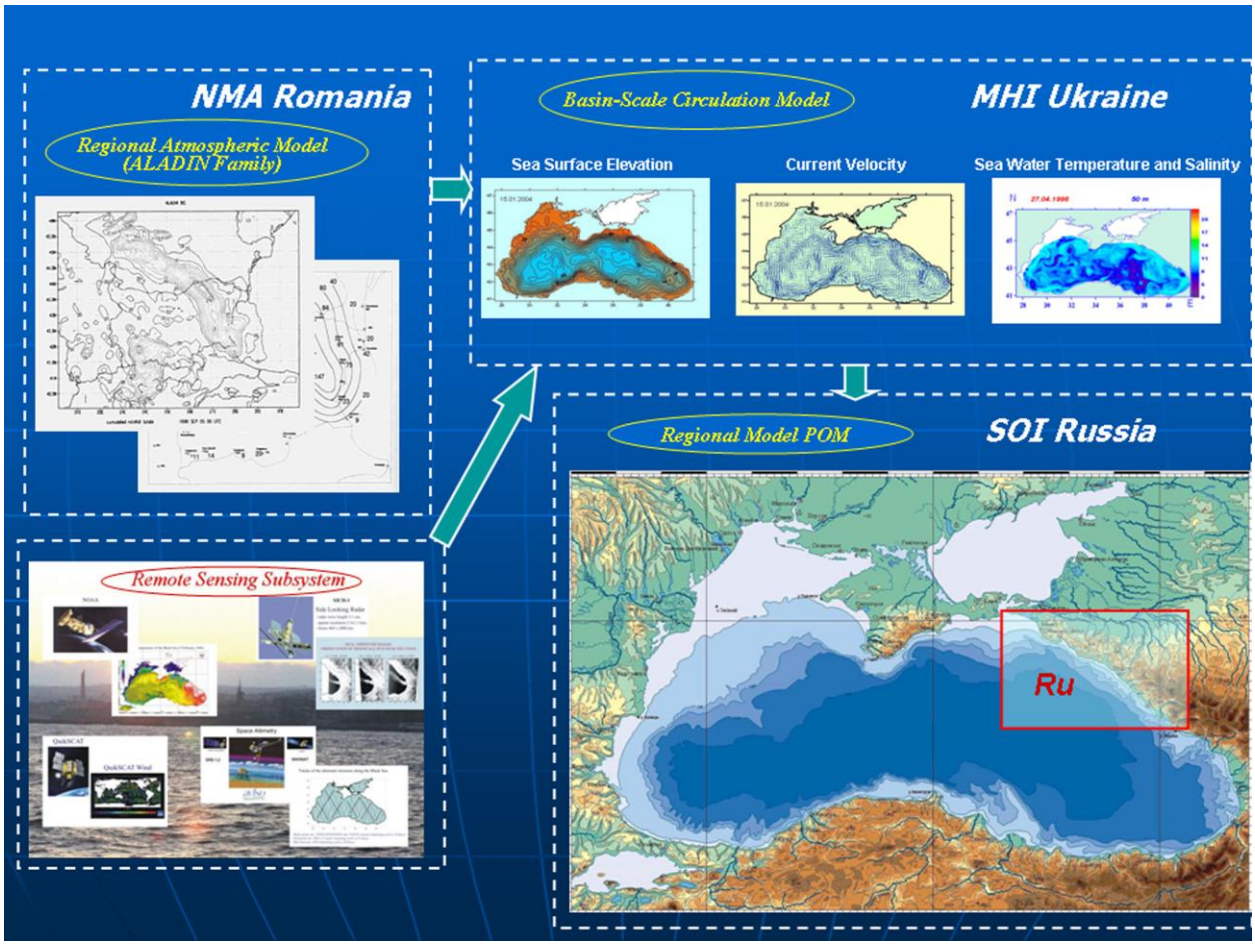

Fig. 1. System of nowcasting and forecasting of Black Sea water dynamics.

Calculations for the Russian zone of the Black Sea were carried out in the test mode for debugging of technology. The results of the design were compared with the information of in situ (CTD) and remote (SST) observations. An example of these results is shown in Fig.2-5.

One of the first calculations was carried out for the period of 7 June until 14 June 2003. The result of calculations of a field of speed and corresponding in time satellite picture (NOAA) of sea surface temperature (SST) is shown in Fig.2. As seen in Fig.2, the model reproduces both anticyclonic vortexes located on the slope zone with a characteristic horizontal scale of ~80 km (Az_1), and vortexes diagnosed according to the contact and satellite measurements eddies with a scale of ~15 km (Az_2).

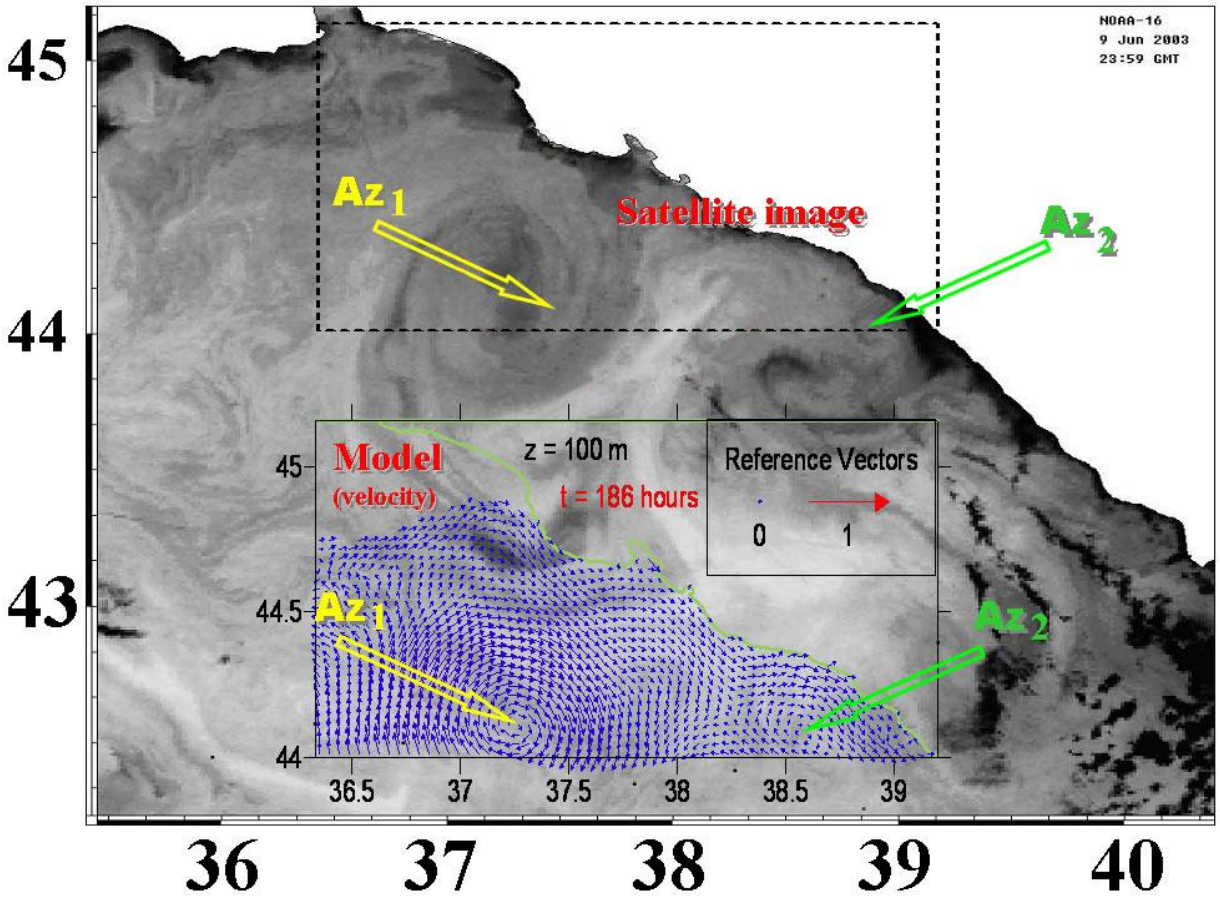

Fig. 2. Comparison of the modeled results (currents) with satellite image. The dotted line allocates area of modeling.

Comparison of modeled results with in situ data has been performed by using the contact measurements (CTD) obtained by R/V *Akvanavt* of "Shirshov's" Institute of Oceanology (IO RAS) in July 2005. In Fig. 3, the regions of R/V *Section* and modeling are shown.

For example, the difference in the distributions of salinity sections constructed from the modeled and in situ data (Fig. 4) can be described as follows. The anticyclonic deflection of the isolines takes place both in CTD and modeled distribution of salinity. Along the section it has the same location. The halocline in the observed data is expressed more clearly than in the modeled. The isolines with equal values in the modeled data are about 20 meters deeper than in situ. In general we can note the qualitative agreement between the modeled and in situ data.

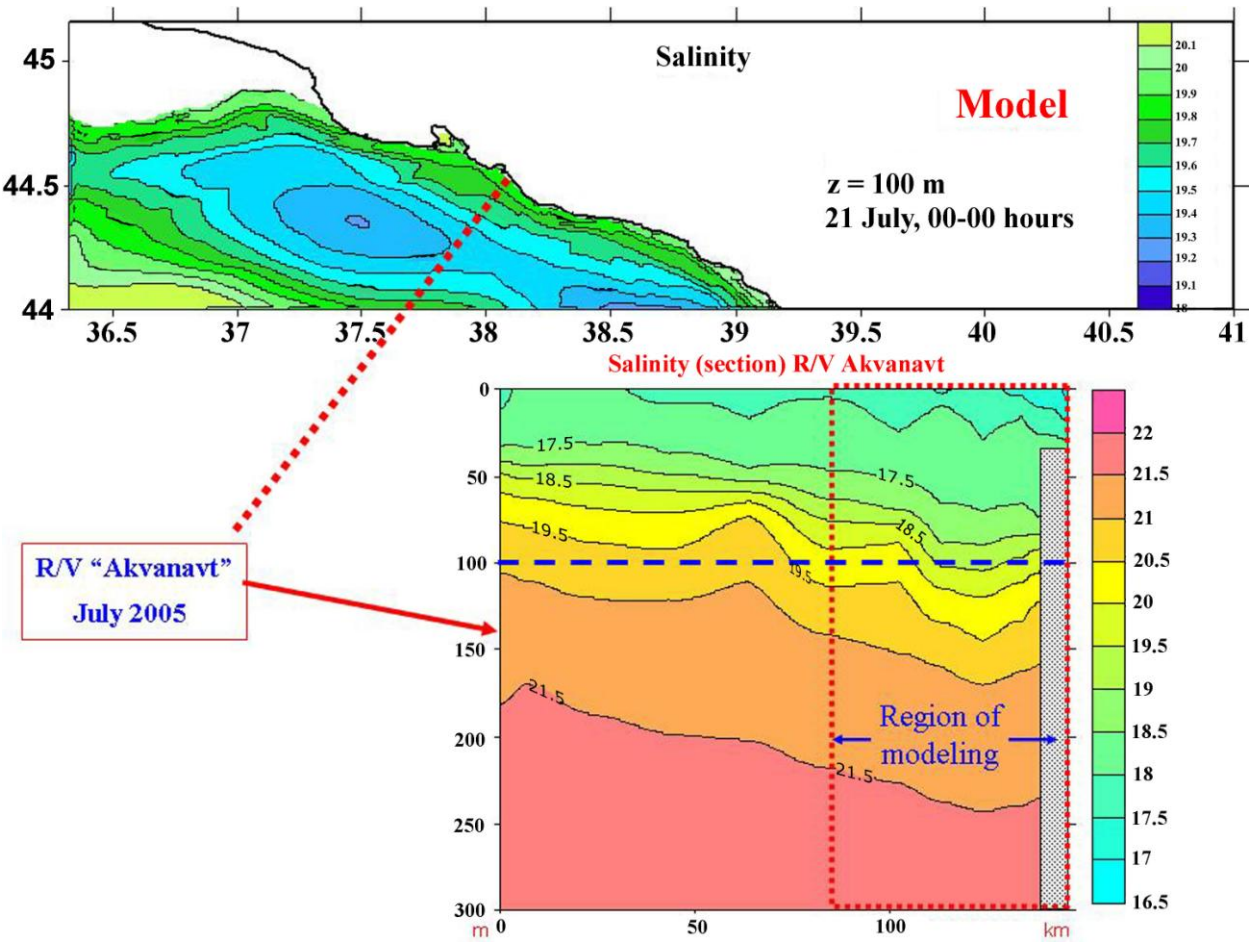

Fig. 3. Region of R/V *Akvanavt* section and modeling area.

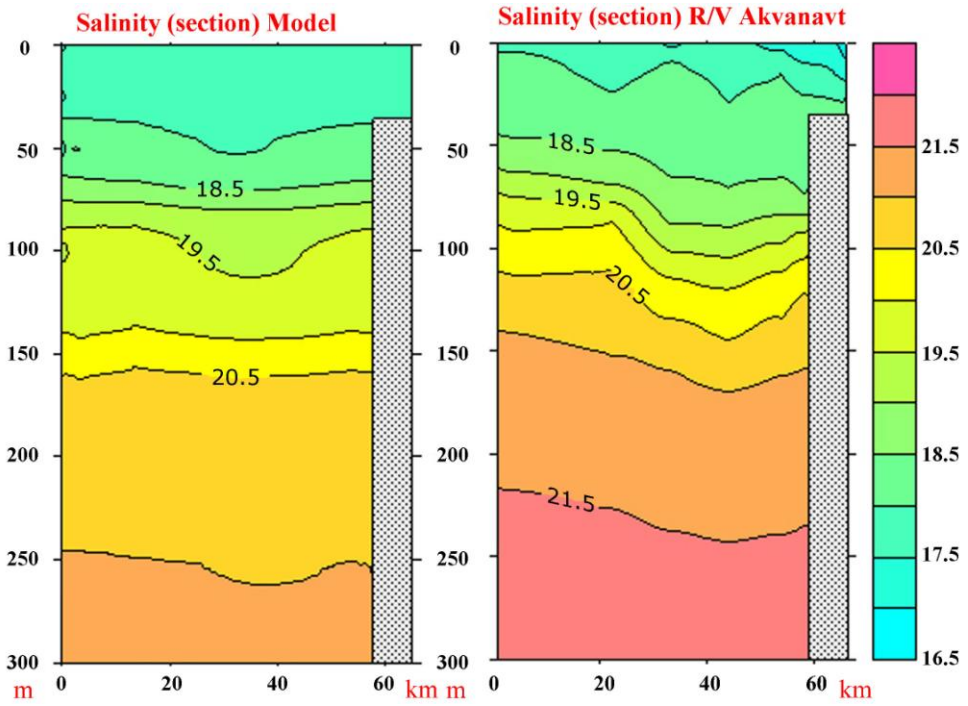

Fig. 4. Comparison of the modeled results (salinity) with in situ data (R/V *Akvanavt*), sections.

Comparison of modeled spatial distributions of salinity with satellite image received during the R/V *Aquanavt* cruise, shows a spatial displacement modeled salinity anomalies caused by anticyclonic eddies, with respect to remote data (Fig. 5). But qualitatively, the modeled vortexes correspond to the satellite image and their spatial sizes are the same (Az_3, Az_4).

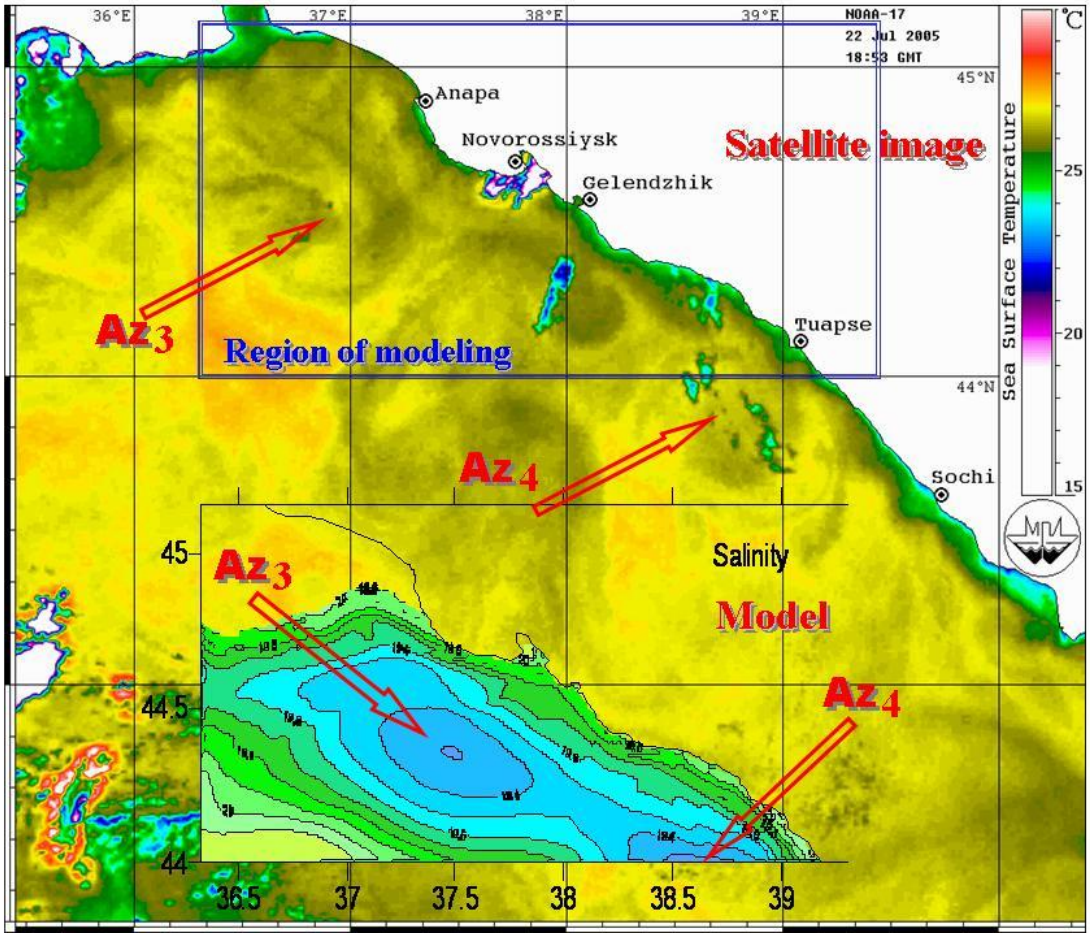

Fig. 5. Comparison of the modeled results (salinity) with satellite image (SST).

Resume of intercomparison between the Russian coastal zone nested model data and the data obtained during the ARENA project (R/V *Akvanavt* cruises and sattelite data) may be follows. Results of modeling are in general physically identical, increasing a spatial permit of processes allows reproduce in calculations the detail of hydrological structure, which do not find displaying in large-scale models. In particular, the eddies with horizontal spatial sizes ~10 km. Model calculations reproduce observed real dynamic structures. Their spatial position not wholly well complies with observed data. The main features of calculate parameters have a good correspondence with a measurements.

Thus, calculations of coastal circulation of waters of Black Sea by a nested grid method have shown the reasonable consent of the received results with available representations about dynamics of waters in considered area. The received conformity of results of modeling calculations to data in situ and remote supervision gives to hope for an opportunity of satisfactory realization of monitoring of hydrophysical fields in coastal area of Black Sea on the basis of use of the described technology for the developed series of regional models (Kubryakov et al., 2006).

Note, the debugging of technology before (and during) ECOOP project was done in close collaboration and cooperation with colleagues from other near Black Sea countries, and especially MHI. In particular, in terms of nesting and the parameterization of surface heat flux. These questions are highlighted in the work of our colleagues (Kubryakov et al., 2004-2011, Kordzadze et al., 2008, 2011) and will not be shown in this article.

During the ECOOP project the calculations were carried out daily for about 2 years, making it possible to obtain a large amount of simulation results. The formal parameters of the numerical regional model according to the terms of the Project in this case were the following: the grid for Russian zone of the sea had dimension 304x254 points and lay in borders of 43.0^{o}-45.26^{o} northern latitude and 37.25^{o}-41.0^{o} east longitude. Horizontal resolution of regional model is ~1 km at 18 vertical sigma-layers (Table 1). The number of vertical layers was limited by computational possibilities (the task was to provide daily the forecasting for 3 days ahead). The sigma-coordinates was follows: 0,-0.004,-0.009,-0.013,-0.022,-0.034,-0.046,-0.058,-0.079-0.11,-0.171,-0.268, -0.366,-0.463,-0.561,-0.78,-0.902,-1. We did not notice any problems with calculation of the pressure gradient forces using the terrain -following grids. The conditions at the lateral boundary: free slip for the flow and zero normal fluxes of salt, heat and momentum.

The cold intermediate layer (CIL) of the Black Sea in this case was resolved and well expressed not only by regional POM, but by the basin scale z-model (Dorofeev and Korotaev, 2004).

Main features of models	**Type**	**Vertical coordinates**	**Grid size**	**Number of grid points**	**Time step**
Basin scale model (MHI)	**MHI-model with remote sensing data assimilation**	**Fixed levels in the vertical z-direction**	**~ 4900 m**	**237 x 131 x 35**	**600 s**
Northeastern Russian Coastal Zone Regional Model	**POM-model**	**Terrain following σ-coordinates**	**~ 1000 m**	**304 x254 x 18**	**120 s (baroclinic mode) 3 s (barotropic mode)**

Table 1. Main features of global and regional models.

As in ARENA case, nested grid technology was used. Necessary data on the open liquid borders of area were calculated by a basin-scale model of circulation of MHI. MHI model uses satellite data assimilation of altimetry and sea surface temperatures and also meteorological data (wind stress, flows of heat and mass) received from the National Meteorological Administration of Romania within the framework of the European cooperation (Fig. 1). The SOI receives the necessary border conditions for the regional Russian model in a daily mode from the MHI server and makes nowcasting and forecasting (for 3 days) calculations of thermohaline structures and water dynamics of the region. The initial data for the forecast is generated daily as a result of the MHI Black Sea Forecasting Operational System work (BSFOS).

Values of parameters in nodes of regional models were calculated first with the use of horizontal linear interpolation of the values in the adjacent nodes of a basin-scale grid, and then by means of splines using vertical interpolation. Total fluxes through the section border in regional and basin-scale models strictly coincided. Both normal and tangential components of baroclinic velocity are specified by the coarse basin scale model interpolated fields, but after application of transport constraint to preserve coarse basin scale model transport. So

$$U_{POM}^{tang} = U_{COARSE}^{tang}$$

$$U_{CORR}^{normal} = U_{INTERP}^{normal} \cdot \left(\frac{Q_{COARSE}}{Q_{INTERP}} \right)$$

In boxes where water flowed into the high-resolution area, values of temperature and salinity were set. In points where water flowed out, the condition was used:

$$\frac{\partial T}{\partial n} = \frac{\partial S}{\partial n} = 0 .$$

For the barotropic mode of normal component of barotropic speed on eastern and western borders, the following conditions were used:

$$\overline{U}_{POM}^{normal} = \overline{U}_{COARSE}^{normal} + \varepsilon \sqrt{\frac{g}{H}} (\eta_{POM} - \eta_{COARSE}),$$

where $\varepsilon = 1$ for the eastern border and $\varepsilon = -1$ for the southern border; η – sea level. The subscript *"coarse"* specifies a large-scale model. *CORR* - corrected; *INTERP* - interpolated; *Q* - is the total mass flux through the lateral liquid wall.

The atmospheric forcing was the same as for MHI model, and the same with bathymetry, but interpolated to the regional grid. The atmospheric data was received from MHI ftr-server in common “CoarseFilds” files of boarder conditions. The impact of the river flow was considered to be not essential in Russian zone of Black Sea.

The process was fully automated in SOI and includes four stages (Fig. 6):

- receipt of initial information from the MHI ftp-server by internet;
- realization of model calculations;
- visualization of the results of calculations (temperature, salinity, current velocity, sea level);
- transmission of results to the SOI server and website and for use in the national JSIWO program (Fig. 7).

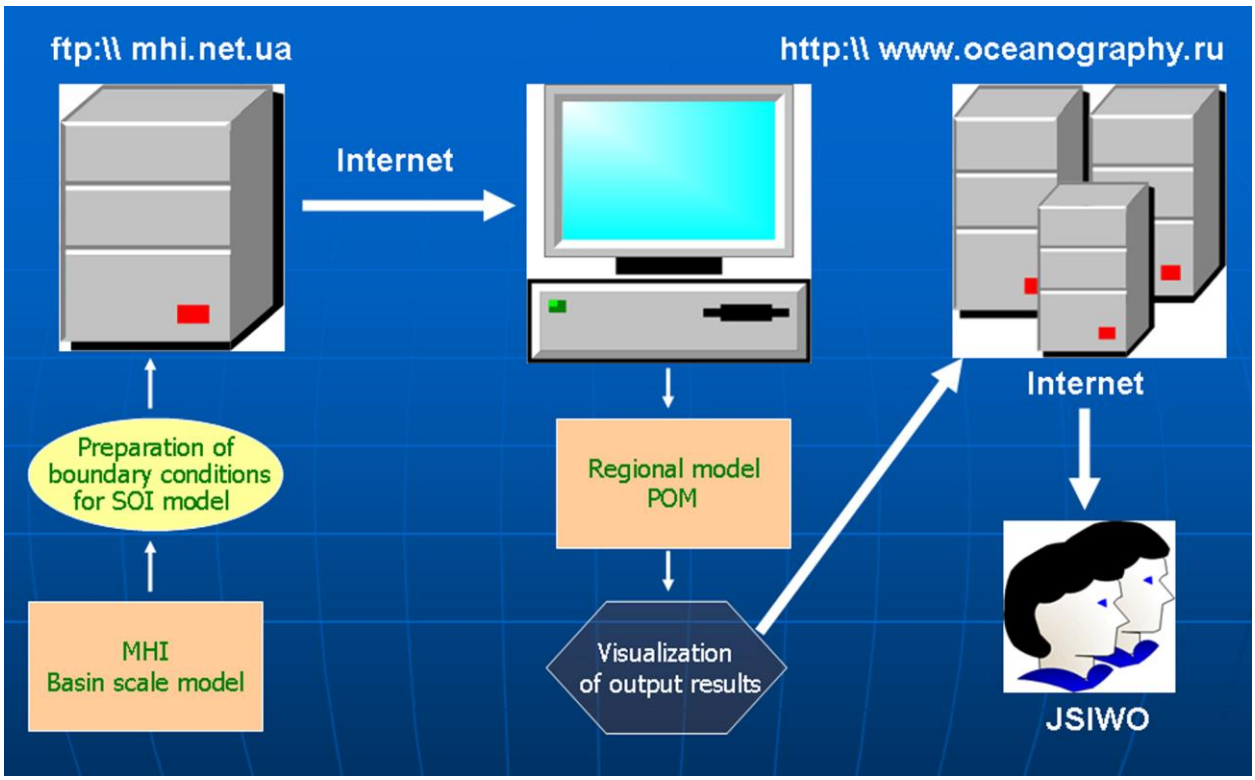

Fig. 6. Scheme of SOI automated system.

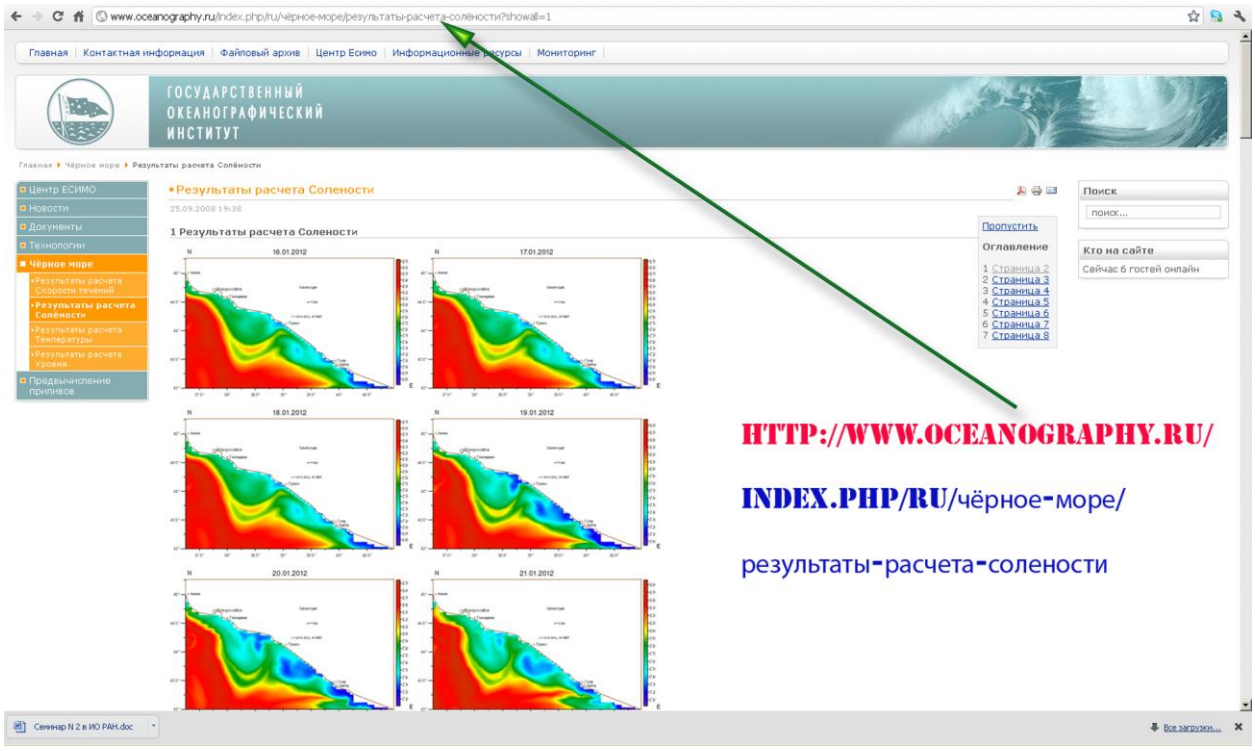

Fig. 7. Example of modeled results shown on the SOI website (in Russian).

It is interesting to compare the results with the measured data, in situ and remote, to assess the quality of modeling of dynamics and the thermohaline structure of waters in that Black

Sea region. Comparison of modeled results with in situ and remote data has been performed. Contact measurements (CTD) obtained by R/V *Professor Shtokman* of "Shirshov's" Institute of Oceanology (IO RAS) for the period of 9 March until 2 April 2009 were used. In Fig. 8, the regions of R/V *Survey* and modeling are shown.

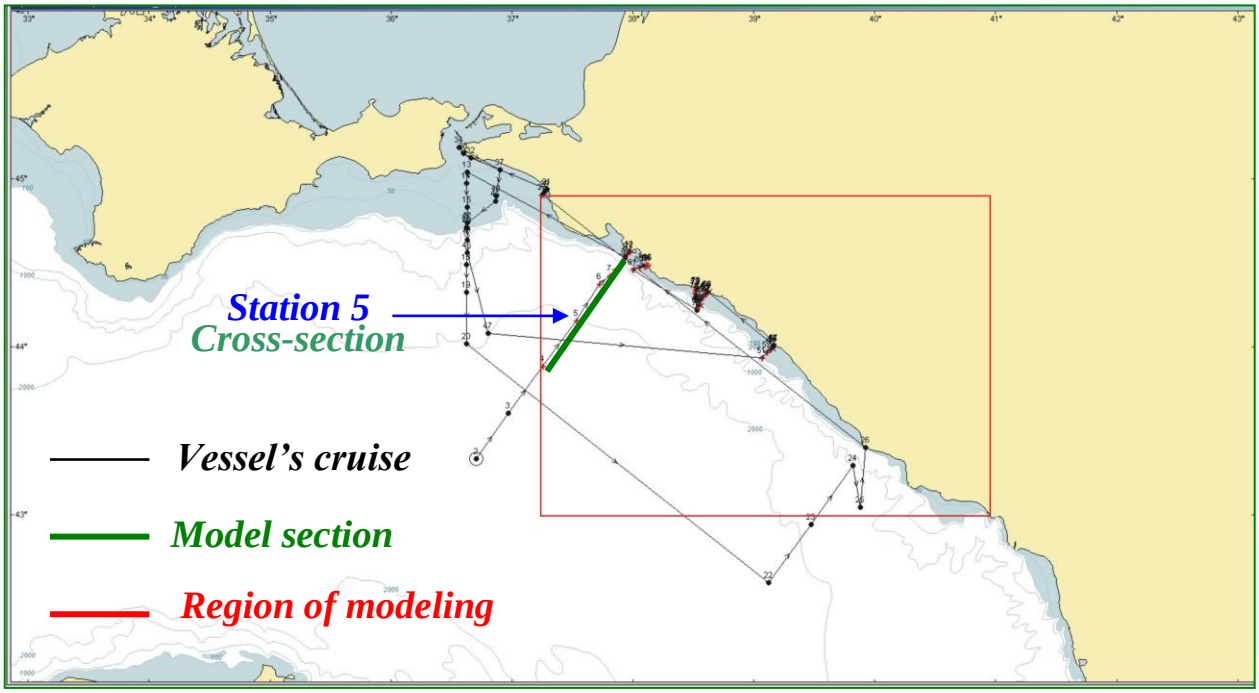

Fig. 8. Region of R/V *Professor Shtokman* survey and modeling area.

It should be noted at the beginning that some characteristics of water in the region in March should be reflected in the measurement data and modeling (Blatov and al., 1984). The vertical structure is an upper quasi-homogeneous layer (UQHL, several tens meters), thermo-halo- pycnocline below to depths of 500 m and the underlying quasi-homogeneous layer. The main feature of the vertical structure of the waters of the Black Sea is the so-called cold intermediate layer (CIL) with the axis at depths of 50-100 m depending on the point of observation. Rim Current has extending along the continental slope, roughly along the isobath 1200 m, and produces a general cyclonic circulation in the sea. In the area of the continental slope, the eddies with spatial scales of ~ 100 km are also observed, and directly in the shelf-slope zone - anticyclonic eddies with horizontal dimensions are about 10 km (see Fig. 2). These dynamic characteristics are reflected in the distributions of isolines in the cross-sections. Note also that the salinity is a major contributor to the spatial distribution of the density of Black Sea water, determining its dynamics. Therefore, profiles, sections and maps are constructed from the values of salinity, the most informative in analyzing the features of water dynamics in the region.

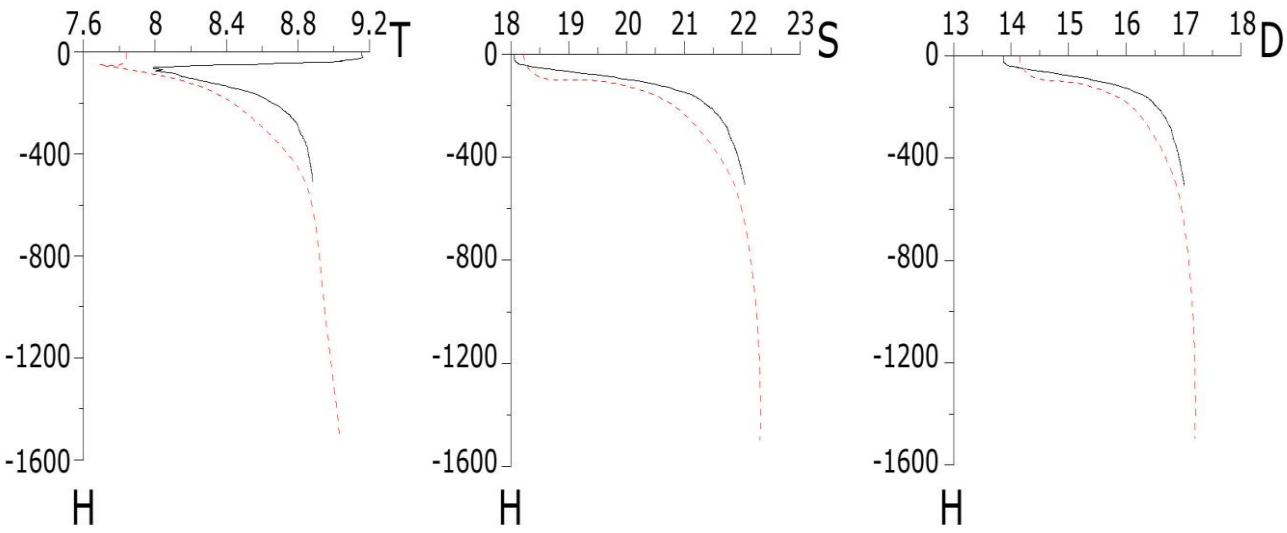

Fig. 9. Vertical profiles of temperature (*T*), salinity (*S*) and density (*D*) for Station No. 5 from CTD data (black) and modeling (red).

Vertical profiles built both from CTD and modeled data reflect the typical vertical structure of waters in the region in March (Fig. 9, for hydrological Station 5), in particular, the presence of the upper quasi-homogeneous layer (UQHL) with a capacity of ~ 40 m, the cold intermediate layer (CIL) with the axis at a depth of 60 m, the main pycnocline to depths of 500 m and the underlying quasi-homogeneous layer. The vertical profiles of salinity and density are of the same type because the water density in Black Sea is mostly defined by salinity. Qualitatively, the model and the observed profiles are very similar. For the salinity difference in values of the order of ~0.1$^{o}/_{oo}$, for the temperature there is the same order in degrees ^{o}C at depth. A maximum difference in temperatures is observed on a surface – approximately 1.5 ^{o}C. As the research of colleagues from MHI showed, this failing can be decreased by including the penetration of short-wave radiation (Kubryakov and al., 2011). But during the experiment we did not include this effect in SOI technology because do not receive the necessary information about the heat flows.

Distribution of thermohaline characteristics at a cross-section perpendicular to the coast (see Fig. 8) is typical for the Black Sea, and shows a decline in the depth of isolines from coast to the center of the sea, caused by a general cyclonic circulation (Fig. 10). The section shown in Fig. 7a is built from asynchronous CTD-data made by R/V *Professor Shtokman* in the period 10/03/2009-13/03/2009. Figure 10b is built from model data corresponding to the points and times of ship observations. Comparing Fig. 10a and b, we can conclude that the salinity distribution in sections are similar and have similar quantitative values. As the differences can be noted, large vertical salinity gradients in halocline on the cross-section, which was built from CTD-data. But reducing the spatial discreteness of the model data in cross-section is well defined deflection contour lines in the slope (right side of Fig. 10c) due to the presence of the anticyclonic vortex with the spatial size of ~ 10 km (see Fig. 11a). Analysis of a similar section for the temperature gives the same results. A similar distribution of isolines on the edge of the continental slope of Black Sea is fixed often from CTD data of many hydrological surveys with a small horizontal step (~1 km).

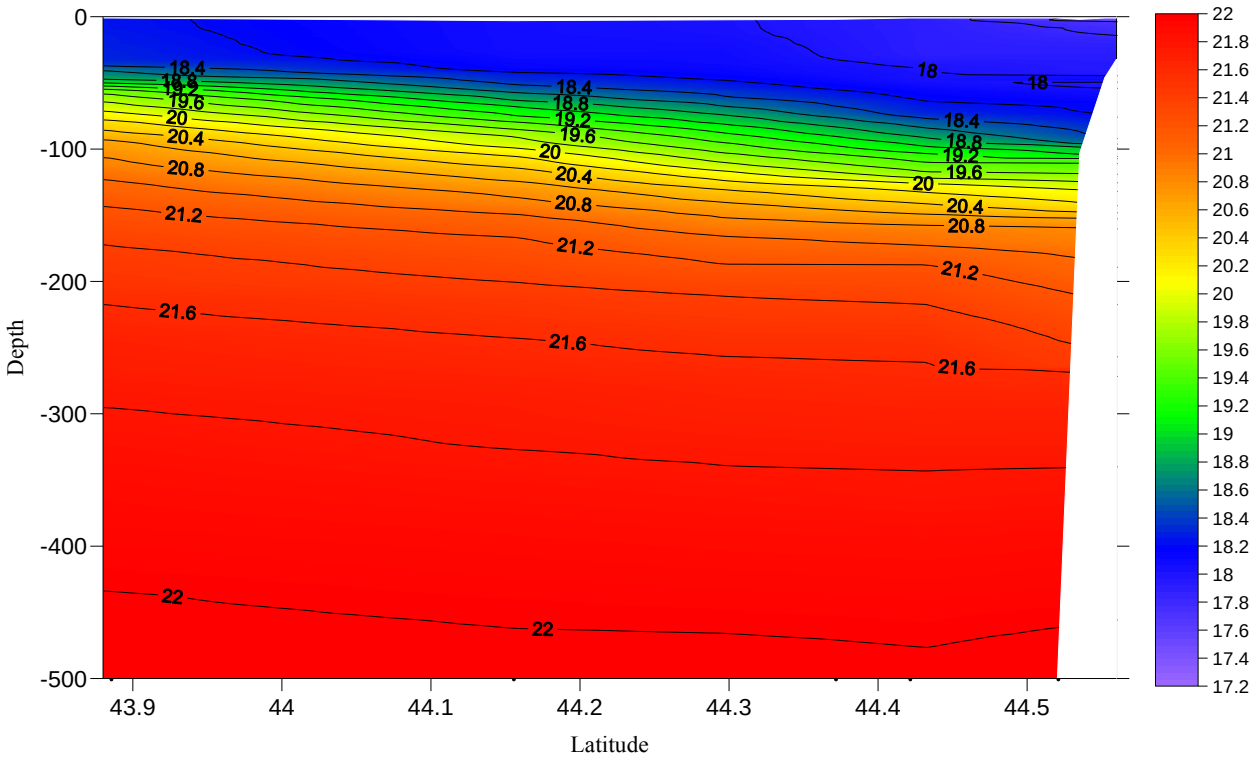
Depth
Latitude
0
-100
-200
-300
-400
-500
43.9
44
44.1
44.2
44.3
44.4
44.5
18
18.4
18.8
19.2
19.6
20
20.4
20.8
21.2
21.6
22
17.2
17.4
17.6
17.8
18
18.2
18.4
18.6
18.8
19
19.2
19.4
19.6
19.8
20
20.2
20.4
20.6
20.8
21
21.2
21.4
21.6
21.8
22

(a)

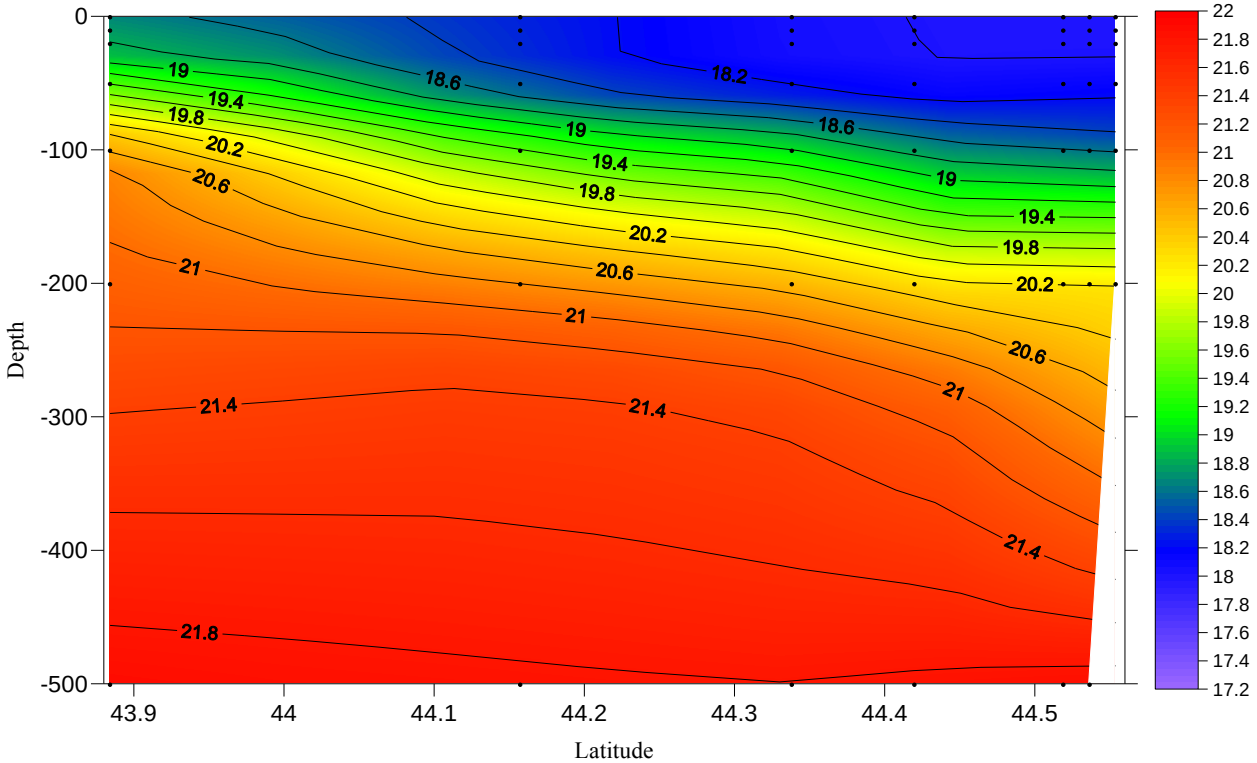
Depth
Latitude
0
-100
-200
-300
-400
-500
43.9
44
44.1
44.2
44.3
44.4
44.5
18.2
18.6
19
19.4
19.8
20.2
20.6
21
21.4
21.8
17.2
17.4
17.6
17.8
18
18.2
18.4
18.6
18.8
19
19.2
19.4
19.6
19.8
20
20.2
20.4
20.6
20.8
21
21.2
21.4
21.6
21.8
22

(b)

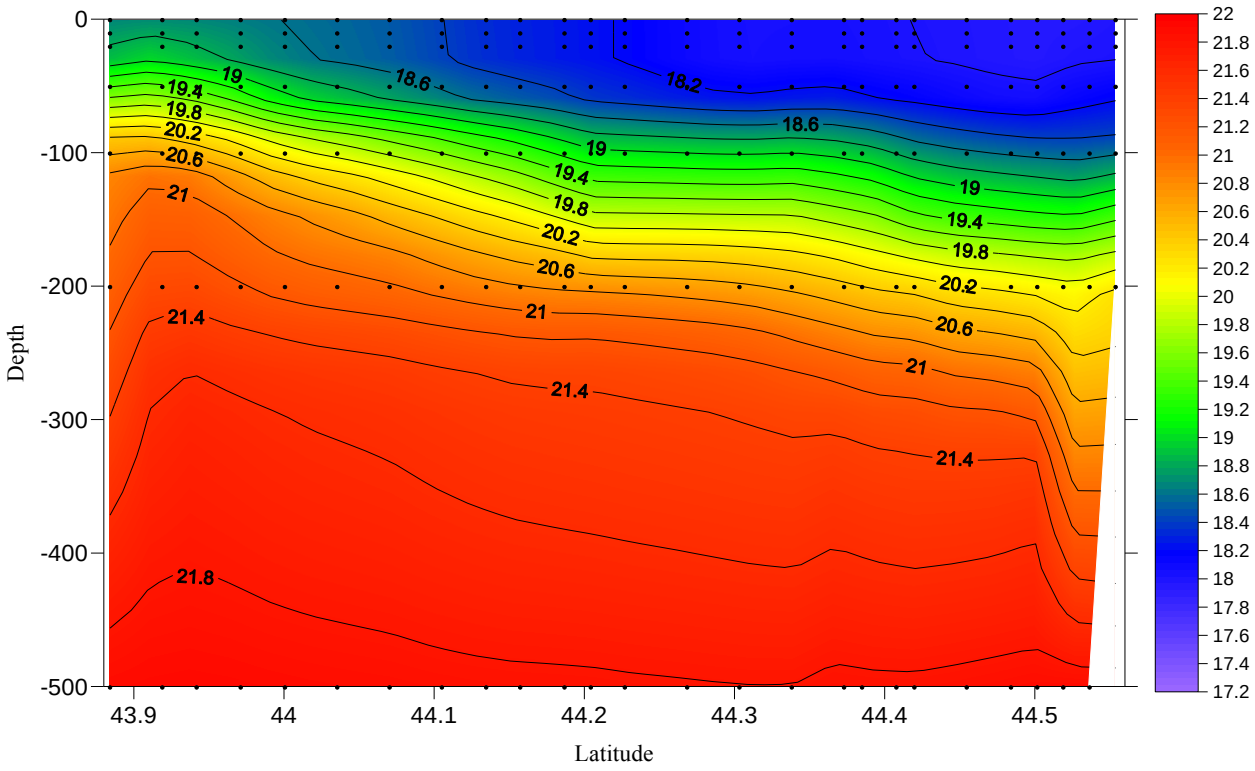

(c)

Fig. 10. Distribution of salinity on a cross-section (see the Fig. 5), obtained from CTD data **(a)** and model data **(b, c).**

Synoptic variability in space and time is clearly expressed in the model calculations of water dynamics in the region. As an example, the model velocity fields corresponding to the beginning and end of hydrological survey R/V *Professor Shtokman* is shown in Fig. 11, and the model temperature and salinity fields corresponding to the beginning and end of section in the period 10/03/2009-13/03/2009 is shown in Fig. 12, 13. With regard to estimates of the degree of differences of model and measured values, then, due to high degree of asynchrony of the hydrological survey, comparison between measured (in situ) and modeled data does not make any sense. Therefore, the estimations of quality of modeling are possible using remote sensing. Examples of comparisons of modeled data with satellite observations are shown in Fig. 14, 15.

Thus, synoptic eddies, reflected in the salinity field (model) and the concentration of chlorophyll A (satellite image) show a high correspondence in the spatial size and horizontal location (Fig. 14). As noted earlier, the salinity fields to better reflect the dynamics of the waters of the Black Sea in comparison with the fields of temperature. As well as images of chlorophyll are the best to fix the dynamic structures and their evolution than the SST (Sea Surface Temperature) images. Unfortunately, the analysis of of conformity the salinity fields and satellite images has only qualitative character. To obtain quantitative characteristics of the spatial accuracy of model estimates makes sense to use a fields of sea surface temperature. For example, the RMS of the difference between the model and the measured SST in area of modeling for 2 July, 2009, was equal to RMS=1.1^{o}C (Fig. 15) and it is typical value. The comparison of modeled temperature field, shown in the Fig. 15, with satellite data also demonstrates their qualitative agreement. But using some standard methods to assess the quality of the model output in extended period of time was not performed, because modeled and observed sea surface temperatures have a big difference. The reasons have been described above (heat flux).

As seen in the figures presented, some shift of location of T, S anomalies in modeled calculations concerning supervision takes place. For elimination of this effect, data assimilation in a local model can be used (now it can only be assimilated in a basin-scale model).

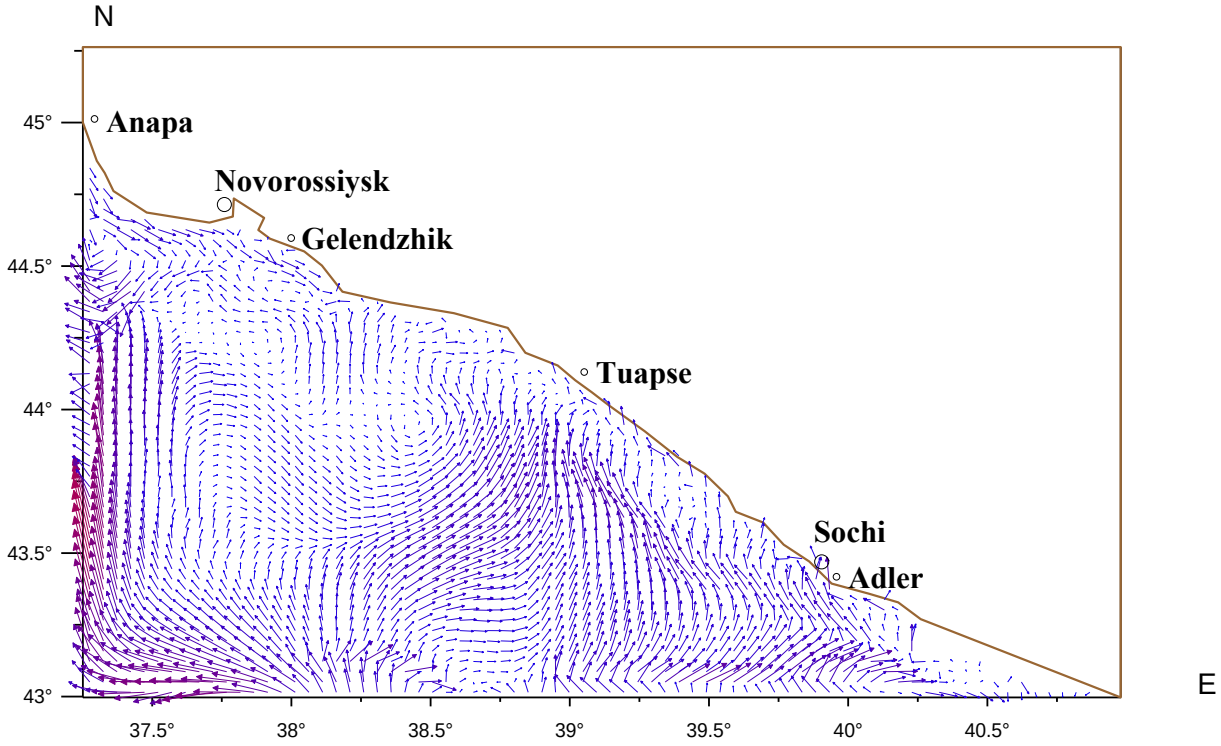

(a)

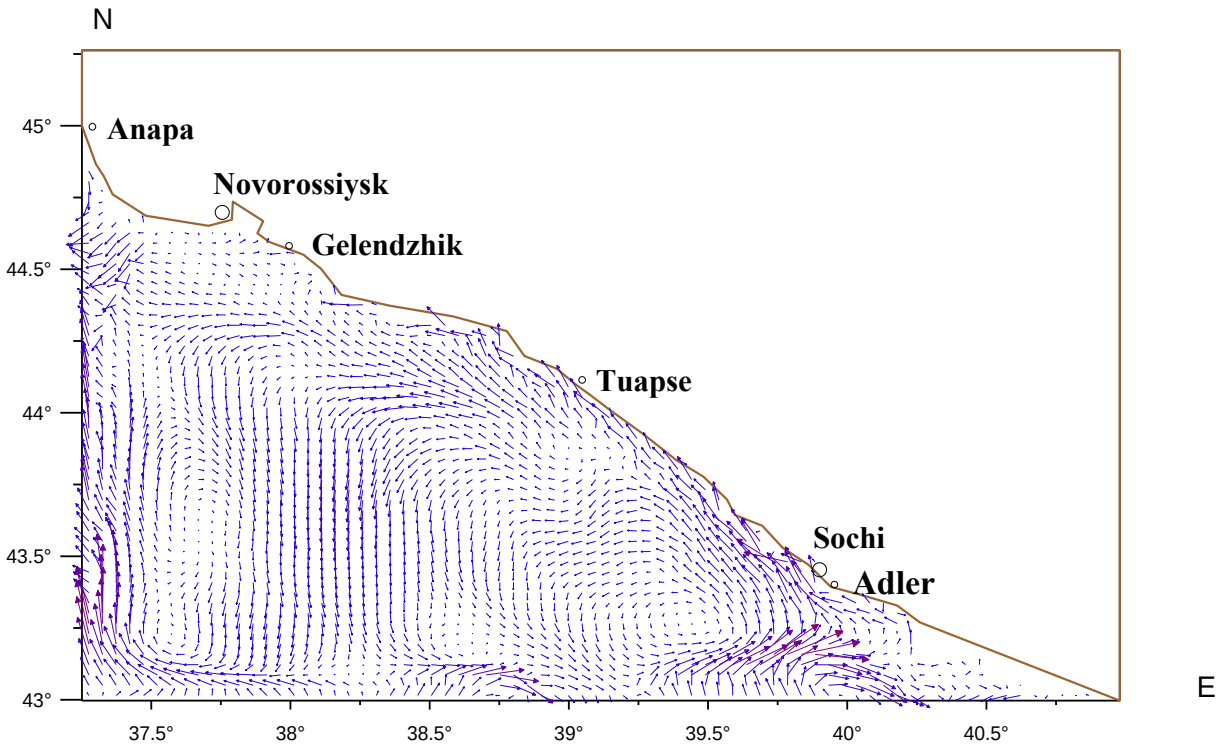

(b)

Fig. 11. Model fields of sea currents at a depth of 10 m 10/03/2009 **(a)** and 02/04/2009 **(b).**

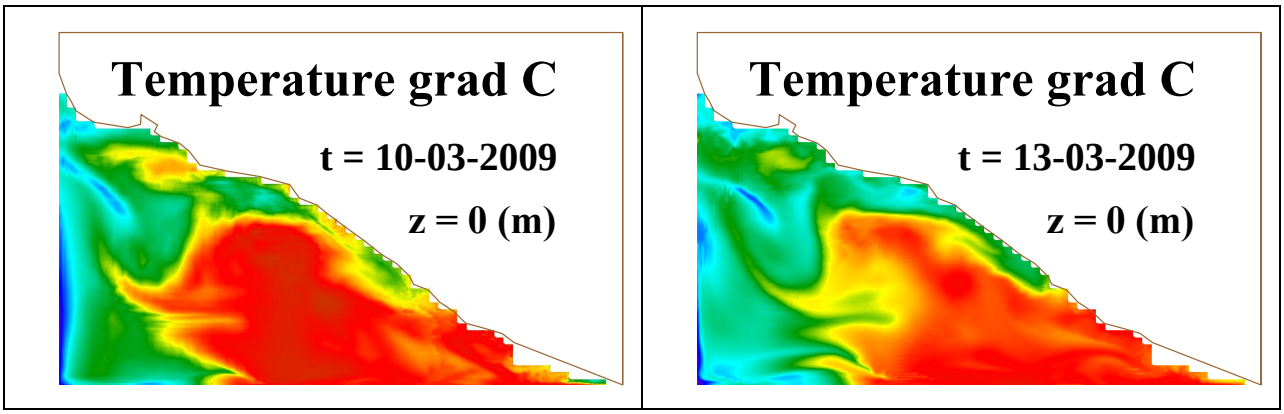

(a) **(b)**

Fig. 12. Model fields of temperature at a depth of 0 m 10/03/2009 **(a)** and 13/03/2009 **(b).**

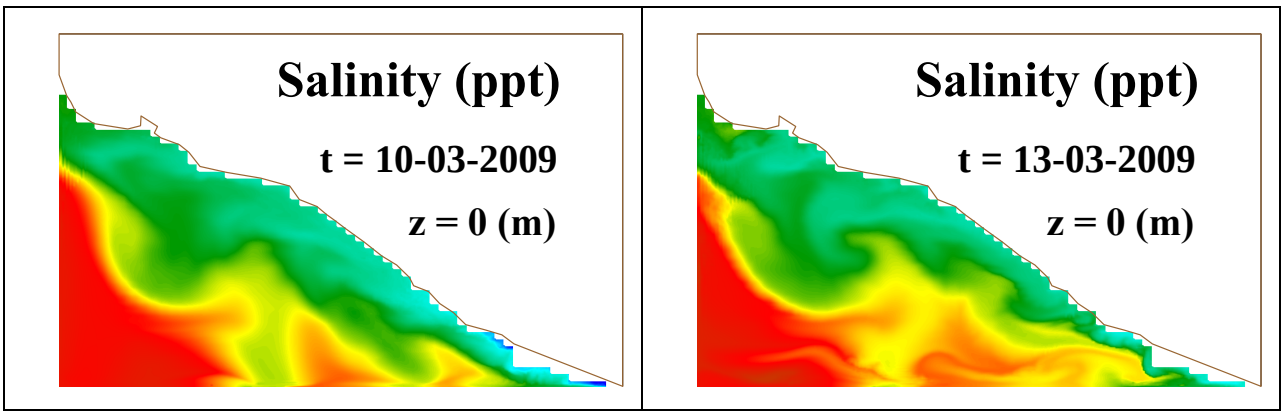

(a) **(b)**

Fig. 13. Model fields of salinity at a depth of 0 m 10/03/2009 **(a)** and 13/03/2009 **(b).**

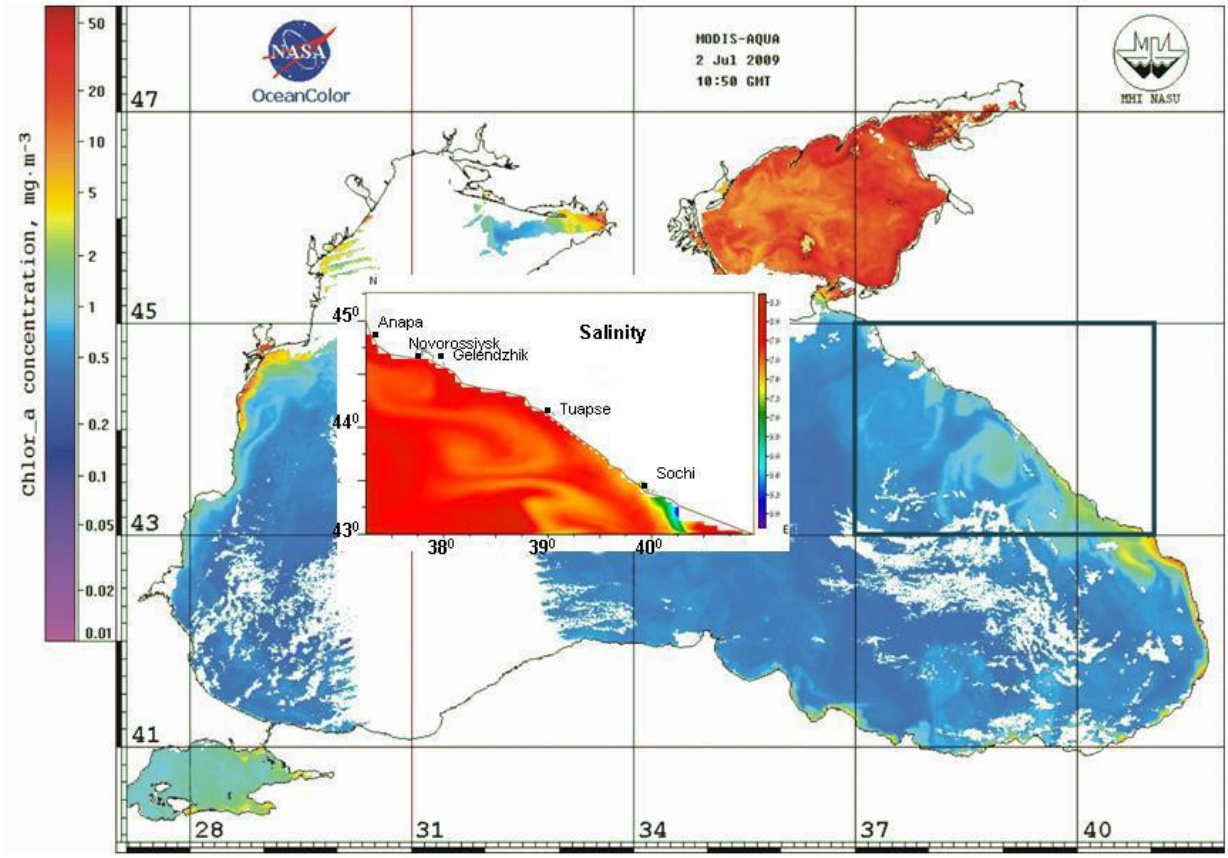

Fig. 14. Satellite image (Chlorophyll concentration) and modeled sea surface salinity at 2 July, 2009.

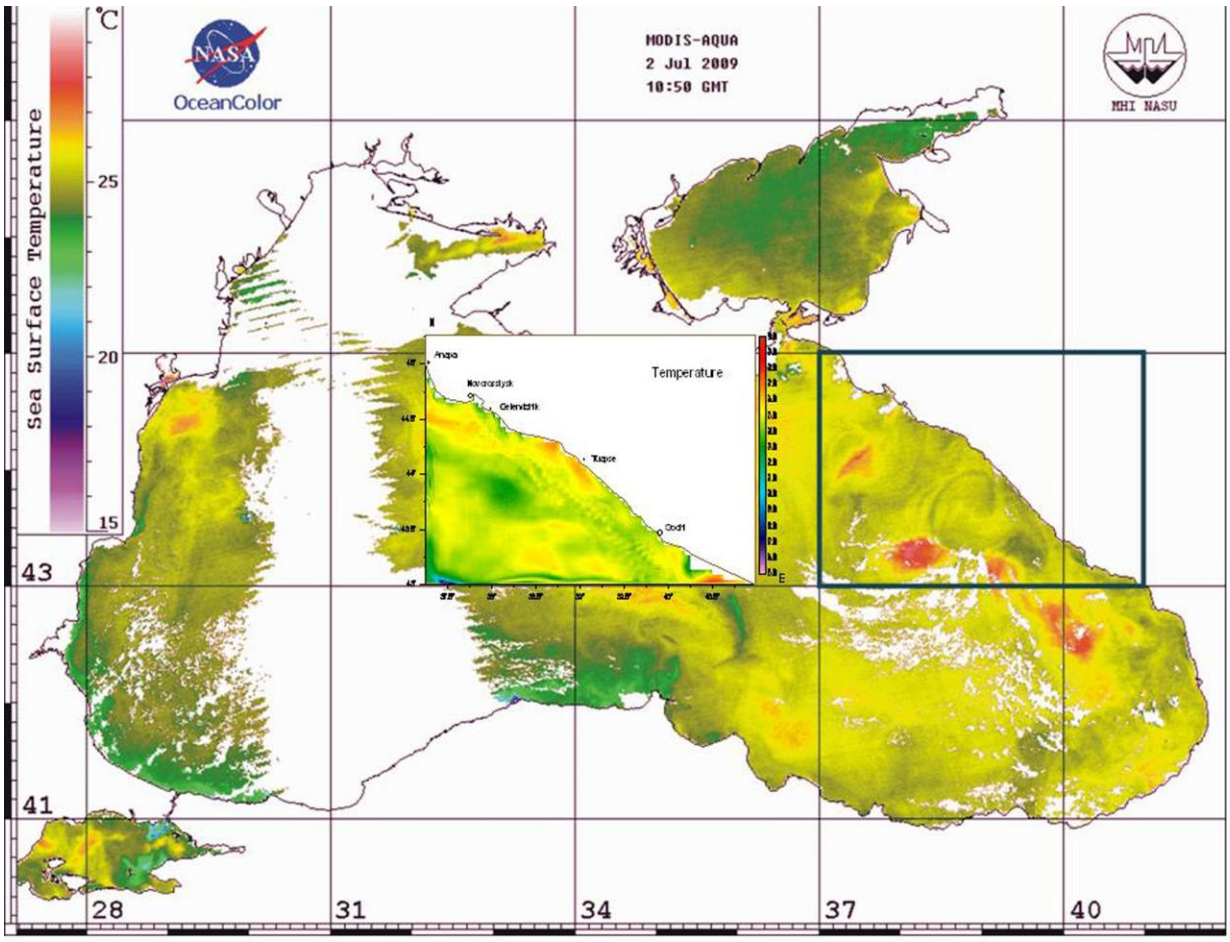

Fig. 15. Satellite image (SST) and modeled sea surface temperature at 2 July, 2009.

It is also interesting to analyze how the magnitude of the errors of forecasting (Fig. 16) is dependent on the time of forecasting. This is done using the information about temperature and salinity at the moments of contact measurements (for Station 5). For temperature, the minimum number of errors takes place in the case of 1-2 days forecasting (except the depths below CIL, where variability is considerably low than within UQHL). In the upper layers, the forecasting is closer to measurements than nowcasting (0 days in the Fig. 16). It is worth mentioning the considerable errors of modeled temperature in the upper layer. For salinity, the maximum of errors is located in the range of depths about 100-200 м (main halo- pycnocline). In the upper layers, the presence of local maximum of errors when forecasting for 2 days is distinct. But in general, a forecasting for 1 day (and at some depths for 3 days) does not yield or excels nowcasting in quality.

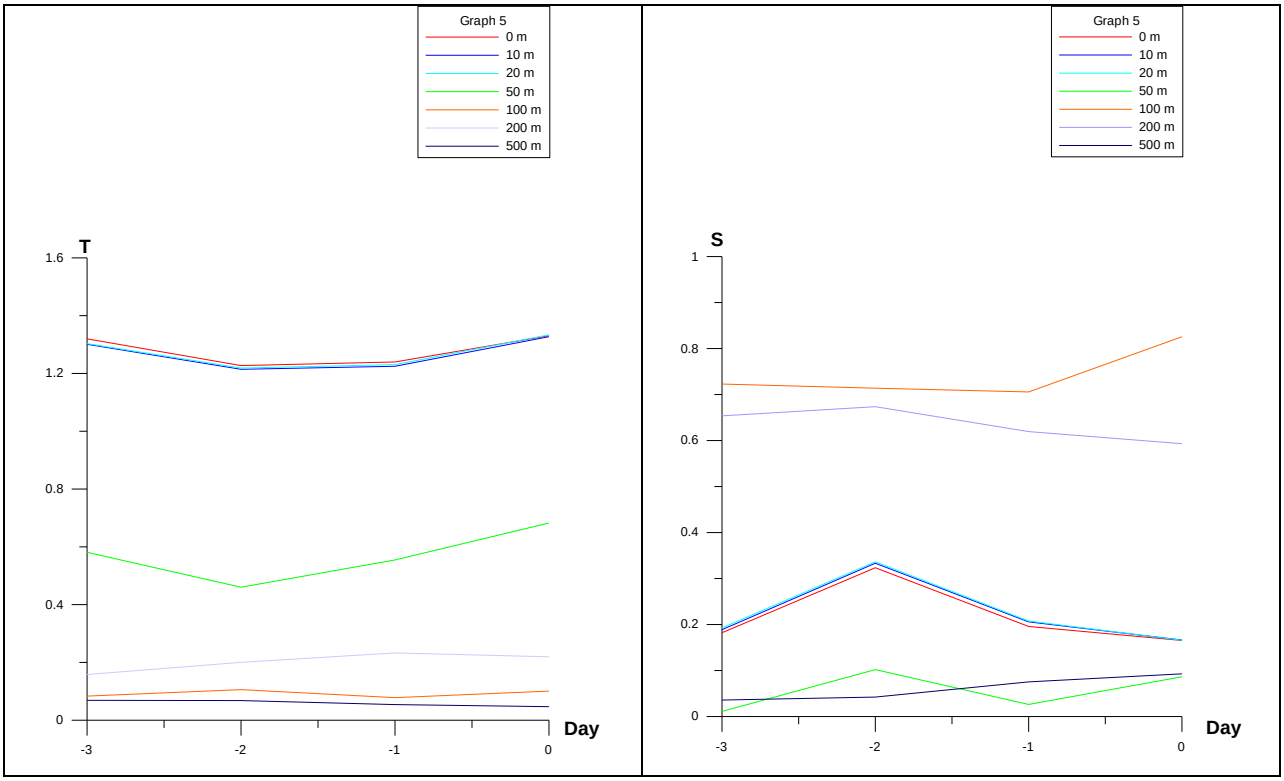

(a) **(b)**

Fig. 16. Differences (absolute value) between measured and modeled temperature **(a)** and salinity **(b)** as a function of time of forecasting (1-3 days, 0 is nowcasting). Station 5.

The reasons for such results could be following:

a) Nowcasting during the Project was carried out by the model for the time span of 1 day. Possibly, this time is not enough and it is necessary to increase that up to 2 days.

b) In addition, dynamic features of interaction between the currents and bottom relief and adaptation with the wind stress likely show up during the forecast, which finds the display in the variability of profiles of temperature and salinity.

Conclusions

During the Project, the automated system of modeling the dynamics of water of the Russian zone of Black Sea was created. It allows generation of physically adequate results of calculations of thermohaline structure of water and current fields. Such calculations are performed in nowcasting and forecasting (3 days) mode.

Results of modeling are in general physically identical. Increasing a spatial permit of processes allows reproduce in calculations the detail of hydrological structure, which do not principally find displaying in large-scale models (vortexes with horizontal spatial sizes ~10 km).

Model data reproduce observed real dynamic structures. The model and the observed vertical profiles are very similar. For the salinity difference in values of the order of ~0.1$^{o}/_{oo}$, for the temperature there is the same order in degrees ^{o}C at depth (but not at a surface). Synoptic eddies, reflected in the modeled salinity field show a high correspondence in the spatial size and horizontal location with satellite images. The comparison of modeled temperature field with satellite data also demonstrates their qualitative agreement. The typical RMS of the difference between the model and the measured SST was equal to RMS=1.1^{o}C.

Some shift of location of T, S anomalies in modeled calculations concerning supervision takes place. For elimination of this effect, data assimilation in a regional model can be used.

In addition to a satisfactory qualitative and quantitative agreement between the model data, CTD and remote measurements of the dynamics and water structure in the Russian Black Sea area, another result is important. On the basis of this experiment, the conclusion that the proposed modeling technology can adequately monitor the variability of the waters of the region with the spatial and temporal resolution, unattainable using only field data, can prove important for operational oceanography.

References

[1] Blatov, A.S., Bulgakov, N.P., Ivanov, V.A., Kosarev, A.N.,. Tujilkin, V.S.: Variability of the hydrophysical fields in the Black Sea. Leningrad, Gidrometeoizdat, p. 240, 1984. (in Russian).

[2] Blumberg, A. F. and Mellor, G. L.: A description of a three-dimensional coastal ocean model. in Three Dimensional Shelf Models, Coast. Estuar. Sci., Vol. 5, edited by: Heaps, N., 1-16, AGU, Washington, D. C., 1987.

[3] Demyshev, S.G., Korotaev G. K.: Numerical energy-balanced model of baroclinic currents in the ocean with bottom topography on the C-grid. In: Numerical models and results of intercalibration simulations in the Atlantic ocean. Moscow, 163-231, 1992. (in Russian).

[4] Dorofeev, V. L. and Korotaev, G.K.: Assimilation of satellite altimetry data in eddy-resolving circulation model of the Black Sea, Marine Hydrophysical J., 1, 52-68, 2004. (in Russian).

[5] Kordzadze A. A., Demetrashvili D. I., and Surmava, A.A.: Numerical modeling of hydrophysical fields of the Black Sea under the conditions of alternation of atmospheric circulation processes, Izvestiya RAS, Atmospheric and Oceanic Physics, 44, 4, 213-224, 2008.

[6] Kordzadze, A. A. and Demetrashvili, D. I.: Operational forecast of hydrophysical fields in the Georgian Black Sea coastal zone within the ECOOP, Ocean Science. 2011, 7, 793–803, www.ocean-sci.net/7/793/2011/, doi: 10.5194/os-7-793-2011.

[7] Kubryakov, A. I.: Application of nested grid technology at the development of the monitoring system of hydrophysical fields in the Black Sea coastal areas, Ecological safety of coastal and shelf zones and complex use of shelf resources, Issue 11, NAS of the Ukraine, edited by: Korotaev, G. K. and Kubryakov, A. I., Sevastopol, 31–50, 2004. (In Russian)

[8] Kubryakov, A., Grigoriev, A., Kordzadze A., Korotaev, G., Stefanescu, S., Trukhchev, D., and Fomin, V.: Nowcasting/Forecasting subsystem of the circulation in the Black Sea nearshore 20 regions, in: European Operational Oceanography: Present and Future, edited by: Dahlin, H., Flemming, N. C., Marshand, P., and Petersson, S. E., Proceedings of the Fourth EuroGOOS International Conference on EuroGOOS, 6–9 June 2005, Brest, France, ISBN 92-894-9788-2, 605–610, 2006.

[9] Kubryakov A. I., Korotaev G. K., Dorofeyev V. L., Ratner Yu. B., Palazov A., Valchev N., Malciu V., Matescu R., and Oguz T.: Black Sea coastal forecasting systems, Ocean Sci. Discuss., 8, 1055–1088, 10 doi:10.5194/osd-8-1055-2011, 2011.

[10] Kubryakov, A., Korotaev, G., Ratner, Yu., Grigoriev, A., Kordzadze, A., Stefanescu, S., Valchev, N., and Matescu, R.: The Black Sea Nearshore Regions Forecasting System: operational implementation, Coastal to Global Operational Oceanography: Achievements and Challenges, edited by: Dahlin, H., Bell, M. J., Flemming, N. C., and Petersson, S. E., Proceedings of the Fifth International Conference on EuroGOOS, 20–22 May, Exeter, UK, 293–296, 2008.

[11] Mellor, G. L.: User's guide for a three dimensional, primitive equation, numerical ocean model, report, Program in Atmos. and Ocean. Sci., Princeton Univ., Princeton, 3, 35 pp., 1991.
[12] Mellor, G. L. and Yamada, T.: Development of turbulence closure model for geophysical fluid problems, Rev. Geophys., 20, 851-875, 1982.
[13] Zatsepin, A. G., Ginzburg, A. I., Kostianoy, A. G., Kremenetskiy, V. V., Krivosheya, V. G., Stanichny, S. V., and Poulain, P. M.: Observations of Black Sea mesoscale eddies and associated horizontal mixing, J. Geophys. Res.,. 108, C8, doi.:10.1029/2002JC001390, 2003.

Численное моделирование динамики вод Российского сектора Черного моря в рамках задач оперативной океанографии

Александр В. Григорьев, Андрей Г. Зацепин

Моделирование динамики вод Черного моря (российская зона) проводилось в рамках европейских проектов ARENA и ECOOP и российского проекта JISWO на основе Принстонской модели океана (POM). Диагноз и прогноз динамики Черного моря на 3 суток проводился в ежедневном режиме с горизонтальным разрешением 1 км для российской зоны бассейна. Приводятся примеры расчетов и их сравнение с данными дистанционных (спутниковых) и *in-situ* (гидрологические измерения) наблюдений, обсуждаются результаты валидации модели. Модельные данные воспроизводят наблюдаемые реальные динамические структуры. Увеличение пространственного разрешения позволяет воспроизводить детали гидрологической структуры (вихри с горизонтальными пространственными размерами ~10 км), которых в принципе невозможно описать в крупномасштабных моделях. Модельные и наблюдаемые вертикальные профили очень сходны. Пространственные размеры и горизонтальные положения синоптических вихрей, которые проявляются в модельном поле солености, находятся в хорошем соответствии со спутниковыми изображениями. Сравнение модельного температурного поля со спутниковыми данными также демонстрирует их количественное совпадение.

შავი ზღვის რუსეთის სექტორის წყლების დინამიკის რიცხვითი მოდელირება ოპერატიული ოკეანოგრაფიის ამოცანათა ჩარჩოებში

ალექსანდრე გრიგორიევი, ანდრეი ზაცეპინი

შავი ზღვის წყლების (რუსეთის ზონა) დინამიკის მოდელირება ხორციელდებოდა ევროპული პროექტების ARENA და ECOOP და რუსეთის პროექტის JISWO ჩარჩოებში პრინსტონის ოკეანის მოდელის (POM) საფუძველზე. შავი ზღვის დინამიკის დიაგნოზი და სამდღიანი პროგნოზი ტარდებოდა ყოველდღიურ რეჟიმში 1კმ ჰორიზონტალური გარჩევისუნარიანობით ზღვის აუზის რუსეთის ზონისათვის. მოყვანილია გამოთვლების მაგალითები და მათი შედარება დისტანციური (თანამგზავრული) ზონდირებისა და *in-situ* (ჰიდროლოგიური დაკვირვებები) მონაცემებთან, განიხილება მოდელის ვალიდაციის შედეგები. მოდელური შედეგები ასახავენ დაკვირვებულ რეალურ დინამიკურ სტრუქტურებს. სივრცითი გარჩევისუნარიანობის გადიდება საშუალებას იძლევა აღვწეროთ ჰიდროლოგიური სტრუქტურის დეტალები

(გრიგალები ჰორიზონტალური სივრცითი ზომებით ~10 კმ), რომელთა იდენტიფიკაცია დიდმასშტაბურ მოდელებში პრინციპულად შეუძლებელია. მოდელური და დაკვირვებული პროფილები ძალიან მსგავსია. სინოპტიკური გრიგალების სივრცითი ზომები და ჰორიზონტალური მდებარეობა, რომლებიც აისახება მარილიანობის მოდელურ ველში, კარგ შესაბამისობაშია თანამგზავრულ გამოსახულებებთან. მოდელური ტემპერატურული ველის შედარება თანამგზავრულ მონაცემებთან აჩვენებს კარგ რაოდენობრივ დამთხვევას.

Information for contributors

Papers intended for the Journal should be submitted in two copies to the Editor-in-Chief. Papers from countries that have a member on the Editorial Board should normally be submitted through that member. The address will be found on the inside front cover.

1. Papers should be written in the concise form. Occasionally long papers, particularly those of a review nature (not exceeding 16 printed pages), will be accepted. Short reports should be written in the most concise form not exceeding 6 printed pages. It is desirable to submit a copy of paper on a diskette.
2. A brief, concise abstract in English is required at the beginning of all papers in Russian and in Georgian at the end of them.
3. Line drawings should include all relevant details. All lettering, graph lines and points on graphs should be sufficiently large and bold to permit reproduction when the diagram has been reduced to a size suitable for inclusion in the Journal.
4. Each figure must be provided with an adequate caption.
5. Figure Captions and table headings should be provided on a separate sheet.
6. Page should be 20 x 28 cm. Large or long tables should be typed on continuing sheets.
7. References should be given in the standard form to be found in this Journal.
8. All copy (including tables, references and figure captions) must be double spaced with wide margins, and all pages must be numbered consecutively.
9. Both System of units in GGS and SI are permitted in manuscript
10. Each manuscript should include the components, which should be presented in the order following as follows:
    Title, name, affiliation and complete postal address of each author and dateline.
    The text should be divided into sections, each with a separate heading or numbered consecutively.
    Acknowledgements. Appendix. Reference.
11. The editors will supply the date of receipt of the manuscript.

CONTENTS

სარჩევი

საქართველოს გეოფიზიკური საზოგადოების ჟურნალი

სერია ბ. ატმოსფეროს, ოკეანესა და კოსმოსური პლაზმის ფიზიკა

ჟურნალი იბეჭდება საქართველოს გეოფიზიკური საზოგადოების პრეზიდიუმის დადგენილების საფუძველზე

ტირაჟი 200 ცალი

ЖУРНАЛ ГРУЗИНСКОГО ГЕОФИЗИЧЕСКОГО ОБЩЕСТВА

Серия Б. Физика Атмосферы, Океана и Космической Плазмы

Журнал печатается по постановлению президиума Грузинского геофизического общества

Тираж 200 экз

JOURNAL OF THE GEORGIAN GEOPHYSICAL SOCIETY

Issue B. Physics of Atmosphere, Ocean and Space Plasma

Printed by the decision of the Georgian Geophysical Society Board

Circulation 200 copies